DEVELOPMENT OF PROGRESSIVE FAILURE MODELS AND THEIR APPLICATION TO OPEN HOLE COMPOSITE LAMINATES AND WIND TURBINE BLADES

A THESIS SUBMITTED TO
THE GRADUATE SCHOOL OF NATURAL AND APPLIED SCIENCES
OF
MIDDLE EAST TECHNICAL UNIVERSITY

BY

MEVLÜT CAN MUYAN

IN PARTIAL FULFILLMENT OF THE REQUIREMENTS
FOR
THE DEGREE OF DOCTOR OF PHILOSOPHY
IN
AEROSPACE ENGINEERING

MARCH 2023

Approval of the thesis:

DEVELOPMENT OF PROGRESSIVE FAILURE MODELS AND THEIR APPLICATION TO OPEN HOLE COMPOSITE LAMINATES AND WIND TURBINE BLADES

submitted by **MEVLÜT CAN MUYAN** in partial fulfillment of the requirements for the degree of **Doctor of Philosophy** i**n Aerospace Engineering, Middle East Technical University** by,

Prof. Dr. Halil Kalıpçılar
Dean, Graduate School of **Natural and Applied Sciences** _____

Prof. Dr. Serkan Özgen
Head of the Department, **Aerospace Engineering** _____

Prof. Dr. Demirkan Çöker
Supervisor, **Aerospace Engineering, METU** _____

Examining Committee Members:

Prof. Dr. Altan Kayran
Aerospace Engineering, METU _____

Prof. Dr. Demirkan Çöker
Aerospace Engineering, METU _____

Prof. Dr. Levend Parnas
Mechanical Engineering, TEDU _____

Assoc. Prof. Dr. Barış Sabuncuoğlu
Mechanical Engineering, Hacettepe University _____

Assoc. Prof. Dr. Ercan Gürses
Aerospace Engineering, METU _____

Date: 02.03.2023

I hereby declare that all information in this document has been obtained and presented in accordance with academic rules and ethical conduct. I also declare that, as required by these rules and conduct, I have fully cited and referenced all material and results that are not original to this work.

Name Last name : Mevlüt Can Muyan

Signature :

ABSTRACT

DEVELOPMENT OF PROGRESSIVE FAILURE MODELS AND THEIR APPLICATION TO OPEN HOLE COMPOSITE LAMINATES AND WIND TURBINE BLADES

Muyan, Mevlüt Can
Doctor of Philosophy, Aerospace Engineering
Supervisor : Prof. Dr. Demirkan Çöker

March 2023, 235 pages

The usage of composite materials in the load carrying aircraft structures has been increasing in the last few decades. Composite materials are also used in wind turbine blades, which are designed to endure extreme weather conditions without being damaged over a lifespan of 20 years. Within the framework of this dissertation, the root cause and propagation of damage in two types of composite structures subjected to uniaxial and combined loading are studied. In the dissertation three different studies are presented. The first study is on the development of a proposed analytic Extended Point Stress Method (EPSM) for the strength prediction of quasi-isotropic carbon-epoxy open hole laminates. EPSM is advantageous over traditional analytical models as it is applicable not only under uniaxial but also combined loading. The second study is on a finite element model incorporating continuum damage model and cohesive zone model for the strength prediction of quasi-isotropic carbon-epoxy open hole tension (OHT) laminates. In the study, the necessity of modeling interface failure in OHT laminates that fail in brittle failure mode with minimal delamination is highlighted. The third study deals with the FE model validation and progressive

damage analysis of a 5-meter composite wind turbine blade under monotonic loading. After validating the FE model based on modal tests, blade progressive damage analysis under flap-wise (max) loading is conducted. The failure initiation region is predicted in the blade root transition region and the blade collapses after maximum loading level.

Keywords: Open hole composite laminate, Finite element model, Progressive damage analysis, Wind turbine blade, Continuum damage model

ÖZ

İLERLEMELİ HASAR MODELLERİNİN GELİŞTİRİLMESİ VE DELİKLİ KOMPOZİT PLAKALAR VE RÜZGAR TÜRBİN KANATLARINA UYGULANMASI

Muyan, Mevlüt Can
Doktora, Havacılık ve Uzay Mühendisliği
Tez Yöneticisi: Prof. Dr. Demirkan Çöker

Mart 2023, 235 sayfa

Son yirmi yılda, yük taşıyan hava aracı yapılarında kompozit malzemelerin kullanımı artmıştır. Kompozit malzemeler aynı zamanda, 20 yıllık çalışma ömrü boyunca hasar görmeden aşırı hava koşullarına dayanacak şekilde tasarlanan rüzgar türbini kanatlarında da kullanılmaktadır. Bu tez kapsamında, tek eksenli ve birleşik yükleme altındaki iki çeşit kompozit yapıda görülen hasarın ana nedeni ve gelişimi incelenmektedir. Tezde üç farklı çalışma sunulmaktadır. İlk çalışma, kuasi-izotropik karbon-epoksi delikli laminatların dayanım tahmini için önerilen analitik Genişletilmiş Nokta Gerilme Yöntemi (GNGY)'nin geliştirilmesi hakkındadır. GNGY sadece tek eksenli değil aynı zamanda birleşik yüklemeler altında da kullanılabilmesi açısından geleneksel analitik modellere göre daha avantajlıdır. İkinci çalışma, kuasi-izotropik karbon-epoksi delikli çeki laminatların (DÇL) dayanım tahmininde kullanılan sürekli ortam hasar modeli ve kohesif arayüz hasar modelini içeren sonlu elemanlar modeli hakkındadır. Çalışmada, minimal delaminasyonla gevrek modda kırılan DÇL kompozit laminatlarında kohesif arayüz hasar modellesinin yapılmasının gerekliliği vurgulanmaktadır. Üçüncü çalışma ise 5-metrelik bir kompozit rüzgar türbini kanadı sonlu modelinin dogrulanması ve

monotonik yükleme altında ilerlemeli hasar analizi ile ilgilidir. Sonlu elemanlar modelinin modal analiz sonuçlarına dayalı doğrulanmasının ardından, kanadın kelebekleme (maksimum) yüklemesi altında ilerlemeli hasar analizi gerçekleştirilmiştir. Hasar başlama bölgesinin kanat kök geçiş bölgesinde olduğu tahmin edilmiştir ve kanadın, maksimum yükleme seviyesi sonrasında çökeceği sonucuna varılmıştır.

Anahtar Kelimeler: Delikli kompozit laminat, Sonlu elemanlar modeli, İlerlemeli hasar modeli, Rüzgar türbin kanadı, Sürekli ortam hasar modeli

To my father Dr. med. Yılmaz Muyan

ACKNOWLEDGEMENTS

First of all, I would like to express my deepest gratitude to my advisor Professor Demirkan Çöker for being a dedicated advisor at every stage of my PhD and for providing essential guidance while I delved into interesting research topics. His in-depth knowledge, experience, positive energy, and high motivation for research allowed me to overcome the challenges I faced during my doctoral studies.

I would also like to thank my dissertation committee members Professor Levend Parnas and Professor Altan Kayran for providing me with valuable comments, which I have benefited from greatly. Their constructive feedback and insightful comments have helped me to refine and improve my work. In addition, I wish to thank my dissertation examining committee members Professor Ercan Gürses and Professor Barış Sabuncuoğlu. Their questions and comments enabled me to improve my dissertation further in the right direction.

I am also grateful to the many past and present graduate students of Professor Çöker who I feel lucky to consider as my friends. Specifically, I would like to thank Dr. Aydın Amireghbali for his unconditional, lasting friendship and fruitful scientific discussions. I am grateful to Onur Ali Batmaz, Onur Miraç Bozkurt, Ali Gezer, Tamer Tahir Ata, Ahmet Çevik, Burcu Demirtaş, Erdem Dinler, Tutku Ilgın Özcan, Umut Altuntaş, Ogün Burak Yavuz, Emine Burçin Özen and Pakize Temiz for supporting and encouraging me with their inspiring discussions and valuable insights. Moreover, I would like to thank Dr. Saeid Dashatan, Professor Touraj Farsadi and Onur Çakmak for their friendship and supporting me during my research.

Next, I wish to express my gratitude to Professor Oğuz Uzol and RÜZGEM Center for Wind Energy established in the Middle East Technical University for providing me with the resources and facilities necessary to conduct this research.

Last but not the least, I would like to express my gratitude to my family. I dedicate my dissertation to my father Yılmaz Muyan, who motivated me to do a PhD. He always encouraged my curiosity for science. Similarly, my mother Candan Muyan always believed in me and provided support especially in the difficult periods of my doctoral studies. Her endless love, generosity, positivity, and strong personality made me believe that people can overcome challenges, if they do not give up and remain determined. Additionally, I thank my brother Cem Muyan and sister Pınar Muyan-Özçelik for being on my side no matter what life brings; their support has made me to feel secure and confident.

TABLE OF CONTENTS

ABSTRACT v

ÖZ vii

ACKNOWLEDGEMENTS x

TABLE OF CONTENTS xii

LIST OF TABLES xvi

LIST OF FIGURES xvii

LIST OF ABBREVIATIONS xxvi

LIST OF SYMBOLS xxviii

1 INTRODUCTION 1

2 LITERATURE REVIEW 7

2.1 Strength Prediction of Open Hole Composite Laminates 7

2.1.1 Analytical Approaches 7

2.1.2 Numerical Approaches 13

2.2 Progressive Damage Analysis of Wind Turbine Blades 21

3 PROGRESSIVE FAILURE ANALYSIS OF UNNOTCHED AND OPEN-HOLE COMPOSITE LAMINATES 27

3.1 Analytical Modeling 27

3.1.1 Composite Laminate Strength Calculation Methods 27

3.1.2 Open Hole Composite Laminate Strength Calculation Method 52

3.2 Numerical Modeling 68

3.2.1 Intralaminar Damage Model 68

3.2.2 Interlaminar Damage Model 74

4 PLAIN STRENGTH ANALYSIS OF COMPOSITE LAMINATES 79
4.1 Plain Strength Analysis Procedure 79
4.2 Results from the Plain Strength Analysis of Multidirectional Laminates 87
4.2.1 Validation of Biaxial Failure Envelopes 87
4.2.2 Validation of the Uniaxial Failure Envelopes with Respect to Fiber Orientation 89
4.2.3 Comparison of Failure Envelopes for IMA/M21 Laminate under Biaxial-Loading 91
4.2.4 Comparison of Unidirectional Strength Curves for IMA/M21 Laminate with Respect to Fiber Orientation 92
4.2.5 Comparison with World Wide Failure Exercise 94
4.3 Conclusions 95
5 ANALYTICAL APPROACH FOR THE OPEN HOLE STRENGTH PREDICTION OF COMPOSITE LAMINATES SUBJECTED TO UNIAXIAL AND BIAXIAL LOADING CONDITIONS 97
5.1 Introduction 97
5.2 Methodology 98
5.2.1 Open Hole Composite Laminate with an Elliptical Hole Subjected to Combined Loading..... 98
5.2.2 Open Hole Composite Laminate with a Circular Hole Subjected to Combined Loading..... 107
5.3 Results and Discussions 112
5.3.1 Open Hole Tension 112
5.3.2 Open Hole Compression 118
5.3.3 Open Hole under Multiaxial Loading 120

5.4 Summary and Conclusions 124

6 NUMERICAL APPROACH FOR THE PREDICTION OF SIZE EFFECTS ON OPEN HOLE TENSION LAMINATES 125

6.1 Introduction 125

6.2 Methodology 126

6.2.1 Intralaminar Damage Model 126

6.2.2 Interlaminar Damage Model 132

6.2.3 Finite Element Model and Boundary Conditions 133

6.2.4 Mesh Convergence Study 135

6.2.5 Validation Study of the ABAQUS User Subroutine (Puck Continuum Damage Model) 138

6.3 Results 144

6.3.1 FE Modeling Approach Using Classical Lamination Theory 144

6.3.2 FE Modeling Approach Using Continuum Shell Elements and Interface Model 151

6.4 Conclusions 168

7 FE MODEL VALIDATION AND PROGRESSIVE DAMAGE ANALYSIS OF A 5-M COMPOSITE WIND TURBINE BLADE UNDER MONOTONIC LOADING 171

7.1 Introduction 171

7.2 Methodology 172

7.2.1 FE Model of the 5-m RUZGEM Wind Turbine Blade 172

7.2.2 Experimental Modal Analysis of the 5-m RUZGEM Wind Turbine Blade 176

7.2.3 Intralaminar Damage Model 178

7.3 Results 183
7.3.1 Validation of the 5-m RUZGEM Wind Turbine Blade FE Model based on the Experimental Modal Analysis 183
7.3.2 Progressive damage analysis of the 5-m RUZGEM Wind Turbine Blade using Puck's damage model 185
7.4 Conclusions 190
8 CONCLUSIONS AND FUTURE WORK 191
8.1 Overall Conclusions 191
8.2 Future Work 193
REFERENCES 195
APPENDICES 209
A. Material Database 209
B. Validation Study for the Stress Field Generated by the Extended Point Stress Method MATLAB Code 210
C. Test Matrix of UD Tape Materials for Determining the Characteristic Distance 227
CURRICULUM VITAE 231

LIST OF TABLES

TABLES

Table 5.1 Mechanical Properties of the IM7/8552 lamina. 113
Table 5.2 Comparison between predictions and experiments for the $[90/0/45/-45]_{3s}$ lay-up. 113
Table 5.3 Mechanical Properties of the IM7/8552 Lamina. 115
Table 5.4 Comparison between predictions and experiments for the $[45/90/-45/0]_{4S}$ lay-up. 115
Table 5.5 Mechanical Properties of the M21/T800 Lamina 117
Table 5.6 Comparison between predictions and OHT experiments for the $[90/45/0/-45]_{3S}$ lay-up. 117
Table 5.7. Comparison between predictions and OHC experiments for the $[90/45/0/-45]_{3S}$ lay-up (Longitudinal compressive stress of the lamina is taken as 1231 MPa [120]. 119
Table 5.8. Comparison between predictions and OHC experiments for the $[90/45/0/-45]_{3S}$ lay-up (Longitudinal compressive stress of the lamina is taken as 1400 MPa). 120
Table 5.9 Mechanical Properties of the IM7/8552 lamina [121]. 122
Table 6.1 Mechanical Properties of the IM7/8552 lamina. 127
Table 6.2 Interlaminar Material Properties. 128
Table 6.3 Comparison between predictions and experiments for the IM7-8552 CFRP $[90/0/45/-45]_{3s}$ lay-up. 147
Table 7.1. Material properties and design allowables of RÜZGEM blade for static analysis [137]. 174
Table 7.2. Degradation rules according to the failure mode. 180
Table 7.3 Comparison of the 5-m RUZGEM blade modal analysis results between tests and FE simulations (adhesive mass included). 184

LIST OF FIGURES

FIGURES

Figure 2.1. Fracture model proposed by Waddoups et al. [14]..... 8
Figure 2.2. Point stress (a) and (b) average stress criterion [15]. 9
Figure 2.3. Cohesive Zone Model proposed by Soutis et al. [24]..... 10
Figure 2.4. (a) Representation of the line crack along y-axis caused by microbuckling under compression-tension loading (b) strength prediction procedure for an XAS/914C $(-45/0/-45/90)_{2s}$ laminate under compression tension loading (loading ratio, $\lambda = -0.3$) [28]. 12
Figure 2.5. Strength reduction of $[0/\pm45/90]_s$ graphite/epoxy open hole laminates subjected to 1:1 biaxial tensile loading [30]. 12
Figure 2.6. Schematic representation of the sublaminate and ply-level scaling methodologies [36]. 14
Figure 2.7. Three different damage mechanisms seen in the OHT tests on quasi-isotropic laminates [37]..... 14
Figure 2.8. Three different damage mechanisms seen in the OHC tests on quasi-isotropic laminates (a) brittle, (b) push-out (c) delamination [35]..... 15
Figure 2.9. Mesh pattern used in the OHT specimen fe models with implementation regions of cohesive interface elements (laminate thickness=2 mm, ply-level scaling laminate configuration) [38]. 16
Figure 2.10. Four meshes for different element sizes. 18
Figure 2.11. Mesh refinement study of different numerical models..... 19
Figure 2.12. (a) Zigzag approach used for approximation the linear softening in a stress-strain curve (b) piecewise constant stiffness values with slight changing strain values [43]. 20
Figure 2.13. Damage evolution in the quarter of the deformed main spar: (a) damage state 1 before structural instability (b) damage state after structural instability ([55],[56])..... 22

Figure 2.14. Comparison between the predicted and observed damage in the root transition region of the 52.3 m composite wind turbine blade [59]. 23
Figure 2.15. 5-m glass-fiber-reinforced-ploymer RÜZGEM wind turbine blade. .. 25
Figure 3.1*:* Failure envelope for unidirectional lamina subjected to biaxial normal loading using maximum stress theory [69]. 30
Figure 3.2*:* Failure envelope for unidirectional lamina subjected to biaxial normal loading using maximum strain theory [69]. 32
Figure 3.3*:* Basic stressings of UD-composite [79] 39
Figure 3.4. Stress of the UD-lamina and stresses on a possible (IFF) fracture plane parallel to fibers [82]. 40
Figure 3.5. Fracture under uniaxial compressive stress $\sigma 2c$ [82]. 41
Figure 3.6*:* (a) Damage hysteresis (DH) caused by micro cracks in a UD-layer in a loading/unloading cycle (b) shear stress $\tau m21$, and transformed principal stresses σmII and $\sigma mIII$ (c) micro cracks between fibers [83]. 45
Figure 3.7. Master Fracture Body in $(\sigma n, \tau nt, \tau n1)$ coordinate system [79]. 46
Figure 3.8. Search for the fracture plane in UD composite [82]. 47
Figure 3.9. Representation stress exposure on the $(\sigma 2, \tau 21)$-stress plane (Lutz, 2006) [79]. 48
Figure 3.10. Laminate strength analysis and load-deformation behavior [73]..... 51
Figure 3.11. Plate with an area S subjected to external forces Xn and Yn at the external contour [90]. 60
Figure 3.12. Plate with an area S subjected to external forces Xn and Yn at the external contour [90]. 61
Figure 3.13. Coordinates of a composite lamina with an elliptical opening subjected to combined loading [18]..... 63
Figure 3.14. Total stress in an infinite plate can be decomposed into two stress states I and II [92]. 65
Figure 3.15. A finite width anisotropic plate with an elliptical opening [86]. 65
Figure 3.16. Stress-strain linear softening response 71

Figure 3.17. Adjusting the stress-strain softening response for different characteristic element sizes. 72
Figure 3.18. Bi-linear damage evolution law. 73
Figure 3.19. The bilinear traction-separation response implemented in the Cohesive Zone Model [106]. 76
Figure 3.20. The bilinear traction-separation response for mixed modes [108]. 77
Figure 4.1: Multidirectional laminate with individual plies and the coordinates [69]. 80
Figure 4.2. Flowchart for the Failure Analysis of a Composite Tape Laminate Using Mode Based Failure Criteria (FPF, First Ply Failure) [69]. 86
Figure 4.3. PLS MATLAB Code for the Progressive Failure Criteria (Yamada-Sun and Puck) of Composite Tape Materials 87
Figure 4.4. Failure envelopes for carbon/epoxy (AS4/3501-6) lamina subjected to biaxial normal loading using different failure criteria. 88
Figure 4.5. Failure envelopes for carbon/epoxy (AS4/3501-6) lamina subjected to transverse normal and shear loading using different failure criteria. 88
Figure 4.6. Normalized Tensile Strength of Unidirectional and Angle-Ply Laminates with Respect to Fiber Orientation (AS4/3501-6 Carbon/Epoxy, Tsai-Wu Criterion, FPF). 89
Figure 4.7. Normalized Compressive Strength of Unidirectional and Angle-Ply Laminates with Respect to Fiber Orientation (AS4/3501-6 Carbon/Epoxy, Tsai-Wu Criterion, FPF). 90
Figure 4.8. Normalized In-Plane Shear Strength of Unidirectional and Angle-Ply Laminates with Respect to Fiber Orientation (AS4/3501-6 Carbon/Epoxy; Tsai-Wu Criterion; FPF). 90
Figure 4.9. Bi-axial failure Envelope for Quasi-Isotropic IMA/M21E Laminate Subjected to Biaxial Normal Loading Using Different Failure Criteria. 92
Figure 4.10. Uniaxial Tensile and Compressive Strength of IMA/M21E laminate (60/30/10 lay-up) with Respect to Fiber Orientation. 93

Figure 4.11. Comparison between the predicted and measured biaxial failure stresses for (0º/±45º/90º) AS4/3501-6 laminates [111]. 95
Figure 5.1. Lamina with an elliptical opening subjected to uniaxial loading [18]. 101
Figure 5.2. Characteristic curve of the laminate with an elliptical opening under combined loading. 103
Figure 5.3. Flowchart of the proposed methodology for the open composite laminate strength prediction. 106
Figure 5.4. Characteristic distance d_0 and coordinate system of a notched composite laminate used for the EPSM. 107
Figure 5.5. OHT strength vs. hole diameter plot for $[90/0/45/-45]_{3S}$ lay-up (PS, AS, IFM and EPSM methods calibrate the characteristic distance at point a) ([9],[13]) 114
Figure 5.6. Open Hole Tension Strength vs. Hole Diameter (PS, AS and IFM methods calibrate the characteristic distance at point a, whereas EPSM calibrates at point b) [13]. 116
Figure 5.7. Open Hole Tension Strength vs. Hole Diameter (PS, AS, IFM and EPSM methods calibrate the characteristic distance at point a) (Ref. [13] [26]). . 118
Figure 5.8. Open Hole Compressive Strength vs. Hole Diameter (PS, AS, IFM and EPSM methods calibrate the characteristic distance at point a) [26]. 120
Figure 5.9. Comparison of biaxial failure envelopes for $[0/45/90/-45]_s$ IM7/8552 laminate [121]. 122
Figure 5.10. Failure pattern of the open hole cruciform specimen subjected to: (a) $1, -1$ (b) $1, 0$ (c) $1, 1$ loading ratios. 123
Figure 6.1. Brittle failure modes of the IM7-8552 OHT specimen with w/d=6 (Camanho et al. (2007) [9]). 126
Figure 6.2. Bi-linear damage evolution law. 131
Figure 6.3. Boundary conditions of the OHT laminate fe model. 134

Figure 6.4. OHT finite element models (hole diameter = 6 mm) with different mesh patterns (a) structured mesh (total number of nodes=4032) (b) non-structured mesh (total number of nodes=14103). 135
Figure 6.5. Influence of the mesh density on the strength of the IM7-8552 CFRP $[90/0/\pm45]_{3s}$ OHT specimen with a hole diameter of 6 mm..... 136
Figure 6.6. OHT finite element models (hole diameter = 6 mm) created using different mesh densities: (a) total number of 1092 nodes (element size=0.5 mm in the vicinity of the hole) (b) total number of 2366 nodes (element size=0.3 mm in the vicinity of the hole) (c) total number of 4032 nodes (element size=0.25 mm in the vicinity of the hole) (d) total number of 4580 nodes (element size=0.20 mm in the vicinity of the hole). 137
Figure 6.7. FE Model of unit cell indicating boundary conditions for uniaxial tension in fiber direction. 140
Figure 6.8. Stress-strain response for the IM7-8552 UD (0-degree) lamina under uniaxial tension. 140
Figure 6.9. FE Model of unit cell indicating loads and boundary conditions for uniaxial compressions in fiber direction. 141
Figure 6.10. Stress-strain response for the IM7-8552 UD (0-degree) lamina under uniaxial compression. 141
Figure 6.11. FE Model of unit cell indicating loads and boundary conditions for uniaxial tension in matrix direction. 142
Figure 6.12. Stress-strain response for the IM7-8552 UD (90-degree) lamina under uniaxial tension. 142
Figure 6.13. FE Model of unit cell indicating loads and boundary conditions for uniaxial compression in matrix direction. 143
Figure 6.14. Stress-strain response for the IM7-8552 UD (90-degree) lamina under uniaxial tension. 143
Figure 6.15. Relation between the applied stress and the longitudinal displacement during the numerical simulation of the IM7-8552 CFRP $[90/0/\pm45]_{3s}$ OHT specimens with different hole sizes using ABAQUS UMAT. 146

Figure 6.16. Strength predictions of the IM7-8552 CFRP $[90/0/\pm45]_{3s}$ OHT specimens with varying hole sizes. 146
Figure 6.17. Average stress distribution for different hole sizes (D=2,6,10) in IM7-8552 CFRP IM7-8552 CFRP $[90/0/\pm45]_{3s}$ OHT specimens in the elastic region before load drop. 148
Figure 6.18. Fiber tensile damage evolution at load drop of the IM7-8552 CFRP $[90/0/\pm45]_{3s}$ OHT specimens with hole sizes (a) 2 mm (b) 6 mm (c) 10 mm using Puck's damage model (ABAQUS UMAT). 149
Figure 6.19. Fiber tensile damage evolution at load drop of the IM7-8552 CFRP $[90/0/\pm45]_{3s}$ OHT specimens with hole sizes (a) 2 mm (b) 4 mm (c) 6 mm (d) 10 mm using Hashin damage model (ABAQUS built-in damage model). 150
Figure 6.20. Fiber tensile damage evolution shortly after load drop for the IM7-8552 CFRP $[90/0/\pm45]_{3s}$ OHT specimen with a hole diameter of 6 mm (a) structured mesh (b) non-structured mesh. 151
Figure 6.21. FE modeling approach of the IM7-8552 CFRP OHT laminate with a hole diameter of 2 mm using continuum shell elements with perfect bonding at ply interfaces. 152
Figure 6.22. Comparison between the experiments and numerical simulation of the IM7-8552 CFRP $[90/0/\pm45]_{3s}$ OHT specimen using plane stress (S4R) and continuum shell (SC8R) elements with perfect bonding at ply interfaces. 153
Figure 6.23. Fiber damage evolution shortly after peak load in the 0°-ply of the IM7-8552 CFRP $[90/0/\pm45]_{3s}$ OHT specimen with a hole diameter of 6 mm using (a) plane stress (S4R) and (b) continuum shell (SC8R) elements with perfect bonding at ply interfaces. 155
Figure 6.24. Damage pattern at peak load in the IM7-8552 CFRP $[90/0/\pm45]_{3s}$ OHT specimen with a hole diameter of 2 mm with perfect bonding at ply interfaces: (a) matrix damage in the 90° ply, (b) fiber damage in the 0°ply, (c) fiber damage in the 45° ply, (d) fiber damage in the -45° ply. 156
Figure 6.25. FE modeling approaches for the open hole tension using detached plies with SC8R elements per ply. 157

Figure 6.26. FE modeling approach for the open hole tension (hole diameter, d=6 mm) using SC8R elements per ply with COH3D8 elements at ply interfaces. 158
Figure 6.27. Relation between remote stress $\sigma\infty$ and longitudinal displacement in the IM7-8552 CFRP $[90/0/\pm45]_{3s}$ OHT specimen with a hole diameter of 2 mm using different fe modeling strategies. 159
Figure 6.28. Strength predictions of the IM7-8552 CFRP $[90/0/\pm45]_{3s}$ OHT specimen with different hole sizes (w/D=6). 161
Figure 6.29. Comparison between the experiments and numerical simulation of the IM7-8552 CFRP $[90/0/\pm45]_{3s}$ OHT specimen using plane stress (S4R) and continuum shell (SC8R) elements with perfect bonding and continuum shell (SC8R) elements with CZM ply interfaces. 161
Figure 6.30. Damage pattern in the IM7-8552 CFRP $[90/0/\pm45]_{3s}$ OHT specimen under ultimate load (hole diameter, D = 2 mm) with frictionless contact at ply interfaces: (a) matrix damage in the 90° ply, (b) fiber damage in the 0° ply, (c) no fiber damage in the 45º ply (d) no damage in the -45º ply. 164
Figure 6.31. Damage extent in the IM7-8552 CFRP $[90/0/\pm45]_{3s}$ OHT top sublaminate under ultimate load (hole diameter, D = 2 mm) with Cohesive Zone Model at ply interfaces..... 165
Figure 6.32. Damage extent in the IM7-8552 CFRP $[90/0/\pm45]_{3s}$ OHT middle sublaminate under ultimate load (hole diameter, D = 2 mm) with Cohesive Zone Model at ply interfaces..... 166
Figure 6.33 Damage extent in the IM7-8552 CFRP $[90/0/\pm45]_{3s}$ OHT bottom (center) sublaminate under ultimate load (hole diameter, D = 2 mm) with Cohesive Zone Model at ply interfaces..... 167
Figure 7.1. Blade assembly for the 5-meter RUZGEM wind turbine blade [137]. 172
Figure 7.2. Mesh independence study of the 5-meter RUZGEM wind turbine blade, where maximum tip displacement and maximum von Mises stress is used as the convergence criterion. 174

Figure 7.3. FE models of the 5-meter RUZGEM turbine blade components: (a) pressure side (b) internal flange (c) chassis (d) suction side. 175
Figure 7.4. (a) Flapwise (max) bending moment distribution on the RUZGEM blade (b) loads and boundary conditions of the RUZGEM blade FE model. 175
Figure 7.5. (a) Distribution of the MASS21 elements in the spanwise direction (b) distribution of the MASS21 elements in the cross-section of the RÜZGEM blade fe model. 177
Figure 7.6. Experimental modal analysis test set-up of the RÜZGEM blade (a) positioning of the accelerometers on the RÜZGEM blade (b) mounting of the shaker to the RÜZGEM blade [140]. 177
Figure 7.7. Validation of the ANSYS APDL Code for the progressive failure analysis of a $[0/90]_s$ GFRP MY750 laminate under σx uniaxial tension load based on Puck's damage model against experimental data [111]. 182
Figure 7.8. Validation of the ANSYS APDL Code for the progressive failure analysis of a $[0/\pm45/90]_s$ CFRP AS4 3501-6 laminate under σy uniaxial tension load based on Puck's damage model [111]. 182
Figure 7.9. Comparison of the 5-m RÜZGEM blade 1st eigenmode between (a) experiment and (b) FE simulation, 5th eigenmode between (c) experiment and (d) fe simulation. 184
Figure 7.10. Load-displacement curves of the 5-m RÜZGEM blade using linear elastic model and progressive damage model (Puck) under flapwise (max) loading. 185
Figure 7.11. Total deformation of the 5-m RÜZGEM blade at 99% flapwise (max) loading (scale factor: × 2). 186
Figure 7.12. Damage evolution – IFF (A) or IFF (B) – in the pressure side, internal flange, spar and suction side of the blade (from top to bottom in a panel) at 93% of flapwise (max) loading. 188
Figure 7.13. Damage evolution – FF or IFF (C) – in the pressure side, internal flange, spar and suction side of the blade (from top to bottom in a panel) at 93% of flapwise (max) loading. 188

Figure 7.14. Element failure pattern in the pressure side, internal flange, spar and suction side of the blade (from top to bottom in a panel) at 99% of flapwise (max) loading..... 189
Figure 7.15. Element failure pattern in the pressure side, internal flange, spar and suction side of the blade (from top to bottom in a panel) before blade collapse under flapwise (max) loading. 189

LIST OF ABBREVIATIONS

APDL ANSYS	Parametric Design Language
AS	Average Stress
ASC	Average Stress Criterion
ASTM	American Society for Testing and Materials
CDM	Continuum Damage Model
CFRP	Carbon-fiber-reinforced-polymer
CLT	Classical Lamination Theory
CZM	Cohesive Zone Model
DH	Damage Hysteresis
EPSM	Extended Point Stress Method
FEA	Finite Element Analysis
FF	Fiber Failure
FFF	First Fiber Failure
FFM	Finite Fracture Model
FFT	Fast-Fourier-Transform
FPF	First Ply Failure
FPFF	First Ply First Fiber
GFRP	Glass-Fiber-Reinforced-Polymer
IFF	Inter Fiber Failure
IFM	Inherent Flaw Model

LEFM	Linear Elastic Fracture Mechanics
OH	Open Hole
OHC	Open Hole Compression
OHT	Open Hole Tension
PLS	Plain Strength
PS	Point Stress
PSC	Point Stress Criterion
RF	Reserve Factor
RFF	Fiber Reserve Factor
RFM	Matrix Reserve Factor
SR	Strength Reduction
UD	Uni-Directional
UMAT	User Material Subroutine
UPL	Ultimate Ply Failure
WWFE	World-Wide Failure Exercise
YS	Yamada-Sun

LIST OF SYMBOLS

$2a$	Major diameter
a_{ij}	Compliances of the laminate
a, b, c, d	Laminate compliance matrices
A, B, D	Laminate stiffness matrices
A_{IP}	Area related to the integration point of an element
B	Mixed mode ratio
C_d	Damaged elasticity matrix
D_k	Linear differential operators
d_f	Damage variable for fiber failure mode
d_m	Damage variable for matrix failure mode
d_s	Damage variable for shear failure mode
E_M	Elasticity modulus for different damage modes
$E_{\parallel}, E_{\parallel f}$	The elasticity moduli of lamina and fibre
$F(x, y)$	Airy stress function
$f_{E,FF}^{T}$	Stress exposure for fiber failure under tension
$f_{E,FF}^{C}$	Stress exposure for fiber failure under compression
$f_{E,IFF}^{A}$	Stress exposure for inter fiber failure mode A
$f_{E,IFF}^{B}$	Stress exposure for inter fiber failure mode B
$f_{E,IFF}^{C}$	Stress exposure for inter fiber failure mode C
f_i	Second order stress tensors

f_{ij}	Fourth order stress tensors
G_M	Fracture toughness for different damage modes
G_1^+	Longitudinal tensile fracture energy
G_1^-	Longitudinal compressive fracture energy
G_2^-	Transverse tensile fracture energy
G_1^+	Transverse compressive fracture energy
G_{Ic}	Mode I critical fracture energy
G_{IIc}	Mode II critical fracture energy
K_I	Stress intensity factor
K_{Ic}	Critical stress intensity factor
K_T	Stress concentration for finite plate
K_T^∞	Stress concentration for infinite plate
L_c	Characteristic element length
l	Crack extension at failure
$l_{ch,II}$	Mode II characteristic length for infinite bodies
$l_{ch,slender,II}$	Mode II characteristic length for slender bodies
$p_{\perp II}^{(+)}, p_{\perp II}^{(-)}, p_{\perp\perp}^{(-)}$	Inclination parameters used in Puck's damage model
d_o	Characteristic distance
S_c	Shear strength of the lamina in the symmetric cross-ply laminate
S_L	Longitudinal lamina shear strength
S^T	Transverse lamina shear strength

t_L	Total laminate thickness
t_n, t_s, t_t	In-plane normal, in-plane shear and out-of-plane shear tractions
t_n^0, t_s^0, t_t^0	Maximum allowable values for in-plane normal, in-plane shear and out-of-plane shear tractions
U_x, U_y, U_z	Translational degrees of freedom
UR_x, UR_y, UR_z	Rotational degrees of freedom
$[Q]_{1,2}$	Ply stiffnesses
W	Plate width
X	Lamina strength in longitudinal directions
X_M	Lamina strength for different damage modes
X_N, Y_N	External forces
X_T	Tensile lamina strength in fiber direction
X_C	Compressive lamina strength in fiber direction
Y_T	Tensile lamina strength in transverse fiber direction
Y_C	Compressive lamina strength in transverse fiber direction
S	Ply shear strength
z_k	Through-the-thickness coordinate
σ_1	Stress component in fiber direction
σ_2	Stress component in transverse fiber direction
σ_6	Shearing stress in 1-2 plane
$[\sigma]_{1,2}^k$	Layer stresses

σ_n	Normal stress on the fracture plane
$\sigma_{\parallel}^{t}, \sigma_{\parallel}^{c}, \sigma_{\perp}^{c}, \sigma_{\perp}^{t}, \tau_{\perp\perp}, \tau_{\perp\parallel}, \tau_{\parallel\perp}$	Stressings (applied stress mode) used in Puck's model
σ_{eq}^{0}	Equivalent stress at damage onset
$\sigma_{II,max}$	Interfacial strength under shear loading
$\varepsilon_1, \varepsilon_2, \gamma_6$	Strain components in material principal axes
$[\varepsilon]_{1,2}^{k}$	Layer strains
$\varepsilon_{1t}^{u}, \varepsilon_{2t}^{u}$	Ultimate tensile strains in fiber and transverse fiber directions
$\varepsilon_{1c}^{u}, \varepsilon_{2c}^{u}$	Ultimate compressive strains in fiber and transverse fiber directions
ϵ_{eq}^{f}	Equivalent strain at final failure
γ_6^u	Ultimate shear strain in 1-2 plane
τ_{12}	In-plane shear stress
τ_A	Axial failure shear
τ_T	Transverse failure shear
τ_{n1}, τ_{nt}	Shear stresses on the fracture plane
μ_k	Roots of the characteristic equation
$\nu_{\perp\parallel}, \nu_{\perp\parallel f}$	Poisson ratios of the lamina and fiber
θ_{fp}	Fracture angle

CHAPTER 1

INTRODUCTION

The usage of Fiber Reinforced Polymers (FRP) are increasing in structural applications for the aerospace, automotive, energy and sports sectors in the last decades. Owing to their superior mechanical properties such as high stiffness, strength, toughness and low density, these materials are ideal candidates as lightweight structures. In addition to this, the layup sequence of the composite laminates can be readily changed to meet stiffness and strength requirements. However, FRP laminates are weak in terms of out-of-plane strength and are susceptible to impact loading and to thermal as well as environmental influences. Moreover, due to multiple interacting damage mechanisms and large scatter in their material properties, it is difficult to predict the damage modes of composite structures [1]. Due to these phenomenological observations analytical and experimental methods developed for metals turned out to be not appropriate for FRP laminates and hence other damage theories were developed for composites. Since composites exhibit complex damage mechanisms under static and fatigue loading conditions, complete physical understanding of the damage mechanims are still challenging. This is why further development of failure theories and prediction models is still ongoing. A further drawback of fiber reinforced polymers is the fact that they are costly.

To improve the economic aspects, cost reduction in manufacturing, design and certification of FRP structures is mandatory. New production techniques such as out-of-autoclave and automated manufacturing technologies help to break down the production costs. However, design and certification requirements are still expensive, because in the case of missing reliable design tools, experimental test programs could

be impractical when large number of design variations, material properties, variables are considered [2]. In order to address the issue of reducing costs in this aspect, it is essential to develop dependable and effective computational tools that have the ability to precisely predict the complete mechanical behavior of the FRP laminate from elastic behavior until structural collapse. In this context, two independent topics are studied: progressive damage analysis and strength prediction of open hole composite laminates and progressive damage analysis and strength prediction of an existing composite wind turbine blade under quasi-static loading. In this chapter, a short summary of the three novel contributions are given to the literature in the two topical areas studied in this thesis.

The first topic that is investigated in this thesis is the failure of open hole composite laminates, i.e. composite plates with circular notches that are loaded to failure. In aerospace structures, holes are frequently used for enabling bolted joints of composite plates, weight reduction, inspection of inner structure and passing wires [3]. These holes cause stress concentrations and lead to strength reduction of composite structures compared to the unnotched composite structures. Moreover, the damage mechanisms of open hole composite structures are rather complex due to the intricate nature of subcritical damage modes such as axial, fiber/matrix splits, transverse matrix cracks and delamination [4]. In order to understand the root cause of complex damage mechanisms, virtual testing methods in combination with experiments are utilized. Virtual testing is conducted at mesoscale level, complex damage mechanisms in the plies, ply interfaces and their interactions are simulated using a finite element (FE) analysis approach. At this point it is worth noting that advanced nonlinear finite element models require long computation times, which make them unsuitable for the preliminary design and optimization of structural components. As a consequence, besides numerical models, aerospace industry is striving for fast and accurate analytical methodologies for the strength prediction of open hole composite laminates. Thus, in the first part of the thesis, failure in open hole composite laminates is investigated (a) by developing a modified analytical

model in chapter 5, and (b) by using a cohesive zone method and continuum damage models in the commercial FE code ABAQUS in chapter 6.

The objective of the first study in the first topical area is to develop an accurate and fast methodology for the strength prediction of quasi-isotropic open hole composite laminates not only under uniaxial, but also under in-plane combined loading conditions. For this purpose, an analytical modelcalled the Extended Point Stress Method (EPSM) is proposed. In the EPSM stress field is calculated on ply level around a hole using Lekhnitskii's Formulation and Classical Lamination Theory (CLT). As proposed by Tan, the strength reduction (SR) due to a hole in the laminate is calculated using a quadratic composite failure model which incorporates the first-ply-fiber-failure criterion. Once the strength reduction is known, notched laminate strength is calculated from the product of the SR by the unnotched laminate strength, which is obtained by an iterative composite failure model. EPSM is validated against tests of open hole laminates with different materials, lay-ups, hole sizes and width-to-hole diameter ratios under uniaxial tension/compression loading as well as biaxial loading conditions. It is shown that EPSM is more accurate than other stress-based failure models. EPSM is also advantageous over traditional analytical models including Finite Fracture Model, as it is applicable not only under uniaxial but also combined loading conditions.

The second study in the first topical area is a numerical investigation of the strength prediction of quasi-isotropic sublaminate-scaled laminates with different hole sizes. The aim of the study is to develop the most suitable progressive damage modeling strategy for the prediction of damage evolution as well as the strength prediction of quasi-isotropic CFRP open hole tension (OHT) laminates, which fail in brittle failure mode. To this end, a Hashin failure initiation-based Continuum Damage Model is implemented in the FE models. It is found that continuum shell elements with perfect bonding and plane stress elements lead to an overprediction of the OHT strength by more than 17% and 27%, respectively. Although the OHT laminate exhibits brittle behavior with minimal delamination modeling technique utilizing continuum shell elements in combination with CZM at the interfaces, best agreement is obtained with

experiments in terms of strength prediction and the failure pattern. Hence, the significance of modeling interface damage for OHT composite laminates, which fail in brittle failure mode is highlighted.

In the second part of the thesis which covers the second topical area, the failure of an existing 5-m RUZGEM wind turbine blade subjected to flapwise maximum loading and the corresponding damage mechanisms are investigated (Chapter 7). Modern wind turbine rotor blades are complex lightweight composite structures, which need to be optimized with regard to aerodynamic and structural design aspects. At the same time manufacturing costs of the blades must be kept low. To be an attractive energy source against other energy sources, wind turbines must be competitive in terms of Cost of Energy (CoE). In order to meet this target, larger wind turbines with longer, slender and more flexible composite blades are built. However, as larger wind turbine rotor blades with innovative designs are built to harvest wind energy in complicated wind conditions, a greater number of blade failures are reported [5]. Moreover, repeating blade failures indicate that the main reason of the failure is not fully understood so that preventive measures in blade designs can be taken. It is difficult to find the root cause of the blade failures, because of the interaction between complicated loading conditions, nonlinear orthotropic material behavior, complicated geometrical structure of the blade, defects in the blade due to the manufacturing process, transportation and/or installation [6]. Developing reliable computation methods for predicting damage initiation and growth is crucial for ensuring the dependable operation of wind turbines and improving the competitiveness of wind energy among other energy sources ([7],[8]).

In thE study, the goal is to predict the main damage mechanisms, which lead to the collapse of an existing 5-meter glass-fiber-reinforced-polymer (GFRP) RÜZGEM wind turbine blade under flapwise (max) loading. For this purpose, by implementing Puck's physically based phenomenological damage model the main failure mechanisms of the blade are investigated. Within the scope of the study, the blade FE model validation methodology based on modal tests is introduced. After validating the elastic behavior of the blade with the experimental results, the

progressive damage analysis is conducted. Load is applied as a single point load in order to simulate full-scale testing conditions of blade subjected to flapwise (max) loading. As a result of progressive damage analysis utilizing Puck's model, the failure initiation region of the blade is predicted in the root transition region, at the spar-suction side intersection. Furthermore, decrease in the load-displacement curve is observed after maximum flapwise loading. The main reason for the blade collapse was found to be a combined effect of delamination and fiber failure.

An outline of the thesis is as follows: In Chapter 2, literature review regarding the strength prediction of open hole composite laminates and progressive damage analysis of wind turbine blades is given. In Chapter 3, theoretical background of the analytical and numerical modeling for the strength prediction of unnotched and open hole laminates with reference to the literature is presented. In Chapter 4, comparisons are made between experimental results and different plain strength analysis procedures from the literature for strength calculation of unnotched laminates subjected to in-plane combined loading. In Chapter 5, an analytical approach for the open hole strength prediction of composite laminates subjected to in-plane combined loading conditions is proposed and compared with the models in the literature. In Chapter 6, the results for FE modeling incorporating Hashin and Puck continuum damage models for the prediction of size effects on open hole tension laminates is presented. In Chapter 7, the FE model is validated with experiments using modal analysis and the failure characteristics of an existing 5-m composite wind turbine blade subjected to monotonic loading are investigated. It is worth noting that Chapters 5-7, cover the development of progressive failure models and their application to composite structures used in aircraft and wind energy industries. Finally, in Chapter 8 overall conclusions of this thesis are drawn and suggestions for future work are provided.

CHAPTER 2

LITERATURE REVIEW

This literature review consists of two independent parts for the two topical areas investigated in this thesis. The first part of the literature survey is devoted to the previous research on the analytical and numerical approaches for strength prediction of open hole composite laminates (Chapter 2.1). In the second part, detailed information regarding the previous works on the progressive damage analysis of composite wind turbine blades can be found (Chapter 2.2).

2.1 Strength Prediction of Open Hole Composite Laminates

2.1.1 Analytical Approaches

Owing to their high strength-to-weight ratios composite materials are widely used in the design of primary aircraft structures with an increasing trend. These structures fail mostly due to stress concentrations, such as holes. In the absence of accurate analysis methodologies for strength prediction of the open hole composite laminates, the design process of these structures will be costly due to large number of mechanical tests and empirical knockdown factors ([9]-[10]). Hence, advancement in the usage of composite materials in aircraft structures relies on the development of analytical and numerical tools that can carry out the strength calculations of the open hole composites accurately and in a short time frame. Approaches for the strength prediction of open-hole composite laminates are based on analytical and numerical methods [11]-[12]. Among numerical approaches, nonlinear finite element models are accurate. Yet computation time needed for the analysis is not suitable for the preliminary design of the aircraft structures [13].

Analytical attempts start with Waddoups et al. [14], who utilized linear elastic fracture mechanics (LEFM) and proposed the Inherent Flaw Model (IFM) for the open hole strength prediction of composite laminates. According to the IFM open hole damage before ultimate failure can be lumped into a "region of intense energy" called "inherent flaw" (See Figure 2.1). Open hole laminate strength depends on the region of intense energy and the unnotched laminate strength.

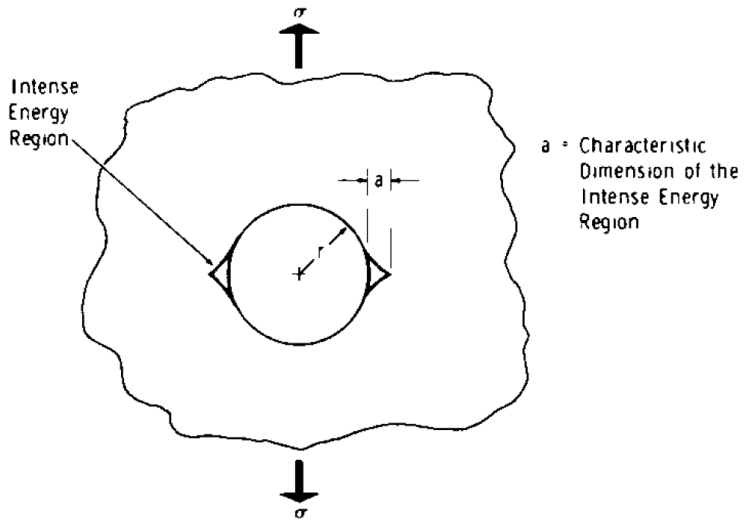

Figure 2.1. Fracture model proposed by Waddoups et al. [14].

Later, Whitney and Nuismer [15] introduced two stress criteria, namely point stress criterion (PSC) and average stress criterion (ASC), for the evaluation of stresses in laminated composites containing open holes. Using the stress criteria proposed by Whitney and Nuismer, size effects of the discontinuities are calculated without referring to LEFM. According to PSC, failure occurs when the point stress value is equal to or greater than the strength of the laminate at some critical distance d_0 away from the notch. Similarly, in ASC, failure occurs when the average stress value is equal or greater than the strength of the laminate until some critical distance a_0 away from the notch. Distances d_0 and a_0 are referred as characteristic distances and regarded as material properties independent of the hole size/width and applied loading. The schematic representation of the point stress and average stress criterion is given in Figure 2.2 (a) and (b), respectively. Karlak [16] argued that the

characteristic distance varies with hole size and incorporated the hole size effect into the PSC. Pipes et al. [17] enhanced the relation developed by Karlak [16] by including notch sensitivity parameter in their formulation. Moreover, instead of the expression for the infinite isotropic plate developed by Whitney and Nuismer, Pipes et al. [17] used the approximate stress distribution expression for an infinite orthotropic plate under uniaxial loading. Pipes et al. stated that the characteristic length is a function of laminate configuration and material properties as well as notch sensitivity which needs to be determined by experiments.

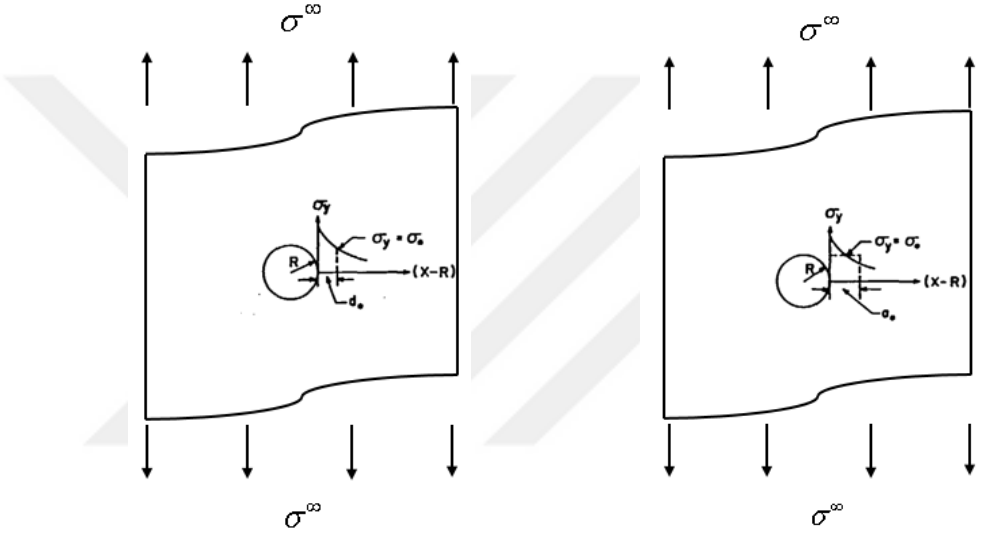

Figure 2.2. Point stress (a) and (b) average stress criterion [15].

Tan ([18],[19]) extended the application of the above-mentioned analytical approaches for more general cases. He introduced finite width corrections for the open hole strength prediction in a finite plate and proposed a methodology for the strength prediction of an open hole composite laminate under combined loading. Taylor [20] made a comprehensive study on the selection of the characteristic distances and state that the assumption of a constant characteristic distance comes up with acceptable small errors in the strength prediction of long-fibre composite laminate materials which are widely used in engineering applications. Analytical methods, with well-defined correction factors, are accurate enough and fast for

simple structures. On the other hand, numerical models are required as the complexity of the problem increases ([12], [21]-[23]).

As an alternative to the analytical models based on characteristic distance, Soutis et al. [24] propose Cohesive Zone Model (CZM) for the strength prediction of the Carbon Fiber-Epoxy laminate with an open hole. According to the model, damage emerging from each hole side is represented with a cohesive crack. As shown in Figure 2.3, damage starts when the stress level in the 0º fibers reach the stress level of the unnotched laminate strength. Damage progression is simulated by replacing the damage zone with an equivalent crack. In the equivalent crack region, crack bridging stresses drop linearly along the crack overlapping region from a maximum value of the unnotched laminate strength. The model requires only two parameters: unnotched laminate strength and the fracture energy. However, the accuracy level of the CZM is low compared to the other analytical models [25].

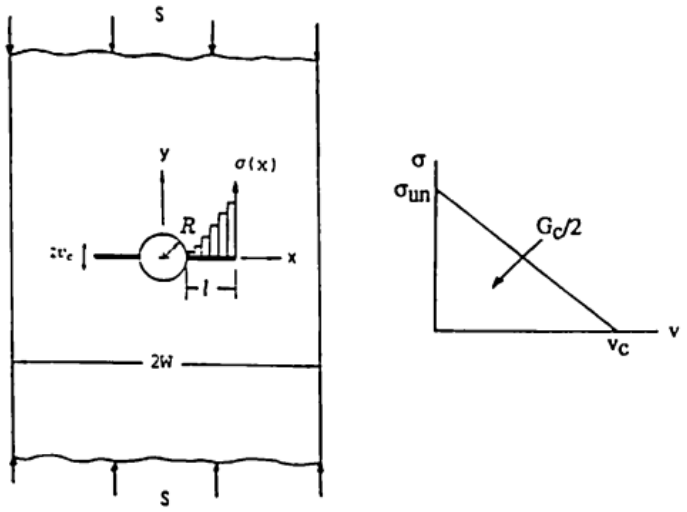

Figure 2.3. Cohesive Zone Model proposed by Soutis et al. [24].

Camanho et al. [13] state that the main drawback of the analytical methods which require characteristic distance information is that large and expensive test programs are needed to determine the characteristic distance for different materials and geometries. Hence Camanho et al. [13] introduced Finite Fracture Model (FFM) to predict the open-hole tension strength of the composite laminates. When both stress-

based and fracture-energy based criteria are met, failure prediction is done. Since ply elastic properties, unnotched laminate strength and fracture toughness is needed as the input, FFM does not require any inverse calculations. This is one of the advantages of the FFM over the alternative methods. When compared with experimental data, FFM is more accurate compared to the traditional methods such as Point Stress (PS), Average Stress (AS), IFM and CZM ([13],[26]) In the follow-up study, Furtado et al. [27] introduce an analytical model which incorporates only the Young's modulus, the strength and the R-curve of the 0-degree ply. The methodology provides advantages in terms of material characterization, computing time and lay-up selection. Although only three material parameters are needed for the analytical model, paper demonstrates that strength prediction accuracy level needed for the preliminary design of the aerospace structures is still provided.

Behavior of composite laminates with an open hole subjected to uniaxial tension and compression loading is studied extensively in literature. However, studies concerning the evaluation of notched laminate strengths under biaxial loading is very few [11]. Strength prediction methods have been mostly limited to uniaxial loading ([29]-[24]). Daniel's [30] analytical method for the strength prediction of open-hole composite laminates subjected to bi-axial loading is based on an ASC and on tensor polynomial criterion. Yet the method was complex and not suitable for industrial design applications. In Figure 2.5, using Daniel's approach strength reduction of a quasi-isotropic graphite/epoxy open hole laminate under biaxial tension-tension loading is plotted.

The analytical model developed by Soutis and Fleck [24] and Soutis et al. [29] is based on the stress distribution at the circular hole edge and stress intensity factor for a crack emerging from the edge of the hole. The prediction of this model was demonstrated for the strength prediction of CFRP plates with a hole under biaxial compression-tension loading only and not for general combined loading conditions [29]. According to the methodology proposed by Soutis and Fleck [24] and Soutis et al. [29] remote stress σ_{xx}^{∞} , which is function of microbuckle length l is plotted using the relation to predict the stable crack growth and the relation to predict the unstable

crack growth (See Figure 2.4). Their intersection point delivers notched strength. At this point, it is worth noting that the aforementioned FFM [13] is only available under uniaxial loading in literature.

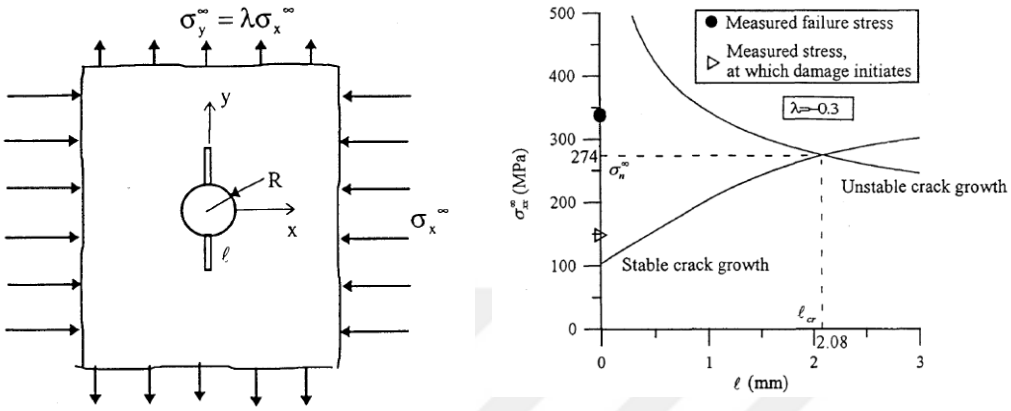

(a) (b)

Figure 2.4. (a) Representation of the line crack along y-axis caused by microbuckling under compression-tension loading (b) strength prediction procedure for an XAS/914C $(-45/0/-45/90)_{2s}$ laminate under compression tension loading (loading ratio, $\lambda = -0.3$) [28].

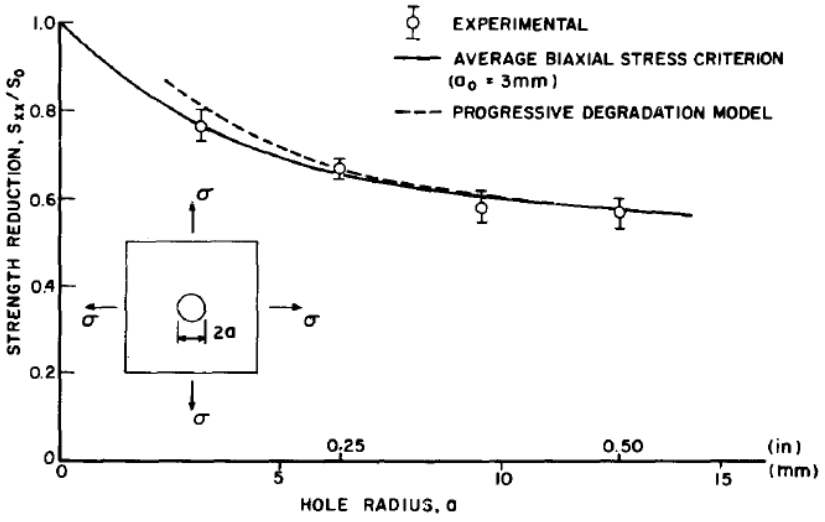

Figure 2.5. Strength reduction of $[0/\pm45/90]_s$ graphite/epoxy open hole laminates subjected to 1:1 biaxial tensile loading [30].

2.1.2 Numerical Approaches

In this section, literature survey on the previous research concerning the numerical approaches for the damage development and strength predictions of open hole composite laminates is presented. Within the scope of this thesis, the main focus in the numerical analysis of open hole laminates is given to the Open Hole Tension (OHT) composite laminates. Since the damage mechanisms observed in open hole composite laminates differ depending on the open hole composite laminate lay-up configurations and geometry, this literature survey begins with a brief explanation of the experimental observations seen in the Open Hole Tension (OHT) and Open Hole Compression (OHC) tests. This part is followed by the numerical approaches used for investigating the damage mechanisms seen in OH composite laminates and their strength predictions.

During the structural implementation of composite materials in automotive, aerospace, wind energy and marine industries, cut-outs and holes are frequently needed. These discontinuities in the composite structures can lead to stress concentrations, which in turn can cause damage initiation and propagation. This damage development may lead to strength or life reduction of composite structures. Hence, open hole tension (OHT) strength of laminated composites plays a crucial role in the design of composite structures which are particularly subjected to tension loading. OHT simulation of composite materials is a challenging task, as it involves a range of multiple damage mechanisms and their interactions. These mechanisms include matrix cracking, fiber failure, pull-out and delamination.

Early studies reveal that the strength of composites depend on the specimen size and the geometric scaling effects ([31]-[33]). According to the more recent studies by Green et al. [34], it is observed that OHT strength and failure modes are influenced by the geometry of the test specimen such as hole diameter, specimen width, stacking sequence and lamina thickness. In Green et al. [34]'s work OHT test results of the quasi-isotropic Hexcel IM7/8552 carbon fiber/epoxy prepreg with $[45_m/90_m/-45_m/0_m]_{ns}$ layup using ply-level scaling (laminate thickness is increased by keeping

n constant and increasing m) and sublaminate level scaling (laminate thickness is increased by keeping m constant and increasing n) are reported. Schematic representation of the aforementioned thickness scaling methodologies is shown in Figure 2.6. Schematic representation of the sublaminate and ply-level scaling methodologies [36]. Green et al. [34] have observed that OHT specimen with ply-level scaling lead to extensive delamination before fibre failure. On the other hand, when sublaminate level scaling technique is used, fiber failure occurs first. In this case, if the specimen size is small, pull-out failure is observed and for larger specimen brittle fracture is seen. In Figure 2.7, depending on the OHT laminate configuration and hole size, three different damage mechanisms are depicted. Wisnom and Hallet's ([35],[37]) research has revealed that although in-plane damage evolution is considered to be main problem in the strength prediction of OHT laminates, delamination also plays a crucial role in the progression of damage and ultimate strength prediction.

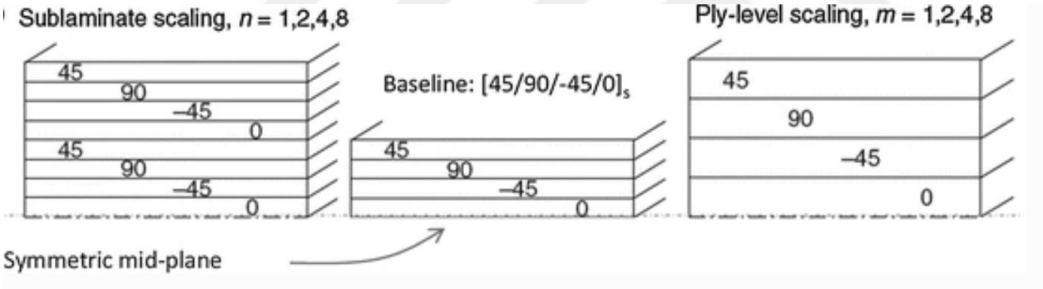

Figure 2.6. Schematic representation of the sublaminate and ply-level scaling methodologies [36].

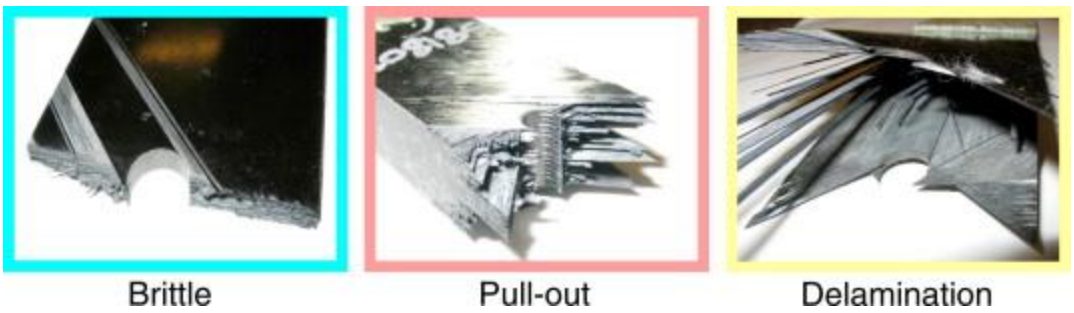

Figure 2.7. Three different damage mechanisms seen in the OHT tests on quasi-isotropic laminates [37].

Three different failure mechanisms seen in the open hole compression (OHC) tests of the quasi-isotropic IM7 8552 OHC specimen are depicted in Figure 2.8 [35]. As seen from the Figure 2.8 (a) sublaminate-scaled specimen showed brittle fracture. Ply-level scaled specimen with 2 and 4 mm thickness exhibited local delamination and push-out failure mode (See Figure 2.8 (b)). 8 mm thick ply-level scaled specimen failed due to delamination as seen in Figure 2.8 (c).

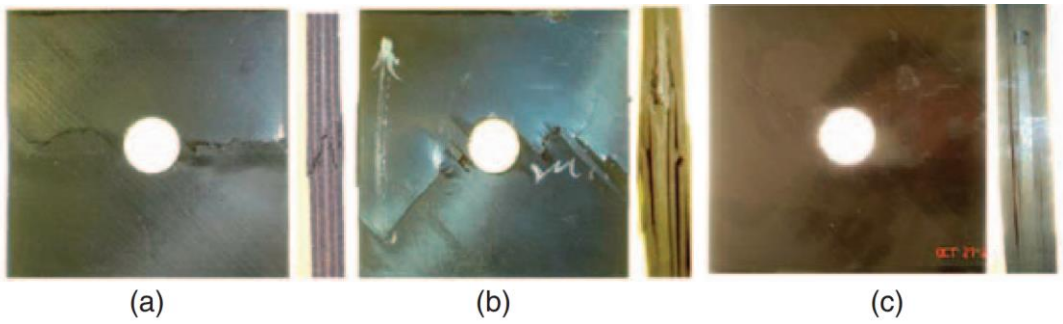

Figure 2.8. Three different damage mechanisms seen in the OHC tests on quasi-isotropic laminates (a) brittle, (b) push-out (c) delamination [35].

Using five different numerical approaches proposed by Camanho et al. [9], Hallett et al. [38], Abisset et al. [41], van der Meer et al. [42] and Chen et al. [12] size effects of open-hole laminated composites under uniaxial tension loading were investigated. Camanho et al. [9] proposed an energy-regularized Continuum Damage Model (CDM) to simulate the local damage evolution in the material. Stress-strain behavior with exponential strain softening of each element was regularized by equating the total energy dissipation to the fracture toughness of the material at failure. OHT specimen fe models were built using layered plane stress elements, which incorporate Classical Lamination Theory (CLT). Camanho et al. [9] predicted the in-plane size effects of open hole tension specimen with five different hole sizes, which fail in brittle failure mode. Good agreement between simulations and experiments is observed. However, it is worth noting that the fracture toughness value in fiber tension direction used in [9] was lower than fracture toughness used in the recent work of Camanho and his coworkers [23]. In addition to this in their recent work [23], fe modeling technique of OHT laminates was changed from layered plane

stress elements to solid elements per ply with cohesive elements are ply interfaces. Using the new fe modeling technique, for the same OHT laminates, a good correlation between simulations and experiments is reported [23].

Hallet et al. ([38],[39]) utilized cohesive interface elements to model matrix cracking as well as interface failure in the regions where potential crack paths in plies and delamination between plies is expected. For the fibre dominated failure modes, an additional failure criterion based on Weibull's statistical model was implemented ([38]). In Figure 2.9, mesh pattern used in the OHT specimen fe models and the implementation of regions of cohesive interface elements are depicted. We further note from Figure 2.9 that the small degenerated elements caused by the implementation of the cohesive elements are removed. This modification in the fe model leads to the misshaping of the hole. However, after the initiation of matrix cracking, exact geometry of the hole does not affect the results. As long as the cohesive elements are placed in the regions, where matrix cracks and delamination occur, the model delivers good predictions. Full range of scaling effects were captured by the fe model with cohesive interface elements presented in [38].

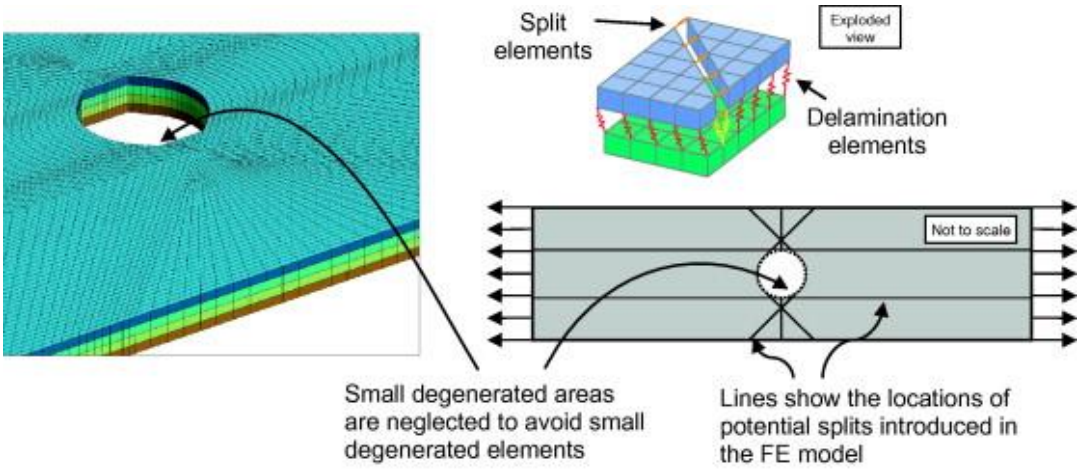

Figure 2.9. Mesh pattern used in the OHT specimen fe models with implementation regions of cohesive interface elements (laminate thickness=2 mm, ply-level scaling laminate configuration) [38].

Utilizing the continuum damage mesomodel based on a micromechanical approach, Abisset et al. [41] investigated the damage evolution in OHT specimen until they fail. According to the model proposed in [41], laminated composite is decomposed into two elementary constituents: the ply and the interface. On ply level, diffuse damage and fiber damage were simulated by progressive and brittle damage laws, respectively. The model was capable of predicting the OHT composite laminate strength, in-plane and ply thickness effects.

In their work, Bao and Liu [22] report on the difficulty to determine the accurate stress concentration level at the hole edge of the composite laminates subjected to tension. Based on the previous studies in literature, it is concluded that the longitudinal splitting during loading reduces the stress concentration. Bao and Liu [22]implemented surface-based cohesive contacts for longitudinal splitting and delamination so that the thickness effect of sublaminate and ply-level scaled open hole laminates under tension can be predicted. After using aligned mesh in fiber direction, they were able to get a good agreement between experiments and simulation results.

van der Meer et al. [42] proposed a phantom-node method, which can be used as a mesh-independent approach for simulating the development of matrix cracks. In addition to this, a continuum damage model and interface elements were used for fiber failure and delamination, respectively. Using ply-level thickness scaling, the decreasing trend of strength in open hole tension composite laminates seen in experiments with increasing laminate thickness are captured with the proposed model. However, for sublaminate-level scaling the small decrease in OHT composite laminate strength with increasing laminate thickness was not captured.

Chen et al. [12] used smeared crack model as the intralaminar damage model and cohesive elements for the interlaminar damage. In order to determine the most suitable fe modeling approach for the strength prediction of IM7/8552 OHT specimen with a lay-up $[-45/90/45/0]_s$ and a hole diameter 3.175 mm, different fe models using layered plane stress elements, continuum shell elements with perfect

bonding at ply interfaces and continuum shell elements with cohesive elements at ply interfaces were built. In Figure 2.10, the aforementioned fe models using four different mesh densities are depicted. Figure 2.11 shows the strength predictions using layered plane stress elements based on Classical Lamination Theory (CLT), reduced translaminar fracture toughness of the 0°-ply (CLT(b)), continuum shell elements at ply interfaces (CSLI) continuum shell elements with two layers of cohesive elements at ply interfaces (CSLI-2e/ply). As seen from the figure, the best agreement with experiments is achieved with continuum shell elements with cohesive elements at ply interfaces. As seen from Figure 2.11, when interface damage is not included in the fe models, mesh dependency occurs and there is an overprediction of OHT composite laminate strength values. In [12], it is reported that the fe model with cohesive elements is able to predict the correct damage mode, which fail in pull-out damage mode. However, the fe model with cohesive elements was not accurate enough for OHT specimen which fail due to delamination.

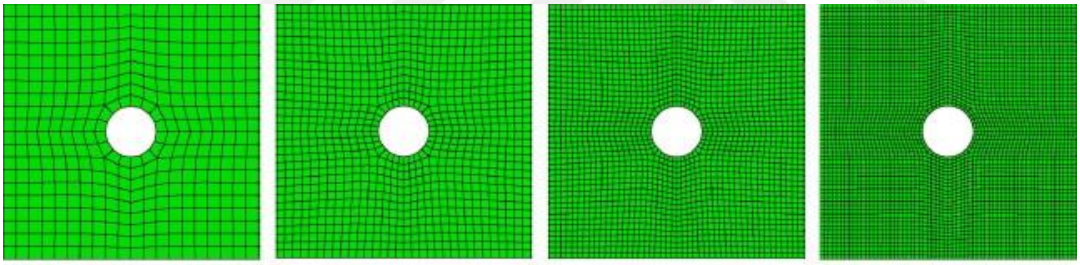

Figure 2.10. Four meshes for different element sizes.

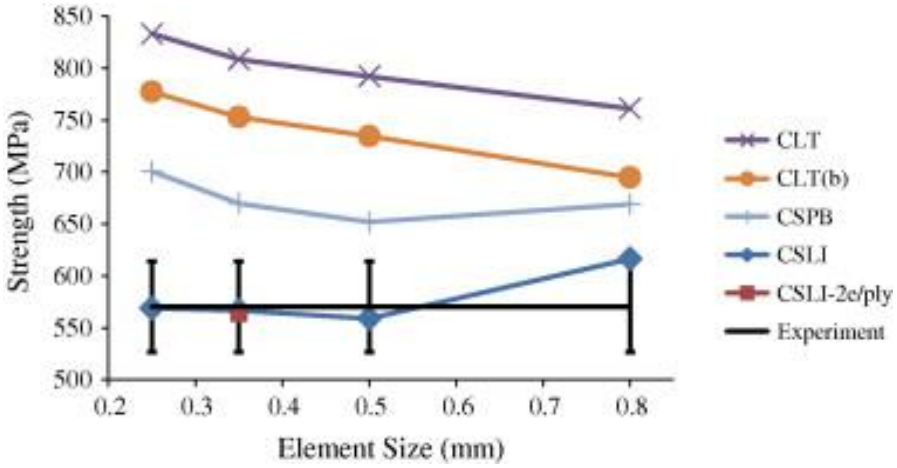

Figure 2.11. Mesh refinement study of different numerical models.

For the strength prediction of CFRP open hole laminates, Aidi and Case [44] and Yoon et al. [45] used Continuum Damage Models (CDM) based on energy-based degradation scheme. In both models bi-linear damage evolution law was implemented. Damage initiation was predicted by multi-continuum theory and Hashin failure criteria in Aidi and Case [44] and Yoon et al. [45]'s work respectively. Aidi and Case [44] conducted eigenfrequency analysis of the OHT specimen to identify the amount of damage. According to Aidi and Case [44] first in-plane mode is appropriate to quantify the amount of damage in the material. In both studies solid elements per ply were used to model the OHT specimen. Good correlation between experiments and numerical analysis is achieved.

Ridha et al. [43] developed a smeared crack model for investigating the size effects of OHT specimen. Their model incorporated max-stress failure criteria and Tsai-Wu failure criteria for fiber and matrix dominated failures, respectively. After damage onset, fracture-mechanics augmented stress-softening model was used to simulate the energy dissipation. Ridha et al. [43] found that for accurate OHT strength predictions delamination and in-plane damage both needs to be included in the fe models. In the follow-up study, based on the model developed by Ridha et al. [43], Su et al. [47] investigated size effects on open hole compression specimen, and compared with the experiments conducted by Lee and Soutis [46]. It is worth noting

that some modifications regarding compressive deformation were implemented to the model in [43] as presented in [47]. They have implemented Hashin failure criteria for the prediction of fiber and matrix failure initiation. As in Ridha et al. [43] damage progression is simulated utilizing an energy-based linear softening law. The delamination is considered using cohesive elements at ply interfaces. In both Ridha et al.[43] and Su et al. [47]'s works, it is concluded that for a good correlation with experimental results the fracture toughness of blocked plies needs to be considered in the numerical model. Furthermore, in both studies ([43],[47]) the issue of numerical instability, i.e. convergence problems due to material softening is addressed by using a zigzagging approach ([48],[49]) to approximate the linear material softening behavior in the stress-strain relationship. This is achieved by reducing the material stiffness (secant stiffness) in a stepwise manner as shown in Figure 2.12 (a). The computational stability is then achieved in two ways:

- Zigzagging approach helps to keep a positive tangent modulus in the stress-strain curve at all times, which leads to easier convergence
- Stiffness is kept constant in a piecewise manner as the strain changes in each iteration (See Figure 2.12 (b)). This method helps to simplify the nonlinear computation problem.

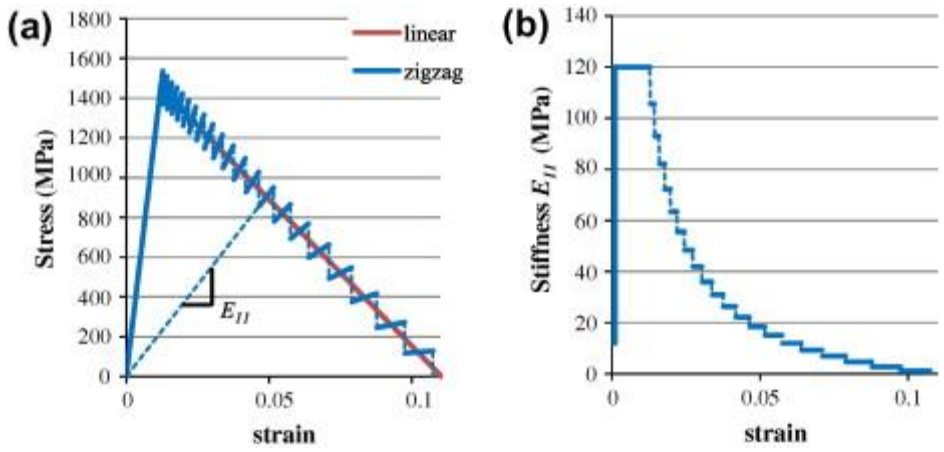

Figure 2.12. (a) Zigzag approach used for approximation the linear softening in a stress-strain curve (b) piecewise constant stiffness values with slight changing strain values [43].

Smeared crack model was also used by Zhou et al. [50] for the Open ,Hole Compression (OHC) strength predictions. According to their work, ultimate strength of the CFRP OHC laminates with different lay-ups were found in the following order: $[45/90/-45/0]_{3s}$>$[45_3/90_3/-45_3/0_3]_s$>>$[45_3/0_3/-45_3/90_3]_s$. This result shows that the sublaminate scaled OHC specimen carries more load compared to ply-level scaled specimen. As a further outcome of the study, under unidirectional compressive loading, strength predictions using Tsai-Wu failure matrix failure initiation criterion were found to be more precise compared to Hoffmann failure [51] criterion.

Hu and Madenci [52] utilized peridynamics (PD) for the OHT/OHC composite laminate strength predictions. A good agreement between numerical simulations and experiments regarding deformation and strength predictions was observed. In addition to this, the PD model proposed by Hu and Madenci [52] was able to capture the damage evolution seen in experiments.

Recently Falco et al. [4] proposed a three-dimensional Continuum Damage Model for simulating the intralaminar damage in laminated composites with open holes. A frictional cohesive surface modeling approach coupled with penalty-based contact surfaces is proposed as the interface damage model. In their work, Falco et al. [4]emphasize the significance of mesh alignment in fiber direction for realistic modeling matrix cracking and delamination propagation.

2.2 Progressive Damage Analysis of Wind Turbine Blades

Wind turbine blades are among the most important components of a wind turbine with respect to turbine efficiency and cost. Severe blade failures, where repair is necessary may lead to a long wind turbine downtime. In order to prevent long wind turbine downtimes due to blade failures, reliable rotor blade designs are essential. This can be achieved with a broad understanding of the blade failure mechanisms. For the understanding of these failure mechanisms well-established structural analysis methodologies in combination with blade tests are essential [53].

In the literature, many studies on the structural behavior of composite turbine blades have been published in the past two decades with most of the studies conducted for large wind turbine blades. Jensen et al. [54] carried out full-scale tests and nonlinear FE simulations of a 34-meter composite wind turbine blade under flap-wise loading. In both the tests and the simulations, they noted that spar cap (suction side) deflected nonlinearly and observed cross-sectional ovalisation, i.e. Brazier effect, arguing that Brazier effect is the main reason for the blade collapse. Overgaard et al. ([55],[56]) reported on testing and numerical analysis of the collapse of a 25-meter composite wind turbine blade subjected to static flap-wise loading. In the study, in contrast to Jensen et al. [54] the main failure mechanism which leads to blade collapse is argued to be delamination and its interaction with local buckling. According to Overgaard et al. [56] (See Figure 2.13) delamination and local buckling occur prior to the Brazier effect observed in spar caps. Once the blade is weakened by the aforementioned failure mechanisms, blade collapses due to the compressive strains in fiber directions.

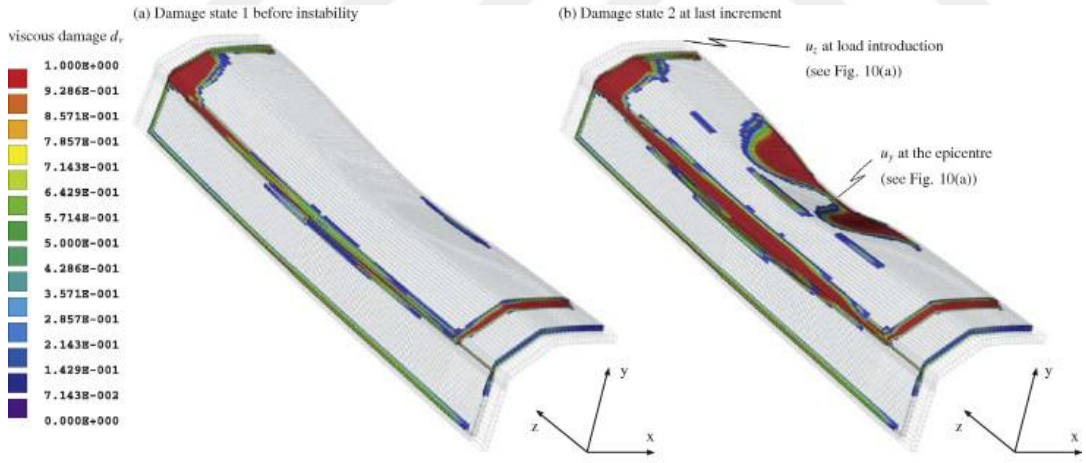

Figure 2.13. Damage evolution in the quarter of the deformed main spar: (a) damage state 1 before structural instability (b) damage state after structural instability ([55],[56]).

Yang et al. [57] investigated the structural collapse of a 40 m blade and based on full-scale test results showed that debonding was the root cause of rotor blade

collapse. Kim et al. [58] studied the structural response of a Multi-MW class wind turbine blade using Puck's 3D damage model and linear buckling analysis. According to the results, blade shows sufficient structural strength and resistance against buckling. When laminate failure is of concern, the major weak point of the blade is located in the skin at the maximum chord. In another study, Chen et al. [59] conducted a full-scale bending test of a 52.3 m wind turbine blade. Delamination in the spar cap and shear web failure at the root transition region were found to be the main failure mechanisms for the blade collapse as shown in Figure 2.14. Local buckling contributed to the main failure mechanism by facilitating local out-of-plane deformation. They conclude that for large blades, through-the-thickness stresses which cause debonding and delamination at the blade root transition region need to be considered in the FEA.

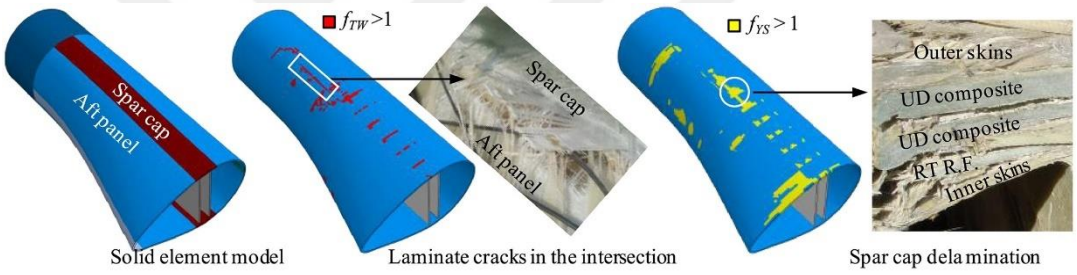

Figure 2.14. Comparison between the predicted and observed damage in the root transition region of the 52.3 m composite wind turbine blade [59].

Haselbach and Branner [60] discuss the initiation and development of trailing edge failure in the full-scale test of a 34-m wind turbine blade. They highlight the influence of buckling on the damage onset in the trailing edge and sandwich panel failure. As a further outcome of the study, they show that modeling technique utilizing cohesive zone modeling approach for the failure in trailing edge delivers good agreement with experiments.

Montesano et al. [61], state that progressive failure models incorporating failure criteria do not consider the progressive nature of sub-critical microscopic intra-laminar damage, which is vital for predicting the onset of macroscopic failure modes.

Therefore, in the study of a physically based multi-scale damage model, which can account for failures of a 33.25 m rotor blade under quasi-static and fatigue loading is introduced. The simulation results show the capability of the model to predict the evolution of sub-critical ply cracks between spar webs located near blade root at maximum chord length. In the follow up work by Zuo et al. [62], the multi-scale model is further expanded to include cohesive zone elements to predict structural debonding failure at the spar/skin interface located near blade root at maximum chord.

In contrast to large wind turbine blades, a fewer number of investigations on the structural analysis of small wind turbine blades exists. Chen et al. [64] focused on the local buckling resistance of 10.3 m wind turbine blades. FE analysis showed that configurations with sharp edges are susceptible to local buckling. During testing of the 10.3 m blade, although local buckling of shear web and flatback airfoil was observed, composite laminate failure in these locations was not observed. These results show the possibility of different failure mechanisms for different blade sizes. In another study, to improve the structural strength of a small size 9-m wind turbine blade, Paquette and Veers [63] carried out a blade system design study (BSDS), where structural innovations such as flatback airfoils, thick root diameter and carbon spar caps were introduced and their advantages were demonstrated. The static strength of the blades was determined by measuring strains to failure by tests and using finite element analysis. Moreover, linear buckling analysis of the blades were conducted.

In their recent paper, Noever-Castelos, Haller and Balzani [65] report on the validation of their fe modeling methodology of a 20-m composite wind turbine blade with experiments. Blade deflections, strain levels, eigenfrequencies and eigenmodes are among the experimental data, which are compared with simulations. Although in general good agreement between tests and simulations is met, improvement is needed for the torsional behavior of the blade.

Ozyildiz et al. [66] conducted the progressive failure analysis of the existing 5-m glass-fiber-reinforced-polymer (GFRP) RÜZGEM wind turbine blade (See Figure 2.15) subjected to flapwise (max) loading. Within the framework of the study the linear Puck material model is compared with the Puck's progressive damage model. It is concluded that progressive failure analysis is necessary to capture a more realistic simulation of damage development. In their following work, Muyan and Coker (2020) [67] focused on the failure characteristics of the RÜZGEM blade subjected to flapwise (max), edgewise (min) and combined flapwise (max) plus edgewise (min) loading conditions. In their latest paper Muyan and Coker [68] present their results on the static and fatigue analysis of the RÜZGEM blade with and without defect in the form of debonding. It is found that the inclusion of defect decreases the static strength and fatigue life of the blade significantly.

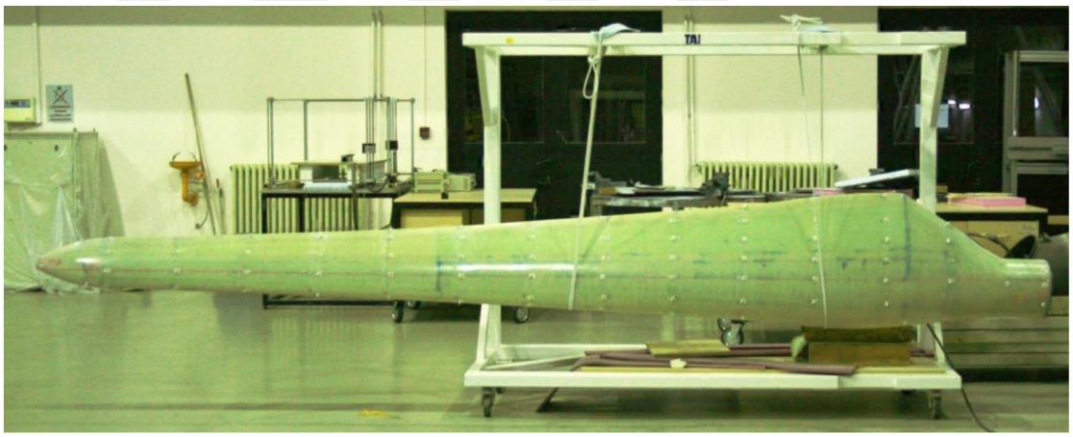

Figure 2.15. 5-m glass-fiber-reinforced-polymer RÜZGEM wind turbine blade.

CHAPTER 3

PROGRESSIVE FAILURE ANALYSIS OF UNNOTCHED AND OPEN-HOLE COMPOSITE LAMINATES

This part of the thesis is devoted to the theoretical background regarding the progressive failure analysis of unnotched and open-hole composite laminates used in this work. In Section 3.1, analytical modeling approaches for the unnotched and open hole composite laminates is given. In Section 3.2, theoretical basis of the numerical approaches used for the intralaminar and interlaminar progressive damage development in composite laminates can be found.

3.1 Analytical Modeling

Analytical modeling approaches for the strength calculation of unnotched composite laminates and open hole composite laminates are presented in this section. Subsection 3.1.1 begins with an explanation of the background of the laminae composite failure theories followed by an explanation of the strength analysis procedure for multidirectional composite laminates. In subsection 3.1.2, theories behind the analytical open hole composite strength calculation methods are given.

3.1.1 Composite Laminate Strength Calculation Methods

In this subsection, existing methodologies for the strength analysis of unnotched laminates (plain strength analysis) with reference to the literature is explained. For this purpose, the most commonly used and representative composite failure theories for composite tape lay-ups, followed by the multidirectional laminate strength analysis procedure are presented. The strength calculation procedures of the

composite laminates for any desired lay-up subjected to in-plane loads and moments are treated.

3.1.1.1 Composite Failure Theories for Unidirectional Laminae

Failure theories for composite materials are developed by extending and adapting failure theories from isotropic materials, such as Maximum Stress (Rankine), Maximum Shear Stress (Tresca) and Maximum Distortional Energy (Von Mises) [69].

Most theories are based on homogenous and linear material property assumptions. However, some phenomenological models such as Puck's model consider the effect of constituent properties in addition to lamina properties and therefore categorized as nonlinear models.

Daniel and Ishai [69] classified failure theories into three main groups:

1. **Limit or non-interactive theories:** Failure modes are identified by comparing individual stress components (Tensile, Compression or Shear) in principal material directions with the corresponding strength properties. Stress components do not interact with each other and are treated independently. Maximum stress and maximum strain failure theories fall into this category.
2. **Interactive theories:** Stress components are fully coupled in one equation. Overall failure is determined without reference to specific failure modes. Tsai-Hill, Yamada-Sun and Tsai-Wu are examples of interactive theories.
3. **Partially interactive or failure mode-based theories:** Fiber and interfiber failure are treated with separate criteria. Failure theories from Hashin-Rotem and Puck are grouped as partially interactive or failure mode-based theories.

Commonly used and representative failure theories are explained in the following subsections:

3.1.1.1.1 Maximum Stress Theory (Non-interactive Theories)

As a representative example of limit or non-interactive failure theory maximum stress theory is introduced. Kelly [70] implemented maximum stress theory to composite materials and predicted off-axis strength of unidirectional composite materials. According to the maximum stress theory, if the stresses in principal material directions exceed the strength in corresponding directions failure occurs, as expressed by the equations below. In the equations σ_1 is the stress component in fiber directions. X_t and X_c represent tensile and compressive strengths in fiber direction, respectively. Similarly, σ_2 is the stress in the transverse fiber direction. Y_t and Y_c are the tensile and compressive material strengths in transverse fiber directions, respectively. In the final expression τ_{12} is the in-plane shear stress and S is the shear strength.

$$\sigma_1 = X_t \text{ when } \sigma_1 > 0 \text{ or } \sigma_1 = -X_c \text{ when } \sigma_1 < 0 \tag{3.1}$$

$$\sigma_2 = Y_t \text{ when } \sigma_2 > 0 \text{ or } \sigma_2 = -Y_c \text{ when } \sigma_2 < 0 \tag{3.2}$$

$$|\tau_{12}| = S \tag{3.3}$$

We note that the shear strength is independent of the sign of the shear stress. Failure envelope for unidirectional lamina under biaxial normal loading using maximum stress theory is depicted in Figure 3.1 below:

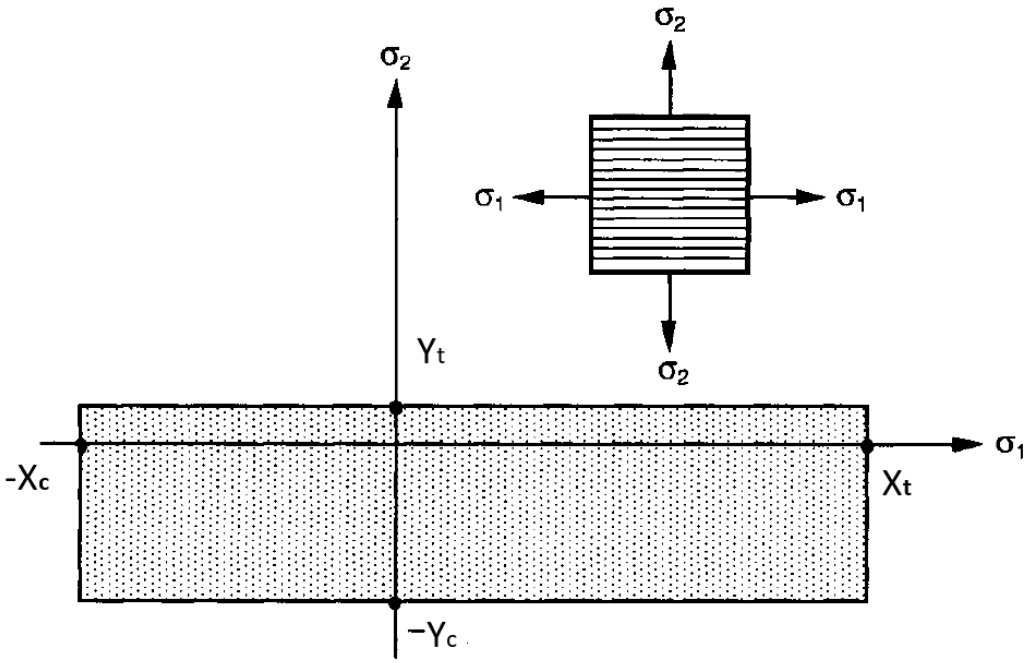

Figure 3.1*:* Failure envelope for unidirectional lamina subjected to biaxial normal loading using maximum stress theory [69].

3.1.1.1.2 Maximum Strain Theory (Non-interactive Theories)

Maximum strain theory [69] is presented as a second example of limit or non-interactive failure theory. According to the maximum strain theory, if the strains in principal material directions exceed the ultimate strains in corresponding directions, failure occurs:

$$\varepsilon_1 = \varepsilon_{1t}^u \text{ when } \varepsilon_1 > 0 \text{ or } \varepsilon_1 = \varepsilon_{1c}^u \text{ when } \varepsilon_1 < 0 \tag{3.4}$$

$$\varepsilon_2 = \varepsilon_{2t}^u \text{ when } \varepsilon_2 > 0 \text{ or } \varepsilon_2 = \varepsilon_{2c}^u \text{ when } \varepsilon_2 < 0 \tag{3.5}$$

$$|\gamma_6| = \gamma_6^u \tag{3.6}$$

where $\varepsilon_1,\ \varepsilon_2, \gamma_6$ are strain components in material principal axes.

ε_{1t}^{u}, ε_{2t}^{u} = ultimate tensile strains in fiber and transverse fiber directions, respectively

ε_{1c}^{u}, ε_{2c}^{u} = ultimate compressive strains in fiber and transverse fiber directions, respectively

γ_{6}^{u} = ultimate shear strain in 1-2 plane

Strains can be expressed in terms of stresses by the following equations:

$$\begin{aligned} \varepsilon_1 &= \frac{\sigma_1}{E_1} - \nu_{21}\frac{\sigma_2}{E_2} = \frac{1}{E_1}(\sigma_1 - \nu_{12}\sigma_2) \\ \varepsilon_2 &= \frac{\sigma_2}{E_2} - \nu_{12}\frac{\sigma_1}{E_1} = \frac{1}{E_2}(\sigma_2 - \nu_{21}\sigma_1) \\ \gamma_6 &= \frac{\tau_6}{G_{12}} \end{aligned} \tag{3.7}$$

Ultimate strains can be expressed in terms of basic strength parameters as follows:

$$\begin{aligned} \varepsilon_{1t}^{u} &= \frac{X_t}{E_1} \qquad & \varepsilon_{1c}^{u} &= -\frac{X_c}{E_1} \\ \varepsilon_{2t}^{u} &= \frac{X_t}{E_1} \qquad & \varepsilon_{2c}^{u} &= -\frac{X_c}{E_2} \\ \gamma_{6}^{u} &= \frac{S}{G_{12}} \end{aligned} \tag{3.8}$$

From (3.7) and (3.8) maximum strain theory can be rewritten as:

$$\begin{aligned} \sigma_1 - \nu_{12}\sigma_2 &= \begin{cases} X_t \text{ when } \varepsilon_1 > 0 \\ -X_c \text{ when } \varepsilon_1 < 0 \end{cases} \\ \sigma_2 - \nu_{21}\sigma_1 &= \begin{cases} Y_t \text{ when } \varepsilon_2 > 0 \\ -Y_c \text{ when } \varepsilon_2 < 0 \end{cases} \\ |\tau_6| &= S \end{aligned} \tag{3.9}$$

Failure envelope for a unidirectional lamina under biaxial normal loading ($\tau_6 = 0$) is depicted in Figure 3.2 below:

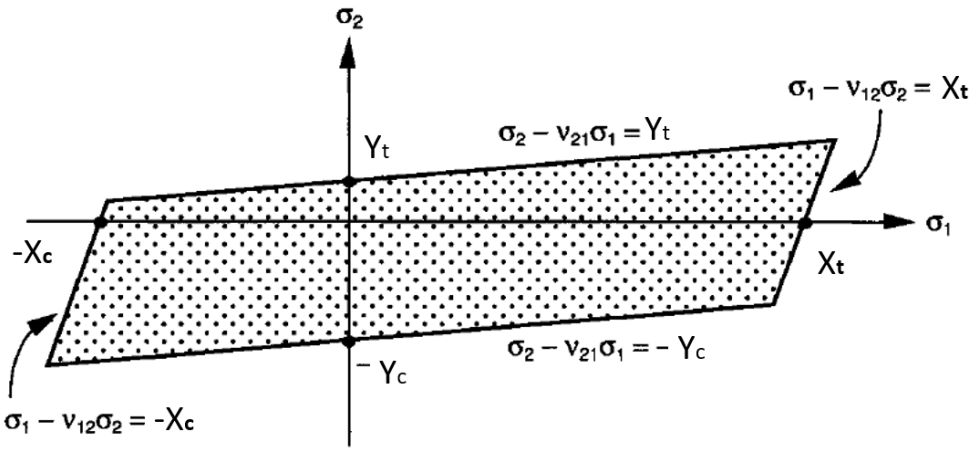

Figure 3.2*:* Failure envelope for unidirectional lamina subjected to biaxial normal loading using maximum strain theory [69].

3.1.1.1.3 Tsai-Hill Failure Criterion (Interactive Theories)

Hill's theory [71] is an extension of Von Mises yield criterion for anisotropic materials in three dimensions. 1- and 2- are in-plane material directions and 3- is the out-of-plane (thickness) direction. Hill's yield criterion is as follows

$$(G+H)\sigma_1^2 + (F+H)\sigma_2^2 + (F+G)\sigma_3^2 - 2H\sigma_1\sigma_2 - 2G\sigma_1\sigma_3 - 2F\sigma_2\sigma_3 + 2L\tau_{23}^2 + 2M\tau_{13}^2 + 2N\tau_{12}^2 = 1 \quad (3.10)$$

The coefficients F, G, H, L, M, N are considered as failure strengths. Tsai [72] related F, G, H, L, M, N with the fundamental strengths of a lamina X, Y and Z [73] In this manner, let us assume only τ_{12} acts on the body, then since its maximum value is F_6,

$$2NS^2 = 1 \;\rightarrow\; 2N = \frac{1}{S^2} \quad (3.11)$$

Likewise, if only σ_1 acts on the body, then it is calculated from

$$(G+H)X^2 = 1 \;\rightarrow\; (G+H) = \frac{1}{X^2} \tag{3.12}$$

In the case where only σ_2 acts on the body

$$(F+H) = \frac{1}{Y^2} \tag{3.13}$$

If only σ_3 acts on the body:

$$(F+G) = \frac{1}{Z^2} \tag{3.14}$$

Solving set of equations (3.12), (3.13) and (3.14), simultaneously yields:

$$2H = \frac{1}{X^2} + \frac{1}{Y^2} - \frac{1}{Z^2} \tag{3.15}$$

$$2G = \frac{1}{X^2} + \frac{1}{Z^2} - \frac{1}{Y^2} \tag{3.16}$$

$$2F = \frac{1}{Y^2} + \frac{1}{Z^2} - \frac{1}{X^2} \tag{3.17}$$

Let us consider the plane stress case in the (1-2) plane.

$$\sigma_3 = \tau_{13} = \tau_{23} = 0 \tag{3.18}$$

Since UD composite has transverse isotropic property, Y is equal to Z.

Hence, failure criteria (3.10) is reduced to

$$\frac{\sigma_1^2}{X^2} - \frac{\sigma_1\sigma_2}{X^2} + \frac{\sigma_2^2}{Y^2} + \frac{\tau_{12}^2}{S^2} = 1 \tag{3.19}$$

Equation (3.10) is known as the Tsai-Hill failure criterion.

According to Jones [73] Tsai-Hill shows better correlation with experimental data of E-Glass/Epoxy under uniaxial loading of an off-angle composite compared to Maximum Strain and Maximum Stress Theories. He further emphasizes that applicability of a failure theory depends on whether the material is brittle or ductile. In other cases, maximum stress and strain theories can give better results compared to Tsai-Hill.

Daniel and Ishai [69] state that the interactive quadratic nature of the Tsai-Hill theory has been criticized, because it is based on Hill's theory, which is suitable for

homogeneous, anisotropic, and ductile materials, whereas most composites are strongly heterogeneous and brittle.

3.1.1.1.4 Tsai-Wu Polynomial Failure Criteria (Interactive Theories)

Bi-axial failure theories, such as Maximum Stress, Maximum Strain and Tsai-Hill show insufficient correlations with experimental data. Tsai and Wu [74] improved this correlation by adding more terms to their quadratic failure criterion. They proposed a failure surface in stress-space in the following form:

$$f_i\sigma_i + f_{ij}\sigma_i\sigma_j = 1 \quad i,j = 1-6 \tag{3.20}$$

In equation (3.20) f_i and f_{ij} are second and fourth order stress tensors. In the equation usual contracted stress notation is used.

Since we are interested in the plane stress conditions, equation (3.20) can be reduced to the following expression.

$$f_1\sigma_1 + f_2\sigma_2 + f_6\tau_6 + f_{11}\sigma_1^2 + f_{22}\sigma_2^2 + f_{66}\tau_6^2 + \frac{2f_{12}^*\sigma_1\sigma_2}{\sqrt{f_{11}f_{22}}} = 1 \tag{3.21}$$

In equation (3.21) linear terms are used to represent strengths in tension, compression or shear. Quadratic terms are used to form the ellipsoid form of the equation. The coefficient $\frac{2f_{12}^*}{\sqrt{f_{11}f_{22}}}$ represents the interaction between normal stresses σ_1 and σ_2.

In the coming paragraphs the procedure for calculating the components of the stress tensors will be explained briefly. Let us consider the case of positive pure shear, i.e., $\sigma_1 = \sigma_2 = 0$ and $\tau_6 > 0$. Applying the above failure criterion, failure occurs when $\tau_6 = S$, where S is the shear strength.

$$f_{66}S^2 + f_6S = 1 \tag{3.22}$$

Now let us consider the case of negative pure shear, i.e., $\sigma_1 = \sigma_2 = 0$ and $\tau_6 < 0$.

Failure occurs when $\tau_6 = -S$, and the failure criterion yields

$$f_{66}S^2 - f_6S = 1 \tag{3.23}$$

Solving equations (3.22) and (3.23) simultaneously

$$f_6 = 0\ ;\ f_{66} = \frac{1}{S^2} \tag{3.24}$$

For the uniaxial tension loading $\sigma_2 = \tau_6 = 0$ and $\sigma_1 > 0$, failure occurs when $\sigma_1 = X$, where X is the longitudinal tensile strength and the strength criterion (3.21) becomes

$$f_1X + f_{11}X^2 = 1 \tag{3.25}$$

For uniaxial compressive loading $\sigma_2 = \tau_6 = 0$ and $\sigma_1 < 0$; failure occurs when $\sigma_1 = -X_c$, where X_c is the longitudinal compressive strength and the strength criterion (3.21) now becomes

$$-f_1X_c + F_{11}(X_c)^2 = 1 \tag{3.26}$$

Upon solving (3.25) and (3.26), we get

$$f_1 = \frac{1}{X_t} - \frac{1}{X_c}\ ;\ f_{11} = \frac{1}{X_t\,X_c} \tag{3.27}$$

In a similar manner, uniaxial loading in transverse direction yields

$$f_2 = \frac{1}{Y_t} - \frac{1}{Y_c}\ ;\ f_{22} = \frac{1}{Y_tY_c} \tag{3.28}$$

where Y_t and Y_c are the tensile and compressive strengths in transverse direction, respectively.

Liu and Tsai [75] expressed that the normalized interaction term f_{12}^* in (3.21) can best be determined by combined stress tests. Instead of performing such complicated tests, Liu and Tsai recommended to use the value $f_{12}^* = -1/2$, as a good approximation. With the strength parameters determined, Tsai-Wu failure criterion (3.21) takes its final form.

$$\frac{\sigma_1^2}{X_t X_c} - \frac{\sigma_1 \sigma_2}{\sqrt{X_t X_c Y_t Y_c}} + \frac{\sigma_2^2}{Y_t Y_c} + \left(\frac{\sigma_6}{S}\right)^2 + \left(\frac{1}{X_t} - \frac{1}{X_c}\right)\sigma_1 + \left(\frac{1}{Y_t} - \frac{1}{Y_c}\right)\sigma_2 = 1 \qquad (3.29)$$

3.1.1.1.5 S.E. Yamada and C.T. Sun Failure Criterion (Interactive Theories)

According to Yamada and Sun [76] a failure in a lamina does not automatically mean that the laminate fails, as well. This is one of the factor that makes failure analysis of laminated composites difficult. The failure theory proposed by Yamada and Sun [76] focuses on the final failure of the laminate and includes the lamination effect on the laminar shear strength.

Regarding the derivation of the failure theory, following assumptions are necessary:

- At the final failure stage of the laminate, it is assumed that all the laminas which constitute the laminate have failed due to transverse cracking along fiber direction. Hence, the transverse stiffness of each lamina is considered to be zero (E_2 and Poisson's ratio are set equal to zero). Only the longitudinal stress (σ_1) and shear stress τ_{12}will be carrying the applied load.
- The shearing strength of lamina is more when it is considered inside a symmetric cross-ply laminate compared to the case when the lamina is considered alone. Symmetric cross-ply laminates provide us the advantage that the pure shear situation (i.e. no interlaminar shear stress is involved) can be produced easily.

Finally, the following criterion for the laminate is proposed by Yamada and Sun [76]:

$$\left(\frac{\sigma_1}{X}\right)^2 + \left(\frac{\tau_{12}}{S_c}\right)^2 = l^2 \qquad (3.30)$$

$$l \geq 1\ failure, \qquad l < 1\ non-failure$$

In equation (3.30) above σ_1 and τ_{12} are longitudinal and shear stresses, respectively. X is the lamina strength in longitudinal direction and S_c is shear strength of the lamina in the symmetric cross-ply laminate. We note that equation (3.30) must be

applied on each ply in a laminate. The quantities S_c and X in (3.30) are obtained by statistical consideration. The model incorporates the probabilistic nature of the composite failure.

3.1.1.1.6 Hashin Failure Criteria (Partially Interactive and Failure Mode Based Theories)

Hashin [78] reviewed theories that were available for the failure prediction of fiber composites. He pointed out that the microstructural aspects of failure are too complicated to be solved using micromechanics approach. In his opinion, defining a three-dimensional failure criterion in terms of macrovariables, such as stresses and strains would be a more promising approach. This can be done with the help polynomials. Tsai-Hill and Tsai-Wu failure theories can be given as examples of this approach. Hashin [78] criticized that the failure criteria based on curve fitting with quadratic stress functions do not have a physical meaning. In order to overcome this difficulty, Hashin and Rotem [77] defined separate expressions for fibre and matrix failure modes. Hashin [78] modified expressions given in Hashin and Rotem [77] by including interactive criteria for tensile failure and for combined transverse compression and shear. Within the scope of this literature review, we will be focusing on in-plane failure, which covers tensile and compressive failure modes for fiber and matrix failures:

Tensile Fiber Mode

$$\left(\frac{\sigma_1}{X_t}\right)^2 + \left(\frac{\sigma_{12}}{S}\right)^2 = 1 \qquad \sigma_1 > 0 \qquad (3.31)$$

Fiber Compressive Mode

$$\sigma_1 = -Y_c \qquad \sigma_1 < 0 \qquad (3.32)$$

Tensile Matrix Mode

$$\left(\frac{\sigma_2}{Y_t}\right)^2 + \left(\frac{\sigma_{12}}{S}\right)^2 = 1 \qquad \sigma_2 > 0 \qquad (3.33)$$

Compressive Matrix Mode

$$\left(\frac{\sigma_2}{2S_T}\right)^2 + \left[\left(\frac{Y_c}{2S_T}\right)^2 - 1\right]\frac{\sigma_2}{Y_c} + \left(\frac{\sigma_{12}}{S}\right)^2 = 1 \qquad \sigma_2 < 0 \qquad (3.34)$$

In the expressions above,

X_t: tensile failure stress in fiber direction

X_c: compressive failure stress in fiber direction (absolute value)

Y_t tensile failure stress transverse to fiber direction

Y_c: compressive failure stress transverse to fiber direction (absolute value)

S_T : transverse failure shear

S_L: axial failure shear

From the failure modes above, it is seen that Hashin's envelope will not consist of a single function, such as in the case of Tsai-Hill and Tsai-Wu's quadratic failure expressions, but will consist of piecewise functions. These piecewise functions represent different failure modes.

3.1.1.1.7 Puck's Theory of Failure in Fiber Polymer Laminae (Partially Interactive and Failure Mode Based Theories)

Puck's physically based phenomenological model is based on experimental observations and Mohr's fracture hypothesis. Hence, after a brief description of the observations concerning basic fracture planes seen in UD composites and failure hypothesis Puck's failure model is presented.

a. Observations of Failure Modes in UD Composites

Basic stressings (stressing is used to mean applied stress mode) of a UD-composite element, which cause fracture is summarized in Figure 3.3. Six different types of stressings, $\sigma_{\parallel}^{t}$, $\sigma_{\parallel}^{c}$,$\sigma_{\perp}^{c}$, $\sigma_{\perp}^{t}$,$\tau_{\perp\perp}$, $\tau_{\perp\parallel}$, $\tau_{\parallel\perp}$ and the corresponding failure modes are

depicted in the figure. The first subscript of the stressing represents the normal of plane on which stressing is acting and the second subscript represents the direction of the stressing."‖" is the fiber direction and "⊥" is the fiber transverse direction.

From the figure the following phenomenological observations can be made:

- $\sigma_{\parallel}^{t}$ and $\sigma_{\parallel}^{c}$ stressing is responsible for fibre failure (FF)
- $\sigma_{\perp}^{c}$, $\sigma_{\perp}^{t}$,$\tau_{\perp\perp}$ and $\tau_{\perp\parallel}$ stressings cause interfiber failure (IFF)
- $\tau_{\parallel\perp}$ cannot produce a fracture on its action plane, because fibres prevent it
- Only $\sigma_{\perp}^{t}$ and $\tau_{\perp\parallel}$ cause fracture in their action planes
- $\sigma_{\perp}^{c}$ cause fracture on an oblique plane against its action plane. Likewise, $\tau_{\perp\perp}$ cause fracture approximately 45° against its action n plane.

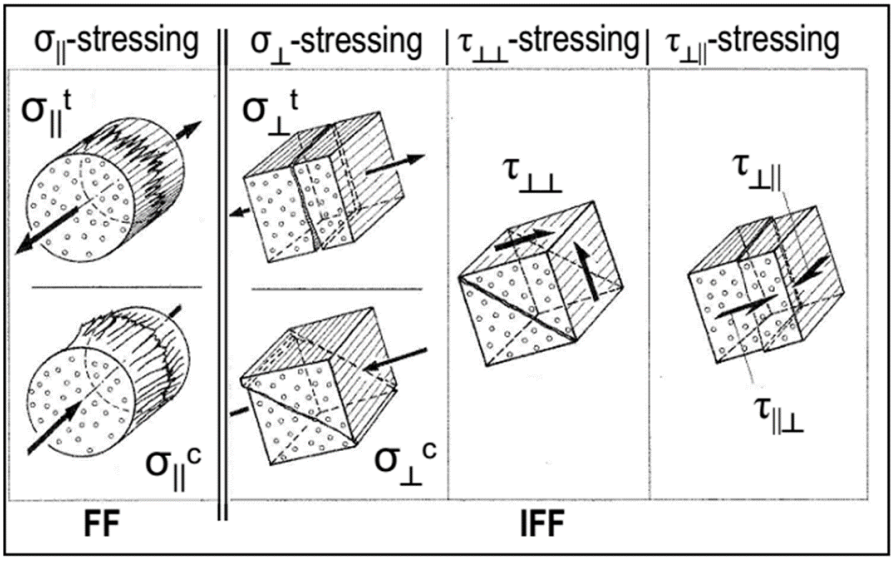

Figure 3.3*:* Basic stressings of UD-composite [79]

At this point, we should note that, in Puck's criteria there are six strengths designated as $R_{\parallel}^{t}$, $R_{\parallel}^{c}$,$R_{\perp}^{c}$, $R_{\perp}^{t}$, $R_{\perp\perp}$, and $R_{\perp\parallel}$.

The failure of the UD composite under transverse compression, $\sigma_{\perp}^{c}$ is caused by shear. Transverse/transverse shear $\tau_{\perp\perp}$ stressing which causes fracture at 45° against the action plane of $\tau_{\perp\perp}$. This type of fracture reminds us the fracture pattern of brittle materials which are subjected to pure shear stress. The observations above lead to

the conclusion that, “brittle fracture behavior” is predicted and takes us to the ideas of Mohr Coulomb.

b. Puck’s failure hypothesis

In 1900 Otto Mohr introduced a simple fracture hypothesis: “The stresses on the fracture plane are decisive for fracture” [79]. The hypothesis is easy but the location of the fracture plane is not known beforehand. Puck modified Coulomb-Mohr’s hypothesis for brittle materials in 1992 and adapted it to UD composites.

In order to have a better understanding of Puck’s hypothesis, Mohr’s failure envelope is constructed for a transversely-isotropic lamina under plane (σ_2, σ_3 and τ_{23}) stress. In Figure 3.4Figure 3.3 stress of the UD-lamina and stresses on a possible IFF fracture plane parallel to fibers is depicted.

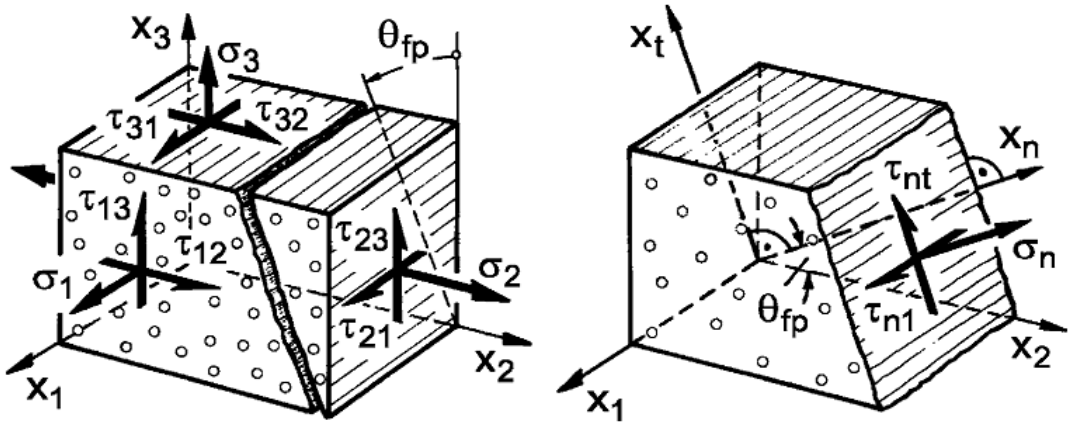

Figure 3.4. Stress of the UD-lamina and stresses on a possible (IFF) fracture plane parallel to fibers [82].

Transverse isotropy of the UD-lamina makes it possible to switch from the (x_2, x_3) coordinate system to a (x_n, x_t) coordinate system using the stress transformation equations:

$$\sigma_n(\theta) = \frac{1}{2}(\sigma_2 + \sigma_3) + \frac{1}{2}(\sigma_2 - \sigma_3)\cos 2\theta + \tau_{23}\sin 2\theta \tag{3.35}$$

$$\tau_{nt}(\theta) = -\frac{1}{2}(\sigma_2 - \sigma_3)\sin 2\theta + \tau_{23}\cos 2\theta \tag{3.36}$$

Figure 3.5 shows fracture under uniaxial compressive stress σ_2^c. Maximum shear stress is reached at $\theta = 45°$. However, at this point we observe from the Mohr's circle that compressive normal stress σ_n^c is also at its maximum value. Since σ_n^c helps to counteract shear fracture, shear fracture of the UD composite is observed to happen at $\theta_{fp} = 54$. This is due to the value of $\sigma_n(\theta_{fp})$ less than $|\sigma_{nmax}|$ ($\sigma_n(\theta_{fp}) < |\sigma_{nmax}|$).

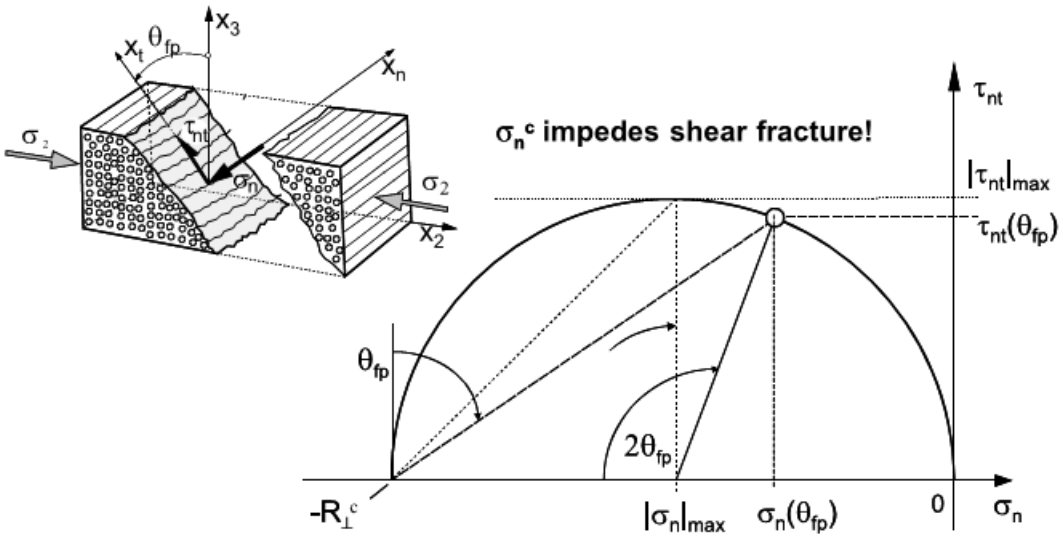

Figure 3.5. Fracture under uniaxial compressive stress σ_2^c [82].

Now, Puck's fracture hypotheses adapted to a UD-composite can be stated as follows:

1. The normal (σ_n) and shear stresses (τ_{n1} and τ_{nt}) on the fracture plane are decisive for IFF (Inter Fiber Failure)

2. If σ_n is a tensile stress, it helps IFF together with the resultant of shear stress τ_ψ ($\tau_\psi = \sqrt{\tau_{n1}^2 + \tau_{nt}^2}$) or even alone ($\tau_\psi$ =0), while compressive normal stress counteracts IFF

3. Fracture occurs either as a tensile fracture due to σ_n (highest normal stress) or as shear fracture due to τ_{nt} – whose effect is reduced by a compressive σ_n. Which of the two kind of stresses takes place depend on the ratio of stresses σ_2, σ_3 or τ_{23}.

It is not possible to define a failure criterion using the stresses $\sigma_2, \sigma_3, \tau_{23}, \tau_{31}, \tau_{21}$ based on the laminate coordinate system (x_1, x_2 and x_3), because brittle fracture hypothesis for the combined action of these stresses does not exist. According to Mohr-Coulomb $\sigma_2, \sigma_3, \tau_{23}, \tau_{31}, \tau_{21}$ must be transfered to the stresses σ_n, τ_{n1}, τ_{nt} on the fracture plane, because these stresses are relevant for inter fiber failure (IFF). This transformation is executed using the equation below [79]:

$$\begin{Bmatrix} \sigma_n(\theta_{fp}) \\ \tau_{nt}(\theta_{fp}) \\ \tau_{n1}(\theta_{fp}) \end{Bmatrix} = \begin{bmatrix} c^2 & s^2 & 2sc & 0 & 0 \\ -sc & sc & (c^2 - s^2) & 0 & 0 \\ 0 & 0 & 0 & s & c \end{bmatrix} \begin{Bmatrix} \sigma_2 \\ \sigma_3 \\ \tau_{23} \\ \tau_{31} \\ \tau_{21} \end{Bmatrix} \tag{3.37}$$

where $c = cos\ \theta_{fp}$ – and $s = sin\theta_{fp}$.

c. Puck's failure models

Puck was the first scientist who argued that Fiber Failure (FF) and Inter Fiber Failure (IFF) must be differentiated and analyzed with independent failure criteria [79]. Puck's oldest criteria known as the "Simplified and Modified Puck Criteria" were introduced in 1969. For the World-Wide Failure Exercise I (WWFE I) [111] Puck introduced an advanced composite failure model known as the "Action Plane Based Damage Model". These failure models are explained in the subsequent subsections.

(I) Simple and Modified Puck Criteria:

Simplified and modified Puck are two of the oldest Puck failure criteria ([80]-[81]). Simplified and modified Puck both calculate fiber failure using the same approach as in the maximum stress criterion:

$$\left|\frac{\sigma_1}{R_{\parallel}^{t,c}}\right| = 1 \tag{3.38}$$

Simplified and modified Puck provide us different expressions for matrix failure criterion. Let us consider simplified Puck failure criteria for matrix failure first:

$$\left(\frac{\sigma_2}{\mathrm{R}_{\perp}^{\mathrm{t,c}}}\right)^2 + \left(\frac{\tau_{12}}{\mathrm{R}_{\perp}^{\mathrm{c}}}\right)^2 = 1 \tag{3.39}$$

In equations (3.38) and (3.39), depending on the type of stress in fiber or transverse fiber direction, the following must be regarded:

$$\begin{aligned} \sigma_1 \geq 0 \ &\rightarrow \ R_{\parallel}^{t,c} = R_{\parallel}^{t} \\ \sigma_1 < 0 \ &\rightarrow \ R_{\parallel}^{t,c} = R_{\parallel}^{c} \\ \sigma_2 \geq 0 \ &\rightarrow \ \mathrm{R}_{\perp}^{\mathrm{t,c}} = \mathrm{R}_{\perp}^{\mathrm{t}} \\ \sigma_2 < 0 \ &\rightarrow \ \mathrm{R}_{\perp}^{\mathrm{t,c}} = \mathrm{R}_{\perp}^{\mathrm{c}} \end{aligned} \tag{3.40}$$

Modified Puck criteria for matrix failure is expressed as:

$$\underbrace{\left(\frac{\sigma_1}{2\mathrm{R}_{\perp}^{\mathrm{t}}}\right)^2}_{*} + \frac{\sigma_2^2}{\mathrm{R}_{\perp}^{\mathrm{t}}\mathrm{R}_{\perp}^{\mathrm{t}}} + \left(\frac{\tau_{12}}{\mathrm{R}_{\perp}^{\mathrm{c}}}\right)^2 + \left(\frac{1}{\mathrm{R}_{\perp}^{\mathrm{t}}} + \frac{1}{\mathrm{R}_{\perp}^{\mathrm{t}}}\right)\sigma_2 = 1 \tag{3.41}$$

The term (*) is not always included in the modified Puck criterion found in literature. This term helps to include the parallel-to-fiber stress σ_1 in matrix failures. Sometimes micro fiber fractures cause local debonding between fiber and matrix, which in turn

reduce the fiber matrix cohesion. As a consequence, matrix resistance to failures reduces [82].

(II) Puck's Physically Based Phenomenological Failure Model

Puck's theory provides information about the following major topics on (i) Non-linear stress and strain analysis before IFF (ii) Action plane related criteria for IFF and FF (iii) Continuous degradation after IFF. In the following paragraphs, these topics are explained in detail.

(i) Non-linear stress and strain behavior before IFF:

According to Puck and Schürmann [83] minor nonlinearity in the stress-strain diagram of carbon fibers before IFF needs to be considered in the material strength calculations. This nonlinearity in the material behavior is assumed to be due to micro damage. Figure 3.6 shows the damage hysteresis caused by micro cracks in a UD-layer in a loading/unloading cycle. This damage hysteresis is caused by the combined influence of σ_2 and τ_{21} on the $(\sigma_2, \varepsilon_2)$ and (τ_{21}, γ_{21})stress-strain diagrams. Puck accounts for this nonlinearity using secant modulus method. This methodology helps to determine the final stress/strain state within one load step. Puck and Mannigel [85] explained their computational method for including the influence of nonlinearity in stress-strain diagram of UD laminas with non-flexibilized thermoset matrix before IFF.

(i) Action plane related fracture criteria for IFF and FF:

The plane on which the stress is acting on is called action plane in Puck's criteria. Failure criteria, which are related to action plane are explained in the following subsections. In this thesis, simple and modified Puck criterion is implemented in the analytical plain strength analysis method developed for composite laminates, whereas Puck's failure criteria developed for the WWFE I are implemented in the numerical models used for the progressive damage analysis of open hole tension composite laminates and wind turbine blade.

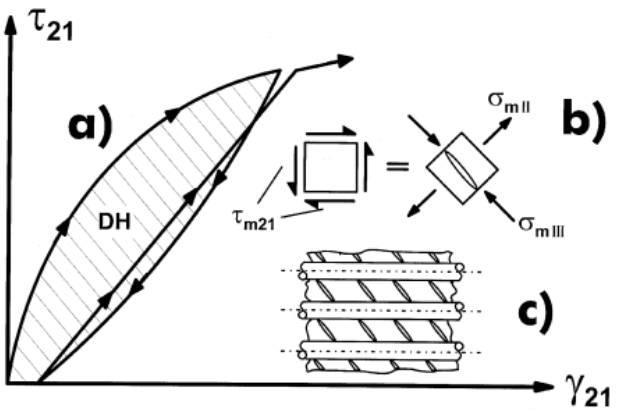

Figure 3.6*:* (a) Damage hysteresis (DH) caused by micro cracks in a UD-layer in a loading/unloading cycle (b) shear stress τ_{m21}, and transformed principal stresses σ_{mII} and σ_{mIII} (c) micro cracks between fibers [83].

Puck's failure model based on action plane strength criteria

Puck and Schürmann [83] presented a more physically correct fiber failure (FF) criterion for the world wide failure exercise I (WWFE I), which is based on a failure hypothesis for the fibers instead of the UD composite. This is due to the fact, that loads are concentrated in fibers. The fiber failure for the plane stress condition is expressed as [82]:

$$\mathrm{f_{E,FF}} = \frac{1}{\pm \mathrm{R}_{\parallel}^{\mathrm{t,c}}}\left[\sigma_1 - \left(\nu_{\perp\parallel} - \nu_{\perp\parallel \mathrm{f}} \mathrm{m}_{\sigma \mathrm{f}} \frac{\mathrm{E}_{\parallel}}{\mathrm{E}_{\parallel \mathrm{f}}}\right)\sigma_2\right] \text{ with} \tag{3.42}$$

$$R_{\parallel}^{t} \text{ for } [\ldots] \geq 0 \text{ and } -R_{\parallel}^{c} \text{ for } [\ldots] < 0 \tag{3.43}$$

In equation (3.42) above $\mathrm{f_{E,FF}}$ stands for the failure exposure, σ_1 and σ_2 are the normal stresses in principal material directions. $\nu_{\perp\parallel}$ and $\nu_{\perp\parallel f}$ are the Poisson ratios of the lamina and fibre, respectively. $E_{\parallel}$ and $E_{\parallel f}$ are the elasticity moduli of the lamina in fiber direction and $E_{\parallel f}$ is the elasticity modulus of the fibre. $m_{\sigma f}$ is a stress modification factor which considers the difference between the elasticity moduli of the fiber and matrix.

Puck's inter fiber failure (IFF) criteria

According to Puck's hypothesis, for the 3D case two different failure conditions are considered [84]:

$$\left(\frac{\sigma_n}{R_{\perp}^{tA}}\right)^2 + \left(\frac{\tau_{nt}}{R_{\perp\perp}^{A}}\right)^2 + \left(\frac{\tau_{n1}}{R_{\perp\parallel}^{A}}\right)^2 = 1 \text{ for } \sigma_n \geq 0 \tag{3.44}$$

$$\left(\frac{\tau_{nt}}{R_{\perp\perp}^{A} - p_{\perp\perp}^{c}\sigma_n}\right)^2 + \left(\frac{\tau_{n1}}{R_{\perp\parallel}^{A} - p_{\perp\parallel}^{c}\sigma_n}\right)^2 = 1 \text{ for } \sigma_n < 0 \tag{3.45}$$

In equations (3.44) and (3.45) the superscript "A" in $R_{\perp}^{tA}, R_{\perp\perp}^{A}$ and $R_{\perp\parallel}^{A}$ stands for action plane. Fracture resistance R^A of an action plane is the maximum resistance with which the action plane can resist fracture. $p_{\perp\parallel}^{c}$ is the slope of the (σ_n, τ_{n1}) fracture envelope for $\sigma_n \leq 0$ at $\sigma_n = 0$. $p_{\perp\perp}^{c}$ is the slope of the (σ_n, τ_{nt}) fracture envelope for $\sigma_n \leq 0$ at $\sigma_n = 0$.

The master fracture body:

At this point plot the fracture body in $(\sigma_n, \tau_{nt}, \tau_{n1})$ three dimensional coordinate system using IFF equations (3.44) and (3.45) can be plotted. This fracture body is called master fracture body, and displayed in Figure 3.7.

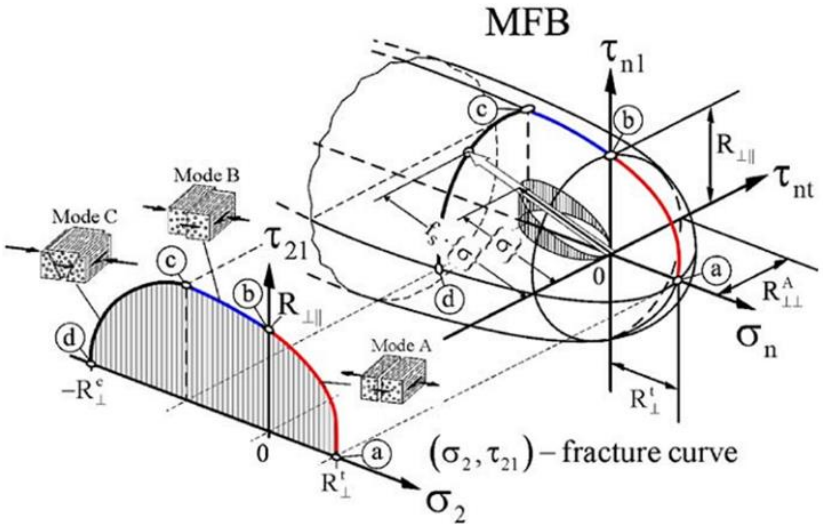

Figure 3.7. Master Fracture Body in $(\sigma_n, \tau_{nt}, \tau_{n1})$ coordinate system [79].

However, the fracture angle θ_{fp} at which fracture happens is not known at this stage. It is known that the fracture can happen parallel to fibers. In order to determine the fracture plane with the highest risk of failure the most critical stress combination $(\sigma_n, \tau_{nt}, \tau_{n1})$,which will lead to fracture is investigated, as shown in Figure 3.8. This investigation can be done using numerical or analytical methods. As seen in Figure 3.8 the search for the fracture plane in UD composite is conducted around x_1-axis, which is parallel to fibers. This search covers the angles $-90° \leq \theta \leq 90°$.

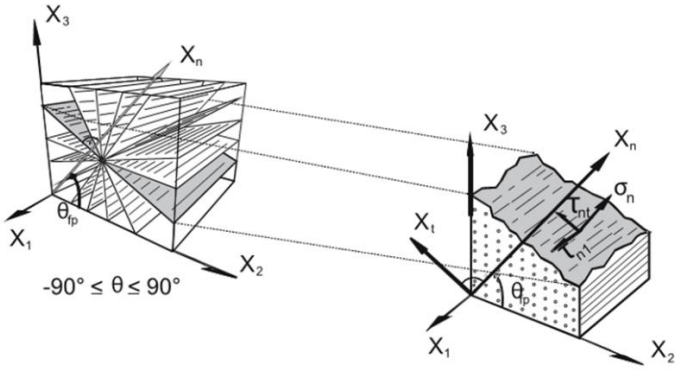

Figure 3.8. Search for the fracture plane in UD composite [82].

The fracture plane is determined after finding the most critical stress $(\sigma_n, \tau_{nt}, \tau_{n1})$ combination. This combination is expressed in terms of stress exposure f_E.In order to understand strMULess exposure used in Puck's theory, stress state on (σ_2, τ_{21})-plane is shown in Figure 3.9. On the figure $\{\sigma\}^r$ is residual stress, which is caused during manufacturing process, and $\{\sigma\}^L$ is the stress caused by loading. When $\{\sigma\}^L$ and $\{\sigma\}^r$ are added we get the resultant stress vector $\{\sigma\}$. If this vector is extended and touches the failure envelope, it corresponds to $\{\sigma\}_{fr}$. Stress exposure is defined as:

$$f_E = \frac{|\{\sigma\}|}{|\{\sigma\}_{fr}|} \tag{3.46}$$

The magnitude of f_E provide information about the risk of failure. If $f_E = 1$, then failure condition is reached. Fracture plane is computed by finding the angle which corresponds to maximum stress exposure as shown by the following expression:

$$f_E(\theta_{fp}) = f_{Emax} \tag{3.47}$$

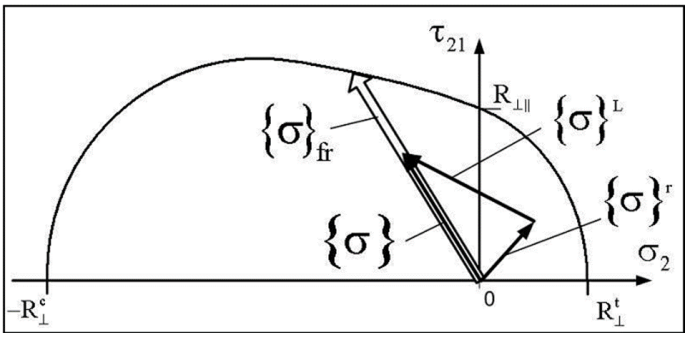

Figure 3.9. Representation stress exposure on the (σ_2, τ_{21})-stress plane (Lutz, 2006) [79].

Inter fiber failure (IFF) modes:

Puck differentiates between different fracture modes based on different stress combinations. For simplification reasons, fracture modes are shown on the (σ_2, τ_{21}) fracture envelope (Referring to Figure 3.7). Fracture modes are as follows:

- Mode A fracture (between points (a) and (b)) is caused by the combination of σ_n^t and τ_{n1} stresses. σ_n^t induces $\sigma_\perp^t$ stressing (tensile stressing) and τ_{n1} induces $\tau_{\perp\parallel}$ (in-plane shear stressing). For this fracture mode, fracture angle $\theta_{fp} = 0°$.
- Mode B fracture (between points (b) and (c)) is caused by the combination of σ_n^c and τ_{n1} stresses. σ_n^c induces $\sigma_\perp^c$ stressing (compressive stressing) and τ_{n1} induces $\tau_{\perp\parallel}$ stressing (in-plane shear stressing). For this fracture mode, fracture angle $\theta_{fp} = 0°$.
- Mode C fracture (between points (c) and (d)) is caused by the combination of σ_n^c, τ_{n1} and τ_{nt} stresses. σ_n^c induces $\sigma_\perp^c$ stressing, and τ_{n1}, $\tau_{\perp\parallel}$ induce τ_{nt} and $\tau_{\perp\perp}$, respectively. In this case, the compressive stresses increase with respect to shear stresses. For this fracture mode, fracture angle starts at $\theta_{fp} =$

0° at point c and increases up to $\theta_{fp} \approx 55°$ at point d. This failure mode is dangerous and causes cracks in oblique fracture planes.

For the 2D plane strength case, no numerical search of fracture plane is required. Analytical methods are sufficient to find the fracture plane. Three IFF modes for the 2D plane strength case are derived from (3.44)-(3.45) at the fracture plane. These IFF modes are described by equations (3.48), (3.49) and (3.50) below:

$$f_{E,IFF}^{A} = \sqrt{\left[\left(\frac{1}{R_{\perp}^{t}} - \frac{p_{\perp\parallel}^{t}}{R_{\perp\parallel}}\right)\sigma_2\right]^2 + \left(\frac{\tau_{21}}{R_{\perp\parallel}}\right)^2} + \frac{p_{\perp\parallel}^{t}}{R_{\perp\parallel}}\sigma_2, \text{ for } \sigma_2 \geq 0 \tag{3.48}$$

$$f_{E,IFF}^{B} = \sqrt{\left(\frac{\tau_{21}}{R_{\perp\parallel}}\right)^2 + \left(\frac{p_{\perp\parallel}^{c}}{R_{\perp\parallel}}\sigma_2\right)^2} + \frac{p_{\perp\parallel}^{c}}{R_{\perp\parallel}}\sigma_2, \sigma_2 < 0 \text{ and } \left|\frac{\sigma_2}{\tau_{21}}\right| \leq \left|\frac{R_{\perp\perp}^{A}}{\tau_{21,c}}\right| \tag{3.49}$$

$$f_{E,IFF}^{C} = \left[\left(\frac{\tau_{21}}{2(1+p_{\perp}^{c})R_{\perp\parallel}}\right)^2 + \left(\frac{\sigma_2}{R_{\perp}^{c}}\right)^2\right]\frac{R_{\perp}^{c}}{-\sigma_2}, \text{ for } \sigma_2 < 0 \text{ and } \left|\frac{\sigma_2}{\tau_{21}}\right| \geq \left|\frac{R_{\perp\perp}^{A}}{\tau_{21,c}}\right| \tag{3.50}$$

In equations (3.48), (3.49) and (3.50) $f_{E,IFF}^{A}$ and $f_{E,IFF}^{B}$ represent failure exposure for failure modes A and B respectively. Similarly, $f_{E,IFF}^{C}$ is the failure exposure for failure mode C.

(ii) Continuous degradation after IFF:

According to Puck's failure criteria for WWFE I under quasi-static loading if IFF occurs, the elastic properties of the matrix in which failure takes place is degraded continuously based on experimental data. A detailed explanation of the continuous degradation method after IFF can be found in subsection 7.2.3 of this thesis, [82] and [83].

3.1.1.2 Multidirectional Laminate Analysis Procedure

Multidirectional laminate strength analysis procedure begins with the calculation of laminae stresses. As long as the laminate exhibits linear elastic behavior, stresses in

the laminate are directly proportional to the applied loads. This allows us to determine the load at which the laminate fails by scaling up the stresses [79].

Laminate strength analysis and load deformation behavior is summarized in Figure 3.10. In the figure, loading is given by in-plane forces and moments, and deformations are given by in-plane strains and curvatures. As seen from the figure the algorithm of the analysis is composed of two loops depending on whether the laminae have failed or not. Laminate stresses are first calculated on laminate coordinates and then converted to stresses in material principal axes using transformation matrices. The load parameter is increased until some individual lamina fails. In order to determine whether a lamina have failed or not, failure criteria are used. The properties of the lamina are degraded in two ways:

(i) completely to zero if the fibers fail
(ii) matrix is degraded if cracking in the matrix parallel to fibers occurs

At this point, we note that degraded properties must not be set to zero, in order to avoid singularities in the calculations. Instead of setting to zero, degraded properties are assigned very small values. After laminae have failed, new laminate extensional, coupling and bending stiffnesses are calculated.

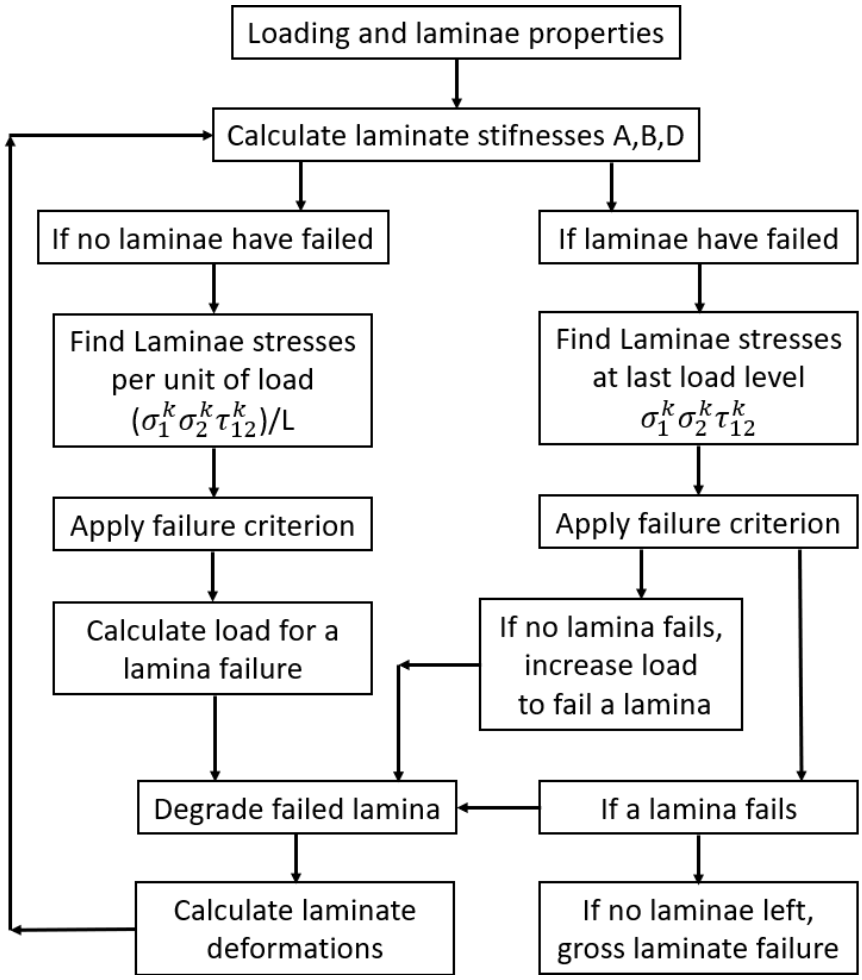

Figure 3.10. Laminate strength analysis and load-deformation behavior [73].

During the strength analysis of the laminate, we must make sure that the laminae does not fail at the same load, which caused the failure of the laminae in the preceding cycle. In order to achieve this, stresses must be successfully redistributed between remaining laminae. In addition to this, load increments must be kept low enough, so that individual failure of the laminae takes place. When multiple laminae fail instantly, gross failure of the laminate occurs. Laminate strength analysis procedure does not depend on the selected failure criteria. Yet the results of the analysis (loads and deformations) are related to the selected failure criteria.

Types of Failure:

Failure in a laminate may be caused by the individual failure of the laminae (intralaminar failure) or by the separation of the laminae (inter-laminar failure). For the prediction of inter-laminar failure, 3-D stress and failure analysis including inter-laminar strength and toughness properties of the laminate are required [69].

First Ply Failure (FPF) is the case when the first ply in a group of plies fail. Ultimate Ply Failure (UPL) is the case when the maximum load level is reached and the laminate cannot sustain any further stresses. For UPL criteria such as first fiber failure, maximum load or last-ply-failure are proposed. First fiber failure approach is recommended for fiber dominated plies, whereas last-ply-failure approach gives more realistic results for matrix dominated plies.

3.1.2 Open Hole Composite Laminate Strength Calculation Method

This subsection includes the theoretical background of the open hole composite laminate strength calculation methodologies. In the first part of the subsection, existing analytical models, which are used for the strength prediction of OH laminates subjected to uniaxial loading are summarized (Section 3.1.2.1). In the second part, the analytical model, which serves as the basis for the proposed strength calculation method of OH laminates under combined loading conditions (Extended Point Stress Method) in this thesis, is introduced (Section 3.1.2.2).

3.1.2.1 Existing Analytical Models

3.1.2.1.1 Point-Stress and Average Stress Models

According to the Point Stress Criterion (PSC) proposed by Whitney and Nuismer [14] failure occurs when the point stress value is equal to or greater than

the strength of the unnotched laminate at some characteristic distance d_0 away from the hole of the laminate. After this definition, for quasi-isotropic open-hole laminates PSC can be expressed as following:

$$\sigma_0 = f_{correction}\left(\frac{W}{2a}\right)\frac{\sigma_N}{2}\left[2+\left(\frac{a}{a+d_0}\right)^2+3\left(\frac{a}{a+d_0}\right)^4\right] \tag{3.51}$$

where, σ_0 and σ_N are the unnotched and notched laminate strengths, respectively, W' and 'a' are the laminate width and hole diameter radius. For quasi-isotropic plates, in order to account for the finite width-to-hole diameter ratio, a simple relation for the correction factor, $f_{correction}\left(\frac{W}{2a}\right)$ proposed by Tan [86] is implemented:

$$f_{correction}\left(\frac{W}{2a}\right) = \frac{2+\left(1-\frac{2a}{W}\right)^3}{3\left(1-\frac{2a}{W}\right)} \tag{3.52}$$

Average stress criterion (ASC) proposed by Whitney and Nuismer [14] states that failure occurs when the average stress value is equal to greater than the unnotched laminate strength at some distance a_0 away from the hole in the laminate. For quasi-isotropic open-hole laminates, the ASC can be expressed as follows:

$$\sigma_0 = \frac{2+\left(1-\frac{2a}{W}\right)^3}{6\left(1-\frac{2a}{W}\right)}\frac{\sigma_N}{\left[1-\left(\frac{a}{a+a_0}\right)\right]}\left[2+\left(\frac{a}{a+a_0}\right)^2+3\left(\frac{a}{a+a_0}\right)^4\right] \tag{3.53}$$

3.1.2.1.2 Linear Elastic Fracture Mechanics Inherent Flaw Model

Linear Elastic Fracture Mechanics Inherent Flaw Model (LEFM IFM) proposed by Waddoups et al. [14] is based on the assumption that, damage mechanisms occurring just before ultimate failure can be lumped into a "region of intense energy" called "inherent flaw" of length 'a_{ifm}'. This approach is similar to Irwin's plastic zone correction in metals. With this assumption, the critical value of the stress intensity factor of an open hole laminate is expressed as:

$$K_{Ic} = f(a_{ifm}, a)\overline{\sigma}^{\infty}\sqrt{\pi a_{ifm}} \tag{3.54}$$

where f(a_{ifm},R) is Bowie's [89] solution for the stress intensity factor of two cracks originating from the circular hole. The strength of an unnotched specimen can be calculated by taking f(a_{ifm}, a)=1. In this case, the critical stress intensity factor K_{Ic} can be rewritten as:

$$K_{Ic} = X_L^T\sqrt{\pi a_{ifm}} \tag{3.55}$$

where X_L^T is the tensile strength of the laminate. After equating (3.54) and (3.55), the remote stress $\overline{\sigma}^{\infty}$ is obtained as:

$$\overline{\sigma}^{\infty} = \frac{X_L^T}{f(a_{ifm}, a)} \tag{3.56}$$

Provided that the hole diameter is known, equation (3.56) shows that the remote stress $\overline{\sigma}^{\infty}$ depends on the region of intense energy a_{ifm} and the laminate unnotched strength X_L^T.

3.1.2.1.3 Cohesive Zone Model

Soutis and Fleck [29] propose a Cohesive Zone Model (CZM) for the strength prediction of the Carbon Fiber-Epoxy laminate with an open hole. According to the model, damage emerging from each hole side is represented by a cohesive crack. Damage initiates when the stress level in the 0º fibers reach the unnotched laminate strength. Damage progression is simulated by replacing the damage zone with an equivalent crack. In the equivalent crack region, crack bridging stresses drop linearly along the crack overlapping region from a maximum value of the unnotched laminate strength. The model requires only two parameters: unnotched laminate strength and the fracture energy. In this thesis, results obtained from the Composite Compressive Strength Modeler Tool developed by Sutcliffe et al. [87] are used for the open-hole tension and compression strength predictions ([25],[26]).

3.1.2.1.4 Finite Fracture Mechanics Model

Finite Fracture Model (FFM) proposed by Cornetti et al. [88] uses the following stress and energy finite fracture mechanics criteria as a couple for strength analysis of a laminate with an open hole subjected to uniaxial loading:

$$\frac{1}{l}\int_{a}^{a+l} \sigma_{yy}(x,0)dx = X_T^L \tag{3.57}$$

$$\frac{1}{l}\int_{a}^{a+l} K_I^2(s)ds = K_{IC}^2 \tag{3.58}$$

In equations (3.57) and (3.58), 'a' is the circular hole radius and 'l' represents crack extension at failure. In equation (3.57), $\sigma_{yy}(x,0)$ and X_T^L are the normal stress in y-direction and the unnotched strength of the laminate, respectively. It is noted that normal stress σ_{yy} is measured along the x-coordinate in the (x-y) cartesian coordinate system. In equation (3.58), K_I and K_{IC} are the mode I stress intensity factor and fracture toughness of the laminate, respectively. The crack extension length is denoted by 's'. Furthermore, equation (3.57) represents the average stress model, which is explained in Whitney and Nuismer [14]'s paper. In addition, the proposed FFM uses equation (3.58) which serves as an energy balance, that must be satisfied during crack propagation. The following two unknowns are determined from the set of equations (3.57) and (3.58) [13]:

- remote notched strength
- crack extension at failure l.

When 'l' is known, it is possible to calculate remote stress at failure from either of the equations (3.57) or (3.58). Hence, there is no need to calculate "characteristic distance" from notched specimen tests. Numerical solution techniques are used for the solution of nonlinear equations, that are encountered during the solution of (3.57). Camanho et. al. [13] state, that characteristic distance, "l" is a function of both geometry and material properties.

The main advantages of the model compared to other approaches for the open-hole strength prediction of laminated composites is that, it is economic, fast and accurate. The proposed model is economic in the sense, that only ply elastic constants, unnotched laminate strength, and fracture toughness is needed. Since it is not based on Finite Element Analysis (FEA) or complex computation methods, it is fast. When compared with experimental data, FFM gives more accurate results compared to point stress model, average stress model and the inherent flaw model.

3.1.2.2 Open Hole Laminate Subjected to Combined Loading

In this subsection, the methodology for the strength prediction of composite plates with openings under uniaxial in-plane tensile, compression, shear or combined loading conditions is introduced. Different notch geometries such as elliptical and circular are considered. The analytical solution to determine the stress field is based on the complex variable mapping method using Lekhnitskii formulation and classical lamination theory. Failure prediction is done using composite failure theory at a critical distance and angle.

Theoretical Background and Derivations for Stress Field Generation

The derivation of Lekhnitskii [90] equations, which are used for the generation of stress fields in an orthotropic plate with an elliptical opening is explained in this subsection. Elastic equilibrium equations are satisfied by the introduction of an Airy stress function F(x,y) [90]. When the body forces are omitted, these equations can be written as:

$$\bar{\sigma}_x = \frac{\partial^2 F}{\partial y^2} \qquad \bar{\sigma}_y = \frac{\partial^2 F}{\partial x^2} \qquad \bar{\tau}_{xy} = \frac{-\partial^2 F}{\partial x \partial y} \tag{3.59}$$

Condition of compatibility for deformation is [91]:

$$\frac{\partial^2 \bar{\varepsilon}_x}{\partial y^2} + \frac{\partial^2 \bar{\varepsilon}_y}{\partial x^2} - \frac{\partial^2 \bar{\gamma}_{xy}}{\partial x \, \partial y} = 0 \tag{3.60}$$

For an anisotropic body average strain values are given below:

$$\bar{\varepsilon}_x = a_{11}\bar{\sigma}_x + a_{12}\bar{\sigma}_y + a_{16}\bar{\tau}_{xy}$$
$$\bar{\varepsilon}_y = a_{12}\bar{\sigma}_x + a_{22}\bar{\sigma}_y + a_{26}\bar{\tau}_{xy} \quad (3.61)$$
$$\bar{\gamma}_{xy} = a_{16}\bar{\sigma}_x + a_{26}\bar{\sigma}_y + a_{66}\bar{\tau}_{xy}$$

where a_{ij} are the compliances of the laminate.

Plugging (3.61) into (3.60) gives the following equation, which must be satisfied by the Airy stress function F(x,y):

$$a_{22}\frac{\partial^4 F}{\partial x^4} - 2a_{26}\frac{\partial^4 F}{\partial x^3 \partial y} + (2a_{12} + a_{66})\frac{\partial^4 F}{\partial x^2 \partial y^2} - 2a_{16}\frac{\partial^4 F}{\partial x \partial y^3} + a_{11}\frac{\partial^4 F}{\partial y^4} = 0 \quad (3.62)$$

Equation (3.62) can be integrated using the linear differential operators below:

$$D_1 D_2 D_3 D_4 F = 0 \quad (3.63)$$

where $D_k = \frac{\partial}{\partial y} - \mu_k \frac{\partial}{\partial x}, k = 1 \ldots 4$

After the integration the characteristic equation below is obtained. In (3.64), μ_k are called the roots of the characteristic equation.

$$a_{11}\mu^4 - 2a_{16}\mu^3 + (2a_{12} + a_{66})\mu^2 - 2a_{26}\mu + a_{22} = 0 \quad (3.64)$$

For orthotropic plates $a_{16} = a_{26} = 0$. Excluding special cases μ_k are either complex or purely imaginary numbers. From (3.64) four roots of the form μ_1, μ_2 and their conjugates $\bar{\mu}_1$, $\bar{\mu}_2$ will be obtained. Among these roots two principal roots will be chosen. According to a complementary definition, principal roots μ_1, μ_2 are always the complex roots that have the least value of argument among all roots. For isotropic plates $\mu_1 = \mu_2 = i$. Characteristic roots can be regarded as values, which define the degree of anisotropy in plane stress problems and with these values one can judge how much a laminate can differ from the isotropic case.

Equation (3.63) can be rewritten as:

$$D_4 F = g_3$$
$$D_3 D_4 F = g_2 \quad (3.65)$$
$$D_2 D_3 D_4 F = g_1$$

$$D_1 g_1 \equiv \frac{\partial g_1}{\partial y} - \mu_1 \frac{\partial g_1}{\partial x} = 0 \tag{3.66}$$

where D_k, k=1,…,4 are partial derivatives of first order.

Integrating equation (3.66) yields:

$$g_1 = f_1(x + \mu_1 y) \tag{3.67}$$

In expression (3.67) f_1 is an arbitrary function of $x + \mu_1 y$. The integration of the set of equations in (3.65), gives:

$$\begin{aligned} \frac{\partial g_2}{\partial y} - \mu_2 \frac{\partial g_2}{\partial x} &= g_1 \\ \frac{\partial g_3}{\partial y} - \bar{\mu}_1 \frac{\partial g_3}{\partial x} &= g_2 \\ \frac{\partial F}{\partial y} - \bar{\mu}_2 \frac{\partial F}{\partial x} &= g_3 \end{aligned} \tag{3.68}$$

By integrating non-homogeneous equations in (3.68) in order the following expression for F is obtained:

$$F = F_1(x + \mu_1 y) + F_2(x + \mu_2 y) + F_3(x + \bar{\mu}_1 y) + F_4(x + \bar{\mu}_2 y) \tag{3.69}$$

Different variables are introduced for different complex numbers:

$$\begin{aligned} z_1 &= x + \mu_1 y \\ z_2 &= x + \mu_2 y \\ z_3 &= x + \bar{\mu}_1 y \\ z_4 &= x + \bar{\mu}_2 y \end{aligned} \tag{3.70}$$

Since stress function is a real function of x and y, for the case of different complex numbers presented in (3.69), the relation below can be written:

$$F = 2\,Re[F_1(z_1) + F_2(z_2)] \tag{3.71}$$

The following functions are defined for the obtaining the stress components in terms of complex parameters:

$$\phi_1(z_1) = \frac{dF_1}{dz_1}$$
$$\phi_2(z_2) = \frac{dF_2}{dz_2}$$
$$\phi_1'(z_1) = \frac{d\phi_1}{dz_1} \tag{3.72}$$
$$\phi_2'(z_2) = \frac{d\phi_2}{dz_2}$$

Stress components in expression (3.59) can be rewritten in terms of the functions defined in (3.72):

$$\begin{aligned} \sigma_x &= 2\,Re[\,\mu_1^2\phi_1'(z_1) + \mu_2^2\phi_2'(z_2)] \\ \sigma_y &= 2\,Re[\,\phi_1'(z_1) + \phi_2'(z_2)] \\ \tau_{xy} &= -2\,Re[\,\mu_1\phi_1'(z_1) + \mu_2\phi_2'(z_2)] \end{aligned} \tag{3.73}$$

We will try to derive the relations for ϕ_1 and ϕ_2 by using the conditions on the surface of a body:

$$\begin{aligned} \sigma_x \cos(n,x) + \tau_{xy} \cos(n,y) &= X_N \\ \sigma_y \cos(n,y) + \tau_{xy} \cos(n,x) &= Y_N \end{aligned} \tag{3.74}$$

where n is the direction normal to the surface of the body X_N and Y_N are external forces.

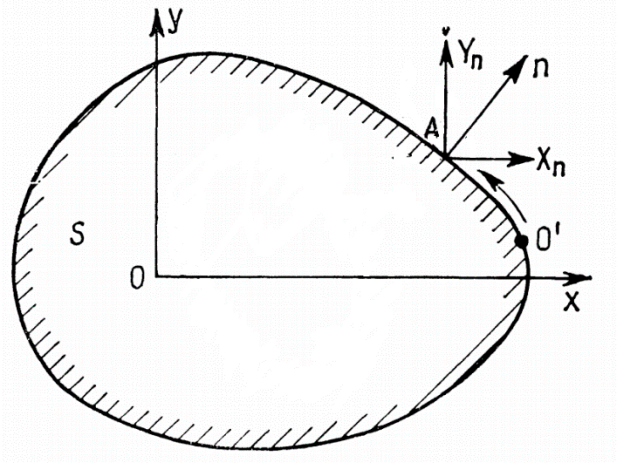

Figure 3.11. Plate with an area S subjected to external forces Xn and Yn at the external contour [90].

Letting $\tau_{xy} = 0$ and $\cos(n,x) = \cos(n,y) = 1$, relations in (3.74) simplify to:

$$\sigma_x = X_N, \quad \sigma_y = Y_N \tag{3.75}$$

Utilizing equation (3.59):

$$\frac{\partial^2 F}{\partial y^2} = X_N \qquad \frac{\partial^2 F}{\partial x^2} = Y_N$$
$$\frac{\partial F}{\partial y} = \int_0^s X_N ds \qquad \frac{\partial F}{\partial x} = \int_0^s Y_N ds \tag{3.76}$$

In (3.76), by integrating oven an arc length 's', which is equal to arc O'A, boundary conditions for the external forces X_N and Y_N are obtained. Expressions in (3.18) can be expressed in terms of stress potentials as:

$$2\,Re[\,\mu_1\phi_1(z_1) + \mu_2\phi_2(z_2)] = \int_0^s X_N ds + c_1$$
$$2\,Re[\,\phi_1(z_1) + \phi_2(z_2)] = -\int_0^s Y_N ds + c_2 \tag{3.77}$$

We note that ϕ_1 and ϕ_2 should satisfy the boundary conditions. Following Lekhnitskii equations are derived for the determination of the stress field for an infinite plate size compared to the size of the opening which is very small. External

forces X_N and Y_N, which are exerted on an infinite orthotropic plate with an opening are depicted in

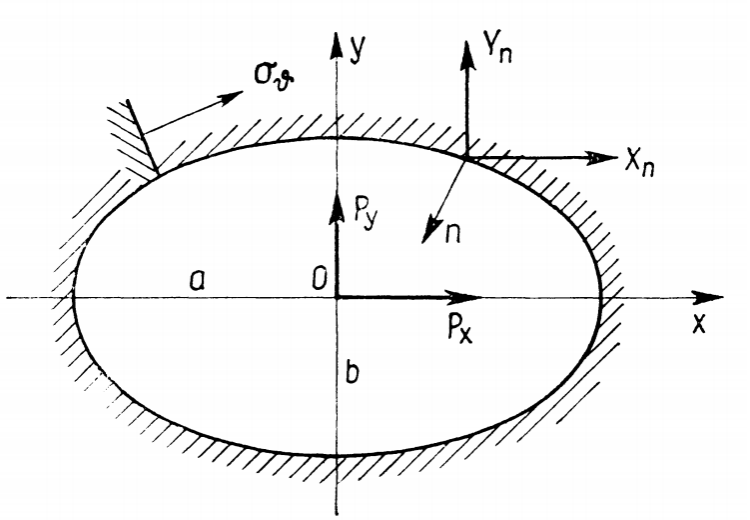

Figure 3.12. Plate with an area S subjected to external forces Xn and Yn at the external contour [90].

In Figure 3.12,

a, b: lengths of the major axis of the elliptical hole

h: plate thickness

X_n, Y_n: forces acting on the opening edge per unit area

P_x, P_y: resultant of the external forces Xn and Yn

Coordinates of the opening edge can be written in parametric form:

$x = \mathrm{acos}(\vartheta), y = \mathrm{bsin}(\vartheta)$.

Forces change with respect to ϑ between range 0-2π. In the coming expressions complex representations of the stress functions ϕ_1 and ϕ_2 will be used. Expanding X_N and Y_N into Fourier series yields:

$$2\,Re[\,\mu_1\phi_1(z_1)+\mu_2\phi_2(z_2)] = \frac{P_y\vartheta}{2\pi h}+\alpha_0+\sum_{m=1}^{\infty}(\,\alpha_m\sigma^m+\bar{\alpha}_m\sigma^{-m})$$
$$2\,Re[\,\phi_1(z_1)+\phi_2(z_2)] = \frac{-P_x\vartheta}{2\pi h}+\beta_0+\sum_{m=1}^{\infty}(\,\beta_m\sigma^m+\bar{\beta}_m\sigma^{-m}) \qquad (3.78)$$

where $\sigma = e^{i\theta}$, α_m and β_m are the known coefficients which depend on the load distribution at the opening edge. $\bar{\alpha}_m$ and $\bar{\beta}_m$ are the respective conjugate values. Constants α_0 and β_0 are arbitrary constants in (3.78). The solution of the stress functions in (3.78) have the form below:

$$\phi_1(z_1) = A_0 + A\cdot\ln\xi_1 + \sum_{m=1}^{\infty}\frac{\bar{\beta}_m-\mu_2\bar{\alpha}_m}{\mu_1-\mu_2}\xi_1^{-m}$$
$$\phi_2(z_2) = B_0 + B\cdot\ln\xi_2 - \sum_{m=1}^{\infty}\frac{\bar{\beta}_m-\mu_1\bar{\alpha}_m}{\mu_1-\mu_2}\xi_2^{-m} \qquad (3.79)$$

where

$$\xi_1 = \frac{z_1+\sqrt{z_1^2-a^2-\mu_1^2b^2}}{a-i\mu_1 b}$$
$$\xi_2 = \frac{z_2+\sqrt{z_2^2-a^2-\mu_2^2b^2}}{a-i\mu_2 b}$$

When plugged into (3.78) funtions ϕ_1 and ϕ_2 will deliver the same values as the external forces of the form $\sigma^{i\theta}$ at the opening edge. A_0 and B_0 are the arbitrary constants. A and B are the constants, which are determined by the equations P_x and P_y. Problems tackled in the open hole calculation does not involve unbalanced external forces applied to the opening edge with respect to major eliptic axes. Hence there will be no resultant force P_x and P_y and the terms related to P_x and P_y, $A\cdot\ln\xi_1$ and $A\cdot\ln\xi_1$ are set to zero. Moreover A_0 and B_0 are arbitrary constants and cancel out α_0 and β_0. This allows us to simplify (3.79):

$$\phi_1(z_1) = \sum_{m=1}^{\infty} \frac{\bar{\beta}_m - \mu_2 \bar{\alpha}_m}{\mu_1 - \mu_2} \xi_1^{-m}$$

$$\phi_2(z_2) = -\sum_{m=1}^{\infty} \frac{\bar{\beta}_m - \mu_1 \bar{\alpha}_m}{\mu_1 - \mu_2} \xi_2^{-m} \tag{3.80}$$

where

$$\xi_1 = \frac{z_1 + \sqrt{z_1^2 - a^2 - \mu_1^2 b^2}}{a - i\mu_1 b}$$

$$\xi_2 = \frac{z_2 + \sqrt{z_2^2 - a^2 - \mu_2^2 b^2}}{a - i\mu_2 b}$$

Let us now consider in-plane combined loading condition, which cause stress distributions in a plate with an elliptical opening. The geometry and the coordinates of an orthotropic plate with an elliptical opening is shown in Figure 3.13.

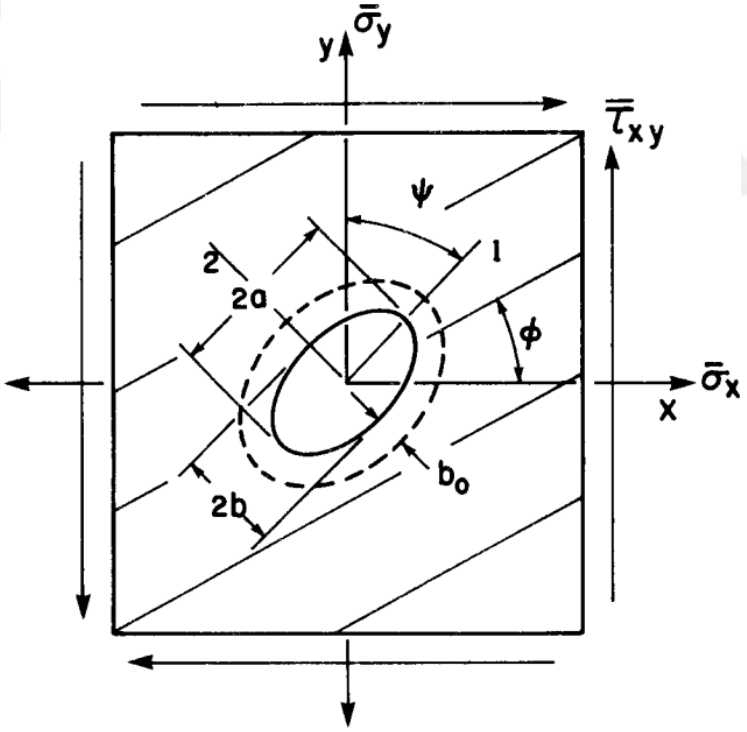

Figure 3.13. Coordinates of a composite lamina with an elliptical opening subjected to combined loading [18].

The following expressions for in-plane stresses are given in the principal coordinates of the opening. Total stress components on the plate can be found by summing the stresses due to:

(i) Uniform stress field:

$$\begin{aligned}\sigma_1^0 &= \bar{\sigma}_x \sin^2\psi + \bar{\sigma}_y \cos^2\psi + \bar{\tau}_{xy} \sin 2\psi \\ \sigma_2^0 &= \bar{\sigma}_x \cos^2\psi + \bar{\sigma}_y \sin^2\psi - \bar{\tau}_{xy} \sin 2\psi \\ \sigma_6^0 &= (\bar{\sigma}_y - \bar{\sigma}_x) \sin\psi \cos\psi - \bar{\tau}_{xy} \cos 2\psi\end{aligned} \tag{3.81}$$

(i) Stress components due to the opening (equations (3.73)) are obtained by the functions ϕ_1 and ϕ_2 in (3.82) (The first term of the series expansion is sufficient for representing applied stresses and hence m=1)

$$\begin{aligned}\phi_1(z_1) &= \frac{\bar{\beta}_1 - \mu_2\bar{\alpha}_1}{\mu_1 - \mu_2}\xi_1^{-1} \\ \phi_2(z_2) &= \frac{-(\bar{\beta}_1 - \mu_1\bar{\alpha}_1)}{\mu_1 - \mu_2}\xi_2^{-1}\end{aligned} \tag{3.82}$$

α_1 and β_1 are expressed more explicitly in (3.83) and (3.84) below:

$$\alpha_1 = -(\overline{\sigma_x}/2)cos\psi(acos\psi + ibsin\psi) - (\overline{\sigma_y}/2)sin\psi(asin\psi - ibcos\psi) + (\overline{\tau_{xy}}/2)(asin2\psi - \text{ibcos}\psi) \tag{3.83}$$

$$\beta_1 = -(\overline{\sigma_x}/2)sin\psi(acos\psi + ibsin\psi) + (\overline{\sigma_y}/2)cos\psi(asin\psi - ibcos\psi) + (\overline{\tau_{xy}}/2)(acos2\psi - \text{ibsin}\psi) \tag{3.84}$$

Total stresses of the plate given in the principal coordinates of the opening are:

$$\begin{aligned}\sigma_1 &= 2\,Re[\,\mu_1^2\phi'_1(z_1) + \mu_2^2\phi'_2(z_2)] + {\sigma_1}^0 \\ \sigma_2 &= 2\,Re[\,\phi'_1(z_1) + \phi'_2(z_2)] + {\sigma_2}^0 \\ \sigma_6 &= -2\,Re[\,\mu_1\phi'_1(z_1) + \mu_2\phi'_2(z_2)] + {\sigma_6}^0\end{aligned} \tag{3.85}$$

In this regard, (3.24) shows an infinite plate with a circular opening subjected to biaxial loading. As mentioned above, this problem is solved by superpositioning stress state I, which resembles the stress distribution plus the stress state II, which is caused by the circular opening in the infinite plate.

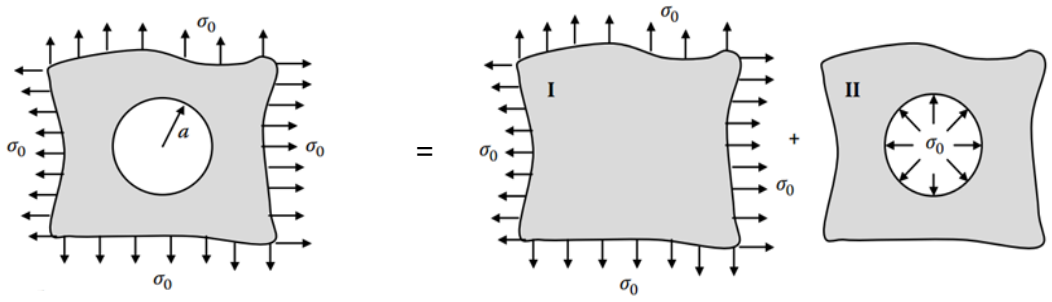

Figure 3.14. Total stress in an infinite plate can be decomposed into two stress states I and II [92].

Finite-width correction for an anisotropic plate containing a central opening:

In the previous section, stress field solutions are derived for infinite anisotropic plates. To apply these results to a finite width plate, a correction factor is needed to account for the finite width effect. In Figure 3.15 a finite-width anisotropic laminate with an elliptical opening is displayed.

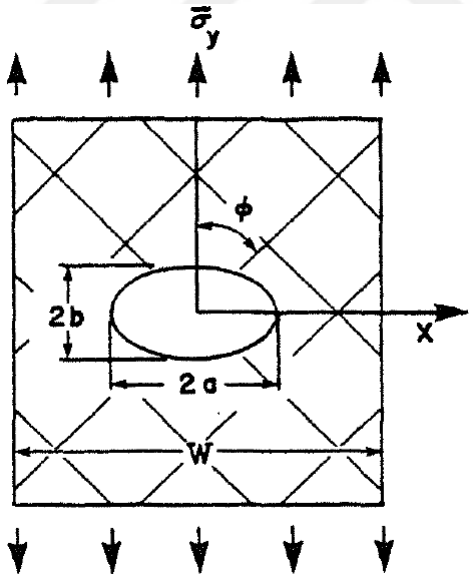

Figure 3.15. A finite width anisotropic plate with an elliptical opening [86].

The relation to account for finite-width correction is expressed as:

$$\begin{Bmatrix} \bar{\sigma}_x \\ \bar{\sigma}_y \\ \bar{\sigma}_{xy} \end{Bmatrix} = f_{\text{correction}}\left(\frac{W}{2a}\right) \cdot \begin{Bmatrix} \bar{\sigma}_x \\ \bar{\sigma}_y \\ \bar{\sigma}_{xy} \end{Bmatrix}_{W=\infty} \tag{3.86}$$

where

$$\frac{\mathrm{W}}{2\mathrm{a}}:\frac{\text{plate width}}{\text{major diameter}}$$

where $f_{correction}$ is the approximate orthotropic finite width correction for a circular hole opening (a=b) as a function of W/2a (plate width divided by the major diameter). The correction factor is expressed explicitly as [86]:

$$f_{\text{correction}}\left(\frac{W}{2a}\right)=\frac{K_T}{K_T^{\infty}}=\left\{\frac{3\left(1-\frac{2a}{W}\right)}{2+\left(1-\frac{2a}{W}\right)^3}+\frac{1}{2}\left(\frac{2a}{W}M\right)^6(K_T^{\infty}-3)\left[1-\left(\frac{2a}{W}M\right)^2\right]\right\}^{-1} \tag{3.87}$$

where

$$\mathrm{K_T}:\text{stress correction for finite plate}$$
$$\mathrm{K_T^{\infty}}:\text{stress correction for infinite plate}$$

$$\mathrm{M}^2=\frac{\sqrt{1-8\left[\frac{3\left(1-\frac{2\mathrm{a}}{\mathrm{W}}\right)}{2+\left(1+\frac{2\mathrm{a}}{\mathrm{W}}\right)^3}-1\right]}-1}{2\left(\frac{2\mathrm{a}}{\mathrm{W}}\right)^2} \tag{3.88}$$

In (3.88) M is defined as the magnification factor and helps us to get more accurate results even for the case where $a/b<4$. K_T^{∞} is calculated from the relation below:

$$K_T^{\infty}=1+\sqrt{\frac{2}{A_{22}}\left[\sqrt{A_{11}A_{22}}-A_{12}+\frac{A_{11}A_{22}-A_{12}^2}{2A_{66}}\right]} \tag{3.89}$$

In (3.89) A_{ij} are the components of the laminate in-plane stiffness matrix. For quasi-isotropic laminates a simpler relation is introduced:

$$\frac{K_T}{K_T^{\infty}} = \frac{2 + \left(1 - \frac{2a}{W}\right)^3}{3\left(1 - \frac{2a}{W}\right)} \tag{3.90}$$

In both equations(3.88) and (3.90), the ratio of the major diameter to the plate width $(2a/W)$ is selected as:

(i) in the case of a circular hole (a=b):

$$\frac{W}{2a} = \min\left(\frac{W_x}{2a}, \frac{W_y}{2a}\right)$$

(ii) in the case of an elliptical hole:

$$\frac{W}{2a} = \min\left(\frac{W_x}{2a}, \frac{W_y}{2b}\right)$$

The proposed open hole composite strength calculation method is developed based on the approach proposed by Tan [86]. He introduces an analytical model for the strength prediction of notched laminated composites subjected to in-plane combined loading. According to the methodology, strength reduction (SR) of the model in Figure 3.13 is calculated using the expression below:

$$SR = \frac{\bar{\sigma}_N^{\infty}}{\bar{\sigma}_o} = \frac{FPFF(Notched)|at\ \frac{x^2}{(a+b_0)^2} + \frac{y^2}{(b+b_0)^2} = 1}{FPFF(Unnotched)} \tag{3.91}$$

In equation (3.91), $\overline{\sigma_N^{\infty}}$ and $\overline{\sigma_o}$ are the notched and unnotched ultimate strength, respectively. The critical distance b_0 needs to be determined experimentally. The notched ultimate strength of the laminate is calculated by multiplying SR with the unnotched laminate strength. The input parameters of the model are material elastic properties, strength parameters and characteristic length.

3.2 Numerical Modeling

3.2.1 Intralaminar Damage Model

In this subsection, continuum damage models (CDM) used for the progressive failure analysis of the unnotched and open hole composite laminates are discussed. In CDM different damage initiation criteria such as Puck, Hashin or LaRC03/LaRC04 are used for determining the damage onset. Damage evolution is carried out utilizing a fracture energy based bilinear degradation scheme [93].

3.2.1.1 Damaged Material Response

In this work, the degraded stiffness matrix coefficients are calculated based on the model suggested by Matzenmiller et al. [94]. According to the model the following relation between the effective stress and the nominal stress is written:

$$\hat{\sigma} = \mathbf{M}\boldsymbol{\sigma} \tag{3.92}$$

where **M** is defined as the damage operator. The diagonal form of **M** is expressed as:

$$\mathbf{M} = \begin{bmatrix} \frac{1}{1-d_f} & 0 & 0 \\ 0 & \frac{1}{1-d_m} & 0 \\ 0 & 0 & \frac{1}{1-d_s} \end{bmatrix} \tag{3.93}$$

In the expression above, d_f, d_m and d_s represent damage variables for fiber, matrix and shear failure modes. Considering (3.92) and degradation of Poisson's ratio ([93], [95],[96]), damaged compliance matrix can be obtained from the second derivative of the complementary free energy function with respect to the stress tensor:

$$\mathbf{H} = \frac{\partial^2 G}{\partial \sigma^2} = \begin{bmatrix} \frac{1}{(1-d_f)E_1} & -\frac{\nu_{21}}{E_2} & 0 \\ -\frac{\nu_{12}}{E_1} & \frac{1}{(1-d_m)E_2} & 0 \\ 0 & 0 & \frac{1}{(1-d_s)G_{12}} \end{bmatrix} \quad (3.94)$$

Where the complementary free energy function is expressed as ([97],[98]):

$$G = \frac{\sigma_{11}^2}{2(1-d_f)E_1} + \frac{\sigma_{22}^2}{2(1-d_m)E_2} - \frac{\nu_{12}}{E_1}\sigma_{11}\sigma_{22} + \frac{\sigma_{12}^2}{2(1-d_s)\sigma_{12}} + (\alpha_{11}\sigma_{11} + \alpha_{22}\sigma_{22})\Delta T + (\beta_{11}\sigma_{11} + \beta_{22}\sigma_{22})\Delta M \quad (3.95)$$

In expressions (3.94) and (3.95), E_1 and E_2 are the longitudinal and transverse in-plane elastic moduli, respectively. G_{12} is the in-plane shear modulus. Stress tensor σ is an average stress tensor over a representative volume larger than the diameter of a fiber. The subscripts 1 and 2 show the fiber (longitudinal) and matrix (transverse fiber), directions, respectively. Thermal expansions in the longitudinal and transverse directions are denoted by α_{11} and α_{22}, respectively. Similarly, β_{11} and β_{22} denote hygroscopic expansion coefficients in longitudinal and transverse directions, respectively. ΔT and ΔM stand for temperature and moisture content differences with respect to their reference values. Utilizing the damaged compliance matrix, the corresponding damages stiffness matrix is expressed as following [93]:

$$C = \frac{1}{D}\begin{bmatrix} (1-d_f)E_1 & (1-d_f)(1-d_m)\nu_{21}E_1 & 0 \\ (1-d_f)(1-d_m)\nu_{12}E_2 & (1-d_m)E_2 & 0 \\ 0 & 0 & D(1-d_s)G_{12} \end{bmatrix} \quad (3.96)$$

where $D = 1 - (1-d_f)(1-d_m)\nu_{12}\nu_{21}$ and

$$d_s = 1 - (1-d_{ft})(1-d_{fc})(1-d_{mt})(1-d_{mc}).$$

3.2.1.2 Energy Dissipation

Rate of energy dissipation occurring due to the evolution is damage is given by:

$$\Theta = \frac{\partial G}{\partial d_{ft}}\dot{d_{ft}} + \frac{\partial G}{\partial d_{fc}}\dot{d_{fc}} + \frac{\partial G}{\partial d_{mt}}\dot{d_{mt}} + \frac{\partial G}{\partial d_{mc}}\dot{d_{mc}} = Y_{ft}\dot{d_{ft}} + Y_{fc}\dot{d_{fc}} + Y_{mt}\dot{d_{mt}} + Y_{mc}\dot{d_{mc}} \quad (3.97)$$

The complementary free energy function (See equation (3.94)) guarantees that the thermodynamic forces (Y_m) conjugated to their corresponding damage variables (d_m) are always positive.

3.2.1.3 Initiation Criteria

As the initiation criteria Puck, Hashin or LaRC03 ([99], [100]),LaRC04 ([101]) can be used.

3.2.1.4 Damage Evolution laws and Numerical Implementation

The evolution law of the damage variable after failure initiation is based on the fracture energy dissipation G. The evolution law is a generalization of the methodology proposed in Camaho and Davilla [102] to simulate interlaminar delamination with cohesive elements. The approach proposed in Bažant's crack band [103] model is utilized to alleviate mesh dependency in the fe model. In the model, mesh objectivity, i.e. element size independency is achieved by regulating the energy dissipation per unit volume using characteristic element length and fracture toughness:

$$g_M = \frac{G_M}{L^*}, \qquad \text{M=1+,1-,2+,2-,6} \tag{3.98}$$

In expression (3.100) g_M is the energy dissipation per unit volume. G_M is the fracture toughness and L^* is the characteristic element length. Bazant and Oh (1983) [103] proposed the following relation for calculating the characteristic length of a square element:

$$L^* = \frac{\sqrt{A_{IP}}}{cos\theta}, \tag{3.99}$$

where, A_{IP} is the area related to the integration point of an element and θ is the angle between the mesh line along which the crack band advances and the crack direction.

In expression (3.99), θ must be restricted to $|\theta| \leq 45$. In expression (3.98), subscript M denotes different damage modes. If stress – linear strain softening behavior for the damage evolution is used (See Figure 3.16), the expression (3.100) can be expanded and rewritten as following:

$$\frac{1}{2}\sigma_0 \varepsilon^f = \frac{G}{L^*} \tag{3.100}$$

Hence, ε_f, strain at failure is determined from:

$$\varepsilon^f = \frac{2G}{\sigma_0 L^*} \tag{3.101}$$

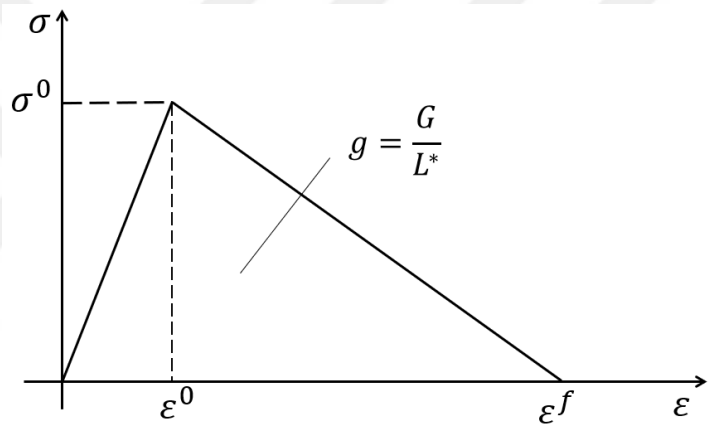

Figure 3.16. Stress-strain linear softening response

From (3.101) it is seen that ε_f, strain at failure, is inversely proportional to the characteristic element length. In other words, if the characteristic element length decreases ε_f must increase and vice versa as depicted in Figure 3.17. This behavior of Bažant's crack band [103] model helps to preserve fracture energy for different characteristic element sizes.

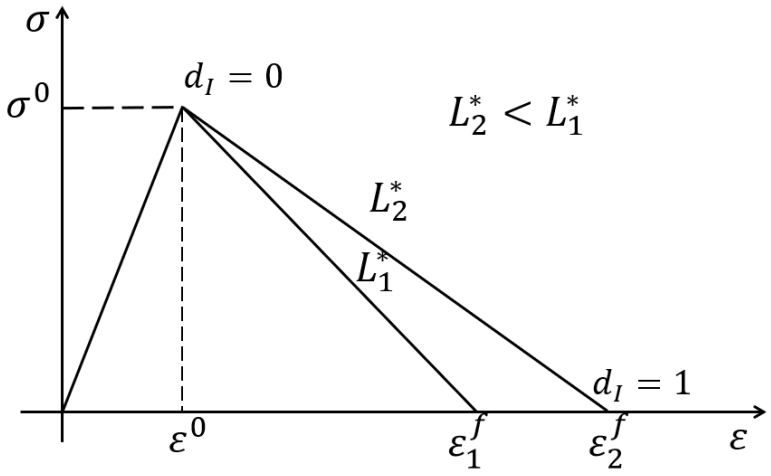

Figure 3.17. Adjusting the stress-strain softening response for different characteristic element sizes.

Damage variables for particular failure modes; fiber tension (f_t), fiber compression (f_c), matrix tension (m_t) and matrix compression (m_c) are calculated based on the relations in (3.102). In the relations below, $\delta_{I,eq}^0$ is the initial displacement at which the failure begins ($d_I = 0$). $\delta_{I,eq}^f$ is the displacement at which the material completely fails ($d_I = 1$). $\delta_{I,}eq$ is the displacement between the state of the material at which the failure begins ($d_I = 0$) and the state at which the complete material failure occurs ($d_I = 1$). The graphical representation of this bi-linear damage evolution law is given in Figure 3.18. In the figure K^0 and K are the initial undamaged and instantaneous stiffnesses, respectively.

$$d_I = \begin{cases} 0, & if \quad \delta_{I,eq} < \delta_{I,eq}^0 \\ \dfrac{\delta_{I,eq}^f\left(\delta_{I,eq} - \delta_{I,eq}^0\right)}{\delta_{I,eq}\left(\delta_{I,eq}^f - \delta_{I,eq}^0\right)}, & if \quad \delta_{I,eq}^0 \le \delta_{I,eq} \le \delta_{I,eq}^f \\ 1, & if \quad \delta_{I,eq} > \delta_{I,eq}^f \end{cases} \qquad (3.102)$$

$$I \in \{f_t, f_c, m_c, m_t\}$$

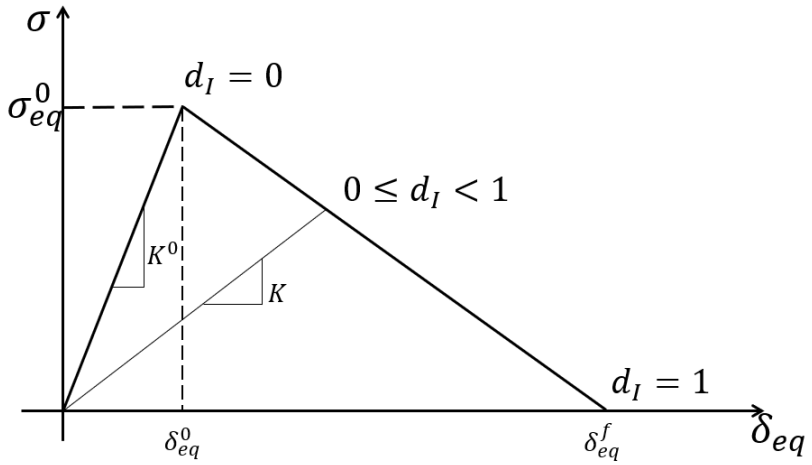

Figure 3.18. Bi-linear damage evolution law.

Depending on the detected failure mode, equivalent displacement and stresses are calculated from the relations below [93]:

Fiber tension ($\hat{\sigma}_{11} \geq 0$):

$$\delta_{eq}^{ft} = L^* \sqrt{< \varepsilon_{11} >^2} \tag{3.103}$$

$$\sigma_{eq} = L^* \frac{(< \sigma_{11} >< \varepsilon_{11} >)}{\delta_{eq}^{ft}} \tag{3.104}$$

Fiber compression ($\hat{\sigma}_{11} < 0$):

$$\delta_{eq}^{fc} = L^* < -\varepsilon_{11} > \tag{3.105}$$

$$\sigma_{eq} = L^* \frac{(< -\sigma_{11} >< -\varepsilon_{11} >)}{\delta_{eq}^{fc}} \tag{3.106}$$

Matrix tension ($\hat{\sigma}_{22} \geq 0$):

$$\delta_{eq}^{mt} = L^* \sqrt{< \varepsilon_{22} >^2 + \varepsilon_{12}^2} \tag{3.107}$$

$$\sigma_{eq} = \frac{L^* (< \sigma_{22} >< \varepsilon_{22} > + \sigma_{12}\varepsilon_{12})}{\delta_{eq}^{mt}} \tag{3.108}$$

Matrix compression ($\hat{\sigma}_{22} < 0$):

$$\delta_{eq}^{mc} = L^* \sqrt{< -\varepsilon_{22} >^2 + \varepsilon_{12}^2} \tag{3.109}$$

$$\sigma_{eq} = \frac{L^*(< -\sigma_{22} >< -\varepsilon_{22} > + \sigma_{12}\varepsilon_{12})}{\delta_{eq}^{mc}} \tag{3.110}$$

In relations (3.103)-(3.111), $< x >$, the Macaulay bracket is related to the absolute value: for every $x \in$ R, $< x >= \frac{x+|x|}{2}$.

3.2.1.5 Critical Finite Element Size

In order to prevent a local snap-back in the stress-strain relation, the elastic energy of an element (with thickness t and strength X_M) at the initiation of failure, which is given by $X_M^2 (L^*)^2 \cdot t/(2E_M)$ (with damage modes $M = 1 \pm, 2 \pm, 6$) must be lower than or equal to the fracture energy $G_M \cdot L^* \cdot t$ of the element. Hence the maximum finite element length for each damage law M is calculated from:

$$L^* \leq \frac{2E_M G_M}{X_M^2}, \qquad M = 1 \pm, 2 \pm, 6 \tag{3.111}$$

3.2.2 Interlaminar Damage Model

In this thesis, Cohesive Zone Model is used to account for the interlaminar damage modes, such as delamination and debonding. The cohesive zone method is built on the assumption that stress transfer between the two separable surfaces of a delamination/debonding interface does not vanish completely at the damage initiation point. After the damage initiation, stiffness at the interface of the separable surfaces reduces progressively. The interface failure between the two separable faces are modeled utilizing cohesive zone elements (COH3D8) available in ABAQUS.

The cohesive behavior is defined with a traction-separation ($\sigma - \delta$) equation as depicted in Figure 3.19. The element stiffness matrix is given by the stiffness of the interface material (named as penalty stiffness in ABAQUS documentation). The CZM element can be regarded as a spring between the corresponding nodes of the element. Using the cohesive element, different fracture modes such as mode I-opening, mode II-shear and mode-III tearing can be simulated.

Under mixed fracture modes, there are three traction components $\sigma_I, \sigma_{II}, \sigma_{III}$ and the corresponding three $\delta_I, \delta_{II}, \delta_{III}$ separation components. In order to reduce the number of tests for determining the penalty stiffness for each fracture mode, same stiffness value is assumed for all fracture modes. In the mixed mode CZM, the following quadratic criterion is used for determining the damage onset [106]

$$\sum_{i=1}^{3} \left(\frac{\sigma_i}{\sigma_i^o} \right)^2 = 1 \tag{3.112}$$

where σ_i^0 are the interface strength values for each crack propagation mode, $\sigma_I^o, \sigma_{II}^o, \sigma_{III}^o$. After the damage initiation, damage mechanics approach is followed. Dissipated fracture energy is calculated as the area OAB in Figure 3.19.

$$A_{OAB} = A_{OAF} - A_{OBF} \tag{3.113}$$

Referring to Figure 3.19, the expression above can be rewritten as:

$$G_i = G_{ic} - \frac{1}{2} K_i \delta_i^o \delta_i^c \frac{\delta_i^c - \delta_i}{\delta_i^c - \delta_i^o} \tag{3.114}$$

where,

G_i: single mode Strain Energy Release Rate (SERR)

G_{ic}: single mode critical SERR

δ_i^o: single displacement at damage initiation

δ_i^c: single mode displacement at fracture

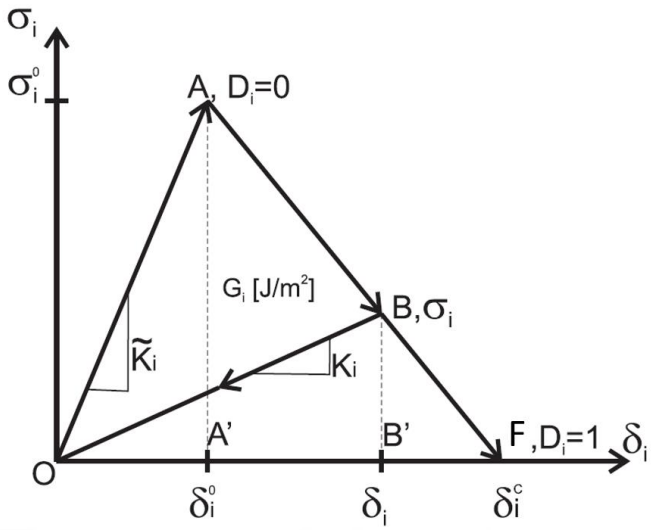

Figure 3.19. The bilinear traction-separation response implemented in the Cohesive Zone Model [106].

Once the SERR for each single fracture mode are calculated from (3.114), Kenane and Benzeggagh's [107] (B-K) criterion is used to check the condition for crack propagation. According to the (B-K) criterion a crack propagation occurs when $G_{tot} > G_{equ}$, where G_{tot} and G_{equ} are given by,

$$G_{tot} = G_I + G_{II} + G_{III} \tag{3.115}$$

$$G_{equ} = G_{Ic} + (G_{IIc} - G_{Ic})\left(\frac{G_{II} + G_{III}}{G_I + G_{II} + G_{III}}\right)^{\eta} \tag{3.116}$$

After damage initiation under mixed mode, damage variable which is used for the degradation of the stiffness matrix is calculated from the equation below:

$$d_m = \frac{\delta_m^c(\delta_m - \delta_m^0)}{\delta_m(\delta_m^c - \delta_m^0)} \tag{3.117}$$

In eq. (3.117):

δ_m^c : mixed mode displacement at fracture

δ_m^0 : mixed mode displacement at damage initiation

δ_m: instantaneous mixed mode displacement

Utilizing eq. (3.117) and the undamaged stiffness value, instantaneous stiffness K can be calculated from:

$$K = (1 - d_m)\tilde{\mathrm{K}} \tag{3.118}$$

At the instance when Mode I, Mode II and Mode III are concurrently observed, the combined effect of mixed modes should be calculated correspondingly. In Figure 3.20, the bilinear traction-separation response of mixed modes is provided.

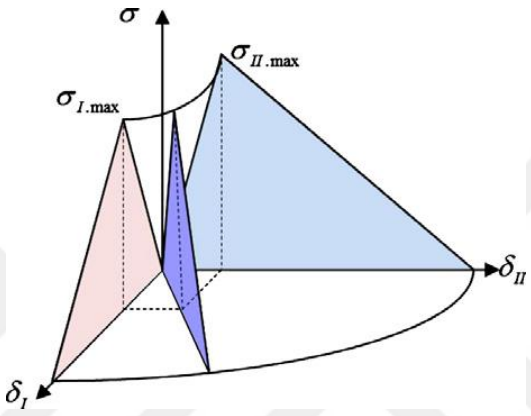

Figure 3.20. The bilinear traction-separation response for mixed modes [108].

CHAPTER 4

PLAIN STRENGTH ANALYSIS OF COMPOSITE LAMINATES

This Chapter summarizes and compares the methodologies used for the plain strength analysis of composite materials in this thesis. The reserve factors are calculated for a composite laminate with any desired layup subjected to in-plane loads and moments using composite failure criteria. Five simple failure criteria in addition to five more progressive failure criteria for tape lay-ups are considered. The most commonly used and representative failure criteria in the literature are implemented in MATLAB [109] codes for the plain strength analysis of composite tape materials. The final choice of the failure criteria must be based on a test program.

4.1 Plain Strength Analysis Procedure

Within the scope of this thesis, MATLAB [109] codes for the plain strength analysis of composite tape materials are developed. These MATLAB codes incorporate the following simple failure criteria:

- Yamada-Sun
- Tsai-Wu
- Tsai-Hill
- Puck (modified)
- Max Stress
- Max Strain

Futhermore, the following iterative composite failure criteria are implemented in MATLAB codes:

- Yamada-Sun + Puck (modified)
- Max Stress + Tsai-Wu

- Yamada-Sun + Tsai-Wu
- Max Strain + Puck (modified)
- Max Stress + Puck (modified)

When simple failure criteria are chosen for the analysis, the reserve factor of the laminate is equal to the reserve factor of the lamina with the minimum value that is attained either due to fiber failure or due to matrix failure. Iterative failure criteria on the other hand determines the reserve factor when first fiber failure (FFF) occurs. In the iterative failure criteria elastic properties of the matrix are degraded until the reserve factor of the fiber is less than the reserve factor of the matrix.

As a representative example for FPF analysis, algorithm of the plain strength analysis is explained using Yamada-Sun plus Puck iterative failure criteria. The algorithm can be easily modified to calculate laminate strength using different simple or iterative failure criteria. The algorithm predicts the strength of the multidirectional laminate subjected to in-plane combined loading. The multidirectional laminate with individual plies and the coordinate system definitions are shown in Figure 4.1.

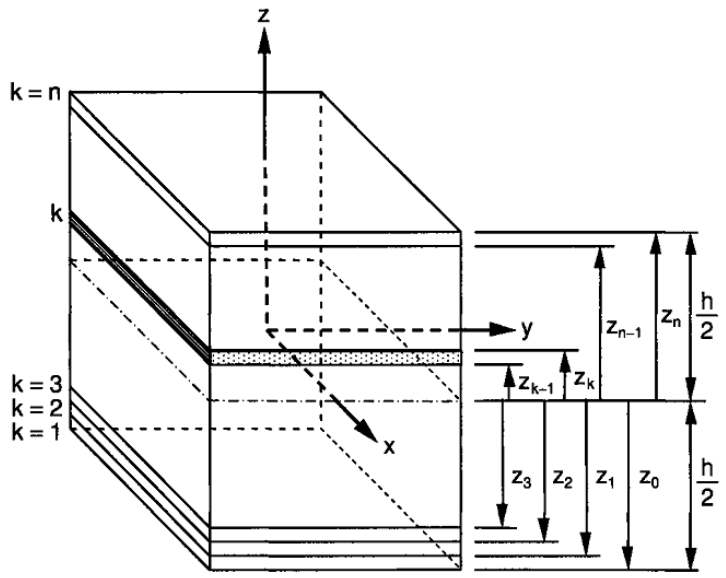

Figure 4.1: Multidirectional laminate with individual plies and the coordinates [69].

The pseudo-code and the algorithm implemented in the Plain Strength (PLS) MATLAB Code is shown Figure 4.2 and Figure 4.3. The steps for calculating the reserve factors are as follows:

1. Ply thickness, ply sequence and material orientation angle are read as an input.

2. Lamina strengths ($X_t,\ X_c,\ Y_t,\ Y_c,\ S$) are entered as an input.

3. Mechanical loading (Forces $[N]_{x,y}$ and Moments $[M]_{x,y}$) are read as an input.

4. Elastic properties ($E_1,\ E_2,\ \upsilon_{12},\ G_{12}$) are entered for each lamina individually.

5. Poisson's ratio υ_{21} is calculated from,

$$\nu_{21} = E_2 \cdot \frac{\nu_{12}}{E_1} \tag{4.1}$$

6. Reduced ply stiffnesses $[Q]_{1,2}$ with respect to material principal axis are computed from relations,

$$Q_{11} = \frac{E_1}{1 - \nu_{12}\nu_{21}}$$

$$Q_{22} = \frac{E_2}{1 - \nu_{12}\nu_{21}} \tag{4.2}$$

$$Q_{12} = \frac{\nu_{21}E_1}{1 - \nu_{12}\nu_{21}}$$

$$Q_{66} = G_{12}$$

7. Transformed reduced stiffnesses with respect to laminate reference axes (x,y) are calculated for each layer (k) using equations,

$$Q_{xx} = m^4Q_{11} + n^4Q_{22} + 2m^2n^2Q_{12} + 4m^2n^2Q_{66}$$

$$Q_{yy} = n^4Q_{11} + m^4Q_{22} + 2m^2n^2Q_{12} + 4m^2n^2Q_{66}$$

$$Q_{xy} = m^2n^2Q_{11} + m^2n^2Q_{22} + (m^4 + n^4)Q_{12} - 4m^2n^2Q_{66}$$

$$Q_{xs} = m^3nQ_{11} - mn^3Q_{22} - mn(m^2 - n^2)Q_{12} - 2mn(m^2 - n^2)Q_{66} \quad (4.3)$$

$$Q_{ys} = mn^3Q_{11} - m^3nQ_{22} + mn(m^2 - n^2)Q_{12} + 2mn(m^2 - n^2)Q_{66}$$

$$Q_{ss} = m^2n^2Q_{11} + m^2n^2Q_{22} - 2m^2n^2Q_{12} + (m^2 - n^2)^2Q_{66}$$

where $m = \cos(\theta)$, n = $\sin(\theta)$

8. Through-the-thickness coordinate z_k (Figure 4.1) for each layer (k) is calculated.

9. Laminate stiffness matrices $[A]$, $[B]$ and $[D]$ are computed from,

$$A_{ij} = \sum_{k=1}^{n} Q_{ij}^{k}(z_k - z_{k-1})$$

$$B_{ij} = \frac{1}{2}\sum_{k=1}^{n} Q_{ij}^{k}({z_k}^2 - {z_{k-1}}^2) \quad (4.4)$$

$$D_{ij} = \frac{1}{3}\sum_{k=1}^{n} Q_{ij}^{k}({z_k}^3 - {z_{k-1}}^3)$$

10. Laminate compliance matrices are computed using,

$$[a] = [A^{-1}] - \{[B^*][D^{*-1}]\}[C^*]$$

$$[b] = [B^*][D^{*-1}]$$

$$[c] = -[D^{*-1}][C^*]$$

$$[d] = [D^{*-1}]$$

where (4.5)

$$[A^{-1}] = inverse\ of\ matrix\ [A]$$

$$[B^*] = -[A^{-1}][B]$$

$$[C^*] = [B][A^{-1}]$$

$$[D^*] = [D] - \{[B][A^{-1}]\}[B]$$

11. Reference plane strains $[\varepsilon^{\circ}]_{x,y}$ and curvatures $[\mathrm{K}]_{x,y}$ are calculated from,

$$\begin{bmatrix} \varepsilon_x^{\circ} \\ \varepsilon_y^{\circ} \\ \gamma_s^{\circ} \\ \mathrm{K}_x \\ \mathrm{K}_y \\ \mathrm{K}_s \end{bmatrix} = \begin{bmatrix} a_{xx} & a_{xy} & a_{xs} & b_{xx} & b_{xy} & b_{xs} \\ a_{yx} & a_{yy} & a_{ys} & b_{yx} & b_{yy} & b_{ys} \\ a_{sx} & a_{sy} & a_{ss} & b_{sx} & b_{sy} & b_{ss} \\ c_{xx} & c_{xy} & c_{xs} & d_{xx} & d_{xy} & d_{xs} \\ c_{yx} & c_{yy} & c_{ys} & d_{yx} & d_{yy} & d_{ys} \\ c_{sx} & c_{sy} & c_{ss} & d_{sx} & d_{sy} & d_{ss} \end{bmatrix} \begin{bmatrix} N_x \\ N_y \\ N_s \\ M_x \\ M_y \\ M_s \end{bmatrix} \quad (4.6)$$

12. Through-the-thickness coordinate of the lamina mid-plane ($\overline{z_k}$) is calculated.

13. Strains at each layer in the laminate with reference to laminate coordinates system is determined using,

$$\begin{bmatrix} \varepsilon_x \\ \varepsilon_y \\ \varepsilon_s \end{bmatrix} = \begin{bmatrix} \varepsilon_x^{\circ} \\ \varepsilon_y^{\circ} \\ \gamma_s^{\circ} \end{bmatrix} + z \begin{bmatrix} \mathrm{K}_x \\ \mathrm{K}_y \\ \mathrm{K}_s \end{bmatrix} \quad (4.7)$$

14. Layer strains $[\varepsilon]_{1,2}^{k}$ with respect to material principal axis (1,2) using the transformation matrix in calculated from,

$$\begin{bmatrix} \varepsilon_1 \\ \varepsilon_2 \\ 1 \\ \frac{1}{2}\gamma_6 \end{bmatrix} = \begin{bmatrix} m^2 & n^2 & 2mn \\ n^2 & m^2 & -2mn \\ -mn & mn & m^2 - n^2 \end{bmatrix} \begin{bmatrix} \varepsilon_x \\ \varepsilon_y \\ \varepsilon_s \end{bmatrix} \tag{4.8}$$

where $m = \cos(\theta)$, n = $\sin(\theta)$

15. Layer stresses $[\sigma]_{1,2}^{k}$ with respect to material principal axis (1,2) are calculated using the expression,

$$\begin{bmatrix} \sigma_1 \\ \sigma_2 \\ \tau_6 \end{bmatrix} = \begin{bmatrix} Q_{11} & Q_{12} & 0 \\ Q_{12} & Q_{22} & 0 \\ 0 & 0 & Q_{66} \end{bmatrix} \begin{bmatrix} \varepsilon_1 \\ \varepsilon_2 \\ \gamma_6 \end{bmatrix} \tag{4.9}$$

16. Progressive Faliure Criteria (Yamada-Sun and Puck) is implemented as explained below:

Yamada-Sun Failure Criteria for Fiber Failure

Lamina strengths ($X_t,\ X_c,\ S$) are substituted into (4.10) based on the sign of the stress component in material axis:

$$\left(\frac{\sigma_1(k) \cdot RFF(k)}{X}\right)^2 + \left(\frac{\tau_{12}(k) \cdot RFF(k)}{S}\right)^2 = 1 \tag{4.10}$$

For example, if $\sigma_1 \geq 0,\ X_t$ and $\sigma_1 < 0,\ X_c$ must be considered. For positive and negative values of $\tau_{12},\ S$ value is entered. From the solution of equation (4.10), fiber reserve factor RFF(k) of the lamina is obtained.

Modified Puck Failure Criteria

Lamina strengths ($X_t,\ X_c,\ Y_t,\ Y_c, S$) are substituted into (4.11):

$$RFM(k)^2 \left[\left(\frac{\sigma_1(k)}{2X_t}\right)^2 + \frac{(\sigma_2(k))^2}{|Y_t Y_c|} + \frac{\tau_{12}}{(S)^2}\right] + RFM(k) \cdot \left(\frac{\sigma_2(k)}{Y_c + Y_t}\right) = 1 \tag{4.11}$$

From the solution of (4.11) $RFM(k)_1$ and $RFM(k)_2$ are obtained. Reserve factor of the lamina is given by, $RFM(k) = max(\,RFM(k)_1, RFM(k)_2)$.

17. Matrix reserve factor (RFM(k)) and fiber reserve factor (RRF(k)) are obtained for each ply.

18. (i) Min(RFM(k)) and Min(RRF(k)) are determined on a ply-by-ply basis. If Min(RFF(k))<Min(RFM(k)) fiber failure point is reached and the laminate fails due to First Fiber Failure (FFF). Then, reserve factor of the laminate is equal to the reserve factor of the fiber:

$RF_{Laminate} = min(RFF(k))$. Program ends!

(ii) If all the laminae are degraded, which is checked by the following condition:

SUM (E2) = (number of plies) x 0.001

$RF_{Laminate} = min(RFF(k))$. Program ends!

At this point we obtain following additional information from the program:

- Critical ply is equal to the ply number "k" with min (RFF) and its angle is known from the input data
- The sign of the stress in fiber direction σ_1 in critical ply gives us information about the failure type. If it is positive fiber tension, if it is negative fiber compression is the reason for failure
- σ_1 in critical ply is the failure stress

19. If Min(RFM(k))<Min(RFF(k)) matrix failure point is reached and the properties of the lamina(e) must be degraded according to the following rule:

$E_2,\ G_{12}\ and\ \upsilon_{12}$ for the lamina(e) with min(RFM(k)) are set to a very small value 0.001.

20. As long as $RF_{Laminate}$ is not calculated in steps (16) and (18), PLS MATLAB code is restarted from STEP 4 with the new material properties of the laminate

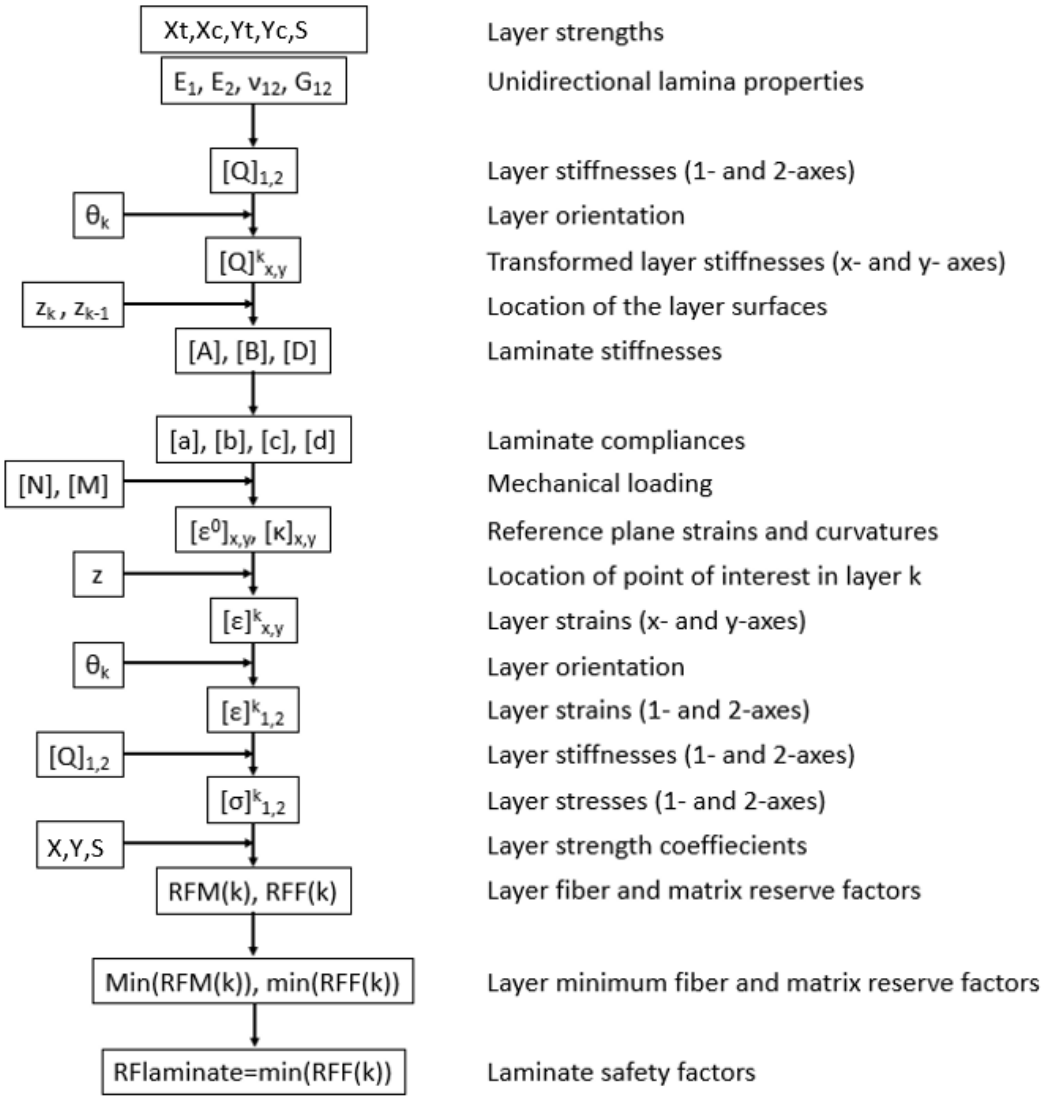

Figure 4.2. Flowchart for the Failure Analysis of a Composite Tape Laminate Using Mode Based Failure Criteria (FPF, First Ply Failure) [69].

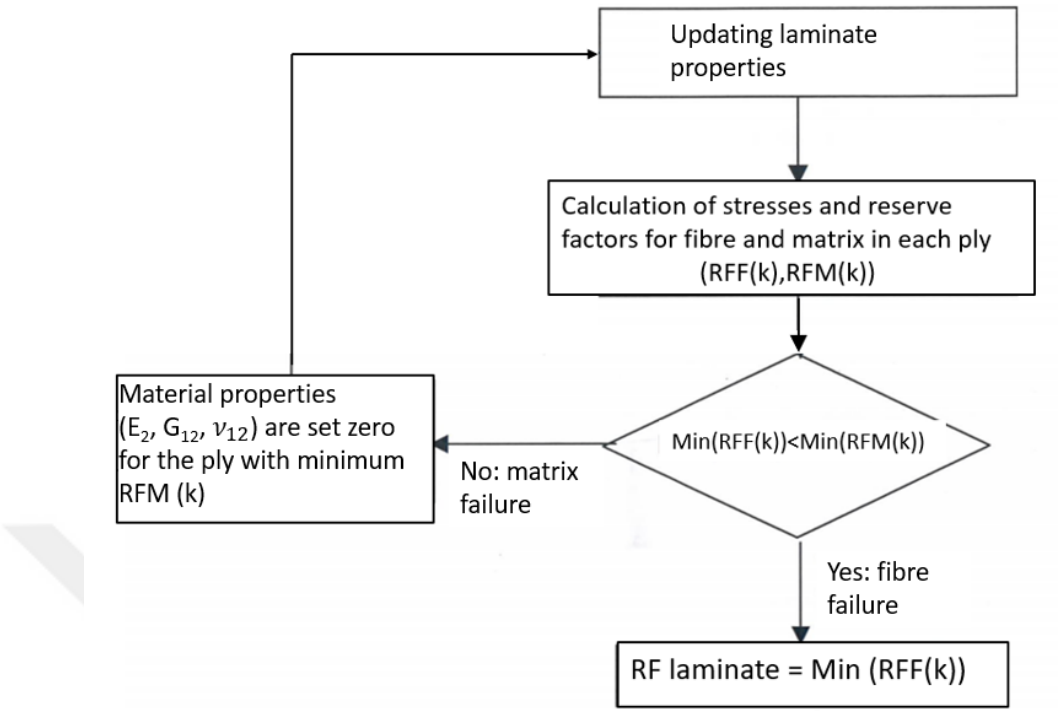

Figure 4.3. PLS MATLAB Code for the Progressive Failure Criteria (Yamada-Sun and Puck) of Composite Tape Materials

4.2 Results from the Plain Strength Analysis of Multidirectional Laminates

In this section, biaxial failure envelopes and unidirectional tensile strength curves of laminates with respect to fiber orientation are compared with the available graphs in literature for validation.

4.2.1 Validation of Biaxial Failure Envelopes

Figure 4.4 shows failure envelopes for carbon/epoxy (AS4/3501-6) lamina subjected to biaxial normal loading from [69] and the same plots, which are created using MATLAB Codes for laminate strength analysis. The mechanical properties of the AS4/3501-6 carbon/epoxy lamina is listed in Table A.2. In Figure 4.5 failure envelopes for carbon/epoxy (AS4/3501-6) lamina subjected to transverse normal and

shear loading are shown from [69]. The envelopes, which are generated using MATLAB code are plotted in the same figure.

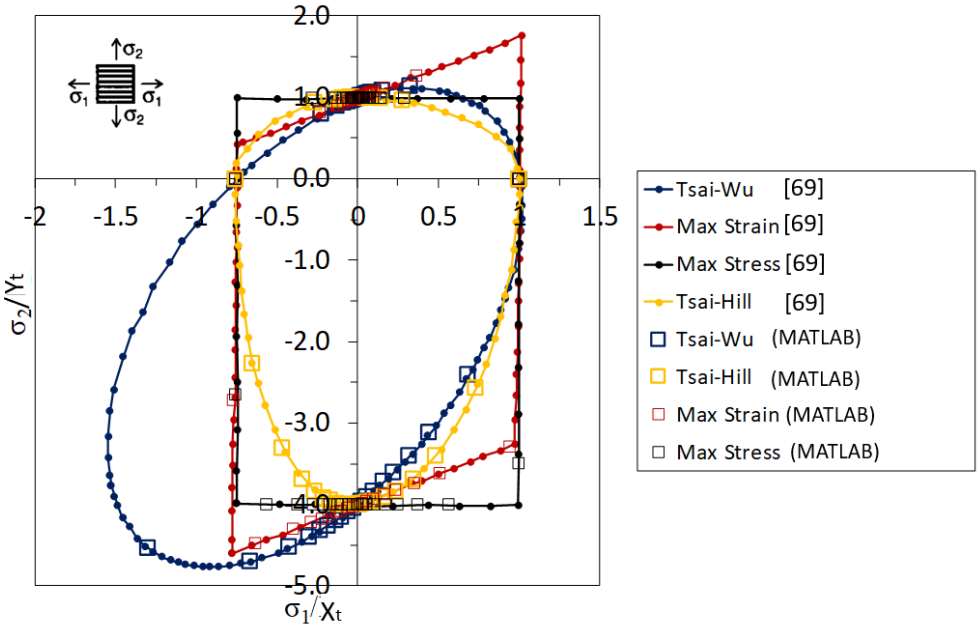

Figure 4.4. Failure envelopes for carbon/epoxy (AS4/3501-6) lamina subjected to biaxial normal loading using different failure criteria.

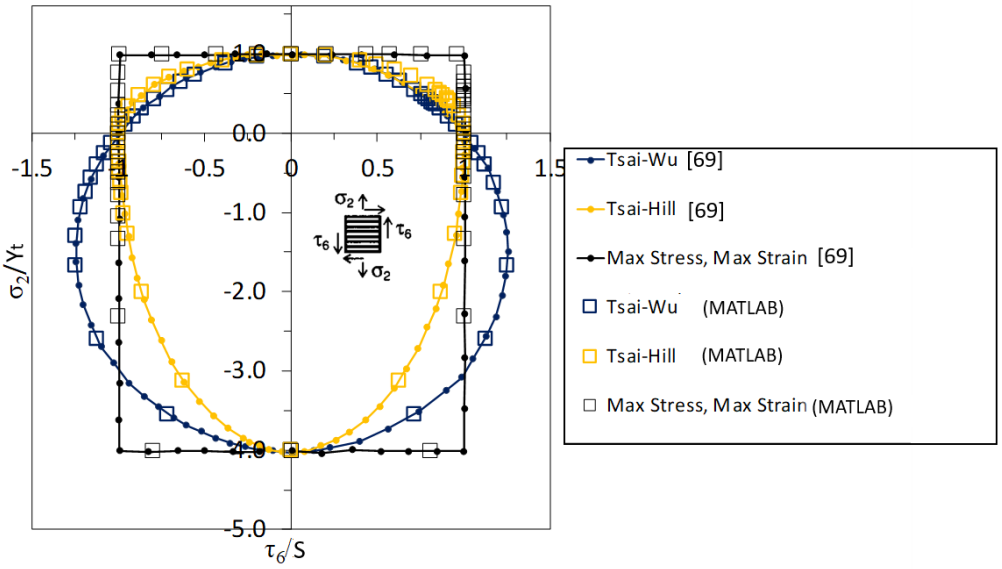

Figure 4.5. Failure envelopes for carbon/epoxy (AS4/3501-6) lamina subjected to transverse normal and shear loading using different failure criteria.

From Figure 4.4 and Figure 4.5 we observe that MATLAB Codes deliver identical results with the plots in Daniel and Ishai [69] and the MATLAB Codes for these loading cases are validated.

4.2.2 Validation of the Uniaxial Failure Envelopes with Respect to Fiber Orientation

In Figure 4.6 normalized tensile strength curves of unidirectional and angle-ply carbon/epoxy (AS4/3501-6) laminates from Daniel and Ishai [69] and MATLAB Code are depicted, respectively. Similarly, Figure 4.7 shows normalized compressive strength curves of unidirectional and angle-ply carbon/epoxy (AS4/3501-6) laminates from Daniel and Ishai [69] and MATLAB Code, respectively. Finally, in Figure 4.8 normalized in-plane shear strength of unidirectional and angle-ply laminates are compared with the curves from Daniel and Ishai [69]. As seen from the figures below, MATLAB Code for the strength analysis of laminates is validated for the loading cases studied.

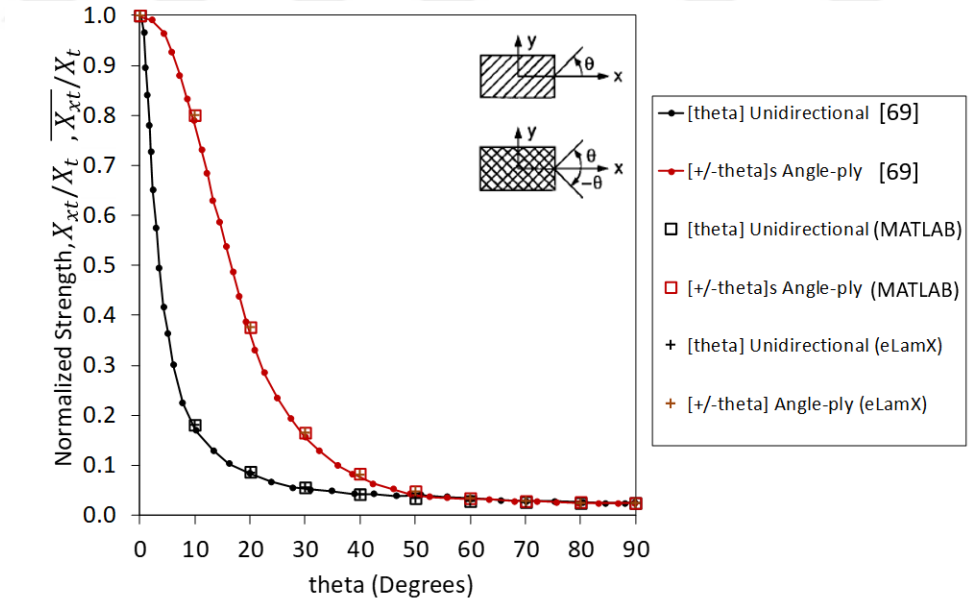

Figure 4.6. Normalized Tensile Strength of Unidirectional and Angle-Ply Laminates with Respect to Fiber Orientation (AS4/3501-6 Carbon/Epoxy, Tsai-Wu Criterion, FPF).

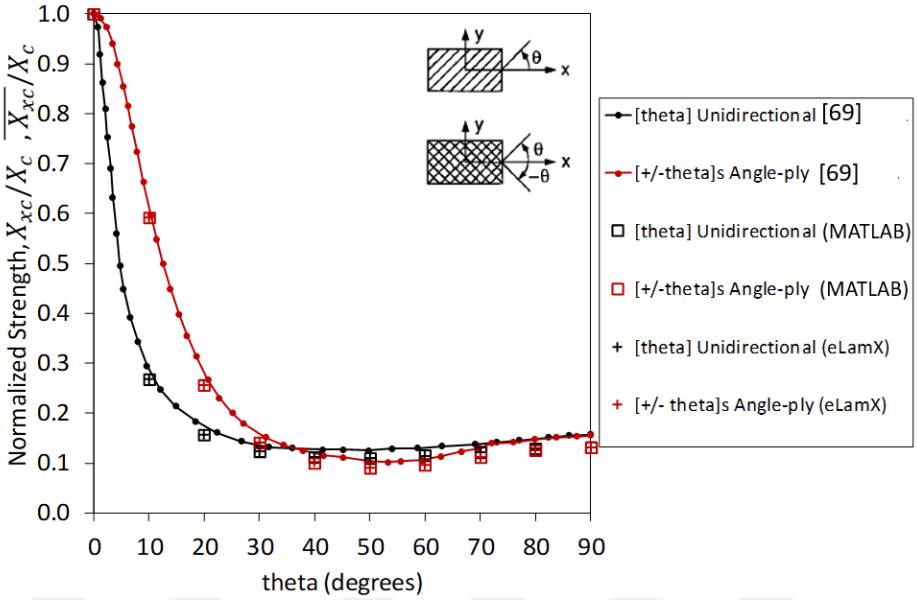

Figure 4.7. Normalized Compressive Strength of Unidirectional and Angle-Ply Laminates with Respect to Fiber Orientation (AS4/3501-6 Carbon/Epoxy, Tsai-Wu Criterion, FPF).

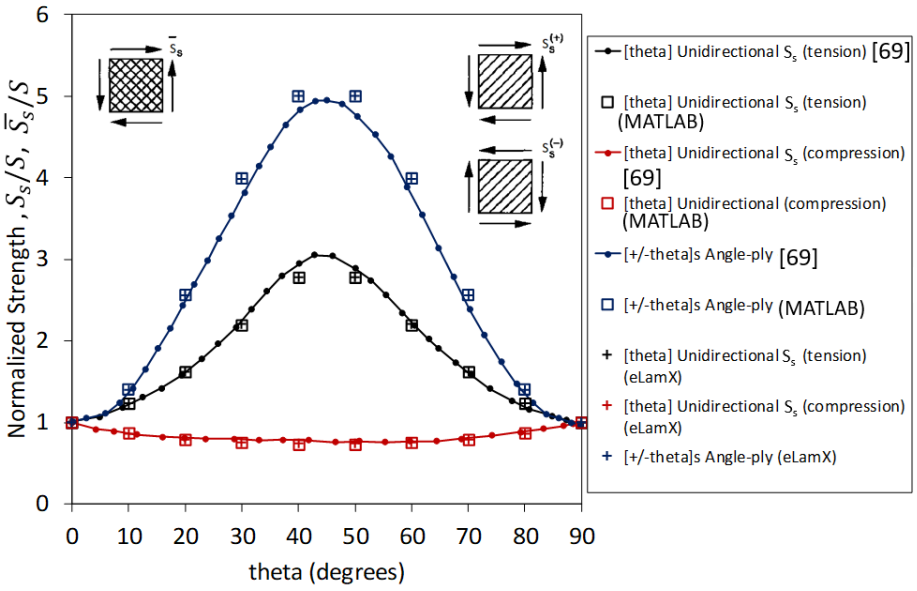

Figure 4.8. Normalized In-Plane Shear Strength of Unidirectional and Angle-Ply Laminates with Respect to Fiber Orientation (AS4/3501-6 Carbon/Epoxy; Tsai-Wu Criterion; FPF).

We observe from Figure 4.6, Figure 4.7 and Figure 4.8 that, there is a good agreement between the results from eLamX (composite calculator from Technical University of Dresden) [110] and the MATLAB code. Although in general plots from Daniel and Ishai [69] correlate well with eLamX and the MATLAB code, slight deviations are seen at some points. These slight deviations are attributed to the fact, that these plots are scanned from the book and may not represent the exact results data at all points.

4.2.3 Comparison of Failure Envelopes for IMA/M21 Laminate under Biaxial-Loading

In this subsection, biaxial failure envelopes of the simple and iterative failure criteria for the quasi-isotropic composite tape laminate made of IMA/M21E are studied. The mechanical properties of the IMA/M21E lamina are given in Table A.1. Since quasi-isotropic lay-up 25/50/25 (Notation used in the industry: 25% of the plies used at 0°, 50% of the plies at +/-45° and 25% at 90°) is among the typical lay-up configurations used for design purposes of aerospace structures, it is chosen for the comparison. Figure 4.9 shows failure envelopes generated using different failure criteria for the quasi-isotropic laminate IMA/M21E under bi-axial loading. We note that test data is not available for the uniaxial and biaxial loading. Envelopes of Yamada-Sun and Puck and Yamada-Sun look similar, whereas the shapes of Tsai-Hill, Hashin, Max Strain, Max Stress criteria and the iterative criteria Max Stress and Tsai Wu are quite different. Tsai Wu failure criterion demonstrates a rather non-conservative behavior in the compression-compression region of biaxial normal loading. Concerning the damage progression in composite tape materials iterative criteria are represented better by the experiments compared to the simple failure criteria. According to the iterative failure criteria first fiber failure leads to ultimate failure of the laminate and the laminate stiffness reduces due to matrix failure. To this end, the iterative failure criteria which show good agreement with experimental data need to be selected and the ones which show poor agreement needs to be eliminated. Since experimental

results are not available, biaxial failure envelopes for the quasi-isotropic IMA/M21E alone are not sufficient to decide for the most appropriate iterative failure criteria. In order to investigate different iterative failure criteria combinations, this topic is further discussed in the following subsection.

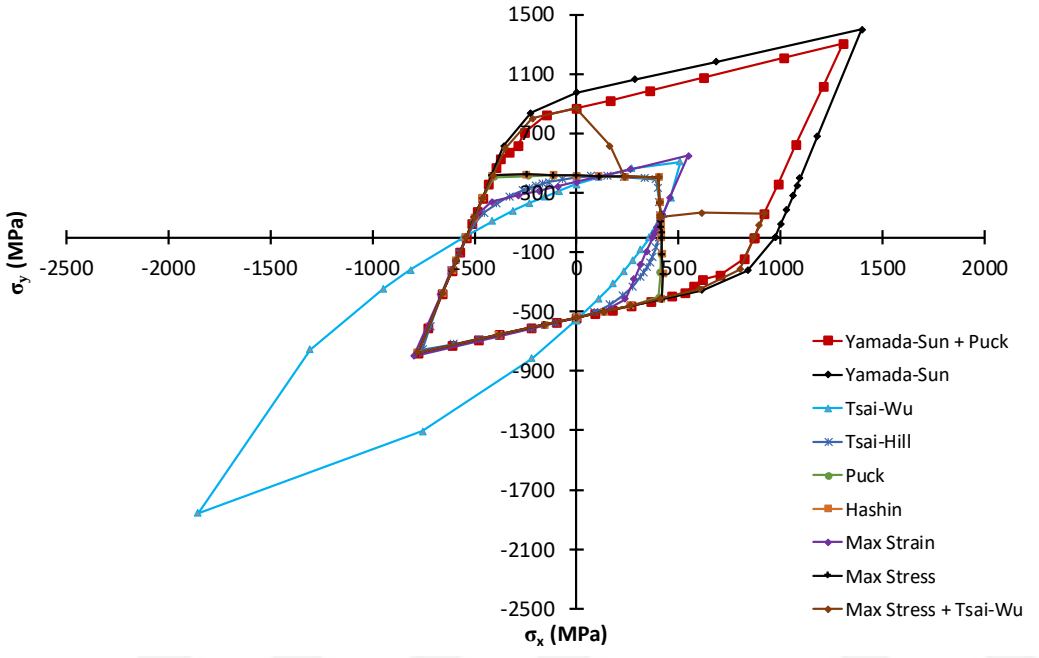

Figure 4.9. Bi-axial failure Envelope for Quasi-Isotropic IMA/M21E Laminate Subjected to Biaxial Normal Loading Using Different Failure Criteria.

4.2.4 Comparison of Unidirectional Strength Curves for IMA/M21 Laminate with Respect to Fiber Orientation

Differentiation between various iterative failure criteria is done by studying the off-axis uniaxial loading influence on the laminate strength. For this purpose, uniaxial tensile and compressive strength of IMA/M21E laminate with a 60/30/10 lay-up (Notation used in the industry: 60% of the plies used at 0°, 30% of the plies at +/-45° and 10% at 90°) with respect to fiber orientation is depicted for different failure criteria as seen in Figure 4.10. As there is no experimental data for the complete off-axis angle range (0°-90°), the decision for the most suitable failure criteria is done

by choosing the one which gives the safest results and closest results to experiments at off-axis angles between 0° and 90°. From Figure 4.10, when the whole range of off-axis angles are considered (0°-90°), we observe that Yamada-Sun plus Puck (under tension and compression) give the most conservative results compared to the other iterative failure criteria. The agreement of these criteria with test data must be checked, as well.

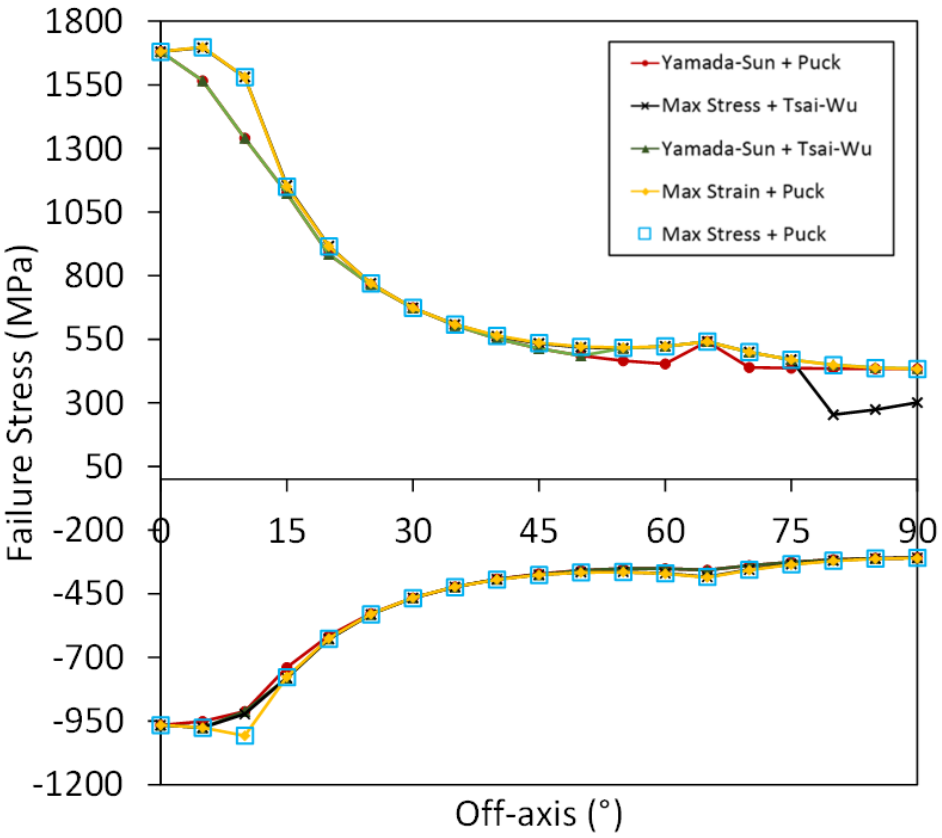

Figure 4.10. Uniaxial Tensile and Compressive Strength of IMA/M21E laminate (60/30/10 lay-up) with Respect to Fiber Orientation.

4.2.5 Comparison with World Wide Failure Exercise

Unnotched laminate strength is predicted using well-known iterative composite failure theories and judged against experimental evidence for the quasi-isotropic $[0^{o}/\pm45^{o}/90^{o}]_{s}$ AS4/3501-6 carbon/epoxy laminate subjected to biaxial loading test case from the World-Wide Failure Exercise I [111] In Figure 4.11, biaxial failure envelopes obtained using 'Yamada-Sun plus Puck', 'Max Stress plus Puck' and 'Max Strain plus Puck' iterative failure models are compared with the experimental results. From Figure 4.11, it is seen that the failure envelopes of the 'Max Stress plus Puck' and 'Max Strain plus Puck' failure models are almost the same. Both failure models exhibit good prediction capabilities for the biaxial tension-tension, uniaxial tension/compression loading cases. However, both failure models are seen to be unconservative in the tension-compression and compression-compression quadrants. On the other hand, Yamada-Sun plus Puck iterative failure model shows good correlation between analytical and experimental results not only for the biaxial tension-tension and uniaxial tension/compression loading cases but also for the biaxial tension-compression loading case. It is further noted that 'Yamada-Sun plus Puck' failure model exhibits better prediction capabilities than the aforementioned failure models in the tension-compression quadrants and for the uniaxial compression loading case. Similar to 'Max Stress plus Puck' and 'Max Strain plus Puck' iterative failure models, 'Yamada-Sun plus Puck' iterative failure theory is observed to be unconservative in the compression-compression quadrant. However, for the compression-compression quadrant it is reported by Hinton et al. [111] in WWFE I that shell buckling might have influenced the test data and therefore test data is possibly unreliable. Due to its better prediction capabilities, Yamada-Sun plus Puck is selected as the most appropriate failure theory for the plain strength prediction of quasi-isotropic carbon fiber/epoxy laminates.

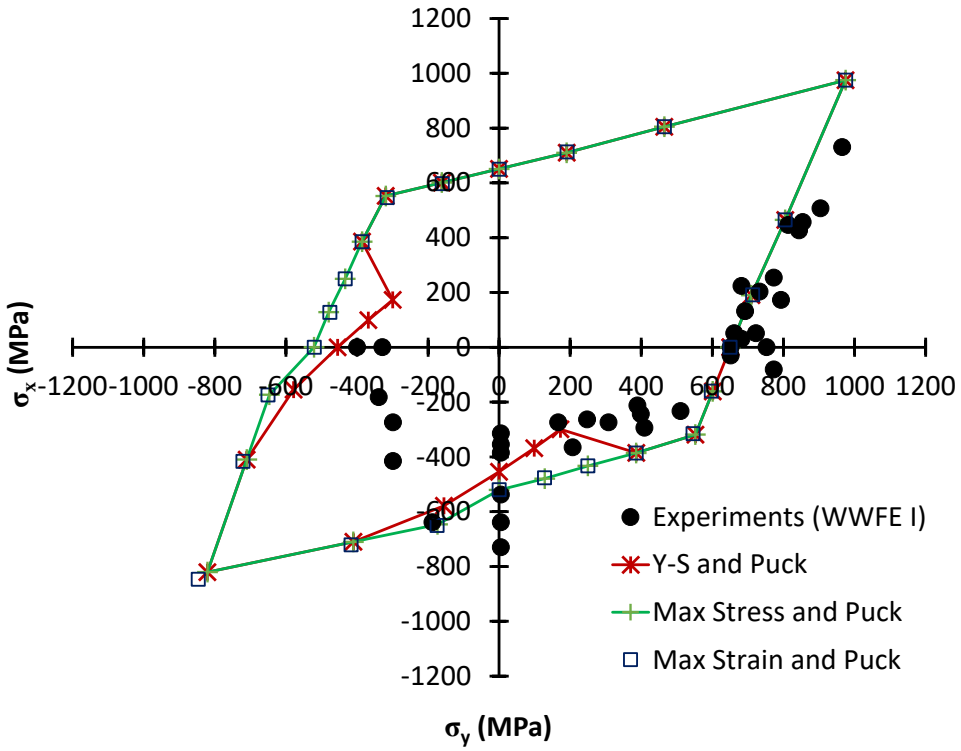

Figure 4.11. Comparison between the predicted and measured biaxial failure stresses for (0º/±45º/90º) AS4/3501-6 laminates [111].

4.3 Conclusions

Within the framework of this thesis methodology for the plain strength analysis of composite tape materials using simple and iterative failure criteria is presented. Regarding composite tape materials the nature of iterative criteria are represented by the experiments better than simple failure criteria, because first fiber failure leads to ultimate failure of the laminate and the laminate stiffness reduces due to matrix failure. The plain strength analysis methodology is partly validated with the available data in literature. Test results are used so that decisions for the most suitable failure criteria is made for composite tape laminates.

Differentiation between various iterative failure criteria is done by studying the off-axis uniaxial loading influence on the laminate strength. As there is no experimental

data for the complete off-axis angle range (0°-90°), the decision for the most suitable failure criteria for tape materials is done by choosing the one which gives the safest results. Yamada-Sun plus Puck gives the most conservative results for both tension and compression loading. The final decision among these criteria is based on their agreement with experiments conducted during the World Wide Failure Exercise I [111]. Due to its better agreement with experimental data, Yamada-Sun plus Puck is selected as the most appropriate iterative failure criteria for the plain strength prediction of quasi-isotropic carbon fiber/epoxy laminates.

CHAPTER 5

ANALYTICAL APPROACH FOR THE OPEN HOLE STRENGTH PREDICTION OF COMPOSITE LAMINATES SUBJECTED TO UNIAXIAL AND BIAXIAL LOADING CONDITIONS

5.1 Introduction

In this chapter, Extended Point Stress Method (EPSM) is proposed for the strength prediction of quasi-isotropic open-hole laminates subjected to in-plane biaxial loading. In the EPSM stress field is calculated on ply level around a hole using Lekhnitskii's Formulation and Classical Lamination Theory (CLT). As proposed by Tan strength reduction (SR) due to the hole in the laminate is calculated using a quadratic composite failure model which incorporates the first-ply-fiber-failure criterion. Once the strength reduction is known, notched laminate strength is calculated from the product of the SR by the unnotched laminate strength, which is obtained by an iterative composite failure model. EPSM is validated against tests of open hole laminates with different materials, lay-ups, hole sizes and width-to-hole diameter ratios under uniaxial tension/compression loading as well as biaxial loading conditions. Within the framework of this thesis, the accuracy level of the EPSM against other traditional stress-based failure models and Finite Fracture Model using open hole laminates with different materials, lay-ups, geometries under different loading conditions is investigated. Moreover, the prediction capability of the EPSM under bi-axial loading condition is studied using the experimental data available in literature.

5.2 Methodology

In the methodology section, analytical strength calculation procedures for the open hole laminate with an elliptical hole and circular hole subjected to in-plane combined loading is explained.

5.2.1 Open Hole Composite Laminate with an Elliptical Hole Subjected to Combined Loading

In this subsection, the algorithm and pseudo-code of the open hole composite tape material strength calculation method is explained in a step-by-step manner. MATLAB codes are utilized for implementing the OH composite tape material strength calculation algorithm. The summary of the implemented algorithm for tape materials is displayed in Figure 5.3.

The calculation steps are explained in detail below.

First, material, geometric data and load cases are given as input:

1. Ply thickness, ply sequence and material orientation angle are read as an input.
2. Elastic properties ($E_1,\ E_2,\ \ \upsilon_{12},\ G_{12}$) are entered for each lamina individually.
3. Lamina strengths ($X_t,\ X_c,\ Y_t,\ Y_c,\ S$) are entered as an input.
4. Unnotched and notched strength ($\sigma_0\ and\ \sigma_N$) of the laminate are entered for the calculation of the characteristic distance.
5. Laminate width and length are entered.
6. Elliptic or cylindrical hole dimensions (a & b values) are entered.
7. Mechanical loading (Forces [N]x,y and Moments [M]x,y) are read as an input. Due to mechanical loading (Forces $[N]_{x,y}$ and Moments $[M]_{x,y}$) stresses ($\overline{\sigma_x}, \overline{\sigma_y}$ and $\overline{\tau_{xy}}$) for the laminate without an opening are computed. A detailed explanation for this step can be found in subsection 3.1.1.2.

8. The geometry and the coordinates of a composite lamina with elliptical opening subjected to combined loading is shown in Figure 3.13. The geometry and coordinate system is used for the strength calculation of the composite laminate. For the stress field calculation principal roots of the characteristic equation μ_1 and μ_2 are calculated from:

$$a_{11}\mu^4 - 2a_{16}\mu^3 + (2a_{12} + a_{66})\mu^2 - 2a_{26}\mu + a_{22} = 0 \qquad (5.1)$$

In Equation (5.1) a_{ij}, i,j=1,2,6 are the laminate compliances with 1 and 2 in the major and minor axes of the opening as seen in Figure 3.13, respectively. The calculation of the laminate compliances is explained in subsection 3.1.1.2. between step 5-10.

From Equation (5.1) four roots will be obtained. According to a complementary definition principal roots of the characteristic equation μ_1 and μ_2 are always the complex roots that have the least value of argument among all roots. For laminates dominated by (±45°) plies Berbinau et al. [104] state that the roots of the characteristic equation are of the form:

$$\mu_1 = F + iG \quad and \quad \mu_2 = -F + iG$$

Berbinau et al. [104] point out that the roots:

$$\mu_1 = F + iG \quad and \quad \mu_2 = F - iG$$

lead to an incorrect stress field in the plate.

9. The total in-plane laminate stress components σ_1', σ_2', and σ_6' given in the principal coordinates of the opening are composed of the stresses due to the opening plus the stresses caused by the uniform stress field ($(\sigma_1')^0$, $(\sigma_2')^0$ and $(\sigma_6')^0$) and are written with refence to Equation (3.85):

$$\begin{aligned}
\sigma_1' &= 2\,\mathrm{Re}[\,\mu_1^2\phi'_1(z_1) + \mu_2^2\phi'_2(z_2)] + (\sigma_1')^0 \\
\sigma_2' &= 2\,\mathrm{Re}[\,\phi'_1(z_1) + \phi'_2(z_2)] + (\sigma_2')^0 \\
\sigma_6' &= -2\,\mathrm{Re}[\,\mu_1\phi'_1(z_1) + \mu_2\phi'_2(z_2)] + (\sigma_6')^0
\end{aligned} \qquad (5.2)$$

where $\phi_1{}'$ and ϕ_2' are the derivatives of the Airy stress functions with respect to z_1 and z_2. These expressions are derived explicitly as:

$$\phi_1{}' = -\frac{-(-a + \mu_1 bi)(-\beta_1 + \mu_2\alpha_1)}{\sqrt{x^2 + 2x\mu_1 y + \mu_1{}^2y^2 - a^2 - \mu_1{}^2b^2}(x + \mu_1 y + \sqrt{x^2 + 2x\mu_1 y + \mu_1{}^2y^2 - a^2 - \mu_1{}^2b^2})(\mu_1 - \mu_2)} \tag{5.3}$$

$$\phi_2{}' = -\frac{(-a + \mu_2 bi)(-\beta_1 + \mu_1\alpha_1)}{\sqrt{x^2 + 2x\mu_2 y + \mu_2{}^2y^2 - a^2 - \mu_2{}^2b^2}(x + \mu_2 y + \sqrt{x^2 + 2x\mu_2 y + \mu_2{}^2y^2 - a^2 - \mu_2{}^2b^2})(\mu_1 - \mu_2)} \tag{5.4}$$

where the z_i are expressed as:

$$z_i = x + \mu_i y \tag{5.5}$$

where x and y are coordinates of a point in the lamina where the stress components are extracted.

In Equations (5.3) and (5.4) α_1 and β_1 were already expressed in Equations (3.83) and (3.84), respectively.

In equation (5.2), $(\sigma_1')^0$, $(\sigma_2')^0$ and $(\sigma_6')^0$ denote the stresses due to the uniform stress field and are written according to:

$$\begin{aligned}(\sigma_1')^0 &= \bar{\sigma}_x \sin^2\psi + \bar{\sigma}_y \cos^2\psi + \bar{\tau}_{xy} \sin 2\psi \\ (\sigma_2')^0 &= \bar{\sigma}_x \cos^2\psi + \bar{\sigma}_y \sin^2\psi + \bar{\tau}_{xy} \sin 2\psi \\ (\sigma_6')^0 &= (\bar{\sigma}_y - \bar{\sigma}_x) \sin\psi \cos\psi - \bar{\tau}_{xy} \cos 2\psi\end{aligned} \tag{5.6}$$

Lekhnitskii stress field solutions are derived for infinite anisotropic plates. Hence, when Lekhnitskii stress field equations are applied to a plate with a finite width, a correction factor is needed to account for this effect. Then similar to Equation (3.86) the relation to account for finite-width correction is expressed as following:

$$\begin{Bmatrix}\sigma_1{}' \\ \sigma_2{}' \\ \sigma_6{}'\end{Bmatrix} = f_{correction}\left(\frac{W}{2a}\right) \cdot \begin{Bmatrix}\sigma_1{}' \\ \sigma_2{}' \\ \sigma_6{}'\end{Bmatrix}_{W=\infty} \tag{5.7}$$

Stress components σ_1', σ_2', and σ_6' are calculated at the characteristic distance, which is represented by b_0 (Figure 3.13) for combined loading case and b_1 for uniaxial loading case as seen in Figure 5.1.

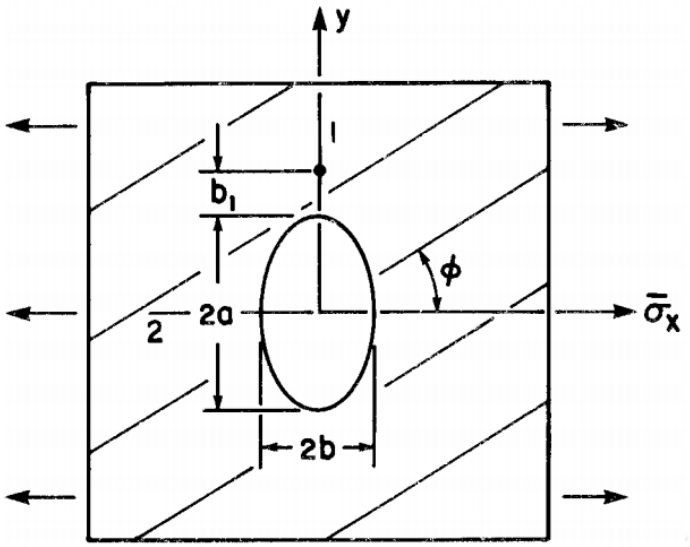

Figure 5.1. Lamina with an elliptical opening subjected to uniaxial loading [18].

10. Characteristic distance b_1 is obtained from the approximate stress distribution expression for an infinite orthotropic plate:

$$\sigma_0 = \frac{\sigma_N}{2}\left\{2 + \left(\frac{a}{a+b_1}\right)^2 + 3\left(\frac{a}{a+b_1}\right)^4 - (K_T^{\infty} - 3)\left[5\left(\frac{a}{a+b_1}\right)^6 - 7\left(\frac{a}{a+b_1}\right)^8\right]\right\} \qquad (5.8)$$

where σ_0 and σ_N are the unnotched and notched strength of the laminate, respectively [105]. K_T^{∞} stands for the orthotropic stress concentration factor for an infinite width plate:

$$K_T^{\infty} = 1 + \sqrt{\frac{2}{A_{22}}\left[\sqrt{A_{11}A_{22}} - A_{12} + \frac{A_{11}A_{22} - A_{12}^2}{2A_{66}}\right]} \qquad (5.9)$$

and A_{ij} (i,j=1,2,6,) are the components of extensional stiffness matrix:

$$A_{ij} = \sum_{k=1}^{N} \left(\overline{Q}_{ij}\right)_k [h_k - h_{k-1}] \qquad (5.10)$$

Determination of the characteristic distance under combined loading is explained in the next step:

11. In Figure 5.2 characteristic curve of the laminate with a circular hole is plotted. In order to determine the characteristic curve under combined loading four characteristic distances are needed:

- $(d_o)_t^0$: characteristic distance due to tension in x-direction
- $(d_o)_t^{90}$: characteristic distance due to tension in y-direction
- $(d_o)_c^0$: characteristic distance due to compression in x-direction
- $(d_o)_c^{90}$: characteristic distance due to compression in y-direction

In the figure characteristic curves of a laminate with an open hole are depicted. Using the above-mentioned characteristic distances, the following elliptic characteristic curves under tension and compression loading are plotted:

Compression loading:

$$\frac{x^2}{(a+(d_o)_t^0)^2}+\frac{y^2}{(a+(d_o)_t^{90})^2}=1 \tag{5.11}$$

Tension loading:

$$\frac{x^2}{(a+(d_o)_c^0)^2}+\frac{y^2}{(a+(d_o)_c^{90})^2}=1 \tag{5.12}$$

In Equations (5.11) and (5.12) $x=(d_0)_{t,c}^{\theta}\cdot\cos(\theta)\,, y=(d_0)_{t,c}^{\theta}\cdot\sin(\theta)$

For the calculation of characteristic distances $(d)_t^0$, $(d)_t^{90}$, $(d)_c^0$, $(d)_c^{90}$ equation (5.8) is used and open hole tensile and compression strength values are needed. From Equations (5.11) and (5.12) $(d)_t^{\theta}$ and $(d)_c^{\theta}$ are determined. Depending on the stress state, i.e. for fiber tension and compression stress states $(d)_t^{\theta}$ and $(d)_c^{\theta}$ characteristic distances must be used, respectively. If both fiber tension and fiber compression stresses are detected, then the characteristic distance which delivers the minimum RF for fiber tension or fiber compression failure modes is used.

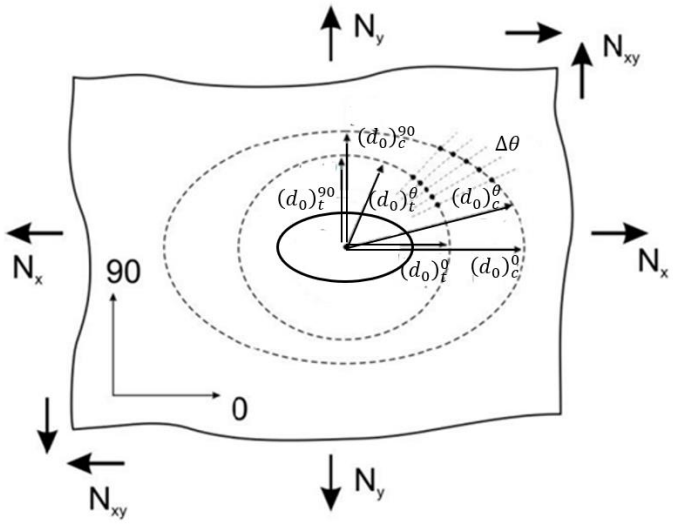

Figure 5.2. Characteristic curve of the laminate with an elliptical opening under combined loading.

Let (1- and 2-) principal axes of the open hole and (x- and y-) problem axes (x- and y-) of the lamina shown in Figure 3.13. For our problem case, these coordinate axes are considered to be the coincident ($\psi = 90°$ in Figure 3.13). Then $\sigma_1' = \sigma_x$, $\sigma_2' = \sigma_y$ and $\sigma_6' = \tau_{xy}$.Hence, in the next steps calculation of layer stresses σ_x^k, σ_y^k and τ_{xy}^k are explained.

12. Reference plane strains $[\varepsilon^\circ]_{x,y}$ are calculated from:

$$\begin{bmatrix} \varepsilon_x^0 \\ \varepsilon_y^0 \\ \gamma_s^0 \end{bmatrix} = \begin{bmatrix} a_{xx}/t_L & a_{xy}/t_L & a_{xs}/t_L \\ a_{yx}/t_L & a_{yy}/t_L & a_{ys}/t_L \\ a_{sx}/t_L & a_{sy}/t_L & a_{ss}/t_L \end{bmatrix} \begin{bmatrix} \sigma_x \\ \sigma_y \\ \tau_{xy} \end{bmatrix} \quad (5.13)$$

where t_L is total laminate thickness

13. Layer stresses $[\sigma]_{x,y}^k$ with respect to load application axes (x,y) are calculated using:

$$\begin{bmatrix} \sigma_x^k \\ \sigma_y^k \\ \tau_{xy}^k \end{bmatrix} = \begin{bmatrix} Q_{xx}^k & Q_{xy}^k & Q_{xs}^k \\ Q_{xy}^k & Q_{yy}^k & Q_{ys}^k \\ Q_{xs}^k & Q_{ys}^k & Q_{ss}^k \end{bmatrix} \begin{bmatrix} \varepsilon_x^0 \\ \varepsilon_y^0 \\ \gamma_s^0 \end{bmatrix} \tag{5.14}$$

14. Stress components $\sigma_x(\theta, b_0)$, $\sigma_y(\theta, b_0)$ and $\sigma_{xy}(\theta, b_0)$ from Equations (5.14) are computed at the critical distance b_0 (See Figure 3.13), and for over an angle $0 \leq \theta \leq 180$ when combined loading is considered. Critical distance b_0 is taken as constant value for all plies.

15. Layer stresses $[\sigma]_{1,2}^k$ with respect to material axis (1,2) are calculates using the transformation matrix in equation below:

$$\begin{bmatrix} \sigma_1^k \\ \sigma_2^k \\ \sigma_6^k \end{bmatrix} = \begin{bmatrix} m^2 & n^2 & 2mn \\ n^2 & m^2 & -2mn \\ -mn & mn & m^2 - n^2 \end{bmatrix} \begin{bmatrix} (\sigma_1^k)' \\ (\sigma_2^k)' \\ (\sigma_6^k)' \end{bmatrix} \tag{15}$$

where $m = \cos(\theta)$, $n = \sin(\theta)$

The proposed methodology utilizes Tan's approach, where the reserve factor of the laminated composite with an opening is calculated based on the strength ratio of the notched and unnotched laminates. In the proposed approach Yamada Sun plus Puck (YS+Puck) iterative failure criteria is implemented for calculating reserve factor of the unnotched laminate.

16. Reserve factor for each ply is calculated from Tsai-Wu Tensor Polynomial Failure Criterion for Fiber Failure over an angle $0 \leq \theta \leq 180$. RF at the critical angle of failure and distance is obtained from:

$$\mathrm{RF}^2 \left(\frac{\sigma_1^2}{X_t \mathrm{X_c}} \right) + \mathrm{RF} \left(\frac{1}{X_t} - \frac{1}{\mathrm{X_c}} \right) \sigma_1 = 1 \tag{5.16}$$

17. Reserve factor of the open hole laminate is equal to the reserve factor of the lamina with the minimum reserve factor. The lamina with the minimum reserve factor is expected to fail first. This criterion is known as First-Ply-First-Fiber (FPFF) Failure.

18. The modified strength ratio (S.R.) of the laminate is set equal to the ratio of the reserve factor of the notched laminate (RF_N) and the reserve factor of the unnotched laminate (RF_0):

$$S.R. = \frac{RF\_Tsai\_Wu\_FPFF(Notched)}{RF\_Tsai\_Wu\_FPFF(Unnotched)} = \frac{RF_N}{RF_0} \qquad (5.17)$$

In the proposed methodology, Yamada-Sun plus Puck (YS+Puck) iterative failure criteria is used for calculating the unnotched laminate:

$$S.R. = \frac{RF\_Tsai\_Wu\_FPFF(Notched)}{RF\_Tsai\_Wu\_FPFF(Unnotched)} = \frac{RF_N}{RF_0(YS + PUCK)} \qquad (5.18)$$

Rearranging Equation (5.18) yields:

$$RF_N = \frac{RF\_Tsai\_Wu\_FPFF(Notched)}{RF\_Tsai\_Wu\_FPFF(Unnotched)} \cdot RF_0(YS + PUCK) \qquad (5.19)$$

RF calculations for the strength reduction ratio are done using Tsai-Wu failure criteria for the first ply fiber failure (FPFF). A detailed explanation of YS-Puck and Tsai-Wu failure criteria can be found in subsection 3.1.1.1.3 of the thesis.

Validation study of the obtained ply stress fields from the EPSM and the proposed methodology for determining the characteristic distance is provided in Appendices B and C, respectively.

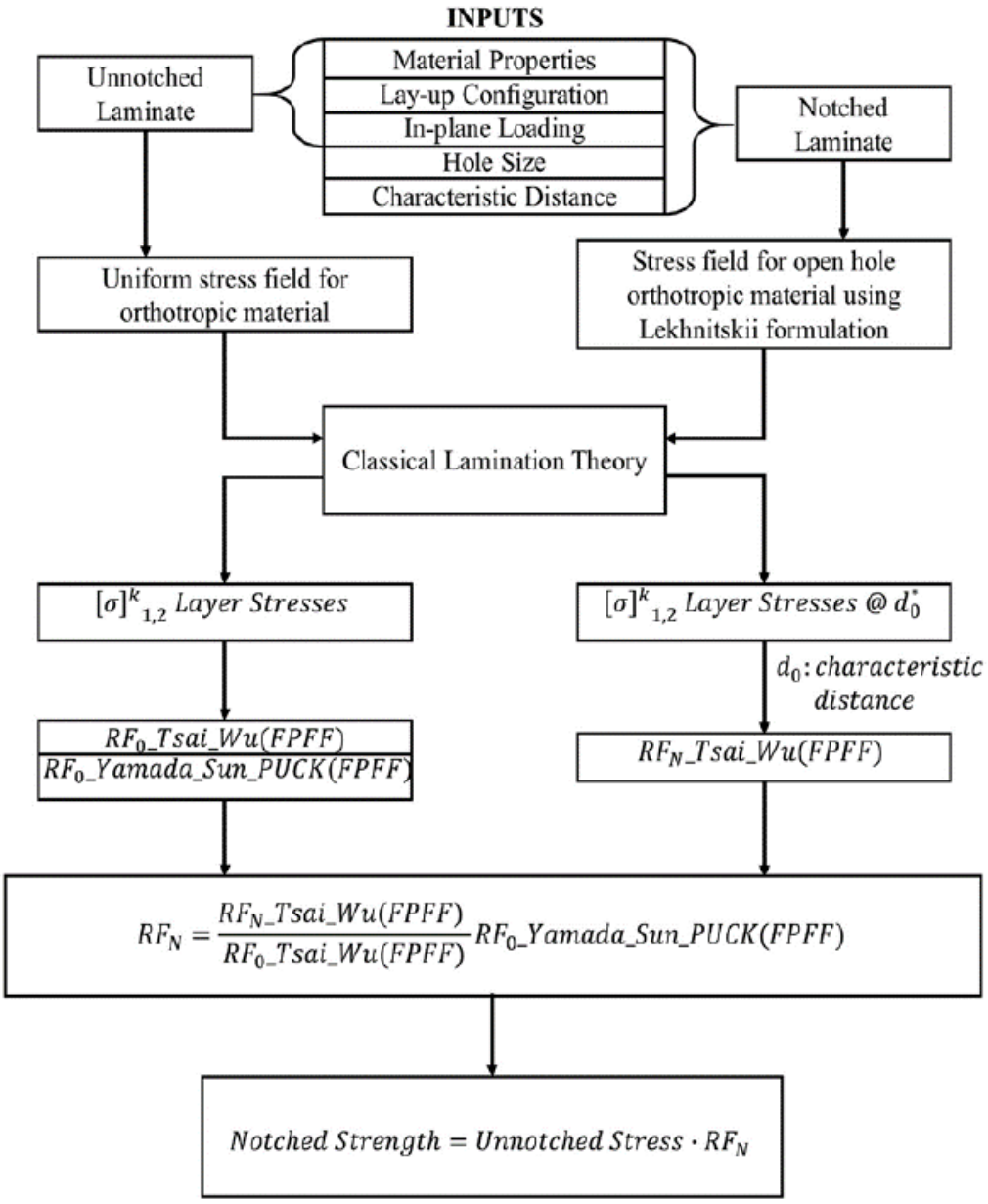

Figure 5.3. Flowchart of the proposed methodology for the open composite laminate strength prediction.

5.2.2 Open Hole Composite Laminate with a Circular Hole Subjected to Combined Loading

In this study, an analytical methodology is proposed for the strength prediction of circular open-hole sublaminate-level scaled composite laminate, depicted in Figure 5.4. Proposed methodology is based on Tan's [86] approach, where the reserve factor of the laminated composite with an opening is calculated based on the strength reduction ratio of notched and unnotched laminates under uniaxial loading. In this study, Yamada Sun [112] plus Puck (YS+Puck) ([80],[81]) iterative failure criterion is implemented for calculating reserve factor of the unnotched laminate, whereas Tsai-Wu quadratic failure criterion is used for calculating strength ratio of the notched laminate, which can be used for multiaxial loading.

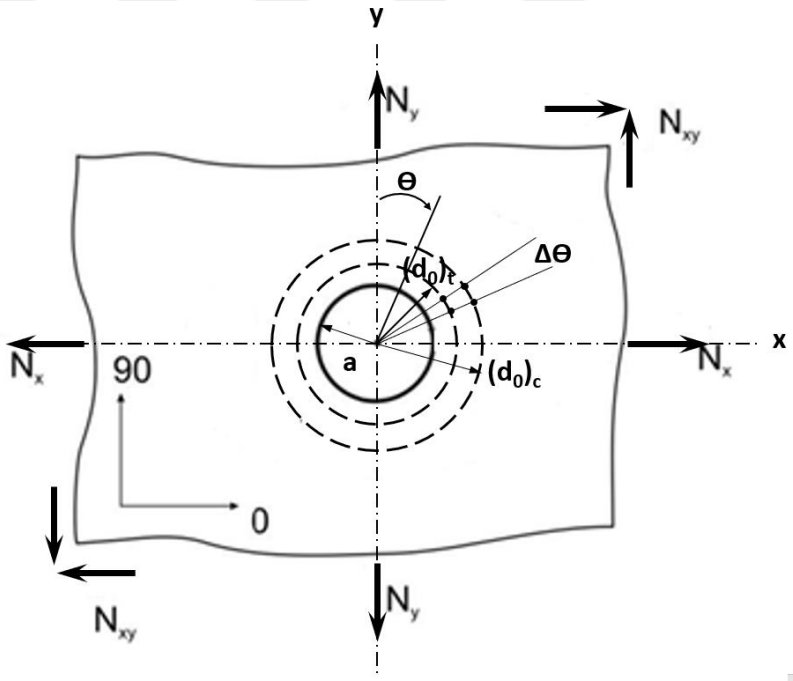

Figure 5.4. Characteristic distance d_0 and coordinate system of a notched composite laminate used for the EPSM.

Algorithm of the proposed methodology is depicted in Figure 5.3. According to the algorithm, first material properties, laminate geometry and load cases are given as

input. For the unnotched laminate layer stresses are found using CLT, whereas for the notched laminate stress field is generated using Lekhnitskii's complex variable mapping method [90]. Stress distribution of an infinite open-hole laminate can be solved by super-positioning the uniform stress field plus the stress field due to the circular opening [92]. For the notched laminate depicted in Figure 5.4, uniform stress field can be expressed as:

$$\begin{aligned} \sigma_x^0 &= N_x/h \\ \sigma_y^0 &= N_y/h \\ \tau_{xy}^0 &= N_{xy}/h \end{aligned} \tag{5.20}$$

Stress components due to opening are:

$$\begin{aligned} \sigma_x' &= 2\,Re[\,\mu_1^2\phi'_1(z_1) + \mu_2^2\phi'_2(z_2)] \\ \sigma_y' &= 2\,Re[\,\phi'_1(z_1) + \phi'_2(z_2)] \\ \tau_{xy}' &= -2\,Re[\,\mu_1\phi'_1(z_1) + \mu_2\phi'_2(z_2)] \end{aligned} \tag{5.21}$$

where ϕ_1' and ϕ_2' are the derivatives of the Airy stress functions with respect to z_1 and z_2. These expressions are derived explicitly as:

$$\phi_1' = -\frac{(-a+\mu_1 ai)(-\beta_1+\mu_2\alpha_1)}{\sqrt{x^2+2x\mu_1 y+\mu_1^2y^2-a^2-\mu_1^2a^2}\left[x+\mu_1 y+\sqrt{x^2+2x\mu_1 y+\mu_1^2y^2-a^2-\mu_1^2a^2}\right](\mu_1-\mu_2)} \tag{5.22}$$

$$\phi_2' = -\frac{(-a+\mu_2 ai)(-\beta_1+\mu_1\alpha_1)}{\sqrt{x^2+2x\mu_2 y+\mu_2^2y^2-a^2-\mu_2^2a^2}\left[x+\mu_2 y+\sqrt{x^2+2x\mu_2 y+\mu_2^2y^2-a^2-\mu_1^2a^2}\right](\mu_1-\mu_2)} \tag{5.23}$$

z_i can be expressed as:

$$z_i = x + \mu_i y, \qquad i = 1,2 \tag{5.24}$$

where x and y are coordinates of a point in the lamina where the stress components are extracted. In equations (5.22) and (5.23), a is the hole radius. α_1 and β_1 are expressed as:

$$\alpha_1 = a\left[-\left(N_y/2h\right) + i\left(N_{xy}/2h\right)\right] \tag{5.25}$$

$$\beta_1 = a\left[\left(N_{xy}/2h\right) - i\left(N_x/2h\right)\right] \tag{5.26}$$

For the stress field calculation principal roots of the characteristic equation μ_1 and

μ_2 in Equations (5.21)-(5.23) are calculated from Equation (5.27):

$$a_{11}\mu^4 - 2a_{16}\mu^3 + (2a_{12} + a_{66})\mu^2 - 2a_{26}\mu + a_{22} = 0 \quad (5.27)$$

In Equation (5.27) a_{ij}, i,j=1,2 are the laminate compliances with 1 and 2 in the major and minor axes of the opening as seen on Figure 5.4, respectively. From equation (5.27) four roots will be obtained. According to a complementary definition principal roots of the characteristic equation μ_1 and μ_2 are always the complex roots that have the least value of argument among all roots. For laminates dominated by (±45°) plies Berbinau et al.[104] state that the roots of the characteristic equation are of the form:

$$\mu_1 = F + iG \quad and \quad \mu_2 = -F + iG \quad (5.28)$$

The total in-plane laminate stress components σ_x, σ_y, and τ_{xy} given in the principal coordinates of the opening are composed of the stresses due to the opening plus the stresses caused by the uniform stress field (σ'_x, σ'_y and τ'_{xy}).

$$\begin{aligned} \sigma_x &= \sigma_x^0 + 2\,Re[\,\mu_1^2\phi'_1(z_1) + \mu_2^2\phi'_2(z_2)] \\ \sigma_y &= \sigma_y^0 + 2\,Re[\,\phi'_1(z_1) + \phi'_2(z_2)] \\ \tau_{xy} &= \tau_{xy}^0 - 2\,Re[\,\mu_1\phi'_1(z_1) + \mu_2\phi'_2(z_2)] \end{aligned} \quad (5.29)$$

Lekhnitskii stress field relations are derived for infinite anisotropic plates [90]. Hence, when Lekhnitskii stress field equations are applied to a plate with a finite width, a correction factor is needed to account for this effect. Then, similar to Equations (3.51) and (3.53) the equation to account for the finite-width correction is expressed as:

$$\begin{Bmatrix} \sigma_x \\ \sigma_y \\ \tau_{xy} \end{Bmatrix} = \frac{2 + \left(1 - \frac{2a}{W}\right)^3}{3\left(1 - \frac{2a}{W}\right)} \begin{Bmatrix} \sigma_x \\ \sigma_y \\ \tau_{xy} \end{Bmatrix}_\infty \quad (5.30)$$

Layer stresses are obtained at characteristic distance, d_0, using CLT. For this purpose, the unnotched and notched strengths of the open-hole laminate is needed. The characteristic distance is extracted from Equation (3.51) used for the PSC.

Finite-width effect is also taken into account using the relation below proposed by Karlak [16]:

$$d_0 = \frac{d_{ref}}{\sqrt{\frac{2a}{2a_{ref}}}} \tag{5.31}$$

Once the layer stresses are obtained for the unnotched and notched laminate, reserve factors (RF) can be calculated for the given load case. As shown in Figure 5.3, strength reduction (SR) ratio is calculated by dividing the reserve factor of the notched laminate by the reserve factor of the unnotched laminate as written below:

$$S.R. = \frac{RF_N\_Tsai\_Wu\_FPFF\ at\ \frac{x^2}{(a+d_0)^2} + \frac{y^2}{(a\ +d_0)^2}}{RF_0\_Tsai\_Wu\_FPFF} \tag{5.32}$$

Reserve factors of the unnotched and notched laminates are calculated using the Tsai-Wu quadratic failure criterion, which is reduced to the following form for the calculation of the first-ply-fiber-failure (FPFF):

$$\left(\frac{\sigma_1}{X_T X_c}\right)^2 + \sigma_1\left(\frac{1}{X_t} - \frac{1}{X_c}\right) = 1 \tag{5.33}$$

In Equation (5.33) σ_1 is the stress in longitudinal direction. X_t and X_c are longitudinal tensile and compressive strengths, respectively. From the multiplication of the strength reduction ratio by the reserve factor the unnotched laminate, which is obtained using the Yamada-Sun) plus Puck failure model gives the reserve factor the open-hole laminate. In the final step of the flow chart of the EPSM in Figure 5.3, the multiplication of the applied stress by the reserve factor of the notched laminate delivers the notched laminate strength. The flowchart of the Yamada-Sun plus Puck iterative failure model is shown Figure 4.2. As seen from the flowchart, Y-S plus Puck failure model is based on the reduction of stiffness due to matrix failure. First-ply-fiber-failure is used to predict the reserve factor of the unnotched laminate.

In the Y-S plus Puck failure model, modified Puck criterion [81] is used to predict matrix failure and expressed as:

$$\frac{\sigma_2^2}{Y_t Y_c} + \left(\frac{\tau_{12}}{S}\right)^2 + \left(\frac{1}{Y_t} + \frac{1}{Y_c}\right)\sigma_2 = 1 \tag{5.34}$$

where σ_2 and τ_{12} are the transverse and shear stresses respectively. Y_T and Y_C denote transverse tensile and compressive strength, respectively. S is shear strength. For the fiber failure prediction, Y-S failure model is used to predict the fiber failure [112]:

$$\left(\frac{\sigma_1}{X}\right)^2 + \left(\frac{\tau_{12}}{S}\right)^2 = l^2$$
$$l \geq 1\ failure, \qquad l < 1\ non-failure \tag{5.35}$$

where σ_1 and $\tau_{12}$are longitudinal and shear stresses, respectively. Depending on the sign of σ_2 is the lamina, X is taken as the tensile or compressive strength in longitudinal direction and S is shear strength of the lamina.

5.3 Results and Discussions

For the validation of the proposed Extended Point Stress Method (EPSM), experimental data available in literature is utilized. As a part of the open-hole strength prediction methodology, unnotched laminate strength needs to be predicted analytically. In the subsequent subsections, validation studies of the EPSM for the unnotched laminate subjected to biaxial loading, open-hole laminate under uniaxial tension, open-hole under uniaxial compression and open-hole laminate subjected to biaxial loading cases are presented.

5.3.1 Open Hole Tension

In order to validate the proposed semi-analytical model, the predictions of the model are compared with the experimental data available in literature for the uniaxial tension loading case. For this purpose, IM7-8552 quasi-isotropic open-hole laminates with different thicknesses and M21/800 CFRP open hole-laminate is chosen([13],[26]). In Table 5.1, elastic and strength properties of the IM7/8552 lamina are listed. According to the ASTM D-5766 Standard [113] ,open-hole test specimen used for the tension test have hole diameters, D=2, 4, 6, 8, 10, 12 mm and their width-to-hole diameter ratio is constant $\frac{w}{d} = 6$. Lamina thickness is reported as 0.131 mm. Baseline specimen with a hole diameter of 6 mm is used to determine the characteristic distance for the PS, AS, EPSM and the inherent flaw length needed for the IFM. Unnotched laminate strength is 845.1 MPa. According to Camanho et al. [13] characteristic distances for PS and AS are 0.83 and 2.08 mm, respectively. In addition, the length of the inherent flaw is 1.28 mm. Including the correction factor proposed by Tan [86], the characteristic distance needed for the EPSM is calculated as 0.835 mm. From tests, the mean value of the fracture toughness is determined as 48.0 $MPa\sqrt{m}$ [13]. The results in Table 5.2, indicate that FFM, EPSM and AS are among the most accurate models. The variation of the OHT strength of the $[90/0/45/-45]_{3s}$ lay-up with respect to different hole diameters is plotted in Figure

5.5. From the figure we note that the prediction capabilities of the point stress and inherent flaw model are good for the hole diameters larger than the ones used to calculate the characteristic distance and the inherent flaw length. Yet, the accuracy level of PS and IFM decrease for small hole diameters. Accuracy of the analytical models which rely on characteristic distance can be improved by taking geometric dependency into account ([17],[114],[115]). For this reason, in the EPSM characteristic distance for different hole sizes is calculated based on the relation proposed by Karlak [16].

Table 5.1 Mechanical Properties of the IM7/8552 lamina.

Material Data for IM7/8552 Lamina					
Longitudinal Modulus,	E_1	=	171420	(MPa)	[9],[13]
Transverse Modulus,	E_2	=	9080	(MPa)	[9],[13]
In-plane Shear Modulus,	G_{12}	=	5290	(MPa)	[9],[13]
Major Poisson's Ratio,	υ_{12}	=	0.32	(MPa)	[9],[13]
Longitudinal Tensile Strength,	X_t	=	2326.2	(MPa)	[9],[13]
Longitudinal Compressive Strength,	X_c	=	1200.1	(MPa)	[9],[13]
Transverse Tensile Strength,	Y_t	=	62.3	(MPa)	[9],[13]
Transverse Compressive Strength,	Y_c	=	199.3	(MPa)	[9],[13]
In-plane Shear Strength,	S	=	92.3	(MPa)	[9],[13]

Table 5.2 Comparison between predictions and experiments for the $[90/0/45/-45]_{3s}$ lay-up.

D (mm)	$\bar{\sigma}^{\infty}$ (Exp.) (MPa) [9],[13]	$\bar{\sigma}^{\infty}$ (FFM) (MPa) [13]	E (%)	$\bar{\sigma}^{\infty}$ (PS) (MPa) [13]	E (%)	$\bar{\sigma}^{\infty}$ (AS) (MPa) [13]	E (%)	$\bar{\sigma}^{\infty}$ (IFM) (MPa) [13]	E (%)	$\bar{\sigma}^{\infty}$ (EPSM) (MPa)	E (%)
2	555.7	560	0.8	639	15	588	5.8	627	13	523	-5.9
4	480.6	470	-2.2	506	5.3	491	2.2	505	5.1	462	-4.0
6	438.7	420	-4.3	n/a	n/a	n/a	n/a	n/a	n/a	428	-2.5
8	375.7	390	3.8	401	6.3	406	8.1	398	5.9	406	8.0
10	373.7	370	-1.0	376	0.6	384	2.8	371	-0.7	391	4.5

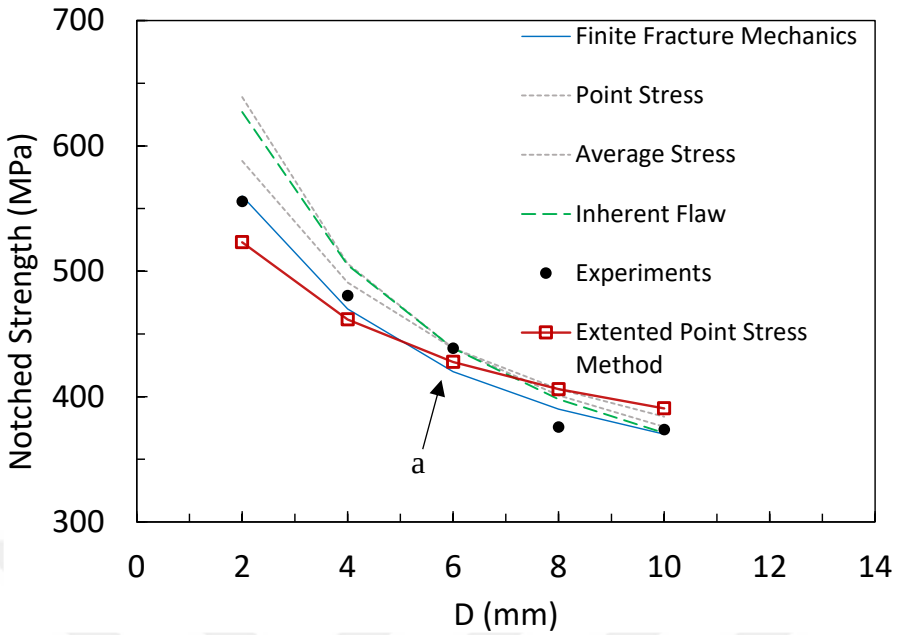

Figure 5.5. OHT strength vs. hole diameter plot for $[90/0/45/-45]_{3S}$ lay-up (PS, AS, IFM and EPSM methods calibrate the characteristic distance at point a) ([9],[13])

As another validation study, open-hole tensile strength prediction of the IM7-8552 $[45/90/-45/0]_{4s}$ lay-up is compared with experimental results. In Table 5.3, mechanical properties of the IM7/8552 lamina are listed. As reported by Green et al. [116] unidirectional carbon-fibre/epoxy pre-preg system manufactured by Hexcel has a nominal ply thickness of 0.125 mm. The open-hole specimens used for the tests have a constant width-to-hole diameter ratio of $\frac{w}{d} = 5$ with hole diameters D=3.175, 6.35, 12.7 and 25.4 mm. Unnotched laminate strength used for the characteristic distance calculation is taken as 929 MPa [117]. In Table 5.4, the strength predictions using FFM, PS, AS, IFM and EPSM against experimental results are tabularized. Using the baseline specimen with a hole diameter of 3.175 mm, characteristic distances for the PS and AS are determined as 0.45 mm and 1.12 mm, respectively [13]. In addition, the length of the inherent flaw needed for the IFM is reported as 0.66 using the baseline specimen. Since the experimental fracture toughness value required for FFM was not available, using notched strength of the specimen with a hole diameter of 3.175 mm and unnotched laminate strength, Equations (3.57) and (3.58) are solved simultaneously. From the solution of (3.57)

and (3.58), crack extension at failure, l ,as well as fracture toughness value K_{Ic} can be determined. K_{Ic} is calculated as 42.3 MPa$\sqrt{m}$. Characteristic distance required for the EPSM is determined from the specimen with a hole size of 12.7 mm as 0.73 mm. It is observed from Table 5.4 that EPSM delivers the most accurate results when compared to alternative analytical models including the FFM.

Table 5.3 Mechanical Properties of the IM7/8552 Lamina.

Material Data for IM7/8552 Lamina					
Longitudinal Modulus,	E_1	=	161000	(MPa)	[25]
Transverse Modulus,	E_2	=	11380	(MPa)	[25]
In-plane Shear Modulus,	G_{12}	=	5170	(MPa)	[25]
Major Poisson's Ratio,	υ_{12}	=	0.32	(MPa)	[25]
Longitudinal Tensile Strength,	X_t	=	2724	(MPa)	[119]
Longitudinal Compressive Strength,	X_c	=	1690	(MPa)	[119]
Transverse Tensile Strength,	Y_t	=	64	(MPa)	[119]
Transverse Compressive Strength,	Y_c	=	199.8	(MPa)	[9],[13]
In-plane Shear Strength,	S	=	92.3	(MPa)	[9],[13]

Table 5.4 Comparison between predictions and experiments for the $[45/90/-45/0]_{4S}$ lay-up.

D (mm)	$\bar{\sigma}^{\infty}$ (Exp.) (MPa) Ref.[13]	$\bar{\sigma}^{\infty}$ (FFM) (MPa) Ref.[13]	E (%)	$\bar{\sigma}^{\infty}$ (PS) (MPa) Ref.[13]	E (%)	$\bar{\sigma}^{\infty}$ (AS) (MPa) Ref.[13]	E (%)	$\bar{\sigma}^{\infty}$ (IFM) (MPa) Ref.[13]	E (%)	$\bar{\sigma}^{\infty}$ (EPSM) (MPa)	E (%)
3.175	478	n/a	n/a	n/a	n/a	n/a	n/a	n/a	n/a	460	-3.7
6.35	433	400	-7.6	392	-9.5	401	-7.4	385	-11.1	412	-4.8
12.7	374	351	-6.1	344	-8.0	353	-5.6	332	-11.2	377	0.8
25.4	331	324	-2.1	320	-3.3	325	-1.8	304	-8.2	351	6.1

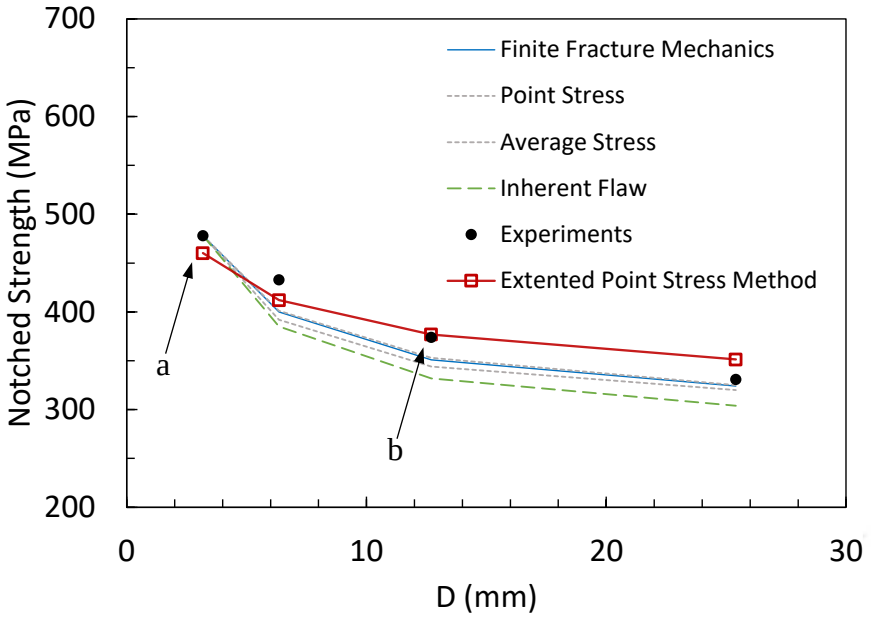

Figure 5.6. Open Hole Tension Strength vs. Hole Diameter (PS, AS and IFM methods calibrate the characteristic distance at point a, whereas EPSM calibrates at point b) [13].

As a further validation study, open-hole tensile strength prediction for the M21/T800 $[90/45/0/-45]_{3s}$ lay-up is done and compared with experimental data presented in [25] and [26]. In Table 5.5, material properties for the M21/T800 lamina are listed. The open hole tensile test specimens have a constant width-to-diameter ratio $\frac{w}{d} = 4$ with hole diameters D = 3, 5and 7. Ply thickness is 0.132 mm as reported in [25]. Baseline specimen for the characteristic distance and inherent flaw length, the specimen with a hole diameter of 5 mm is chosen. Characteristic distances required for the PS and AS are reported as 0.7 mm and 2.5 mm, respectively. The inherent flaw length is calculated as 1.0 mm. Using the unnotched laminate thickness of 1053.5 MPa, characteristic distance required for the EPSM is determined is 0.74 mm. In Table 5.6, predictions of the FFM, PS, AS, CZM, IFM and EPSM are compared with the experimental results. From the results, it is seen that FFM and EPSM are among the most accurate models.

Table 5.5 Mechanical Properties of the M21/T800 Lamina

Material Data for M21/T800 Lamina					
Longitudinal Modulus,	E_1	=	172000	(MPa)	[13]
Transverse Modulus,	E_2	=	8900	(MPa)	[13]
In-plane Shear Modulus,	G_{12}	=	5000	(MPa)	[13]
Major Poisson's Ratio,	υ_{12}	=	0.32	(MPa)	[13]
Longitudinal Tensile Strength,	X_t	=	3039	(MPa)	[25]
Longitudinal Compressive Strength,	X_c	=	1231	(MPa)	[120]
Transverse Tensile Strength,	Y_t	=	75	(MPa)	[25]
Transverse Compressive Strength,	Y_c	=	250	(MPa)	**[27]**
In-plane Shear Strength,	S	=	95	(MPa)	[25]

Table 5.6 Comparison between predictions and OHT experiments for the $[90/45/0/-45]_{3S}$ lay-up.

D (mm)	$\bar{\sigma}^{\infty}$ (Exp.) (MPa) [26]	$\bar{\sigma}^{\infty}$ (FFM) (MPa) [26]	E (%)	$\bar{\sigma}^{\infty}$ (PS) (MPa) [26]	E (%)	$\bar{\sigma}^{\infty}$ (AS) (MPa) [26]	E (%)	$\bar{\sigma}^{\infty}$ (CZM) (MPa) [26]	E (%)	$\bar{\sigma}^{\infty}$ (IFM) (MPa) [26]	E (%)	$\bar{\sigma}^{\infty}$ (EPSM) (MPa)	E (%)
3	560	578	3.2	639	14.1	614	9.6	-2.0	13	637	13.8	602	7.5
5	534	507	-5.1	n/a	n/a	n/a	n/a	477	-10.7	n/a	n/a	546	2.2
7	500	466	-6.8	479	-4.2	487	-2.6	438	-12.4	478	-4.4	515	3.0

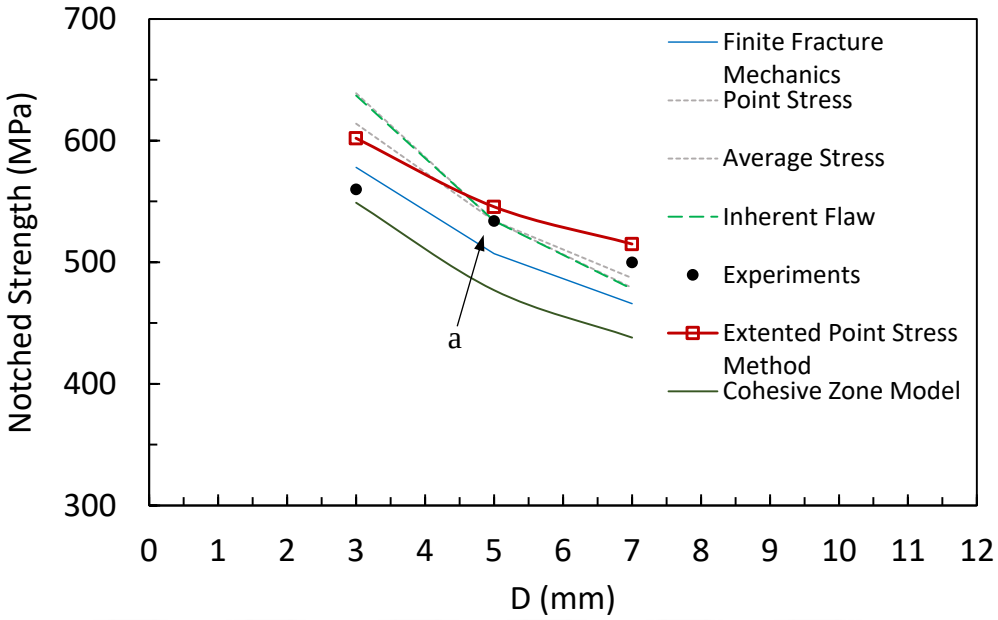

Figure 5.7. Open Hole Tension Strength vs. Hole Diameter (PS, AS, IFM and EPSM methods calibrate the characteristic distance at point a) (Ref. [13] [26]).

5.3.2 Open Hole Compression

In this subsection, the prediction capability of the proposed semi-analytical model is judged against the open-hole compression tests for the M21/T800 $[90/45/0/-45]_{3s}$ lay-up [26]. As in the open-hole tension tests, for the compressive tests open-hole specimens have a constant width-to-hole diameter ratio $\frac{w}{d} = 4$ with hole diameters D=3, 5 and 7 mm. The specimen with a hole diameter of 5 mm is selected as the baseline specimen for the characteristic length and inherent flaw length calculation. Using the unnotched compressive laminate strength 279.8 MPa, characteristic length for the PS and EPSM are calculated as 0.8 mm. For the AS and IFM the characteristic length and inherent flaw length are reported as 2.0 mm and 1.1 mm, respectively. Comparison between the predictions obtained from analytical models and experiments are summarized in Table 5.7. The results in Table 5.7 show that FFM, PS, AS and IFM are among the most accurate models, whereas the predictions done by CZM and EPSM are poor. The reason for the poor prediction of the EPSM might

be due to the lamina longitudinal compressive strength value. This value is taken from the Hexcel data sheet [120] and might be lower than the real value of the specimens used in the tests. In order to investigate this issue, longitudinal compressive strength value of the lamina is found by reverse engineering calculations from the compressive strength of the $[90/45/0/-45]_{3s}$ OHC laminates obtained from the experiments [26]. Longitudinal compressive strength value of the lamina is calculated as 1400 MPa and using this value the open-hole strength calculations are repeated with EPSM. The new results, which are tabularized in Table 5.8 show that when the longitudinal compressive strength value is increased the absolute value of the prediction error in EPSM reduces from 16.0% to 5.2%.

Table 5.7. Comparison between predictions and OHC experiments for the $[90/45/0/-45]_{3S}$ lay-up (Longitudinal compressive stress of the lamina is taken as 1231 MPa [120].

D (mm)	$\bar{\sigma}^{\infty}$ (Exp.) (MPa) [26]	$\bar{\sigma}^{\infty}$ (FFMs) (MPa) [26]	E (%)	$\bar{\sigma}^{\infty}$ (PS) (MPa) [26]	E (%)	$\bar{\sigma}^{\infty}$ (AS) (MPa) [26]	E (%)	$\bar{\sigma}^{\infty}$ (CZM) (MPa) [26]	E (%)	$\bar{\sigma}^{\infty}$ (IFM) (MPa) [26]	E (%)	$\bar{\sigma}^{\infty}$ (EPSM) (MPa)	E (%)
3	335	319	-4.8	337	0.6	322	-3.9	296	-11.6	335	0.0	281	-16.0
5	280	283	1.1	280	n/a	280	n/a	258	-7.9	280	n/a	255	-8.9
7	259	259	0.0	252	-2.7	255	-1.5	235	-9.3	250	-3.5	239	-7.5

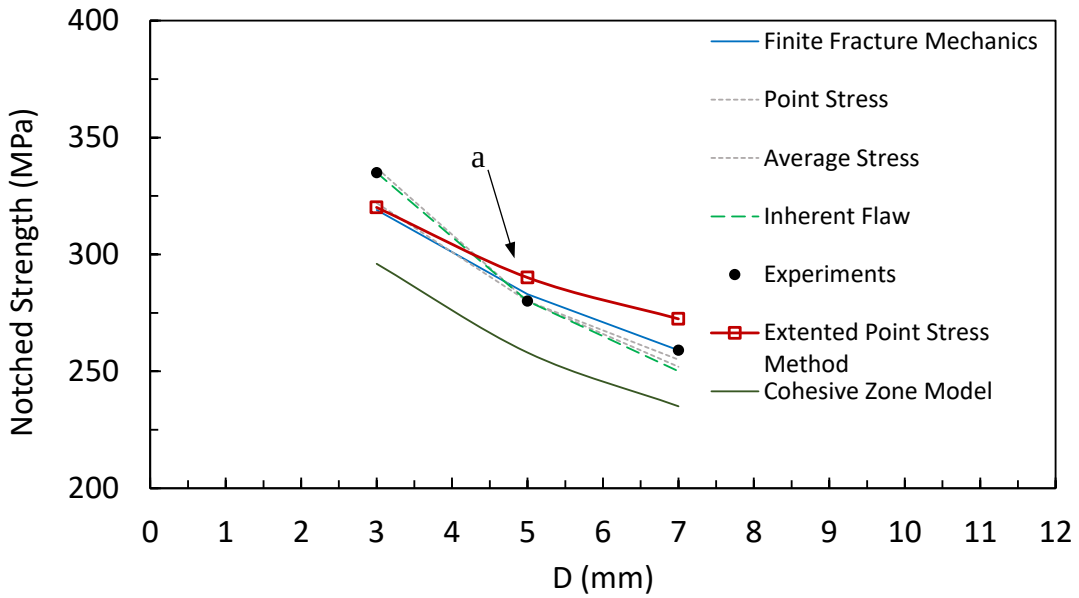

Figure 5.8. Open Hole Compressive Strength vs. Hole Diameter (PS, AS, IFM and EPSM methods calibrate the characteristic distance at point a) [26].

Table 5.8. Comparison between predictions and OHC experiments for the [90/45/0/-45]$_{3S}$ lay-up (Longitudinal compressive stress of the lamina is taken as 1400 MPa).

D (mm)	$\bar{\sigma}^{\infty}$ (Exp.) (MPa) [26]	$\bar{\sigma}^{\infty}$ (FFMs) (MPa) [26]	E (%)	$\bar{\sigma}^{\infty}$ (PS) (MPa) [26]	E (%)	$\bar{\sigma}^{\infty}$ (AS) (MPa) [26]	E (%)	$\bar{\sigma}^{\infty}$ (CZM) (MPa) [26]	E (%)	$\bar{\sigma}^{\infty}$ (IFM) (MPa) [26]	E (%)	$\bar{\sigma}^{\infty}$ (EPSM) (MPa)	E (%)
3	335	319	-4.8	337	0.6	322	-3.9	296	-11.6	335	0.0	320	-4.5
5	280	283	1.1	280	n/a	280	n/a	258	-7.9	280	n/a	290	3.6
7	259	259	0.0	252	-2.7	255	-1.5	235	-9.3	250	-3.5	272	5.2

5.3.3 Open Hole under Multiaxial Loading

As a final validation study for the EPSM, biaxial failure envelope of the [0/45/90/-45]$_s$ IM7/8552 open hole laminate is plotted and compared with the experimental data in literature [121]. In Table 5.9, mechanical properties of the IM7/8552 lamina

are listed. Unnotched tensile laminate strength of the $[0/45/90/-45]_s$ IM7/8552 laminate required for the characteristic distance calculation is taken as the unnotched laminate strength of the IM7/8552 $[45/90/-45/0]_{2S}$ lay-up (ply thickness=0.125 mm) which is obtained as 911 MPa from [122]. Notched strength of the smooth cruciform specimen with a hole diameter of 10 mm is given as 702.6 MPa. Besides, width-to-hole diameter of the cruciform specimen is given as $\frac{w}{D} = 8$. Using unnotched strength, notched strength and width-to-hole diameter for the finite width correction calculation proposed by Peterson [123], the characteristic distance is calculated as 2.05 mm for tension loading. According to Tan [19] when strength prediction for the quasi-isotropic laminates is done based on minimum strength model, which incorporates fiber failure criteria, characteristic distance is independent of loading conditions. Hence, for the generation of the biaxial failure envelope of the cruciform specimen, the characteristic length under compression is assumed to be equal to the characteristic length under tension in the EPSM, as well. This assumption can be justified by the fact that the characteristic lengths for the M21/T800 $[90/45/0/-45]_{3s}$ lay-up under tension and compression were close and calculated as 0.74 and 0.79 mm, respectively [26].

Comparison of biaxial failure envelopes between tests and analytical predictions for the $[0/45/90/-45]_s$ IM7/8552 open hole cruciform laminate is depicted in Figure 5.9. Biaxial loadings are done in the $\{\sigma_x, \sigma_y\}$ stress space: $\{1, -1\}$, $\{1,0\}$, $\{1,1\}$. From Figure 5.9, it is seen that there is a good agreement between biaxial tests and the analytical predictions. In addition, failure pattern pictures of the $[0/45/90/-45]_s$ IM7/8552 open hole cruciform specimen subjected to the aforementioned loading conditions as well as the predictions from EPSM are shown. Using EPSM, it is possible to predict the failure initiation angle (θ), and first-ply-fiber failure initiation. As displayed in Figure 5.10, when compared with the pictures from tests, EPSM is able to make close predictions in terms of failure initiation angle. Since information about the first-ply-fiber-failure is not provided, it is not possible to compare first-ply-fiber-failure data obtained from EPSM with tests.

Table 5.9 Mechanical Properties of the IM7/8552 lamina [121].

Material Data for IM7/8552 Lamina					
Longitudinal Modulus,	E_1	=	170000	(MPa)	[121]
Transverse Modulus,	E_2	=	12000	(MPa)	[121]
In-plane Shear Modulus,	G_{12}	=	4600	(MPa)	[121]
Major Poisson's Ratio,	υ_{12}	=	0.28	(MPa)	[121]
Longitudinal Tensile Strength,	X_t	=	2400	(MPa)	[121]
Longitudinal Compressive Strength,	X_c	=	1600	(MPa)	[121]
Transverse Tensile Strength,	Y_t	=	40	(MPa)	[121]
Transverse Compressive Strength,	Y_c	=	80	(MPa)	[121]
In-plane Shear Strength,	S	=	50	(MPa)	[121]

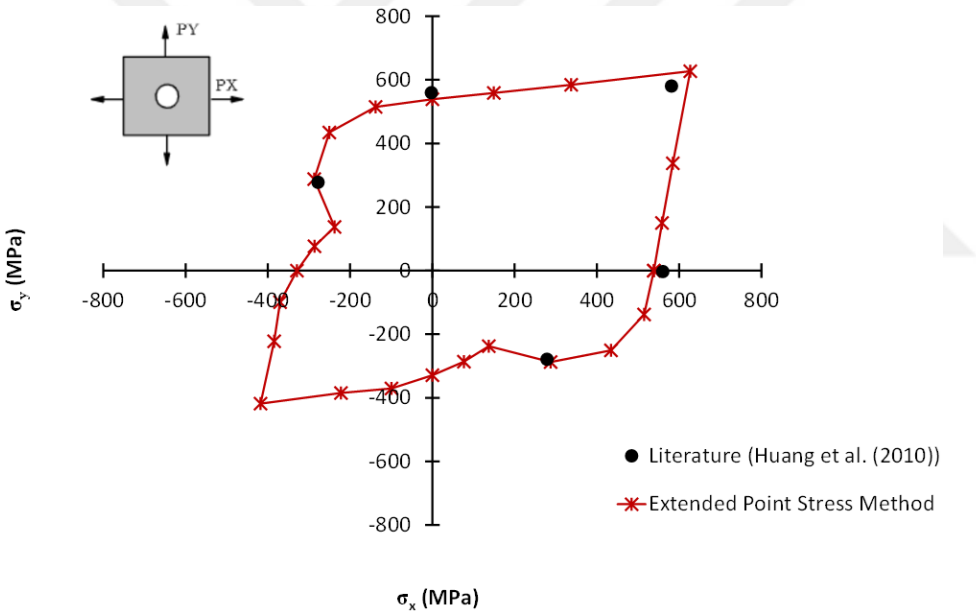

Figure 5.9. Comparison of biaxial failure envelopes for $[0/45/90/-45]_s$ IM7/8552 laminate [121].

Bi-axial tests (Huang et al., 2010)[121]	theta (θ)	EPSM First-ply-fiber-failure
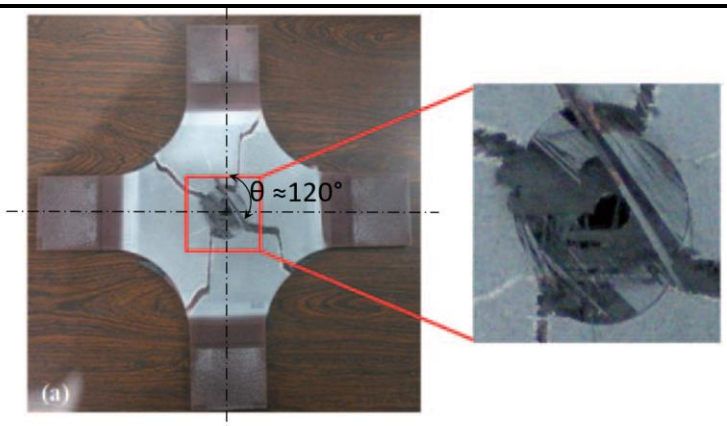	60º, 120º	90 (compression)
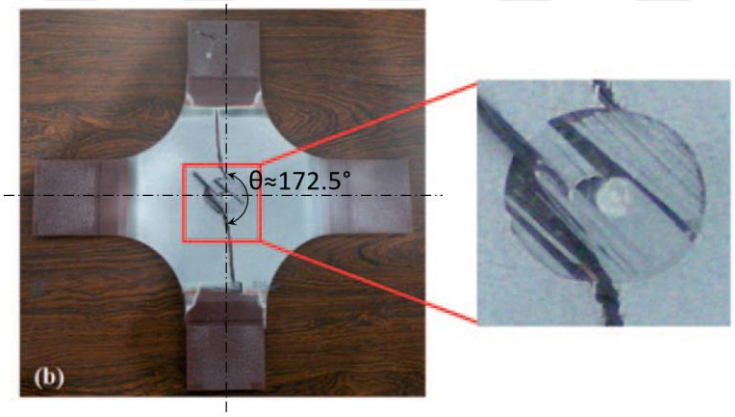	7.5º, 172.5º	0 (tension)
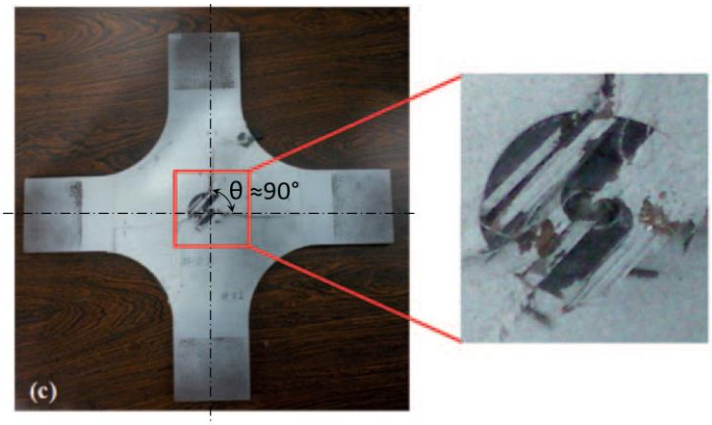	0º, 45º, -45º,90º	0 (tension) 45 (tension) -45 (tension) 90 (tension)

Figure 5.10. Failure pattern of the open hole cruciform specimen subjected to: (a) $\{1, -1\}$ (b) $\{1, 0\}$ (c) $\{1, 1\}$ loading ratios.

5.4 Summary and Conclusions

In this study, Extended Point Stress Method (EPSM) for the strength prediction of open-hole quasi-isotropic laminates subjected to uniaxial tension/compression, in-plane shear and combined loading conditions is introduced. EPSM is developed based on Tan's approach. In Tan's approach, once the strength reduction ratio is determined, notched laminate strength is found by the multiplication of the SR by the unnotched laminate strength. In the proposed EPSM, the unnotched laminate strength is calculated by the iterative Yamada-Sun plus Puck failure model. EPSM is compared with other analytical methods and open hole tension and compression tests with different materials, lay-ups, hole sizes and width-to-hole diameter ratios from the literature. In addition, to the author's knowledge bi-axial failure envelope is compared with experiments for the first time in the literature.

The main conclusions are as follows:

- When compared with Point Stress Method (PSM), Average Stress Method (ASM), Inherent Flaw Model (IFM), Cohesive Zone Model (CZM) and Finite Fracture Mechanics Model (FFM), EPSM and FFM are among the most accurate models.

- Good agreement of the failure envelope prediction of an OH composite laminate subjected to bi-axial loading using an analytical approach and test data is observed.

- EPSM provides advantages over FFM and other traditional analytical models as it is applicable to combined loading conditions, where as other models are currently applicable only to uniaxial loading. Moreover, since EPSM uses a ply-by-ply failure analysis scheme, information concerning the first-ply-fiber failure and fracture angle can be given, whereas this information cannot be provided by other analytical models.

CHAPTER 6

NUMERICAL APPROACH FOR THE PREDICTION OF SIZE EFFECTS ON OPEN HOLE TENSION LAMINATES

6.1 Introduction

Damage mechanisms and tensile strength of the carbon fiber reinforced open hole laminates differ based on the in-plane, sublaminate and ply scaling laminate configurations. Within the scope of this thesis, a numerical study on the strength prediction of quasi-isotropic sublaminate-scaled laminates with different hole sizes, which fail in brittle failure mode are presented. The objective of this work is to develop the most suitable progressive damage finite element modeling strategy for the prediction of the damage evolution as well as the strength of quasi-isotropic CFRP OHT laminates which fail in brittle failure mode. The results obtained from the fe simulations are compared with the experiments conducted by Camanho et al. [9]. As depicted in Figure 6.1 these experiments were conducted for IM7-8552 CFRP $[90/0/\pm45]_{3s}$ OHT specimen with five different hole diameters built using sublaminate-level scaling technique. The OHT specimen were prepared following the ASTM D-5766 [113] standard with a width-to-hole (w/d) ratio equal to 6. As seen in Figure 6.1, the OHT specimen fail in brittle failure mode with minimal delamination.

In the first stage of the study, two different Continuum Damage Models utilizing Puck and Hashin failure initiation criteria are implemented into open hole composite laminate finite element models composed of layered plane stress elements. In both models fracture energy-based degradation scheme is used. The results obtained from Puck and Hashin Continuum Damage Models are compared. In the second stage of the study, incorporating Hashin Continuum Damage Model five different fe models using layered plane stress elements, detached plies modeled using continuum shell

elements, continuum shell elements per ply with frictionless contact at ply interfaces, continuum shell elements per ply with perfect bonding at ply interfaces, continuum shell elements per ply with Cohesive Zone Model (CZM) at ply interfaces are prepared and their strength predictions are compared.

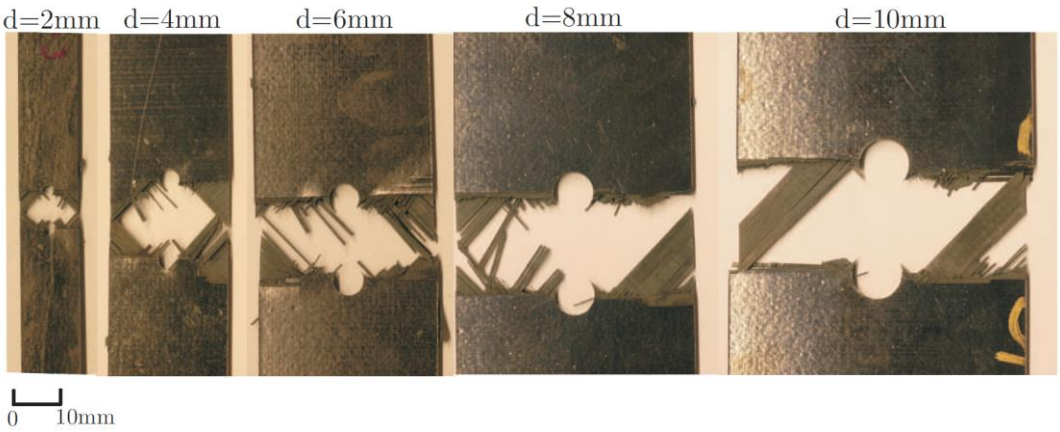

Figure 6.1. Brittle failure modes of the IM7-8552 OHT specimen with w/d=6 (Camanho et al. (2007) [9]).

6.2 Methodology

6.2.1 Intralaminar Damage Model

In this work, two different continuum damage models (CDMs), namely, Puck [84] and Hashin ([77]-[78]) CDMs are utilized to predict the strength and size effects in OHT carbon epoxy laminates. The continuum damage models differ in the failure criteria used for the damage onset. A fracture energy based bi-linear strain-stress softening degradation scheme for damage evolution is used in both models. An ABAQUS User-Material (UMAT) subroutine is developed for the implementation of Puck's damage model into the OHT laminate fe models. The other CDM utilizes the Hashin damage model implemented in ABAQUS [124]. In this work, quasi-isotropic IM7/8552 CFRP OHT laminates with a stacking sequence of $[90/0/\pm45]_{3s}$ and hole sizes 2, 4, 6, 8, and 10 mm reported in Camanho et al. (2007) [9] are used.

Mechanical and interlaminar properties of the CFRP material IM7/8552 are listed in Table 6.1 and Table 6.2, respectively.

In the Puck Continuum Damage Model, fiber failure is determined from the relations below:

Fiber tension ($\sigma_1 \geq 0$):

$$f_{E(FF)}^{T} = \frac{\sigma_1}{X_T} = 1 \tag{6.1}$$

Fiber compression ($\sigma_1 < 0$):

$$f_{E(FF)}^{C} = \frac{\sigma_1}{X_C} = 1 \tag{6.2}$$

where $f_{E(FF)}^{T}$ and $f_{E(FF)}^{C}$ are stress exposures for fiber failure under tension and compression loading. X_T and X_c represent the tensile and compressive lamina strengths in fiber direction, respectively.

Table 6.1 Mechanical Properties of the IM7/8552 lamina.

Material Data for IM7/8552 Lamina					
Longitudinal Modulus,	E_1	=	171420	(MPa)	[9]
Transverse Modulus,	E_2	=	9080	(MPa)	[9]
In-plane Shear Modulus,	G_{12}	=	5290	(MPa)	[9]
Major Poisson's Ratio,	υ_{12}	=	0.32	(MPa)	[9]
Longitudinal Tensile Strength,	X_t	=	2326.2	(MPa)	[9]
Longitudinal Compressive Strength,	X_c	=	1200.1	(MPa)	[9]
Transverse Tensile Strength,	Y_t	=	62.3	(MPa)	[9]
Transverse Compressive Strength,	Y_c	=	199.3	(MPa)	[9]
In-plane Shear Strength,	S	=	92.3	(MPa)	[9]
Longitudinal tensile fracture energy	G_1^+	=	81.5	(kJ/m^2)	[9]
Longitudinal comp. fracture energy	G_1^-	=	106.3	(kJ/m^2)	[9]
Transvese tensile fracture energy	G_2^+	=	0.28	(kJ/m^2)	[9]
Transverse comp. fracture energy	G_2^-	=	1.3	(kJ/m^2)	[23],[25]
Density	ρ	=	1590	(kg/m^3)	[125]

Table 6.2 Interlaminar Material Properties.

Material Data for IM7/8552					
Interface stiffness,	K_n	=	10^6	(N/mm^3)	[126]
Normal Strength	τ_n		62.3	(MPa)	[9],[114]
Shear Strength,	τ_s	=	92.3	(MPa)	[9],[114]
Normal Toughness,	G_n	=	0.28	(MPa)	[9],[114]
Shear Toughness,	G_s	=	0.79	(MPa)	[9],[114]
Mixed mode interaction parameter,	$\eta_{B\text{-}K}$	=	1.45	(MPa)	[127],[128]

Depending on the region of the failure envelope, three different inter-fiber-failure expressions are written:

Matrix tension (Mode A) ($\sigma_2 \geq 0$):

$$f^A_{E(IFF)} = \left[\left(\frac{\sigma_6}{S}\right)^2 + \left(1 - p^{(+)}_{\perp II}\frac{Y_T}{S}\right)^2\left(\frac{\sigma_2}{Y_T}\right)^2\right]^{1/2} + p^{(+)}_{\perp II}\frac{\sigma_2}{S} = 1 \tag{6.3}$$

Matrix compression (Mode B) ($\hat{\sigma}_2 < 0$ and $\left|\frac{\sigma_2}{\sigma_6}\right| \leq \frac{R^A_{\perp\perp}}{\tau_{21C}}$):

$$f^B_{E(IFF)} = \frac{1}{S}\left\{\left[(\sigma_6)^2 + \left(p^{(-)}_{\perp II}\sigma_2\right)^2\right]^{1/2} + p^{(-)}_{\perp II}\sigma_2\right\} = 1 \tag{6.4}$$

Matrix compression (Mode C) ($\hat{\sigma}_2 < 0$ and $\left|\frac{\sigma_2}{\sigma_6}\right| \geq \frac{R^A_{\perp\perp}}{\tau_{21C}}$):

$$f^C_{E(IFF)} = \left[\left(\frac{\sigma_6}{2(1+p^{(-)}_{\perp\perp})S}\right)^2 + \left(\frac{\sigma_2}{Y_C}\right)^2\right]\frac{Y_C}{(-\sigma_2)} = 1 \tag{6.5}$$

The transition point from failure mode B to C is denoted by the point $(R^A_{\perp\perp}, \tau_{21C})$ and calculated from the expressions below:

$$R^A_{\perp\perp} = \frac{S}{2p^{(-)}_{\perp\parallel}}\left[\sqrt{1 + 2p^{(-)}_{\perp\parallel}\frac{Y_c}{S}} - 1\right] \tag{6.6}$$

$$\tau_{21_c} = R_{\perp\parallel}\sqrt{1 + 2p^{(-)}_{\perp\perp}} \tag{6.7}$$

$$\text{and } p^{(-)}_{\perp\perp} = p^{(-)}_{\perp\parallel}\frac{R^A_{\perp\perp}}{S} \tag{6.8}$$

In the expressions (6.3) - (6.8) $p_{\perp II}^{(+)}, p_{\perp II}^{(-)}$ and $p_{\perp\perp}^{(-)}$ are the inclination parameters that control the shape of the failure envelope. Referring to [82] $p_{\perp II}^{(+)} = 0.35$ and $p_{\perp II}^{(-)} = 0.3$ are selected for the CFRP material. Y_t and Y_c are the tensile and compressive lamina strengths in transverse fiber direction. σ_6 and S denote shear stress and shear strength, respectively. If the value of stress exposure f_E exceeds 1, failure onset takes place.

Hashin CDM uses the same failure criteria as in the Puck CDM. However, different failure criteria for matrix damage initiation are used as written below:

Matrix tension ($\hat{\sigma}_{22} \geq 0$):

$$F_{mt} = \left(\frac{\hat{\sigma}_{22}}{Y_t}\right)^2 + \left(\frac{\hat{\sigma}_{12}}{S_L}\right)^2 = 1 \tag{6.9}$$

Matrix compression ($\hat{\sigma}_{22} < 0$):

$$F_{mc} = \left(\frac{\hat{\sigma}_{22}}{2S^T}\right)^2 + \left[\left(\frac{Y_C}{2S^T}\right)^2 - 1\right]\frac{\hat{\sigma}_{22}}{Y_c} + \left(\frac{\hat{\sigma}_{12}}{S_L}\right)^2 = 1 \tag{6.10}$$

In (6.9)-(6.10) S_L and S^T stand for the longitudinal and transverse lamina shear strengths.

In both Puck and Hashin CDM before damage onset, the material behavior is linearly elastic and the stiffness matrix of a 2D plane stress orthotropic material is used for the computations. If the material is damaged then degradation occurs and the material behavior is calculated from the relation below (ABAQUS, 2019) [124]:

$$\sigma = \mathbf{C_d}\epsilon \tag{6.11}$$

where σ is the stress tensor. C_d and ϵ represent the damaged elasticity matrix and the strain tensor, respectively. In this study, the damage model proposed by Matzenmiller et al. (1994) [94] is utilized to compute the components of the stiffness matrix due to degradation. The stiffness matrix including the damage variables are obtained from:

$$\mathbf{C_d} = \frac{1}{\mathrm{D}}\begin{bmatrix} (1-\mathrm{d_f})\mathrm{E_1} & (1-\mathrm{d_f})(1-\mathrm{d_m})\nu_{21}\mathrm{E_1} & 0 \\ (1-\mathrm{d_f})(1-\mathrm{d_m})\nu_{12}\mathrm{E_2} & (1-\mathrm{d_m})\mathrm{E_2} & 0 \\ 0 & 0 & \mathrm{D}(1-\mathrm{d_s})\mathrm{G_{12}} \end{bmatrix} \tag{6.12}$$

where $D = 1 - \left(1 - d_f\right)(1 - d_m)\nu_{12}\nu_{21}$. E_1, E_2 and G_{12} are the undamaged elasticity moduli. $\mathrm{d_f}$, $\mathrm{d_m}$ and d_s represent damage variables for fiber, matrix and shear failure modes. Shear damage variable $\mathrm{d_s}$ is calculated from the relation in (6.13) below. In relation (6.13), t and c subscripts damage stand for fiber/matrix damage variables under tension and compression, respectively.

$$\mathrm{d_s} = 1 - (1 - d_{ft})(1 - d_{fc})(1 - d_{mt})(1 - d_{mc}) \tag{6.13}$$

Damage variables for particular failure modes are calculated from the expression (6.14) below. In the relation below, δ_{eq}^{0} is the initial equivalent displacement at which the failure initiation for a particular failure mode begins ($\mathrm{d_I} = 0$) and δ_{eq}^{f} is the displacement at which the material is completely damaged at this failure mode ($\mathrm{d_I} = 1$). The graphical representation of this bi-linear damage evolution law is given in Figure 6.2.

$$\mathrm{d_I} = \frac{\delta_{I,eq}^{f}\left(\delta_{I,eq} - \delta_{I,eq}^{0}\right)}{\delta_{I,eq}\left(\delta_{I,eq}^{f} - \delta_{I,eq}^{0}\right)}, \qquad \delta_{I,eq}^{0} \le \delta_{I,eq} \le \delta_{I,eq}^{f}, \qquad \mathrm{I} \in \{ft, fc, mc, mt\} \tag{6.14}$$

The fracture energy dissipated during a particular damage mode is represented by the area under the bi-linear curve. The total fracture energy dissipation for a particular damage mode is calculated from the relation (6.15) below:

$$G_C = \frac{1}{2}\sigma_{eq}^{0}\varepsilon_{eq}^{f}L_c \tag{6.15}$$

where σ_{eq}^{0} is the equivalent stress at damage onset, ε_{eq}^{f} is the equivalent strain at final failure ($\mathrm{d_I} = 0$) and L_c is the characteristic element length. The relation for calculating the characteristic length of a square element is given in (3.99).

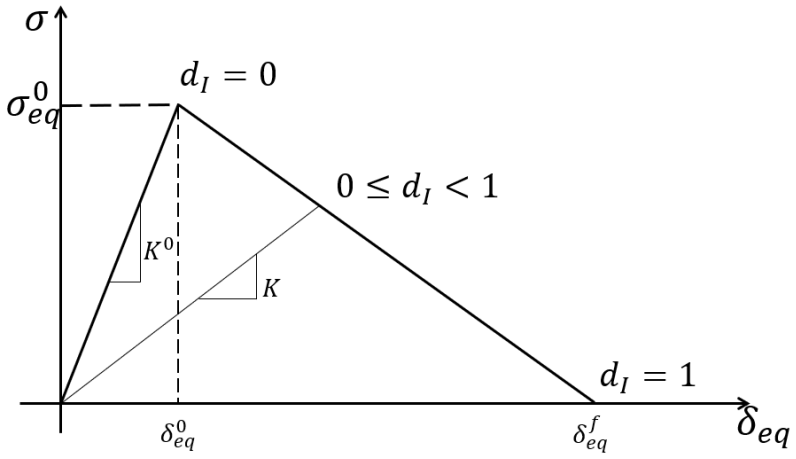

Figure 6.2. Bi-linear damage evolution law.

In order to prevent snapback of the constitutive softening branch of each damage mode, the maximum characteristic element length is calculated from the expression (6.16) below [133]:

$$L_{max}^{*} = \frac{2E_M G_M}{X_M^2}, \qquad M = 1+,1-,2+,2-,6 \tag{6.16}$$

In expression above E_M, G_M and X_M are the elasticity modulus, fracture toughness and lamina strength for different damage modes.

Accurate analysis of composite delamination requires the minimum number of cohesive elements within the softening region, i.e. cohesive zone in front of the crack tip ([129] - [131]). As stated in [12] and [117] in general the in-plane tension loading in quasi-isotropic OHT laminates leads to delamination failure, which is mainly driven by shear. For this reason, for the calculation of the cohesive zone length only the characteristic cohesive zone length for Mode II given in [131] is used:

$$l_{ch} = 0.5 \times \min(l_{ch,II}, l_{ch,slender,II}) \tag{6.17}$$

where,

$$l_{ch,II} = E'_{II} \frac{G_{IIc}}{(\sigma_{II,max})^2} \tag{6.18}$$

$$l_{ch,slender,II} = \sqrt{(E'_{II,slender} \frac{G_{IIc}}{(\sigma_{II,max})^2})h} \tag{6.19}$$

In expressions (6.17)-(6.19), $l_{ch,II}$ and $l_{ch,slender,II}$ are the mode I and II characteristic lengths for infinite bodies and slender bodies, respectively. E'_{II} stands for the mode II equivalent elastic modulus for orthotropic materials. The procedure for calculating E'_{II} is provided in ([131], [132]). $\sigma_{II,max}$ is the interfacial strength under shear loading and G_{IIc} is the mode II critical fracture energy. h represents the single ply thickness. According to [131] two or more elements are recommended in the cohesive length for accurate delamination modeling.

6.2.2 Interlaminar Damage Model

The delamination failure simulation between ply interfaces is carried out by means of the cohesive elements (COH3D8) available in ABAQUS ([102], [124]) and accounting for geometric and material nonlinearity. To model the progressive damage of adhesive interfaces, the predefined cohesive zone model in ABAQUS (2019) ([102], [124]) is utilized. According to the bilinear traction-separation law used in ABAQUS, traction-separation behavior is assumed as linear elastic up to damage initiation followed by the damage evolution which is a linear softening response. The damage is assumed to initiate when the quadratic nominal stress criterion given in eq. (6.20) is met. In this equation t_n, t_s and t_t are in-plane normal, in-plane shear, and out-of-plane shear tractions, respectively. Also, t_n^0, t_s^0, t_t^0 values are corresponding maximum allowable values for interface stresses.

$$\left(\frac{< t_n >}{t_n^0}\right)^2 + \left(\frac{t_s}{t_s^0}\right)^2 + \left(\frac{t_t}{t_t^0}\right)^2 = 1 \tag{6.20}$$

Since the compressive stresses on the crack surfaces are assumed to have no contribution to the damage mechanisms, Macaulay operator is utilized on the opening mode tractions to differentiate tensile and compressive modes in the initiation criterion.

At the instance when Mode I, Mode II and Mode III are concurrently observed, the combined effect of mixed modes should be calculated correspondingly. Considering the nonlinearity and complexity of OHT laminate problem., the mode-mixity is taken into account while modelling the cohesive zone. After the cohesive damage is initiated, the propagation of damage in mixed modes are modelled by using the Benzeggagh-Kenane [107] criterion given in eq. (6.21). When the calculated G_{equ} value exceeds the fracture toughness, the damage propagation will be observed. The damage will be simulated via assigning linear softening response to damaged elements.

$$G_{equ} = G_{Ic} + (G_{IIc} - G_{Ic}) \left(\frac{G_{II} + G_{III}}{G_I + G_{II} + G_{III}}\right)^{\eta} \tag{6.21}$$

6.2.3 Finite Element Model and Boundary Conditions

Boundary conditions of the fe models used for the IM7-8552 CFRP $[90/0/\pm45]_{3s}$ OHT laminates with different hole sizes are depicted in Figure 6.3. The OHT laminates are meshed with ABAQUS four-node layered S4 plane stress elements. As seen from the figure all the translational (U_x, U_y and U_z) and rotational degrees (UR_x, UR_y and UR_z) of freedom of the OHT laminate are fixed at one end. Since the OHT lay-ups are symmetric, plane symmetry conditions are applied with respect to the z-axis. Load application is done by applying constant displacement at the other end

incrementally. ABAQUS Implicit solver is used for the simulations and failure load is determined by measuring the reaction force at the fixed end.

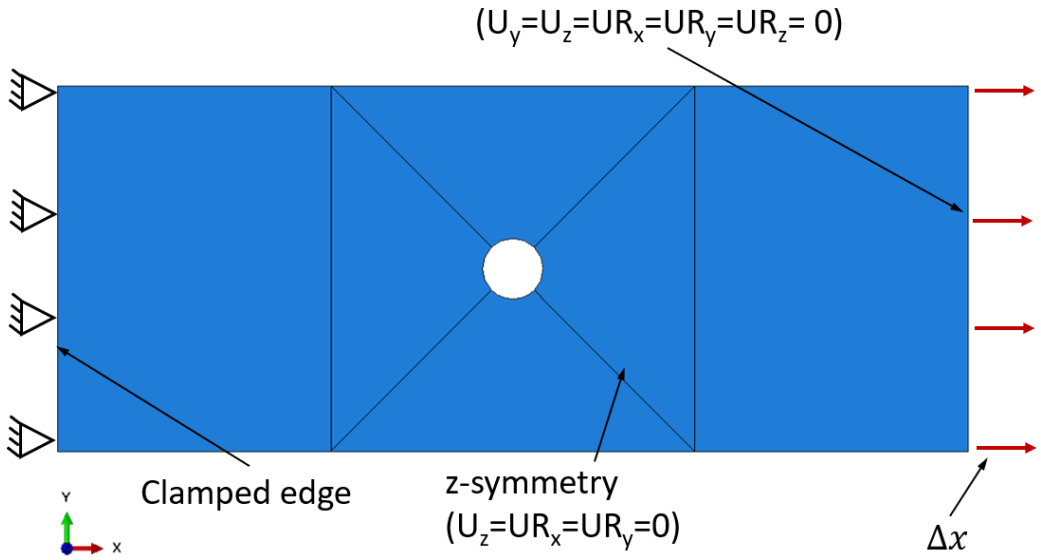

Figure 6.3. Boundary conditions of the OHT laminate fe model.

In order to investigate the influence of different mesh patterns on the OHT laminate strength, OHT laminate FE Models with different mesh patterns are built. In Figure 6.4 OHT laminate finite element models with a hole diameter of 6 mm using structured and nonstructured meshing techniques are depicted. When structured mesh is used, mesh density is kept fine in the stress concentration regions in the vicinity of the hole and a total number of 4032 nodes are needed to build up the fe model. On the other hand, for the fe model with the non-structured mesh, fine mesh density is kept fine over a much larger area and a total number of 14103 nodes are needed in the current study. Observation of the damage propagation in the vicinity of the hole is sufficient for predicting the OHT laminate strength. Hence in the current study, utilizing structured mesh technique was advantageous in terms of computation time compared to the non-structured mesh technique.

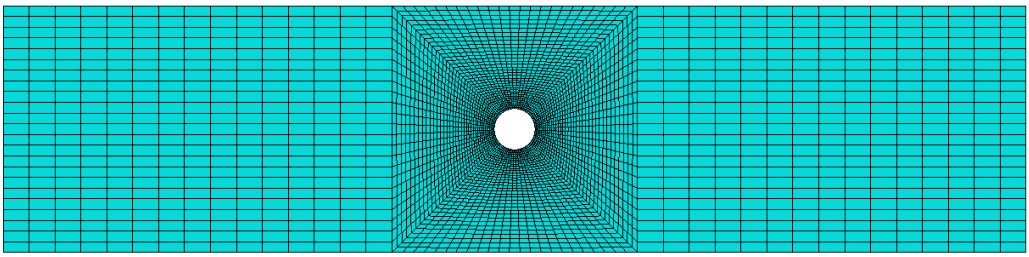

(a)

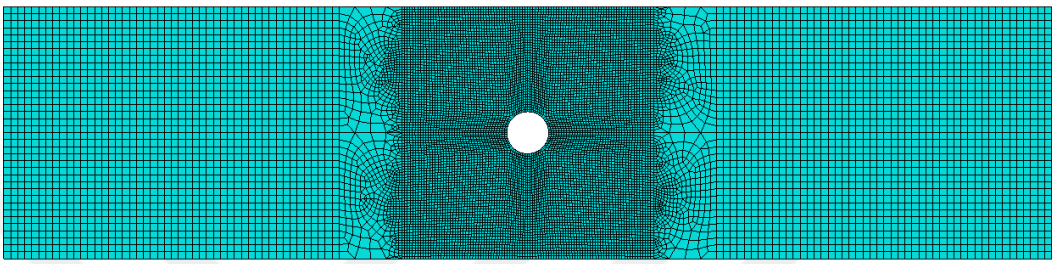

(b)

Figure 6.4. OHT finite element models (hole diameter = 6 mm) with different mesh patterns (a) structured mesh (total number of nodes=4032) (b) non-structured mesh (total number of nodes=14103).

6.2.4 Mesh Convergence Study

Fracture energy-based degradation scheme alleviates mesh dependency, but does not eliminate it completely (Lapcyzk and Hurtado, 2007) [93]. According to the expression (6.16) the maximum characteristic element length is calculated as 0.6 mm. In order to determine the suitable mesh density, OHT laminate fe models with different minimum element sizes of 0.2, 0.25, 0.3 and 0.5 mm in the neighborhood of the hole are built. The results of the mesh convergence study and the FE Models with different element size are shown in Figure 6.5 and Figure 6.6, respectively. As seen in Figure 6.5, using element sizes 0.5, 0.3, 0.25 and 0.2 mm, failure stresses of 545, 547, 555 and 548 MPa are obtained correspondingly. As the element size is changed from 0.25 mm to 0.2 mm, the change in stress level is 1% and mesh convergence is considered to be achieved. It is of interest to observe the damage progression in the hole neighborhood. Hence, element size should be small enough

to capture the damage pattern correctly in the regions near the hole. To meet this requirement and reasonable computation time an element length of 0.25 mm is deemed appropriate for the OHT laminate with a hole diameter of 6 mm. Using a similar, approach mesh densities for the remaining OHT laminates are determined.

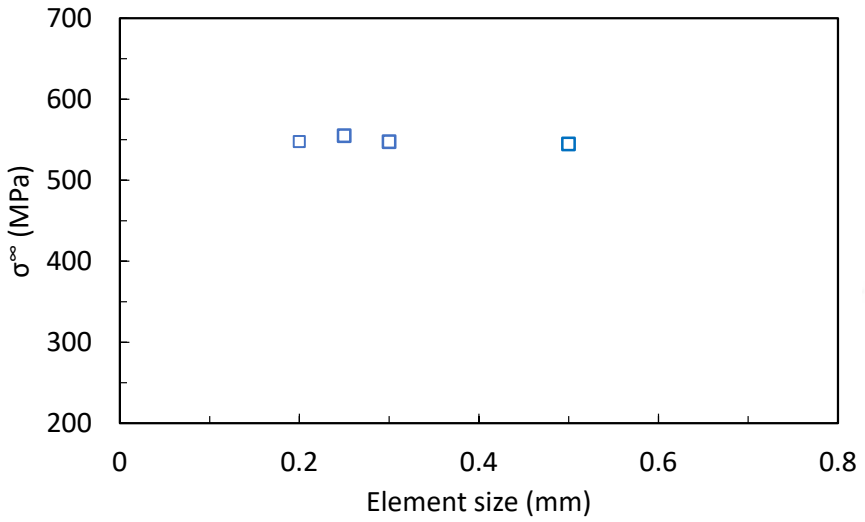

Figure 6.5. Influence of the mesh density on the strength of the IM7-8552 CFRP $[90/0/\pm45]_{3s}$ OHT specimen with a hole diameter of 6 mm.

From eqs. (6.17) - (6.19) given in the methodology section, the characteristic cohesive zone length is calculated as 0.405 mm for failure mode II. Referring to [131] a minimum of 2 elements are required in the cohesive zone, hence a maximum cohesive element length of 0.2 mm is calculated for the delamination area.

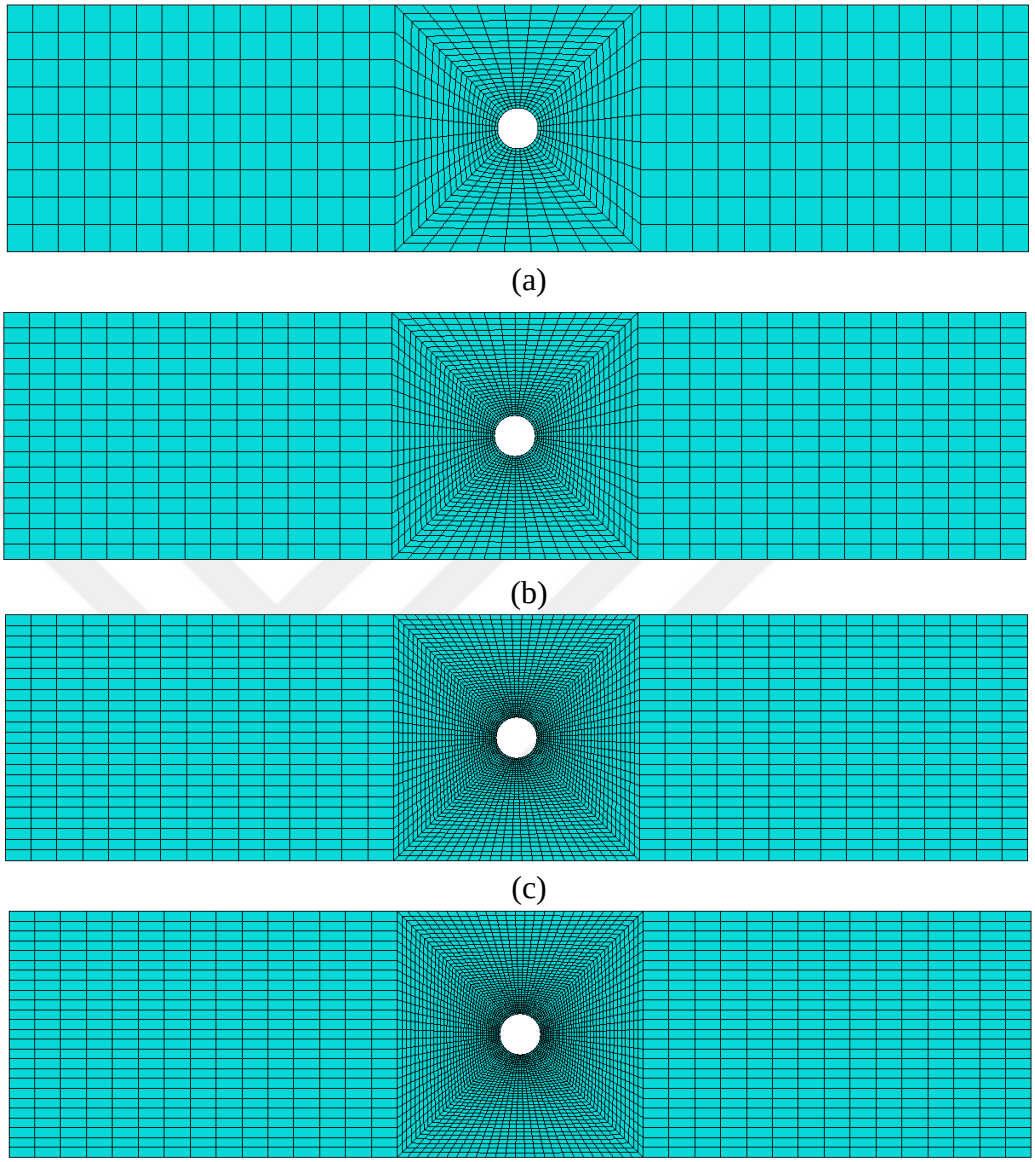

Figure 6.6. OHT finite element models (hole diameter = 6 mm) created using different mesh densities: (a) total number of 1092 nodes (element size=0.5 mm in the vicinity of the hole) (b) total number of 2366 nodes (element size=0.3 mm in the vicinity of the hole) (c) total number of 4032 nodes (element size=0.25 mm in the vicinity of the hole) (d) total number of 4580 nodes (element size=0.20 mm in the vicinity of the hole).

6.2.5 Validation Study of the ABAQUS User Subroutine (Puck Continuum Damage Model)

Puck Continuum Damage Model is implemented into an ABAQUS User Subroutine (UMAT). In this subsection, the validation study of the ABAQUS UMAT utilizing ABAQUS built-in model is presented. In Figure 6.7 FE model of the IM7-8552 UD 0-degree lamina is represented with a unit cell. From eq. (3.111) critical finite element size is calculated as 5.16, 1.34 and 1.3 mm for fiber tension, fiber compression and matrix tension fracture modes, respectively. Hence an element edge length of the unit cell is chosen as 1 mm for these fracture modes. Regarding the matrix compression fracture mode, the critical finite element length is calculated as 0.6. Consequently, an element edge length of 0.3 mm is selected for the matrix compression fracture mode.

In Figure 6.7, the unit cell and the boundary conditions under uniaxial tension loading in fiber direction is shown. The unit cell is meshed with a single with four-node reduced integration S4R plane stress element. As seen from the figure the displacement degrees of freedom of the unit cell on one of its edges is fixed, while loading is given as a displacement of 0.125 mm in fiber direction incrementally. On the fixed edge all the translational degrees of freedom of the one node are fixed. For the other node of the fixed edge only the translation degree of freedom in loading direction is fixed, so that the displacement degree of freedom perpendicular to the loading direction is kept free and contraction of the unit cell due to Poisson effect is not restricted. The strain-stress response of the IM7-8552 UD (0-degree) lamina under uniaxial tension loading is depicted in Figure 6.8. It is observed that there is a good agreement between ABAQUS UMAT and ABAQUS built-in model.

Following the same approach for the validation of the IM7-8552 UD (0-degree) lamina subjected to uniaxial tension loading, unit cell fe models of the 0-degree lamina under compression, 90-degree lamina subjected to tension/compression are are built (See Figure 6.9, Figure 6.11 and Figure 6.13). Stress-strain responses are plotted and compared with the results obtained from the ABAQUS built-in CDM

model (See Figure 6.10, Figure 6.12 and Figure 6.14). As seen from the figures, the results obtained from the ABAQUS UMAT and ABAQUS built-in agree well. This leads to the conclusion that ABAQUS UMAT is validated for the chosen load cases.

We further note that, a convergence problem is encountered when the stress-strain response of the IM7-8552 UD (0-degree) lamina under uniaxial compression loading is plotted. In case of certain static/quasi-static nonlinear problems involving contact/material nonlinearities causing convergence problems, ABAQUS Explicit solver has proven to be advantageous over the ABAQUS Implicit solver ([23], [39]). In order to overcome the convergence difficulty encountered with the implicit solver, explicit solver can be used for this load case.

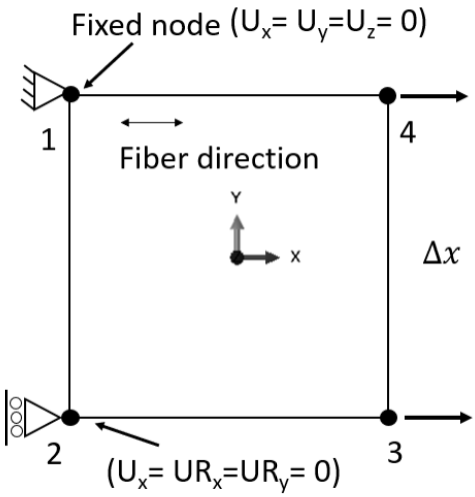

Figure 6.7. FE Model of unit cell indicating boundary conditions for uniaxial tension in fiber direction.

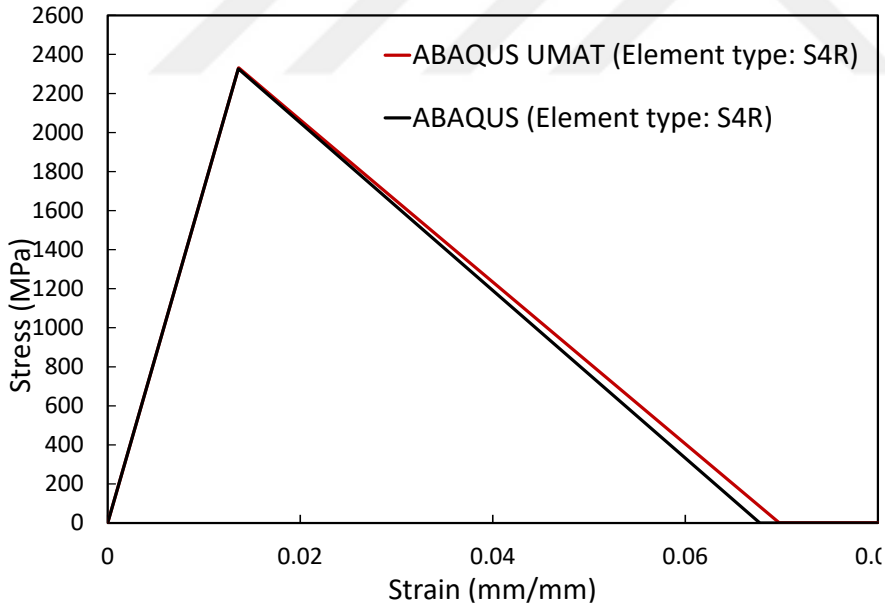

Figure 6.8. Stress-strain response for the IM7-8552 UD (0-degree) lamina under uniaxial tension.

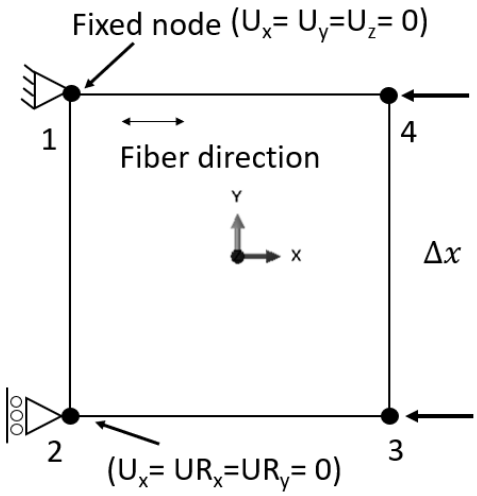

Figure 6.9. FE Model of unit cell indicating loads and boundary conditions for uniaxial compressions in fiber direction.

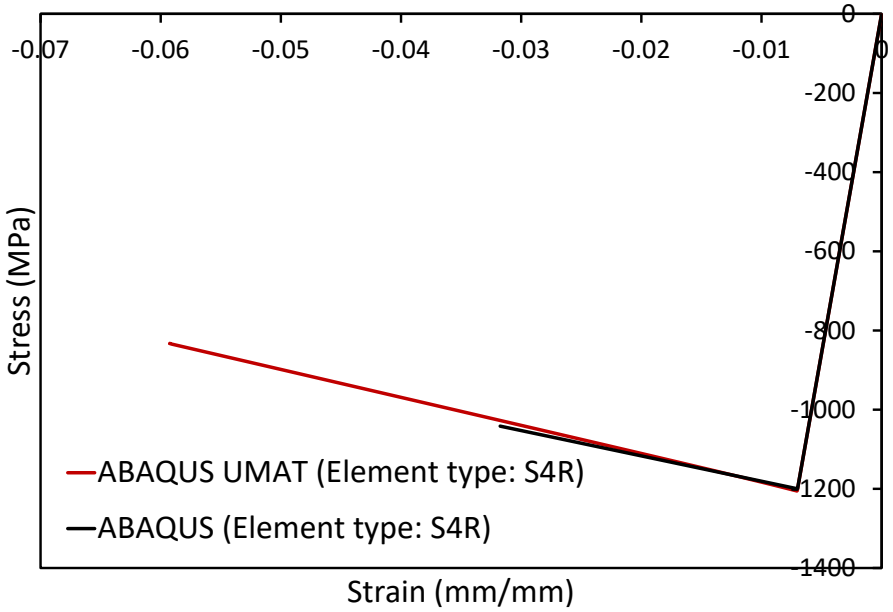

Figure 6.10. Stress-strain response for the IM7-8552 UD (0-degree) lamina under uniaxial compression.

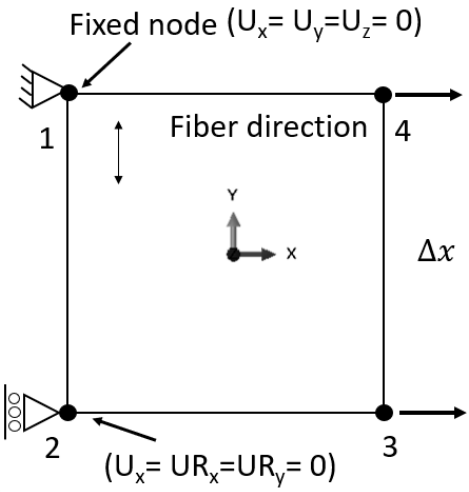

Figure 6.11. FE Model of unit cell indicating loads and boundary conditions for uniaxial tension in matrix direction.

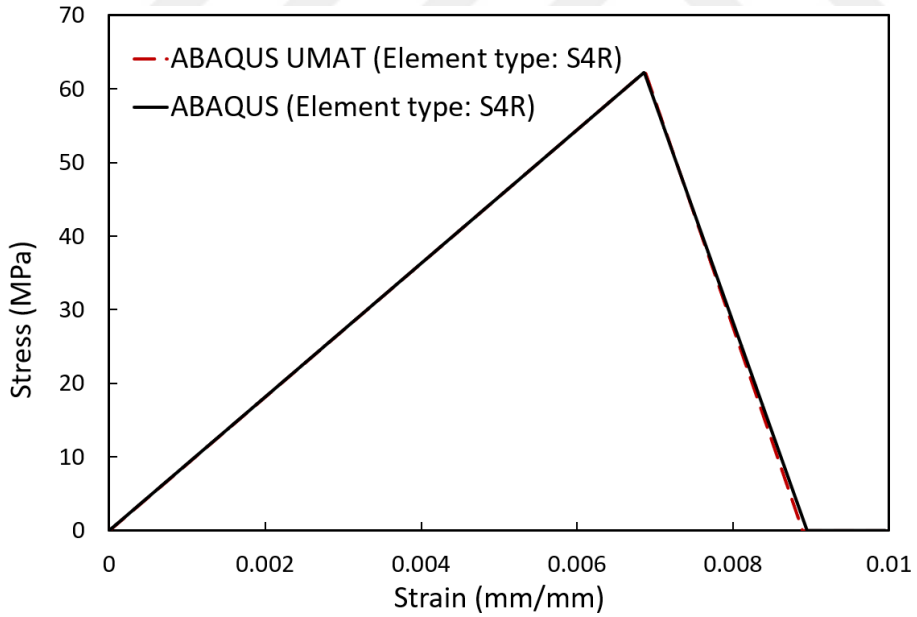

Figure 6.12. Stress-strain response for the IM7-8552 UD (90-degree) lamina under uniaxial tension.

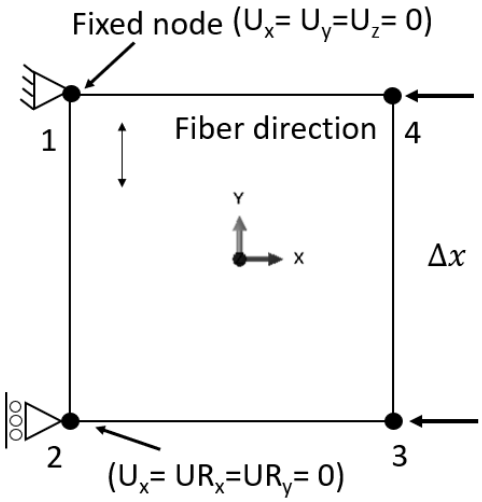

Figure 6.13. FE Model of unit cell indicating loads and boundary conditions for uniaxial compression in matrix direction.

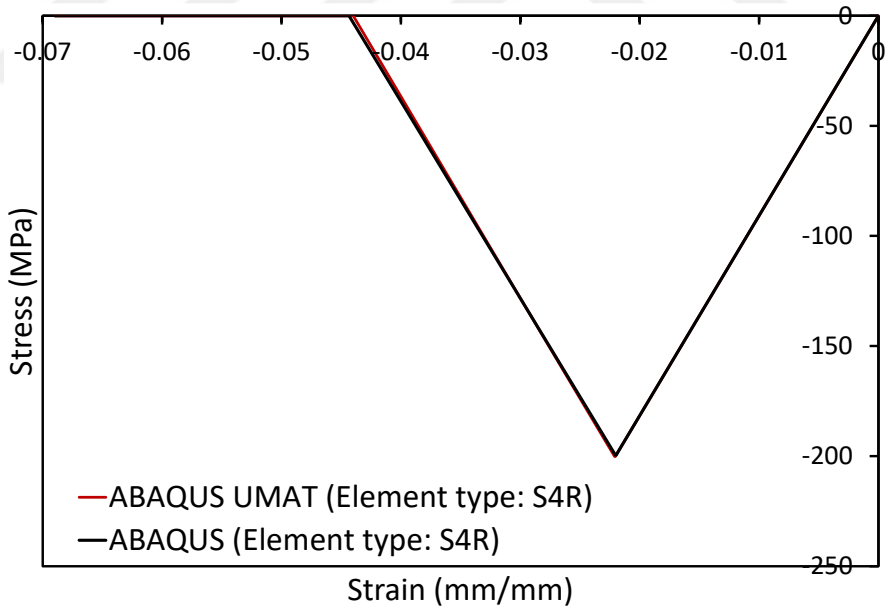

Figure 6.14. Stress-strain response for the IM7-8552 UD (90-degree) lamina under uniaxial tension.

6.3 Results

As explained in the methodology section, two different intralaminar damage models, a Continuum Damage Model (CDM) which use Puck failure criteria for the damage initiation with bilinear fracture energy based degradation scheme and a second CDM which use Hashin failure criteria for damage initiation with bilinear fracture energy based degradation scheme are utilized for predicting the OHT strength of composite laminates. The results obtained from the fe simulations are compared with the experiments conducted by Camanho et al. (2007) [9]. For sublaminate level scaled laminates used in the experiments delamination is not the main damage mechanism Green et al., 2007 [116]. In accordance with the observations in Green et al., 2007 [116], the sublaminate level scaled OHT specimen used in this study fail in a brittle failure mode with minimal delamination as seen in Figure 6.1. For this reason, as the first fe modeling approach layered plane stress elements without interface failure model were used for the OHT laminate strength predictions as in Camanho et al. (2007) [9]. As the second approach, fe models using continuum shell elements per ply and interface failure model based on cohesive elements is built. The results of different OHT laminate fe modeling strategies are discussed in the coming subsections.

6.3.1 FE Modeling Approach Using Classical Lamination Theory

In Figure 6.15, a plot of the applied remote stress versus the longitudinal displacement obtained from the progressive failure analysis of the IM7-8552 CFRP $[90/0/\pm45]_{3s}$ OHT specimens with hole sizes, 2, 6 and 10 mm are shown. For the progressive failure analysis Puck failure criteria are used for the failure initiation and damage evolution is computed based on a bilinear fracture energy-based degradation scheme. The remote stress is defined using the reaction force at the fixed edge obtained from the fe simulation divided by the cross-sectional area of the specimen without the hole. OHT laminate strength predictions are obtained from the remote

stresses at the maximum stress where the stress suddenly drops in Figure 6.15. As the OHT laminate hole size increases, the laminate strength decreases. Since the width-to-hole diameter is kept constant at 6 mm for all OHT specimen, this result shows size effect.

The strength predictions of the notched specimen as a function of different hole diameters are plotted in Figure 6.16 and listed in Table 6.3. The results show the comparison of the numerical predictions from Puck's damage model (ABAQUS UMAT) and Hashin's damage model (ABAQUS built-in CDM) with the experimental results reported in Camanho et al. (2007)[9]. Although the Finite Element Models incorporating ABAQUS built-in CDM prepared using structured and nonstructured meshes predict the decreasing trend in notched strengths with increasing hole diameters, they overestimate OHT laminate strengths. The same observation is done for the continuum damage model based on Puck's failure criteria (ABAQUS UMAT). It is noted that there is no significant difference of OHT laminate strength predictions when ABAQUS CDM based on Hashin failure criteria using structured and nonstructured discretization techniques. When the continuum damage model utilizing Puck's initiation criteria is compared with the continuum damage model utilizing Hashin failure criteria, the strength predictions are close. For the hole size of 2 mm the deviation between the models is less than 7.4 %, and for hole sizes 6 and 10 mm the deviation is found to be less than 5.2%. The minimum error compared to experiments is obtained for the ABAQUS CDM incorporating Hashin failure criteria and it is computed for the OHT laminate with a hole diameter of 2 mm as 16.8 %. The maximum error obtained using Hashin damage model is the for the OHT laminare with a hole diameter of 10 mm as 38.4%. Puck's damage model implemented using ABAQUS UMAT subroutine is able to predict the OHT strength of the OHT with a hole diameter of 2 mm within a minimum error of 24.5% and a maximum error of 43.6% for the OHT laminate with a hole diameter of 10 mm.

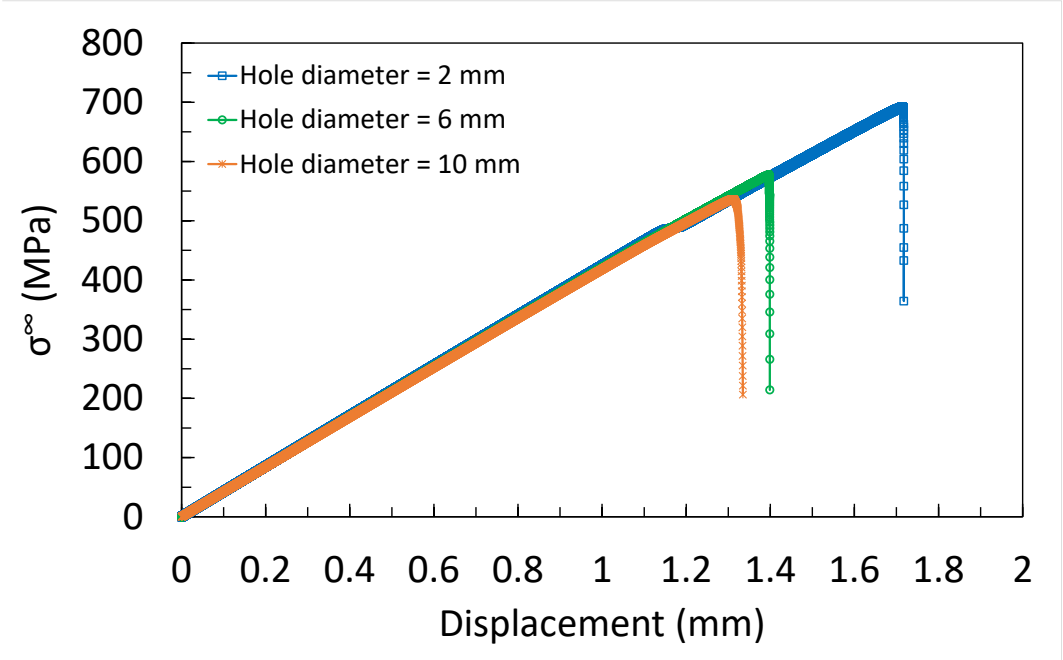

Figure 6.15. Relation between the applied stress and the longitudinal displacement during the numerical simulation of the IM7-8552 CFRP $[90/0/\pm45]_{3s}$ OHT specimens with different hole sizes using ABAQUS UMAT.

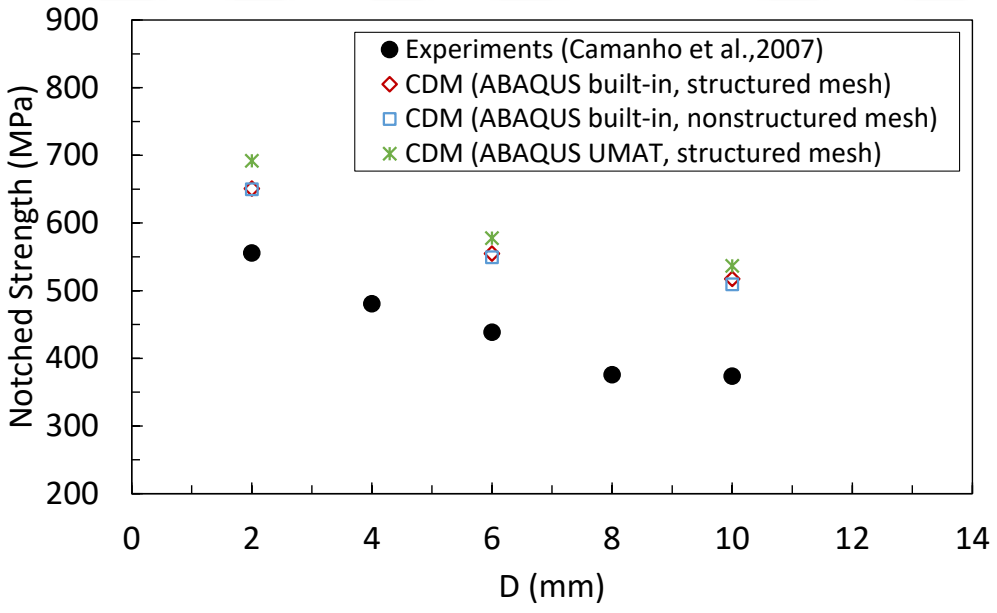

Figure 6.16. Strength predictions of the IM7-8552 CFRP $[90/0/\pm45]_{3s}$ OHT specimens with varying hole sizes.

Table 6.3 Comparison between predictions and experiments for the IM7-8552 CFRP $[90/0/45/-45]_{3s}$ lay-up.

D (mm)	$\bar{\sigma}^{\infty}$ (Exp.) (MPa) (Camanho,2007)	$\bar{\sigma}^{\infty}$(CDM) (MPa) (ABAQUS UMAT, structured mesh)	Error (%)	$\bar{\sigma}^{\infty}$(CDM) (MPa) (ABAQUS built-in, structured mesh)	Error (%)	$\bar{\sigma}^{\infty}$(CDM) (MPa) (ABAQUS built-in, non-structured mesh)	Error (%)
2	555.7	692.0	+24.5	650.9	+17.1	649.0	+16.9
6	438.7	577.7	+31.7	554.8	+26.5	549.0	+25.2
10	373.7	536.6	+43.6	517.3	+38.4	509.4	+36.3

According to the experimental results in [9] IM7 8552 OHT laminates with $[90/0/\pm45]_{3s}$ layup fail in a brittle manner with minimum delamination. Hence delamination is not modeled in the Finite Element Models. Since fiber failure is the main damage mode, fiber damage progressions for the OHT laminates are investigated in more detail. At the peak load, where load drops are seen, fiber damage extension plots obtained using Puck's and Hashin's damage models for the OHT specimens with different hole diameters are depicted in Figure 6.18 and Figure 6.19, respectively. In all OHT simulations fiber damage is located at the hole vicinity and evolves perpendicular to the hole at the onset of failures. This damage evolution pattern is consistent with the findings reported in [9]. The contour levels for the fiber tension damage variable denoted by SDV6 (ABAQUS UMAT) and DAMAGEFT (ABAQUS 2020)[124] is kept the same, so that fiber damage propagations for the three different hole sizes can be compared easily. It is observed that for the smaller hole sizes damage evolution is larger at maximum load. As depicted in Figure 6.17, this damage development can be caused by the stress concentrations, which are much more localized for smaller radius holes [15]. At this point one would expect that the OHT laminate with the larger hole diameter to have lower strength compared to the laminate with the smaller hole. Due to the damage evolution in the vicinity of the hole subcritical damage region increases for the

smaller hole diameter, which redistributes the stress concentration and leads to more stress relief for smaller holes [116]. As a consequence, residual strength is found to be higher for OHT laminates with smaller holes. When fiber damage extension plots obtained from Puck's and Hashin's damage models are compared a very similar damage extension for the OHT laminates with hole sizes, 2, 6, and 10 mm are observed(See Figure 6.18 and Figure 6.19).

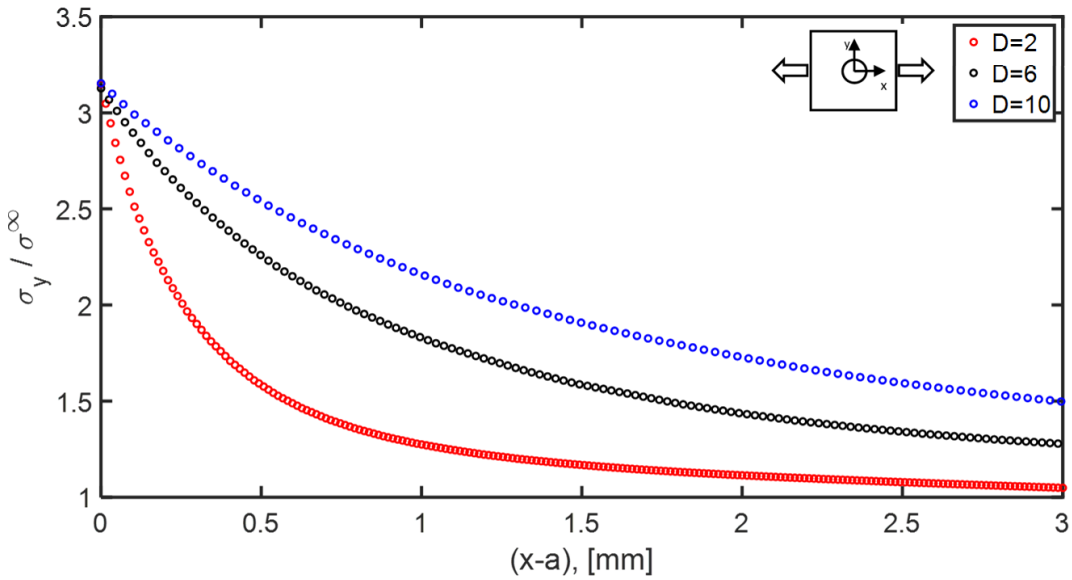

Figure 6.17. Average stress distribution for different hole sizes (D=2,6,10) in IM7-8552 CFRP IM7-8552 CFRP $[90/0/\pm45]_{3s}$ OHT specimens in the elastic region before load drop.

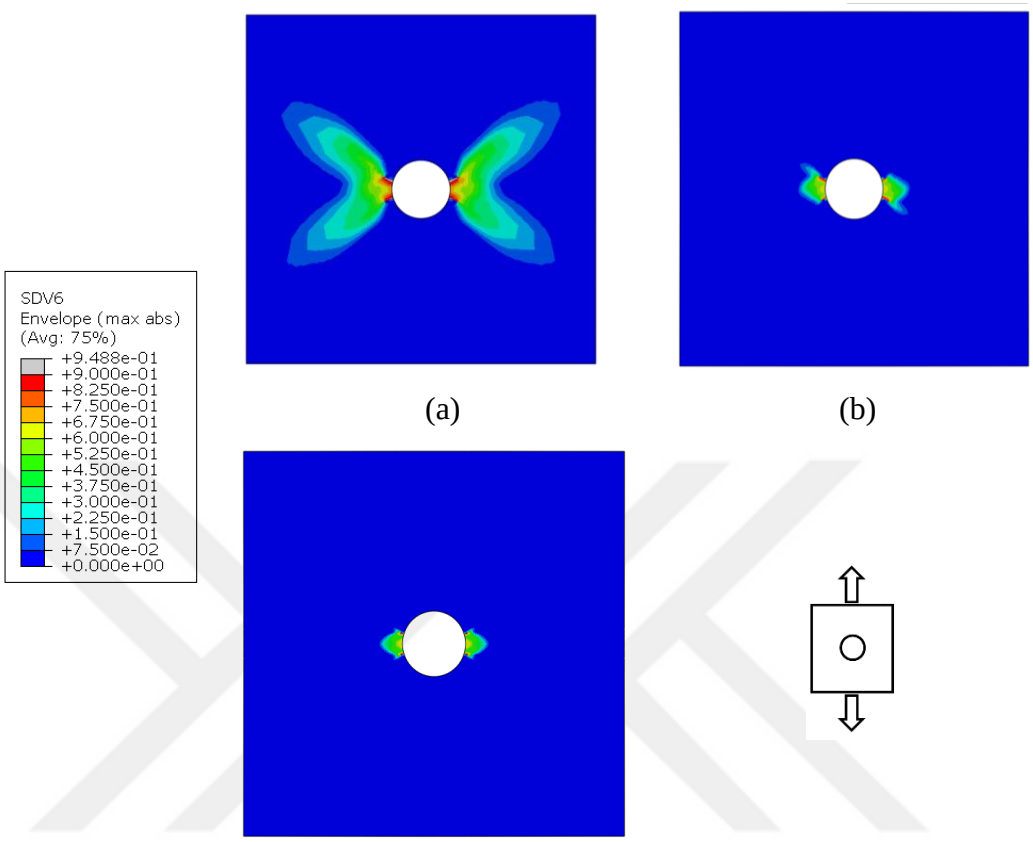

Figure 6.18. Fiber tensile damage evolution at load drop of the IM7-8552 CFRP $[90/0/\pm45]_{3s}$ OHT specimens with hole sizes (a) 2 mm (b) 6 mm (c) 10 mm using Puck's damage model (ABAQUS UMAT).

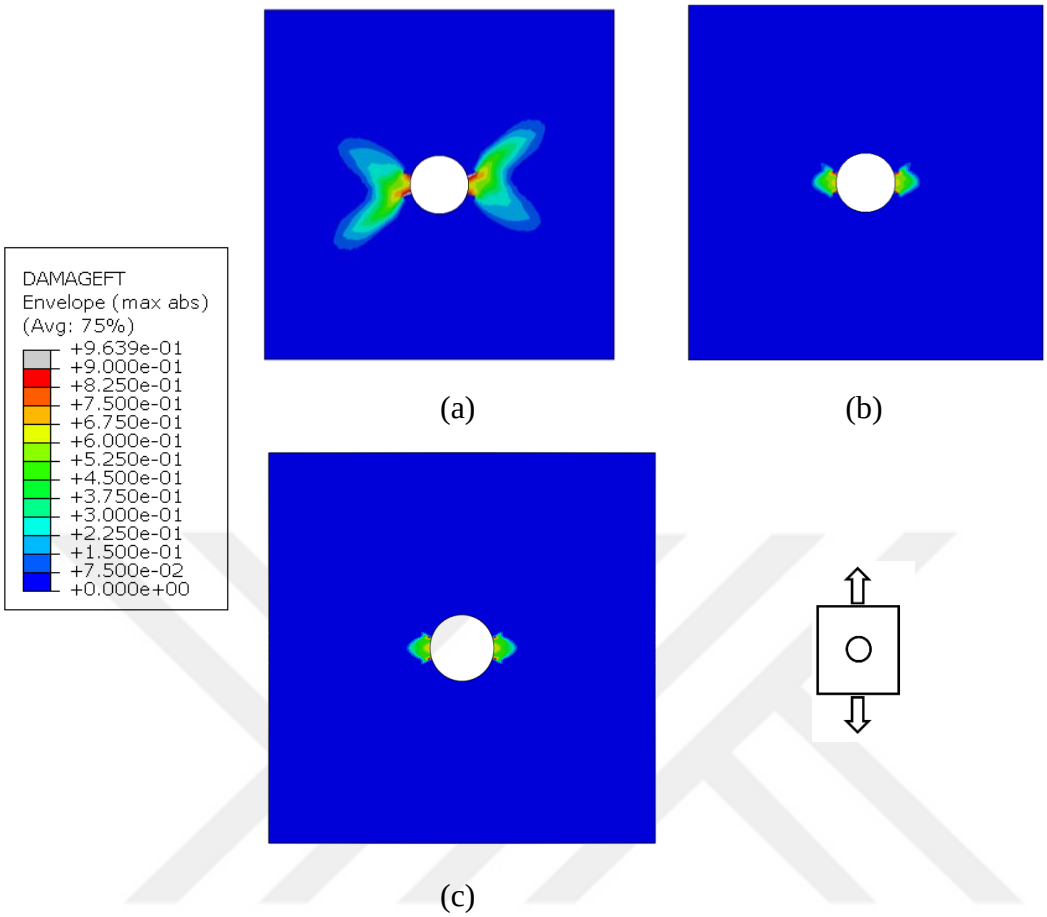

Figure 6.19. Fiber tensile damage evolution at load drop of the IM7-8552 CFRP $[90/0/\pm45]_{3s}$ OHT specimens with hole sizes (a) 2 mm (b) 4 mm (c) 6 mm (d) 10 mm using Hashin damage model (ABAQUS built-in damage model).

Fiber tensile damage evolution after load drop for the CFRP laminate with a hole diameter of 6 mm using structured and non-structured mesh is depicted in Figure 6.20. It is noted that fiber damage initiation perpendicular to the loading direction is captured using both meshing techniques. As the fiber fracture plane propagates towards the laminate edges, it follows the element edges. Therefore, the fracture plane is inclined at a radial angle for the structured mesh, whereas it is perpendicular to the loading direction for the non-structured, which is in accordance with the experiments in [9]. However, as mentioned in the preceding paragraphs both structured and non-structured meshes lead to an overestimation of OHT laminate strength values. Since in the current study, less number of elements were used for

the structured mesh, computation time needed for the structured mesh is considerably less compared to the non-structured mesh. Consequently, as proposed in [134] different fe modeling approaches implementing structured mesh are presented in the next subsection.

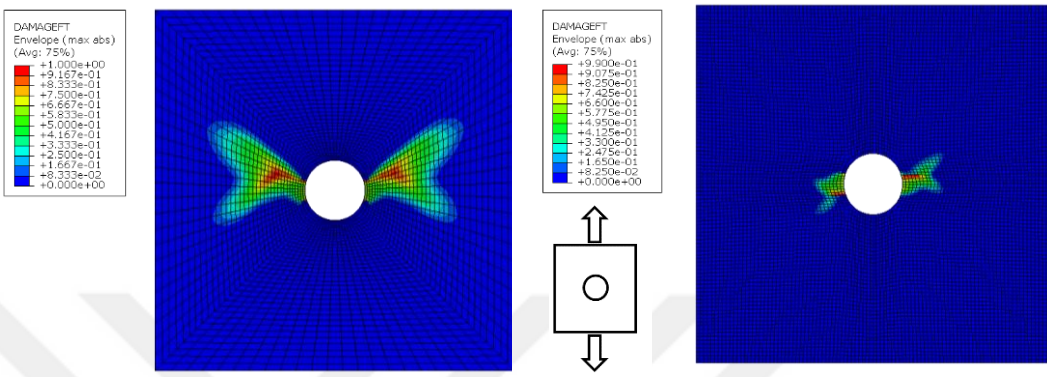

(a) (b)

Figure 6.20. Fiber tensile damage evolution shortly after load drop for the IM7-8552 CFRP $[90/0/\pm45]_{3s}$ OHT specimen with a hole diameter of 6 mm (a) structured mesh (b) non-structured mesh.

6.3.2 FE Modeling Approach Using Continuum Shell Elements and Interface Model

In the preceding subsection it is shown that, when Puck/Hashin continuum damage models are implemented into FE Models composed of layered plane stress elements, OHT laminate strength predictions are overestimated by more than 17%. In this subsection different FE Modeling strategies utilizing continuum shell in combination with/without cohesive elements are investigated, so that better OHT strength predictions as well as failure patterns of the OHT laminates can be achieved.

6.3.2.1 Continuum Shell with Perfect Bonding

In Figure 6.21, FE Modeling approach for the IM7-8552 laminate with a hole diameter of 2 mm using continuum shell elements with reduced integration (SC8R) are displayed. As seen in the figure, since the fe models composed of continuum

shell elements are computationally expensive, continuum damage models are implemented only in the regions where damage initiation and propagation occur. Remaining region of the fe models are computed using an elastic model. As the first modeling approach using continuum shell elements, perfect bonding is created by using coincident nodes between the continuum shell elements which represent each ply. The same boundary conditions which are applied to the OHT laminate fe models built with plane stress are applied to the OHT laminates composed of continuum shell elements (See Figure 6.3). The comparison of the continuum shell elements using perfect bonding at ply interfaces with layered plane stress elements is summarized in Figure 6.22 for OHT laminates with hole diameters 2 and 6. Using continuum shell elements (SC8R) with perfect bonding at ply interfaces increases the overestimation of the OHT laminate strength predictions compared to the plane stress elements(S4R). For the OHT laminate with a hole diameter of 2, continuum shell elements lead to a further increase in strength predictions from 17.1% to 27.3%. Likewise, the OHT strength predictions for the OHT laminate with a hole diameter of 6 increase from 26.5% to 35.8%, when continuum shell elements are used.

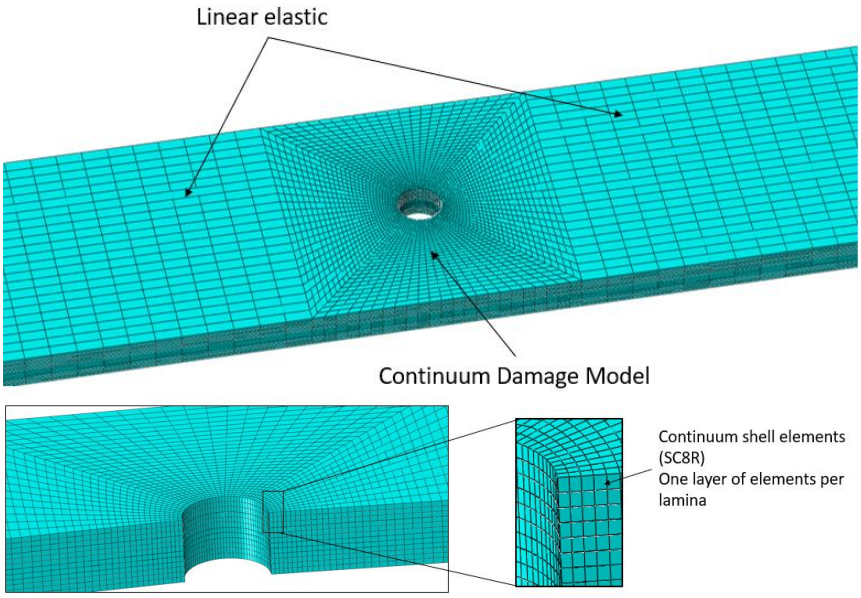

Figure 6.21. FE modeling approach of the IM7-8552 CFRP OHT laminate with a hole diameter of 2 mm using continuum shell elements with perfect bonding at ply interfaces.

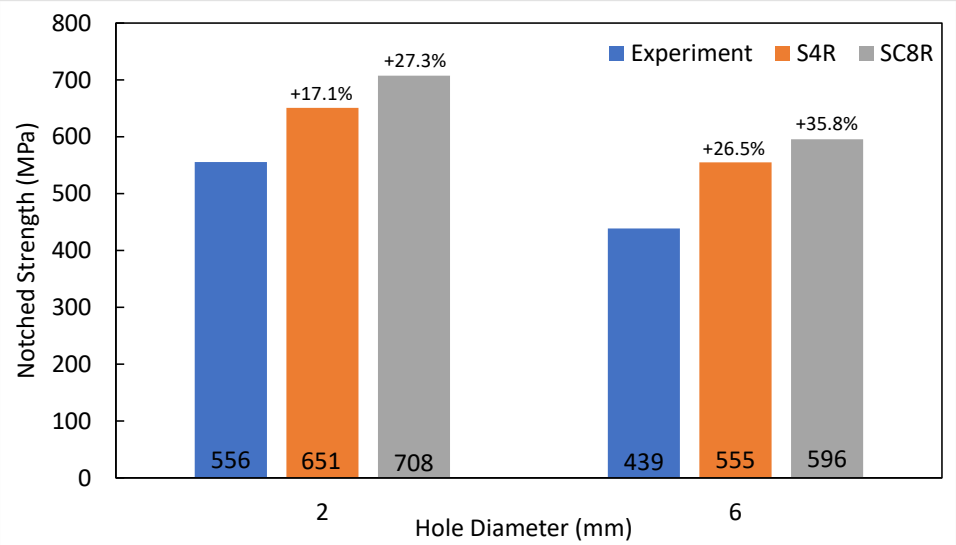

Figure 6.22. Comparison between the experiments and numerical simulation of the IM7-8552 CFRP $[90/0/\pm45]_{3s}$ OHT specimen using plane stress (S4R) and continuum shell (SC8R) elements with perfect bonding at ply interfaces.

In order to understand the reason for the further OHT strength overpredictions caused by continuum shell elements with perfect bonding, damage patterns of the OHT laminate fe models built using plane stress and continuum shell elements are plotted. In Figure 6.23, fiber damage extension shortly after the peak load in the 0º ply of the IM7 8552 quasi isotropic laminate using plane stress and continuum shell elements with perfect bonding are displayed. Referring to the experiments conducted by Camanho et al. [9] fiber damage pattern is expected to be perpendicular to the loading direction. From Figure 6.23 (a), it is seen that this damage progression is represented more correctly by the fe model composed of plane stress elements compared to the continuum shell elements. The fiber damage progression of the continuum shell elements is inclined at an angle of approximately 45. This damage progression can be due to the fact that damage evolution in the 0º plies are affected by the ±45º plies as perfect bonding is present at the ply interfaces. Hence, this behavior can be the reason for the higher strength overpredictions. We note that stress fields in each ply in layered plane stress elements is computed based on Classical Lamination Theory (CLT). Despite the fact that there is perfect bonding

assumption in the CLT, the influence of the perfect bonding at ply interfaces is not so significant as in the case where each ply is modeled with continuum shell elements. Chen et al. [12] simulated the open hole tension test of the IM7 8552 OHT laminate with $[-45/90/45/0]_s$ layup and a hole diameter d=3.175 mm, which fail in pull-out mode. They have chosen smeared crack model [135] for the OHT laminate strength predictions and worked on different fe modeling strategies, including layered plane stress elements (S4R), continuum shell elements (SC8R) with perfect bonding and continuum shell elements with cohesive zone elements (COH3D8) at ply interfaces. According their study, OHT laminate strength overprediction is seen when layered plane stress and continuum shell elements with perfect bonding are used. However, unlike the findings in the current study overpredictions obtained with continuum shell elements with perfect bonding were less than the layered plane stress elements.

Influence of perfect bonding at ply interfaces when continuum shell elements are used, is studied in more detail as displayed in Figure 6.24. In the figure the damage pattern under peak load in the 90º, 0º, 45º and -45º plies are shown. 'X' shaped failure pattern in the 90º and 0º plies implies the influence of the ±45° plies on the damage development. The fracture plane perpendicular to the loading direction seen in the experiments is not represented correctly with the continuum shell elements with perfect bonding. This damage evolution can be an explanation for the OHT laminate strength overpredictions.

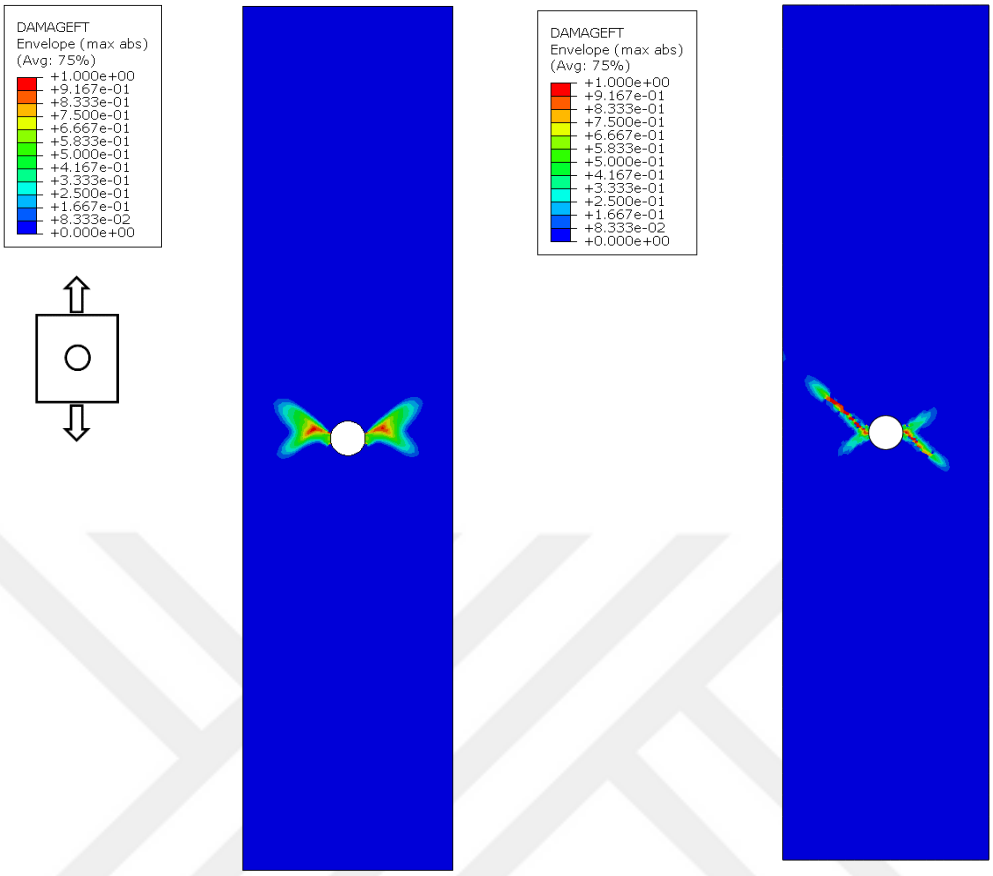

(a) (b)

Figure 6.23. Fiber damage evolution shortly after peak load in the 0°-ply of the IM7-8552 CFRP $[90/0/\pm45]_{3s}$ OHT specimen with a hole diameter of 6 mm using (a) plane stress (S4R) and (b) continuum shell (SC8R) elements with perfect bonding at ply interfaces.

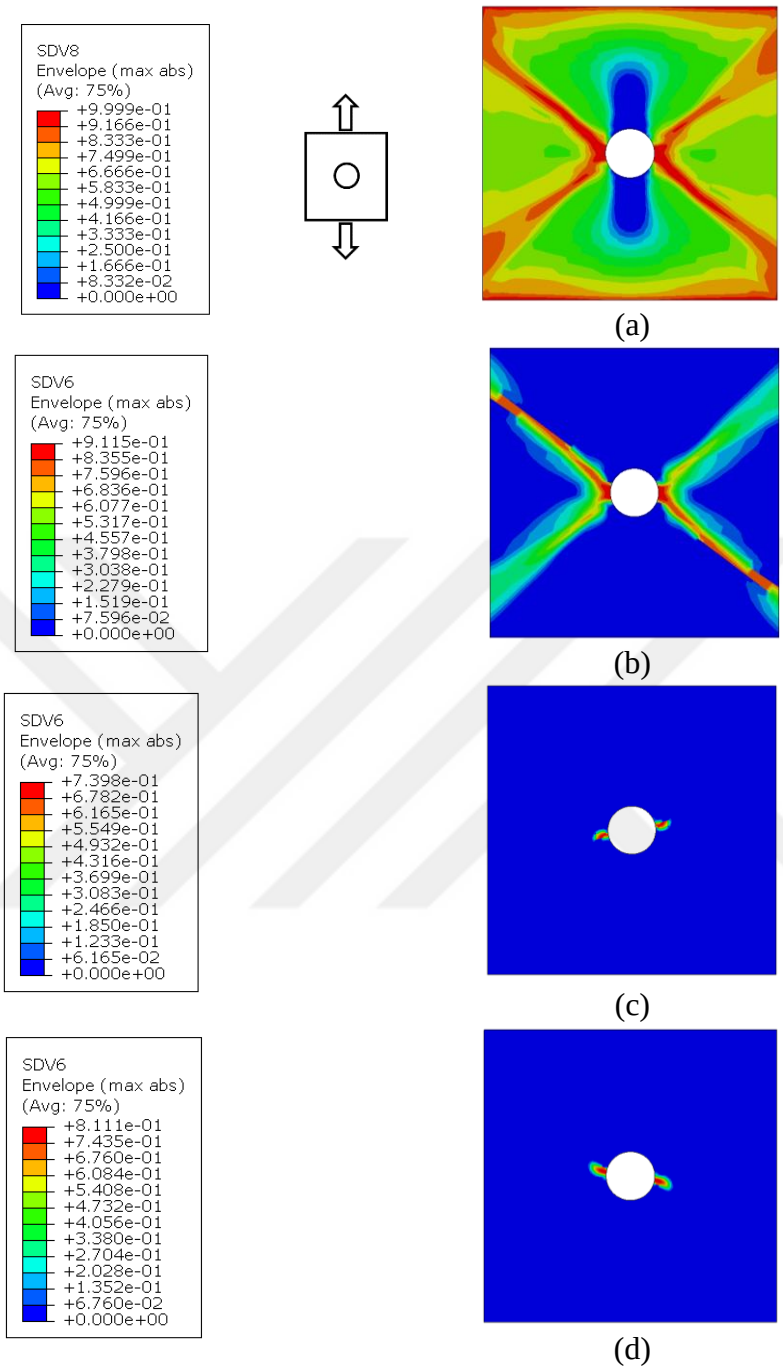

Figure 6.24. Damage pattern at peak load in the IM7-8552 CFRP $[90/0/\pm45]_{3s}$ OHT specimen with a hole diameter of 2 mm with perfect bonding at ply interfaces: (a) matrix damage in the 90° ply, (b) fiber damage in the 0°ply, (c) fiber damage in the 45° ply, (d) fiber damage in the -45° ply.

6.3.2.2 Continuum Shell with Interface

To eliminate the effect of perfect bonding at ply interfaces and observe its influence on the OHT laminate strength predictions, three different fe models by removing perfect bonding at ply interfaces are built. In the first model, named as detached plies, z-symmetry boundary condition in the fe model (See Figure 6.3) is removed and each ply of the IM7-8552 CFRP $[90/0/\pm45]_{3s}$ OHT specimen is modeled with continuum shell elements. As shown in Figure 6.25 no interaction at the ply interfaces is defined and the fe model is composed of a total number of 24 plies.

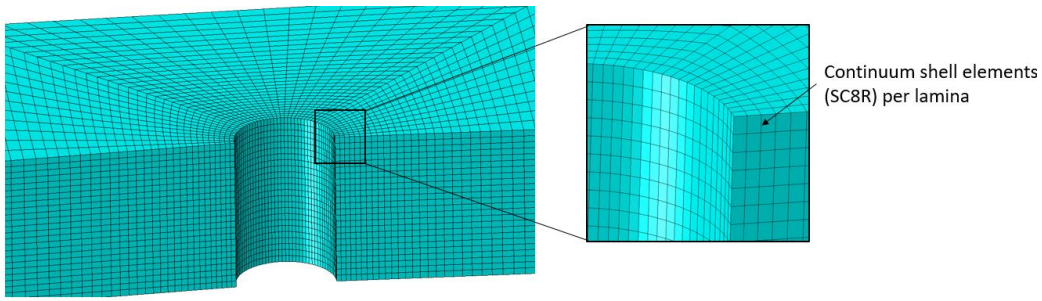

Figure 6.25. FE modeling approaches for the open hole tension using detached plies with SC8R elements per ply.

The interpenetration of the detached plies is prevented in the second fe model with frictionless contact definition at ply interfaces. Plane symmetry boundary condition (See Figure 6.3) is utilized to save computation time. 'Frictionless' contact in tangential behavior and 'Hard' contact as normal behavior with General Contact Algorithm of ABAQUS [124] is defined as the interaction properties of the plies. Due to the convergence difficulties encountered with ABAQUS implicit solver, ABAQUS explicit solver is used for the simulations. Load is applied as displacement and a suitable smooth step amplitude is chosen in order to prevent dynamic effects during loading. In the third fe model, cohesive zone elements are placed at each ply interface as seen in Figure 6.26 to simulate the rich resin between the plies. Plane symmetry boundary is used and the frictionless contact between the plies is defined so that the interpenetration of the plies after cohesive damage is prohibited. As explained in the methodology section, an element length of 0.2 mm with a ply

thickness 0.131 mm is deemed reasonable in the damage propagation regions near the hole for the OHT laminate with hole diameter of 2 mm. Using coincident nodes, the same element length of 0.2 mm with a thickness of 0.01 mm is chosen as the dimensions of the cohesive elements near the hole of the OHT laminate. However, in the OHT laminate with a hole diameter 6, hour-glassing and highly distorted elements are observed for the element length of 0.2 mm. Therefore, the element length near the hole is increased to 0.3 mm with a ply thickness 0.131 mm and the hourglassing problem is solved. Cohesive elements with an element length of 0.3 mm and thickness 0.01 mm are placed at the ply interfaces only in the region of the fe model with the CDM. The region of the fe model continuum damage is connected to the with tie constraints (See Figure 6.26). As in the fe model with continuum shell elements and frictionless contact ABAQUS explicit solver is used for the simulations.

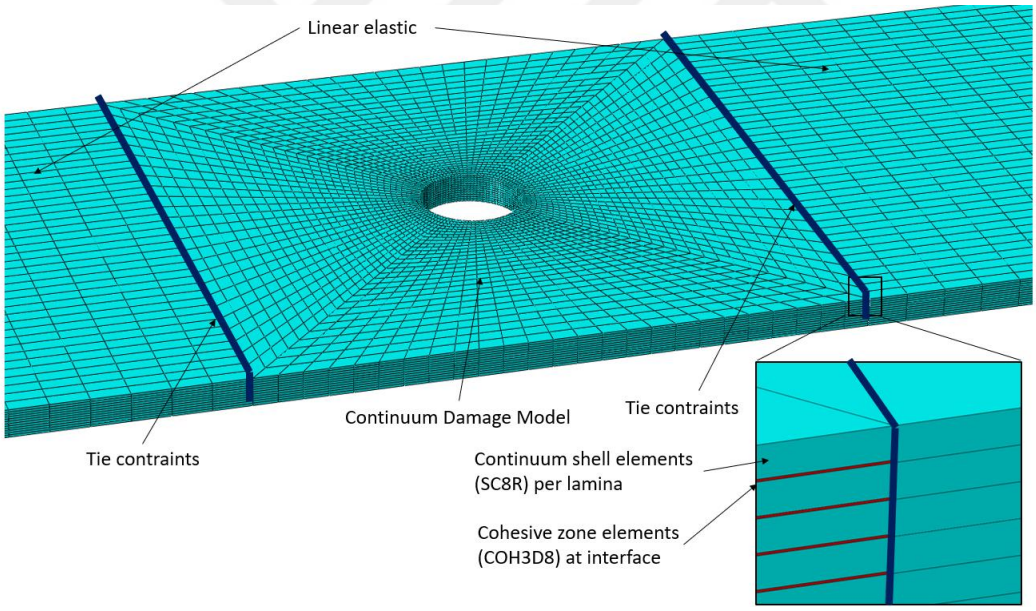

Figure 6.26. FE modeling approach for the open hole tension (hole diameter, d=6 mm) using SC8R elements per ply with COH3D8 elements at ply interfaces.

In Figure 6.27 relation between remote stress (σ^{∞}) versus longitudinal displacement in the IM7-8552 quasi-isotropic laminate with a hole diameter of 2 mm using different fe modeling strategies are plotted. OHT laminate strengths are determined from the peak remote stress values, where the stress suddenly drops. As seen from

the plots, the fe model with the detached plies has the lowest stiffness and strength. This remote stress versus displacement can be explained by the interpenetration of the plies as no constraint is defined at ply interfaces in the case of detached plies. When frictionless contact between ply interfaces is defined the stiffness of the remote stress versus longitudinal displacement curve as well as the OHT laminate strength prediction increases. It is seen from the figure that the stiffness of the fe models with interface perfect bonding, CLT and CZM at ply interfaces is almost the same. The highest strength is computed with the fe model using continuum shell perfect bonding, followed by the CLT model. As expected the OHT laminate strength obtained from the continuum shell laminate with CZM at the ply interface lies between the fe model with the frictionless interface and interface perfect bonding and is lower the fe model with CLT.

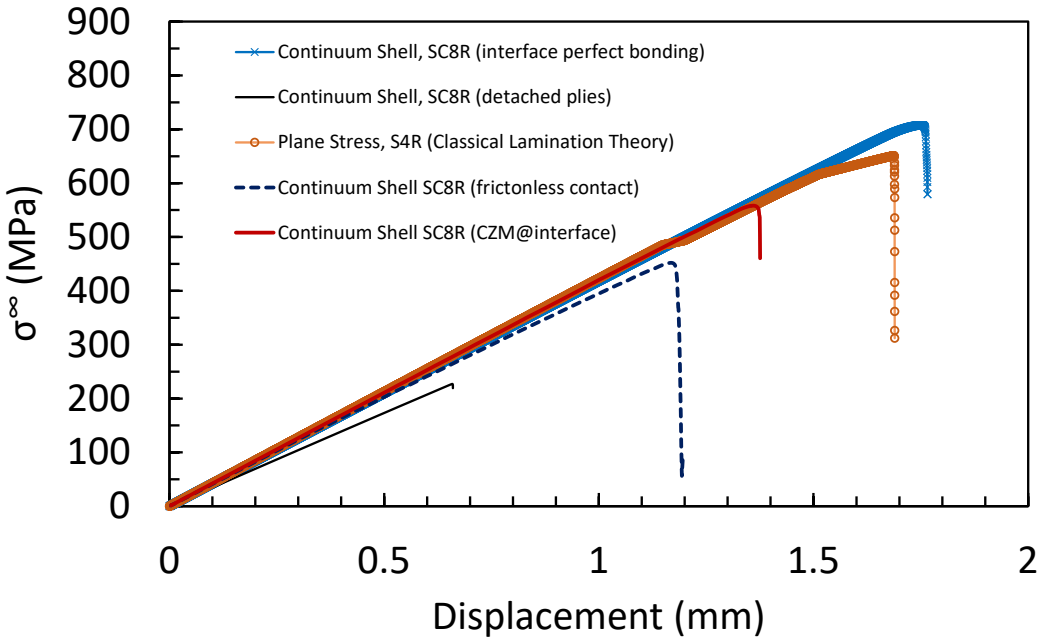

Figure 6.27. Relation between remote stress σ^{∞} and longitudinal displacement in the IM7-8552 CFRP $[90/0/\pm45]_{3s}$ OHT specimen with a hole diameter of 2 mm using different fe modeling strategies.

In Figure 6.28 strength predictions of the IM7 8552 CFRP quasi-isotropic laminates with hole sizes 2, 6 and 10 mm are plotted against experiments [9]. When OHT

laminate with a hole diameter of 2 mm is considered, OHT laminate strengths are underpredicted by both fe models with detached plies and frictionless contact. The error in the strength prediction of the fe model with frictionless contact is -22.9% and less than the error obtained with detached plies. The strength overpredictions calculated by CLT and perfectly bonded plies are +17.1% and +27.3%, respectively. The best strength prediction is done with the FE model using CZM at ply interfaces within an error less 3.3% (See Figure 6.29). For the OHT laminate with a hole diameter of 6 mm, FE model with perfectly bonded plies and CLT lead to strength overpredictions by +26.5% and +35.8%, respectively. The FE model in which continuum shell elements in combination with CZM is used leads to the best prediction of the OHT laminate strength by +15.2% (See Figure 6.29). When continuum shell elements with CZM instead of layered plane stress elements are used, we note that the relative errors compared to experiments is reduced by 13.8% and 11.3%, for hole diameters 2 mm and 6 mm, respectively. However, when it comes to the 10 mm hole diameter, the decline seen in open-hole composite laminate strengths, as shown by layered plane stress elements, is not replicated when using continuum shell elements with CZM at the interfaces. This may be due to two reasons. Firstly, the model does not account for the statistical strength decrease of fibers as the specimen size increases [117]. Secondly, the damage extent at the ply interfaces may not be adequate for the open-hole specimen with a 10 mm hole diameter. For future research, solid elements per ply could be used instead of continuum shell elements to model the open-hole specimen. This approach could potentially improve the interface damage evolution at the ply interfaces, since solid elements allow for through-thickness stresses to be considered, which may improve the correlation with experimental data.

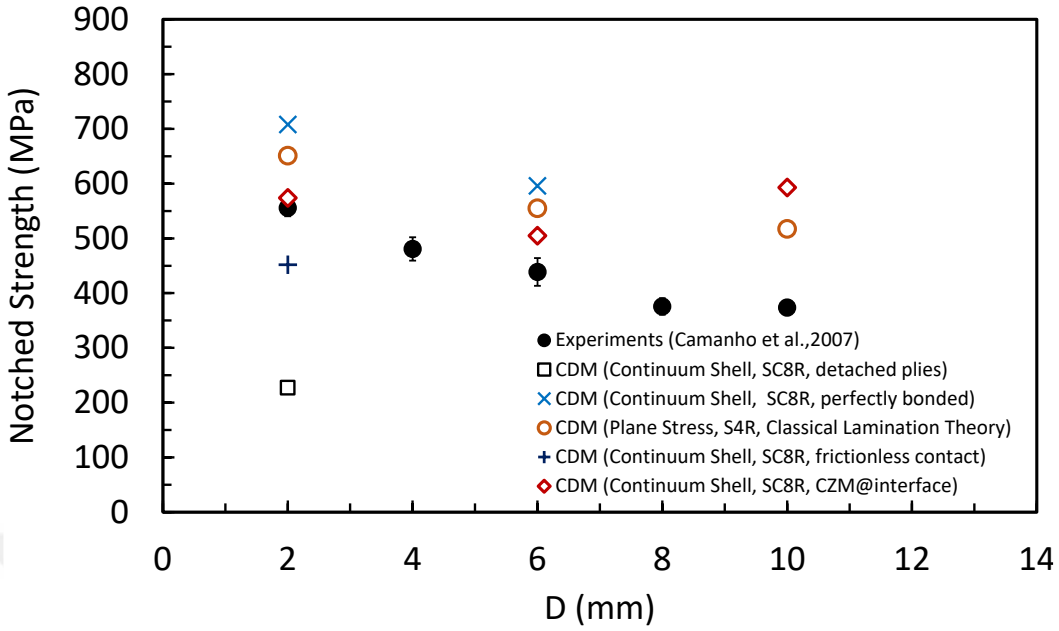

Figure 6.28. Strength predictions of the IM7-8552 CFRP $[90/0/\pm45]_{3s}$ OHT specimen with different hole sizes (w/D=6).

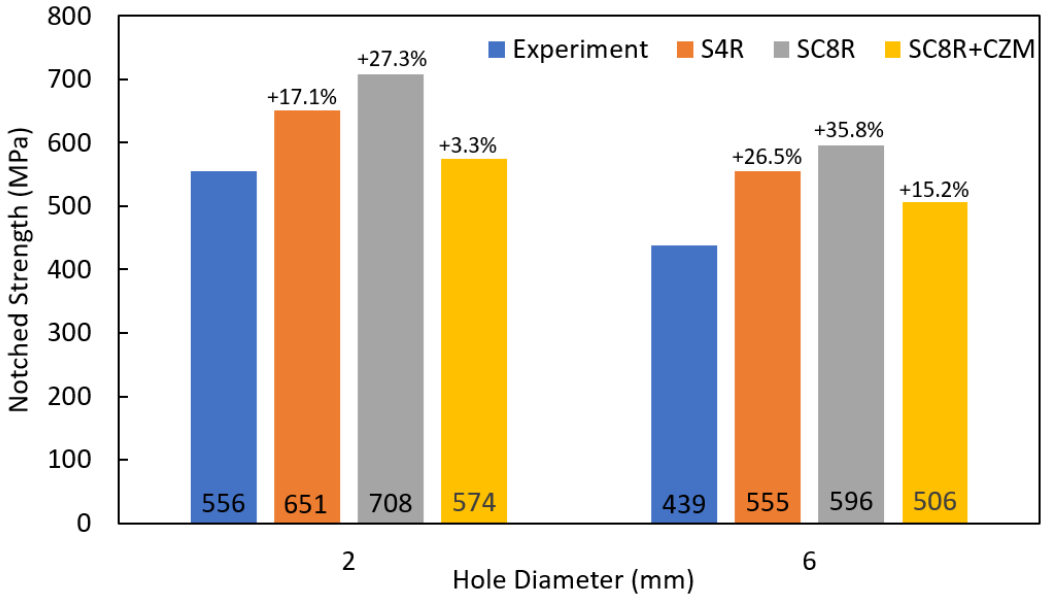

Figure 6.29. Comparison between the experiments and numerical simulation of the IM7-8552 CFRP $[90/0/\pm45]_{3s}$ OHT specimen using plane stress (S4R) and continuum shell (SC8R) elements with perfect bonding and continuum shell (SC8R) elements with CZM at ply interfaces.

The reason for the OHT laminate strength underpredictions determined by the fe models (hole diameter, D = 2 mm) with frictionless contact at ply interfaces is investigated further by referring to the damage progression patterns on ply level. In Figure 6.30, damage patterns in the top 90°, 0°, 45° and -45° plies of the IM7 8552 quasi-isotropic CFRP laminate under peak load, where load drop occurs are shown. Unlike the damage pattern observed in the perfectly bonded plies, the matrix damage extent in the 90° ply is perpendicular to the loading direction and consistent with the experiments as seen in Figure 6.30 (a). Similarly, the fiber damage initiates at the hole edge perpendicular to the loading direction and develops further perpendicular to the loading direction. It is worth noting that under peak load, 90° ply fails completely, but the damage extent in the 0° ply is much smaller (See Figure 6.30 (a)). Moreover, in the ±45 plies no fiber damage is observed at peak load as depicted in Figure 6.30 (c) and (d). This may be attributed to the fact that 0° ply is stiffer compared to the ±45 plies and takes up most of the tension load.

In the IM7 8552 quasi-isotropic OHT laminate fe model composed of continuum shell elements with cohesive elements in the ply interfaces plane symmetry boundary condition is used. Therefore, the fe model is built using only three sublaminates with the lay-up [90/0/±45]. Damage development patterns of the top, middle and bottom (center) sublaminate with respect to the plane symmetry are displayed in Figure 6.31-Figure 6.33 respectively. In the figures, matrix tension damage in 90° ply, and fiber damages in the 0°,+45°,-45° plies are plotted. In addition to the matrix and fiber damage plots, damage in the cohesive elements, which represent delamination are plotted. Matrix damage as well as the fiber damage progression is perpendicular to the loading direction, which is in good agreement with the experiments. Moreover, the damage extent seen in the 90° ply is more than the damage extent in the 0° ply. This is similar to the damage development of the OHT laminate fe model with the frictionless contact. In accordance with the OHT laminate fe model with frictionless contact, the fiber damage extent in the OHT laminate fe model with CZM is significantly more than the fiber damage extent in ±45° plies. Although the OHT specimen fails in brittle mode with minimal delamination, in all

ply interfaces considerable damage development is seen. This damage development which indicates delamination enables the failure progression seen in the experiments. As a consequence, in comparison to other fe modeling strategies, ultimate failure values closer to the experiments can be predicted with continuum shell elements in combination with cohesive zone elements.

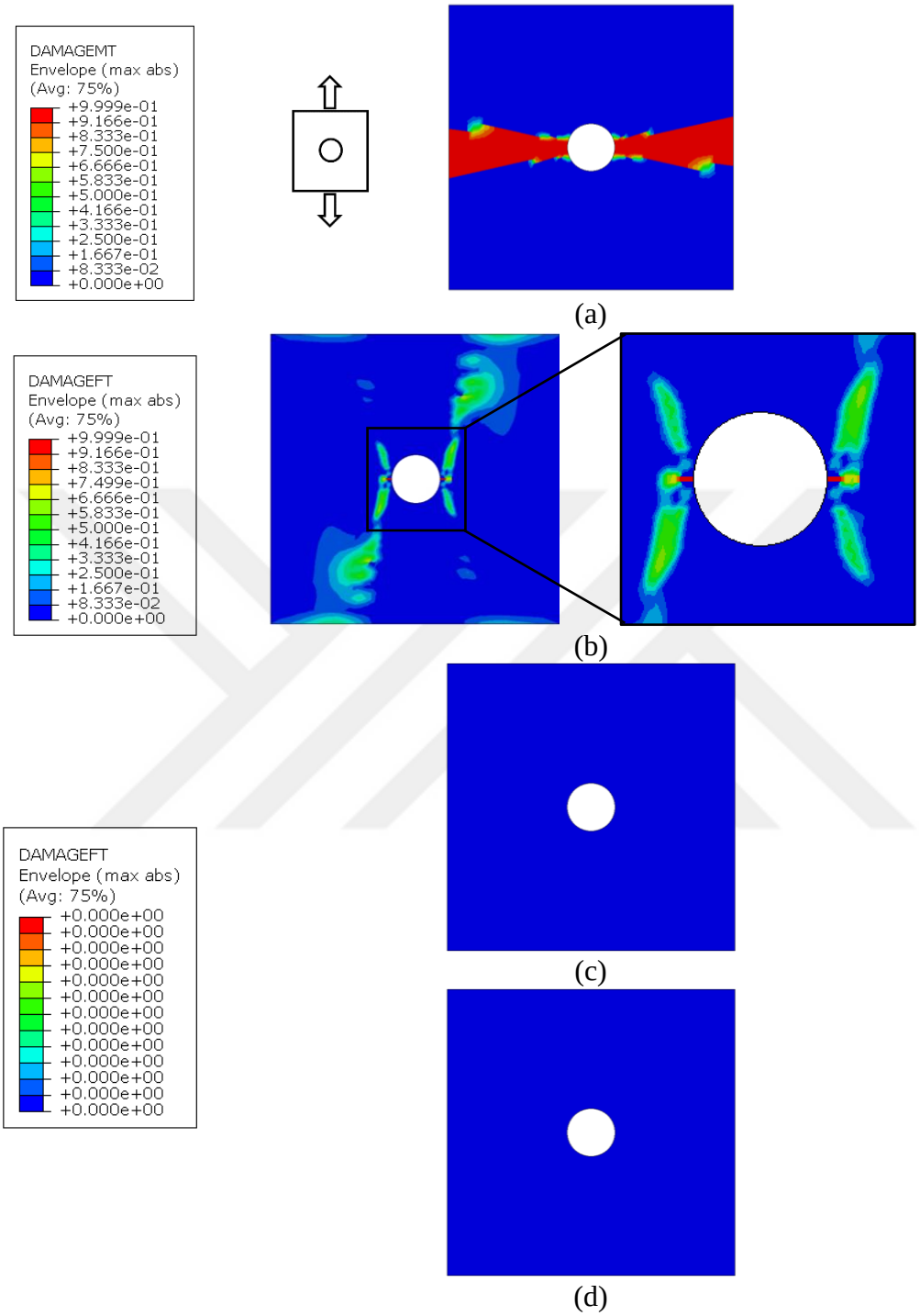

Figure 6.30. Damage pattern in the IM7-8552 CFRP $[90/0/\pm45]_{3s}$ OHT specimen under ultimate load (hole diameter, D = 2 mm) with frictionless contact at ply interfaces: (a) matrix damage in the 90° ply, (b) fiber damage in the 0° ply, (c) no fiber damage in the 45º ply (d) no damage in the -45º ply.

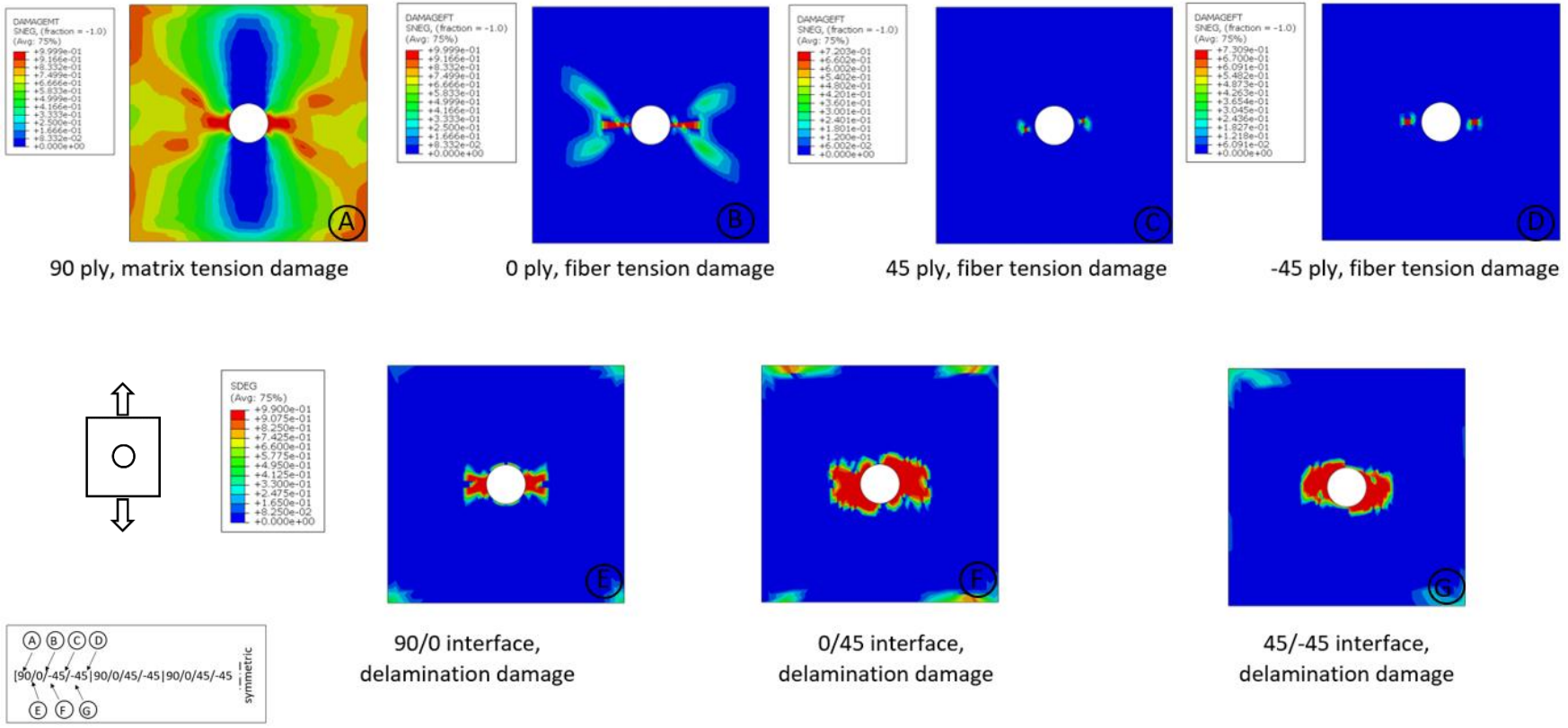

Figure 6.31. Damage extent in the IM7-8552 CFRP $[90/0/\pm45]_{3s}$ OHT top sublaminate under ultimate load (hole diameter, D = 2 mm) with Cohesive Zone Model at ply interfaces.

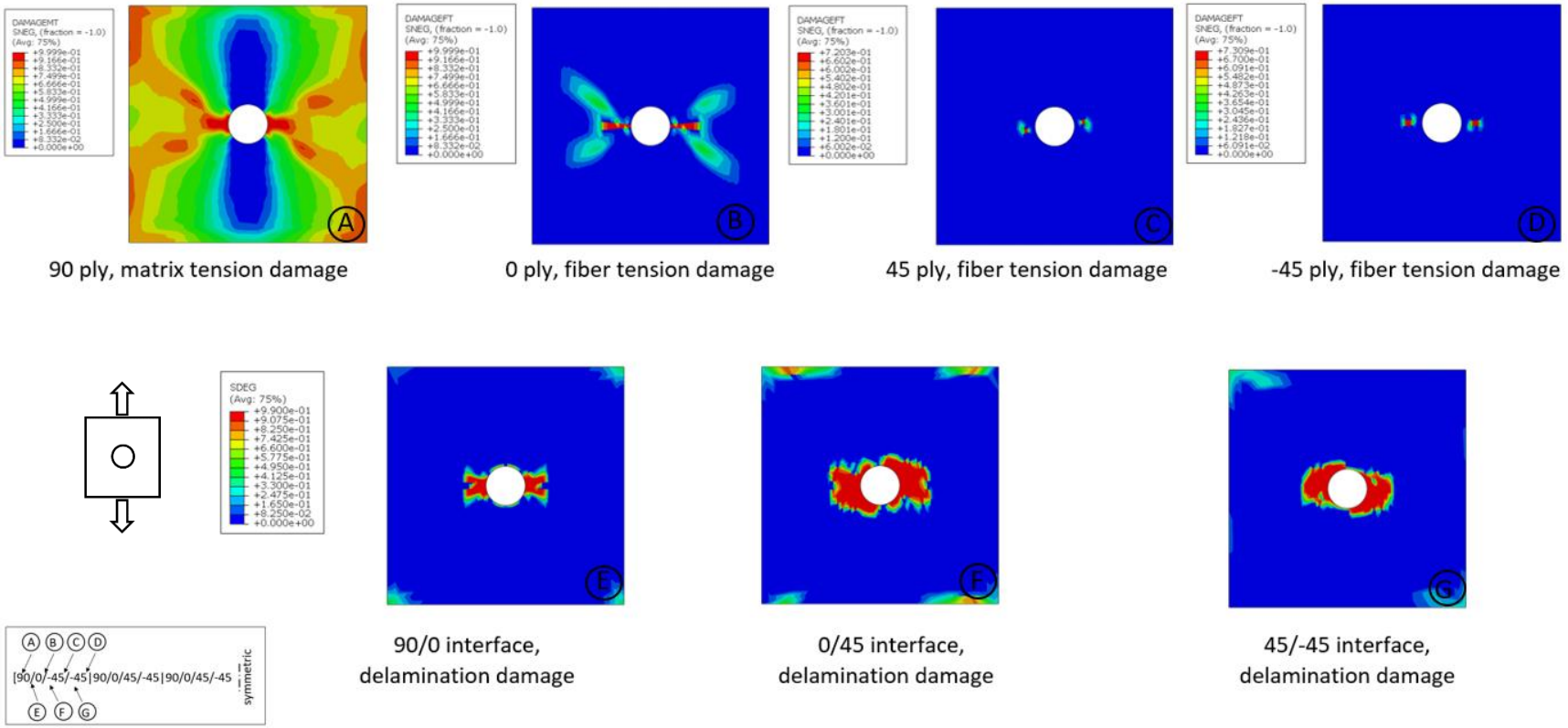

Figure 6.32. Damage extent in the IM7-8552 CFRP $[90/0/\pm45]_{3s}$ OHT middle sublaminate under ultimate load (hole diameter, D = 2 mm) with Cohesive Zone Model at ply interfaces.

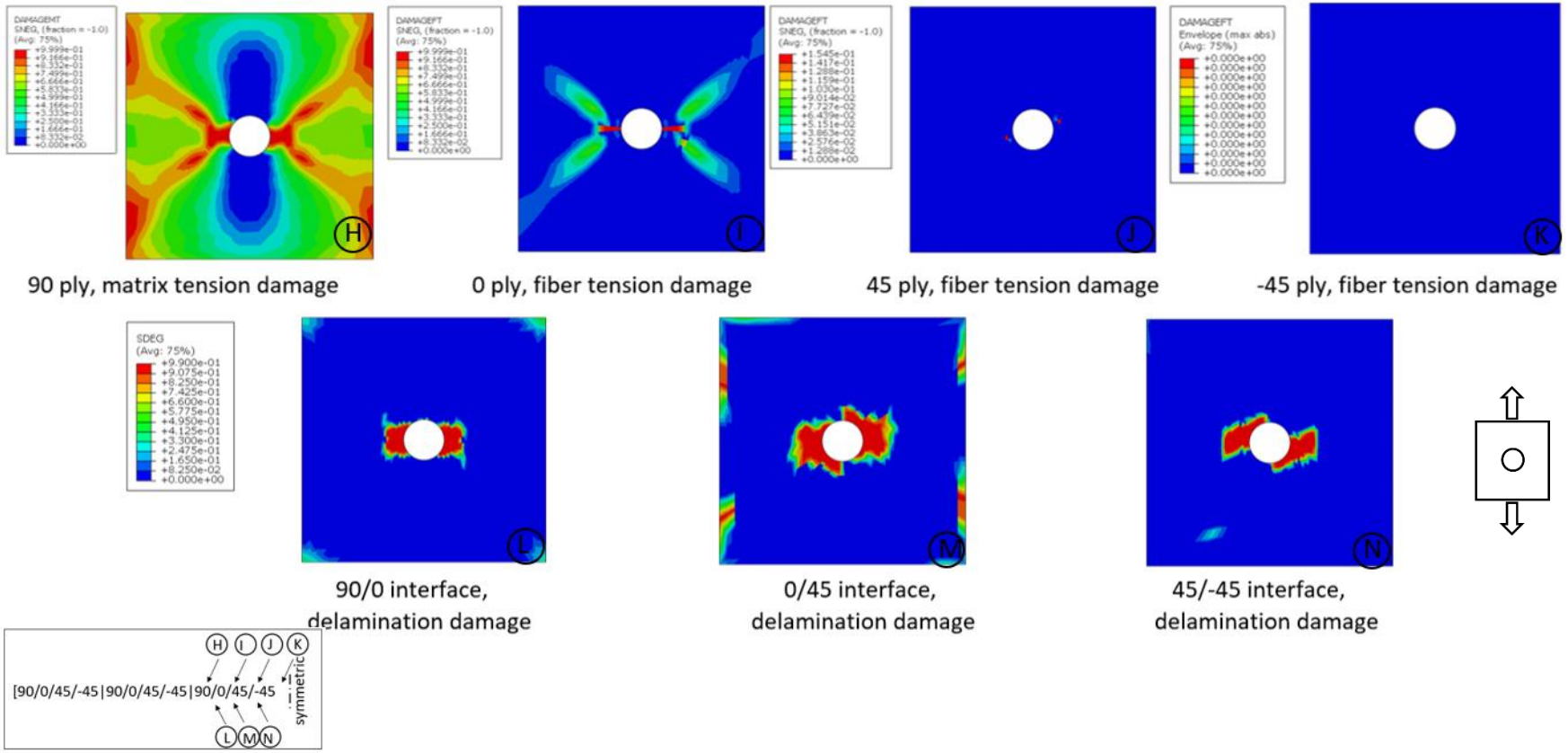

Figure 6.33 Damage extent in the IM7-8552 CFRP $[90/0/\pm45]_{3s}$ OHT bottom (center) sublaminate under ultimate load (hole diameter, D = 2 mm) with Cohesive Zone Model at ply interfaces.

6.4 Conclusions

In this work, utilizing the Hashin continuum damage model (CDM) ABAQUS (2019)[124] and the Puck CDM the influence of different hole sizes on the strength of IM7-8552 OHT $[90/0/\pm45]_{3s}$ are studied. Although different failure initiation criteria are implemented, in both CDM fracture energy based bi-linear degradation schemes are used. To the author's knowledge, for the first time in literature different fe modeling strategies utilizing Hashin failure initiation criteria-based Continuum Damage Model for the OHT laminate strength predictions are presented in this study. The main conclusions of the study are as follows:

- Using layered stress elements based on CLT, Hashin and Puck CDM deliver close strength predictions (deviation less than 7%) and very similar damage patterns. Decreasing strength of the OHT laminates with increasing hole sizes as well as the damage initiation region is captured correctly as observed in experiments using both models. However, usage of plane stress elements in the fe models lead to an overprediction of stress values by more than 17%.

- The influence of different discretization techniques, namely structured and nonstructured meshed using reduced integration plane stress elements (S4R) are studied. The results show that both discretization techniques lead to almost the same OHT laminate strength predictions. Since a smaller number of elements are used for the structured mesh, it is chosen as the discretization technique in this work.

- When OHT laminates are modeled with continuum shell elements (SC8R) per each ply and perfect bonding at ply interfaces, compared to the fe model with plane stress elements the influence of the ±45 plies on the fiber damage development of the 0° and 90º plies increases. This damage development causes higher strength overpredictions compared to the case with plane stress elements.

To eliminate the effect of perfect bonding at ply interfaces, for the OHT laminate with a diameter of 2 mm three FE models composed of continuum shell elements with different interface modeling strategies are introduced. In the first model named as detached plies, interpenetration of the plies is detected. This interpenetration causes significant stiffness and strength underpredictions compared to other modeling approaches. In the second fe model with frictionless contact defined at ply interfaces, strength underpredictions are still present, however strength prediction error is considerably less than the model with detached plies. In addition, better representation of the stiffness of the OHT laminate is achieved. Best strength and damage progression prediction is achieved using the FE model with CZM at ply interfaces with a prediction error less than 3%, which is calculated as 17% with plane stress elements. On top of this, the damage development perpendicular to the loading direction in all plies and interfaces observed in experiments is captured as well. For the OHT laminate with a hole diameter of 6 mm, the FE model with CZM delivers strength prediction error less than 15%, which is calculated as 27% with the plane stress elements. These results highlight the necessity of modeling interface failure not only in OHT laminates in delamination or pull-out failure mode [12], but also in brittle failure mode with minimal delamination. However, for the hole diameter 10 mm, the decreasing trend of open hole composite laminate strength, which was satisfied by layered plane stress elements is not followed with continuum shell element with CZM at interface. One reason for this result can be attributed to the fact that statistical strength decreases of fibers with increasing specimen size [117] is not considered in the damage model. Another reason can be due to the fact that the interface damage at ply interfaces is not sufficient for the open hole specimen with a hole diameter of 10 mm. As a future study the open hole specimen can be modeled with solid elements instead of continuum shell elements. Since through the thickness stresses can also be considered by solid elements, this modeling technique may help improve the interface damage evolution at the ply interfaces and lead to better correlation with experiments.

CHAPTER 7

FE MODEL VALIDATION AND PROGRESSIVE DAMAGE ANALYSIS OF A 5-M COMPOSITE WIND TURBINE BLADE UNDER MONOTONIC LOADING

7.1 Introduction

In this Chapter, main failure mechanisms of an existing 5-meter glass-fiber-reinforced-polymer (GFRP) RÜZGEM wind turbine blade are investigated by implementing Puck's physically based phenomenological damage model. For this purpose, Puck's damage model is incorporated into a global finite element model using ANSYS APDL [136] scripting language. ANSYS APDL Code for the progressive failure analysis of composite laminates is validated againts the experimental data available in literature. Moreover, the blade FE model is validated based on modal tests for the free-free boundary condition. After validating the model, the progressive damage analysis of the blade is conducted. Load is applied as a single point load in order to simulate full-scale testing conditions of blade subjected to flapwise (max) loading.

The existing blade investigated in this work was designed as part of a joint-project between Core Team of the University of Patras and METUWIND (RUZGEM). The blade was designed for a wind turbine that has 30 kW nominal power capacity at 10 m/s wind speed. According to the wind turbine characteristics, optimized aerodynamic blade design was finalized by the blade manufacturer. The existing blade consists of five main parts: suction side, pressure side, internal flange, "hat-shaped" chassis(spar), and flange, as seen in Figure 7.1.

The short length of the RÜZGEM blade is attributed to the fact that the blade is constructed mainly for research purposes. Within the scope of this thesis, the primary goal is to investigate strength characteristics and failure mechanisms of the 5- meter

blade using in-house developed software tools. Furthermore, building of affordable testing facilities are planned so that full-scale blade tests can be conducted and compared with simulations. It is worth noting that the research wind turbine blades used by Paquette and Veers [63] and Chen et al. [64] were also short and only 9-meters and 10.3-meters respectively. Once the simulation results are compared with tests to be conducted in the future and the degree of agreement is assessed, the study can be readily extended to the progressive failure analysis of large blades.

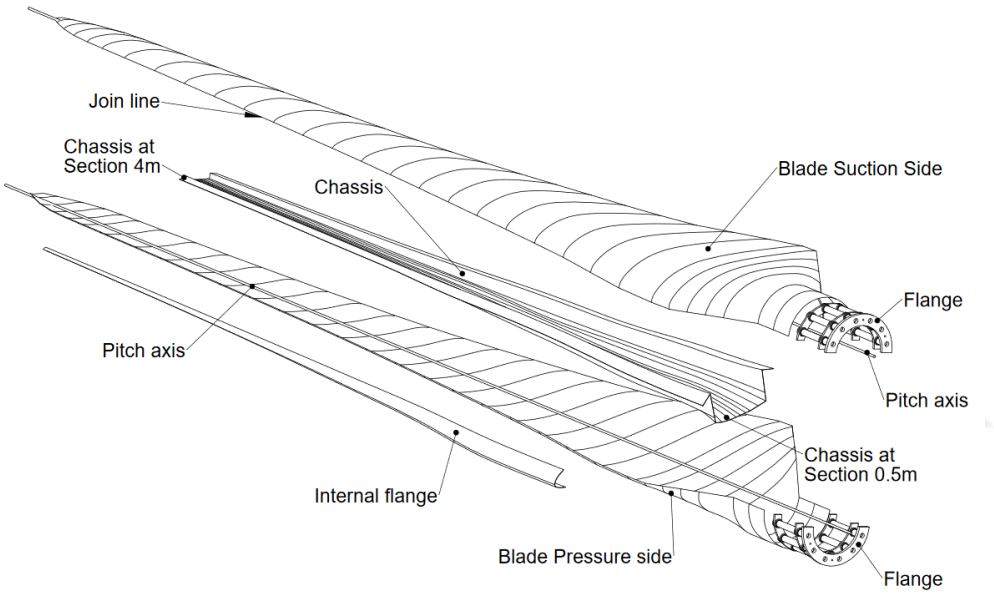

Figure 7.1. Blade assembly for the 5-meter RUZGEM wind turbine blade [137].

7.2 Methodology

7.2.1 FE Model of the 5-m RUZGEM Wind Turbine Blade

In Table 7.1 below the material properties and design allowables of the blade materials for static analysis is listed [137]. Referring to the Germanischer Lloyd (2010) [138] design allowables are obtained from the knockdown of the experimental strength values by a safety factor of 2.406.

RÜZGEM blade is meshed with ANSYS [136] SHELL181 plane stress elements. In Figure 7.2 mesh convergence study based on total blade displacement and maximum von Mises stress level in the blade is depicted. At this point, it is worth noting that the maximum stress is always measured from the same location on the blade. From the results, a shell element size of 15x15 mm (32985 elements) is deemed reasonable for a good compromise between accuracy and computation time. This mesh density achieved a converged solution within 1% and 8% in terms of total displacement in flap-wise direction and maximum von Mises stresses, respectively. In Figure 7.3, discretized 5-meter RUZGEM wind blade components are displayed. Geometric nonlinearity is included in the FE analysis. Flapwise (max) bending moment distribution, which will be used for the full-scale test of the RÜZGEM blade is depicted in Figure 7.4 (a). In order to simulate testing condition, the load which resembles the bending moment over the blade segment 0-3.25 m range is applied using a displacement-controlled approach at station 3.25-m as a single load shown Figure 7.4 (b). According to the recommendations of IEC 61400-23 [139] standard a partial safety factor 1.35 is included in the flapwise (max) loading. The single load is applied at the aeroelastic center of the at the station of 3.25 m from the root. Continuum distributing coupling constraints are used to connect this node to the shell nodes of the upper and lower spar caps. As can be seen Figure 7.4 (b), all the degrees of freedom are fixed at blade root region.

The adhesive interfaces between the blade components, i.e. pressure side, internal flange, spar and suction side of the blade are modeled using Multi-Point-Constraints [68]. At this point, it is worth noting using the default bonded contact augmented Lagrange algorithm in ANSYS for the modeling of adhesive interfaces leads to incorrect results regarding the structural behavior of the blade. This issue was addressed using two different adhesive modeling techniques using Multi-Point-Constraints and augmented Lagrange algorithm. Then modal analysis of the 5-m RUZGEM blade was carried out. Afterwards, simulations results were compared with modal analysis results from experiments, which were conducted at RÜZGEM facilities [140]. It was found out that Multi-Point-Constraints modeling approach at

the adhesive interfaces was able to deliver a good correlation between simulation and test results, whereas augmented Lagrange contact algortihm leads to misleading results.

Table 7.1. Material properties and design allowables of RÜZGEM blade for static analysis [137].

Material Property		UD Laminate	Steel	Gel Coat	CSM 300	Divinycell H45
Density, ρ	(kg/mm^3)	1896	7850	1200	1896	200
Thickness, h	(mm)	0.716	5.3	0.9	0.358	5 or 10
E_1	(GPa)	24.84	210	3.98	9.14	$55x10^{-3}$
E_2	(GPa)	9.14				$55x10^{-3}$
ν_{12}		0.29	0.3	0.34	0.29	0.4
G_{12}	(GPa)	2.83				$15\ x10^{-3}$
X_T	(MPa)	191.73	581.8	35.29	16.86	1.4
X_C	(MPa)	101.16				0.6
Y_T	(MPa)	16.86				1.4
Y_C	(MPa)	50.41				0.6
S	(MPa)	11.29				0.56

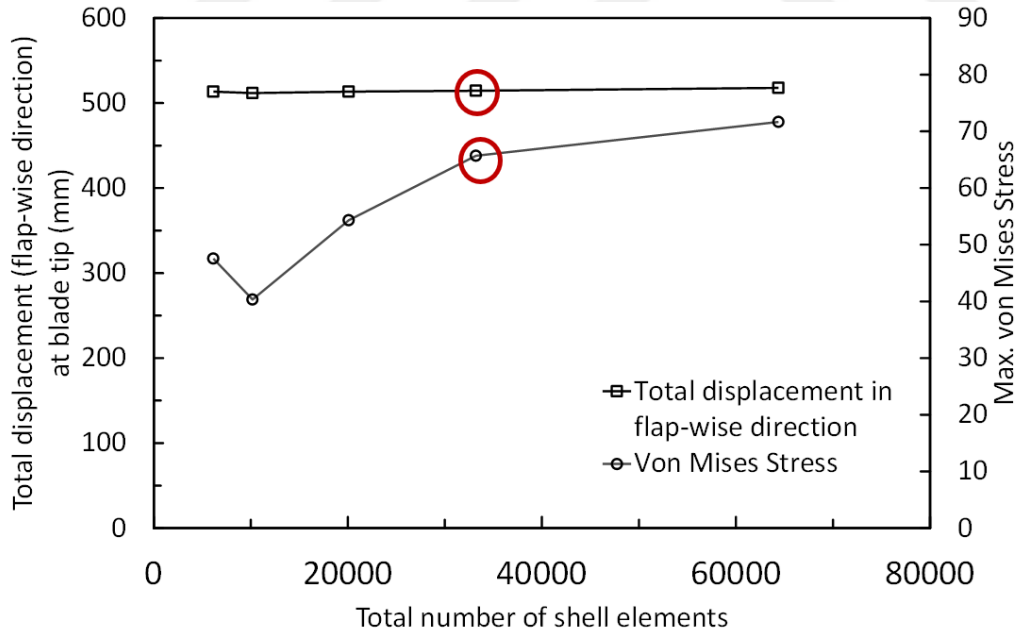

Figure 7.2. Mesh independence study of the 5-meter RUZGEM wind turbine blade, where maximum tip displacement and maximum von Mises stress is used as the convergence criterion.

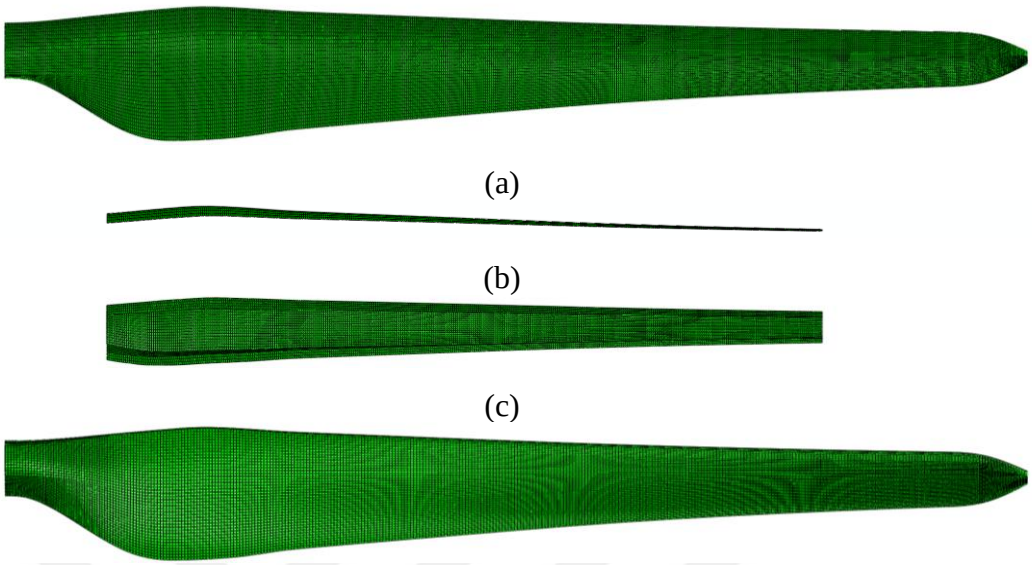

(a)

(b)

(c)

(d)

Figure 7.3. FE models of the 5-meter RUZGEM turbine blade components: (a) pressure side (b) internal flange (c) chassis (d) suction side.

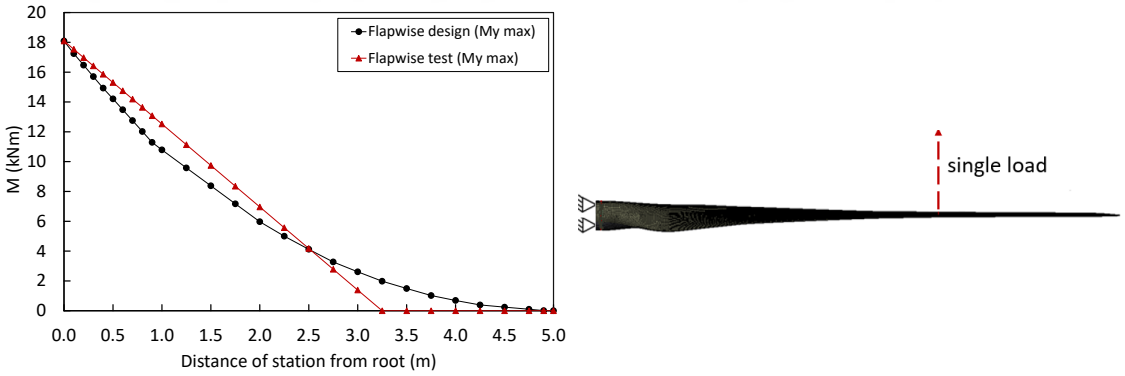

(a) (b)

Figure 7.4. (a) Flapwise (max) bending moment distribution on the RUZGEM blade (b) loads and boundary conditions of the RUZGEM blade FE model.

The mass of the RUZGEM blade from the FE Model must be equal to the actual mass of the RUZGEM blade in order to conduct a vibration analysis comparable to modal tests. Although the mass of the actual blade is 81.5 kg, the mass obtained from the RUZGEM blade FE model is 71.4 kg. This mass difference is caused mostly by the adhesive interfaces, which are not modelled in the FE model. To account for this mass difference ANSYS MASS21, lumped mass elements, are placed in the adhesive interface regions.

7.2.2 Experimental Modal Analysis of the 5-m RUZGEM Wind Turbine Blade

In order to validate the RÜZGEM blade FE model, utilizing a modal shaker, experimental modal analyses are conducted. Using different signals created by a signal generator, different types of excitations can be generated by modal shakers. During modal shaker tests, a random signal is created by the signal generator and the stringer, which is attached to the force transducer is used to excite the structure with this signal. The FFT (Fast-Fourier-Transform) vibration analysis setup is ready for the experiment after defining the geometry and measurement points in the software program [140]. For the vibration measurements, type 4805 accelerometers are rowed to 87 different positions. Since five accelerometers are used, a total of 18 measurements are conducted. The positioning of the accelerometers on the RÜZGEM blade and the mounting of the shaker to the RÜZGEM blade are shown in Figure 7.6 (a) and Figure 7.6 (b), respectively.

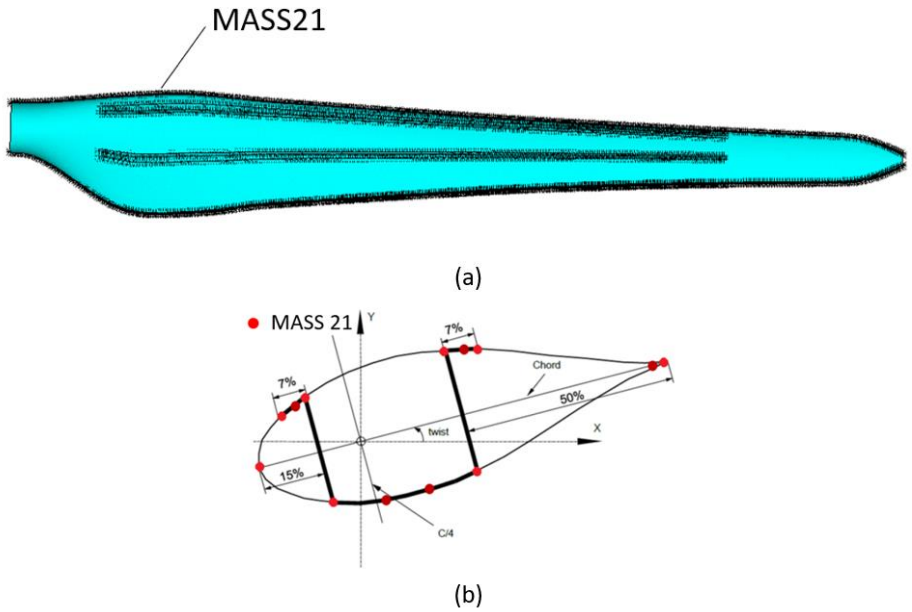

Figure 7.5. (a) Distribution of the MASS21 elements in the spanwise direction (b) distribution of the MASS21 elements in the cross-section of the RÜZGEM blade fe model.

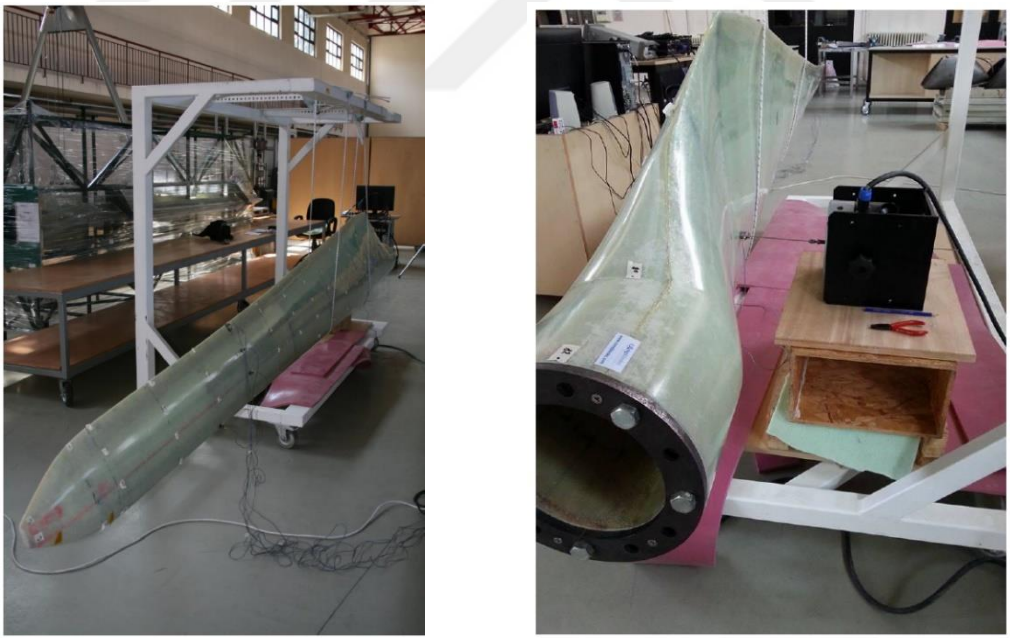

(a) (b)

Figure 7.6. Experimental modal analysis test set-up of the RÜZGEM blade (a) positioning of the accelerometers on the RÜZGEM blade (b) mounting of the shaker to the RÜZGEM blade [140].

7.2.3 Intralaminar Damage Model

For the progressive failure analysis of the blade, Puck's physically based phenomenological model is used [84]. Puck's failure criteria are widely used for the composite failure initiation, which distinguish between two main failure mechanisms: (i) fiber failure and (ii) inter-fiber failure (matrix-dominated cracking) ([84],[141]). Inter-fiber failure model of Puck and Schürmann [84]is based on Mohr-Coulomb criterion.

For fiber failure, Puck's criteria are as follows:

$$f_{E(FF)}^{T} = \frac{\sigma_1}{X_T} = 1 \text{ if } \sigma_1 > 0 \tag{7.1}$$

$$f_{E(FF)}^{C} = \frac{\sigma_1}{X_C} = 1 \text{ if } \sigma_1 < 0 \tag{7.2}$$

where $f_{E(FF)}^{T}$ and $f_{E(FF)}^{c}$ are stress exposures for fiber failure under tension and compression loading cases. σ_1 is the stress value in fiber direction, X_T and X_c are tensile and compressive strengths in fiber direction, respectively. Puck's inter-fiber failure uses different equations depending on the failure mode, which is detected. The transition point from failure mode B to failure mode C is denoted by the point $(R_{\perp\perp}^{A}, \tau_{21c})$ and is calculated by the ratio $R_{\perp\perp}^{A}/\tau_{21c}$. Their values are calculated by the expressions below:

$$R_{\perp\perp}^{A} = \frac{S}{2p_{\perp\parallel}^{(-)}}\left[\sqrt{1 + 2p_{\perp\parallel}^{(-)}\frac{Y_c}{S}} - 1\right] \tag{7.3}$$

$$\tau_{21_c} = R_{\perp\parallel}\sqrt{1 + 2p_{\perp\perp}^{(-)}} \tag{7.4}$$

$$\text{and } p_{\perp\perp}^{(-)} = p_{\perp\parallel}^{(-)}\frac{R_{\perp\perp}^{A}}{S} \tag{7.5}$$

Depending on the region of the failure envelope, the following inter-fiber failure expressions are written:

$$f_{E(IFF)}^{A} = \left[\left(\frac{\sigma_6}{S}\right)^2 + \left(1 - p_{\perp II}^{(+)}\frac{Y_T}{S}\right)^2\left(\frac{\sigma_2}{Y_T}\right)^2\right]^{1/2} + p_{\perp II}^{(+)}\frac{\sigma_2}{S} = 1 \text{ if } \sigma_2 \geq 0 \quad (7.6)$$

$$f_{E(IFF)}^{B} = \frac{1}{S}\left\{\left[(\sigma_6)^2 + \left(p_{\perp II}^{(-)}\sigma_2\right)^2\right]^{1/2} + p_{\perp II}^{(-)}\sigma_2\right\} = 1 \text{ if } \begin{cases} \sigma_2 < 0 \\ \left|\frac{\sigma_2}{\sigma_6}\right| \leq \frac{R_{\perp\perp}^{A}}{\tau_{21C}} \end{cases} \quad (7.7)$$

$$f_{E(IFF)}^{C} = \left[\left(\frac{\sigma_6}{2(1+p_{\perp\perp}^{(-)})S}\right)^2 + \left(\frac{\sigma_2}{Y_C}\right)^2\right]\frac{Y_C}{(-\sigma_2)} = 1 \text{ if } \begin{cases} \sigma_2 < 0 \\ \left|\frac{\sigma_2}{\sigma_6}\right| \geq \frac{R_{\perp\perp}^{A}}{\tau_{21C}} \end{cases} \quad (7.8)$$

In the equations above $p_{\perp II}^{(+)}, p_{\perp II}^{(-)}$ and $p_{\perp\perp}^{(-)}$ represent inclination parameters that control the shape of the failure envelope. According to Puck and Schuermann (1998)[84], $p_{\perp II}^{(+)} = 0.3$ and $p_{\perp II}^{(-)} = 0.25$ are chosen for the GFRP material. σ_2 is the stress value in the transverse fiber direction, Y_T and Y_c are tensile and compressive strengths in the transverse fiber direction. Shear stress and shear strength are represented by σ_6 and S, respectively. If the value of stress exposure (f_E) exceeds 1, failure initiation occurs. Mode A is caused by tensile and shear stresses. Modes B occurs under compressive and shear stresses. Mode C is a dangerous failure mode in compressive shearing, which may lead to delamination. ANSYS Parametric Design Language (APDL) is utilized to implement Puck's 2-D damage progressive model into the RÜZGEM blade FE model. According to the Puck's progressive damage model, the degradation rules are applied to the plane stress elements.

Degradation rules are applied to the elements which fail according to the specific Puck's failure criteria, which are inter-fiber failure (IFF) mode A, B, or C (Eqs.(7.6), (7.7) and (7.8), respectively). As suggested by Passipoularidis et al [142], based on the degradation rules in Table 7.2, transverse elasticity and shear moduli of the damaged elements are reduced accordingly. Recommended parameters c, η_r and ξ for the degradation function of the GFRP material in Eq. (7.9) are taken from Knops and Bögle [143]. $f_{E(IFF)}^{A}$, $f_{E(IFF)}^{B}$ and $f_{E(IFF)}^{C}$ are the stress exposure values that are considered for determining the failure mode during the analysis.

Table 7.2. Degradation rules according to the failure mode.

Failure Mode	Degradation Rule
FF (Tension / Compression) or IFF(C) in at least 1/3 plies of a laminate	Failure of the laminate
IFF (A)	$E_2 = \eta E_2$ $G_{12} = \eta G_{12}$ $\nu_{12} = \eta \nu_{12}$
IFF (B)	$E_2 = \eta E_2$ $G_{12} = \eta G_{12}$ $\nu_{12} = \eta \nu_{12}$
IFF (C)	$E_2 = 0.1 E_2$ $G_{12} = 0.1 G_{12}$ $\nu_{12} = 0.1 \nu_{12}$

In Eq. (7.9) η is known as the degradation factor and can be expressed according to the equation below:

$$\eta = \frac{1 - \eta_r}{1 + c(f_{E(IFF)} - 1)^{\xi}} + \eta_r \tag{7.9}$$

The complete progressive failure analysis algorithm is implemented using ANSYS Parametric Design Language (APDL). First, using ANSYS APDL script, different material numbers are given to each element in of a lamina which constitute the composite laminate. This step is necessary, because during the execution of the progressive damage propagation, each element in a lamina is subjected to different degradation rules. Then, an extreme load case is applied incrementally to the model, and static analysis is run. Afterwards, in the post-processing module, stresses are read. From Puck failure criteria for FF (Eq. (7.1) and Eq. (7.2)) and IFF (Eqs. (7.6), (7.7) and (7.8)), stress exposures are calculated. Depending on the rules presented in Table 7.2 whether ply failure happens is checked. If ply failure occurs due to First-Fiber-Failure (FFF) or if IFF(C) is observed in at least one third of the plies of a laminate, laminate failure is assumed to take place. If IFF A or B or IFF C in any ply is seen, gradual degradation rules are applied, and after the assembly of the new constitutive material model, the load is increased, and the analysis is re-run. This calculation procedure is run until the solution does not converge. If the solution does

not converge, the analysis aborted. As long as no FF or IFF failure occurs, without updating the constitutive material model, load is incremented, and the analysis is executed.

Validation of the APDL Code against experimental data provided by Hinton et al, [111] is done for the [0/90]s GFRP laminate/MY750 and [0/±45/90]s CFRP laminate/AS4 3501-6 under uniaxial tension loading. As seen from Figure 7.7 ad Figure 7.8, there is a good agreement between ANSYS APDL Code and experimental data for the progressive failure analysis of [0/90]s GFRP/MY750 and [0/±45/90]s CFRP/AS4 3501-6 laminates.

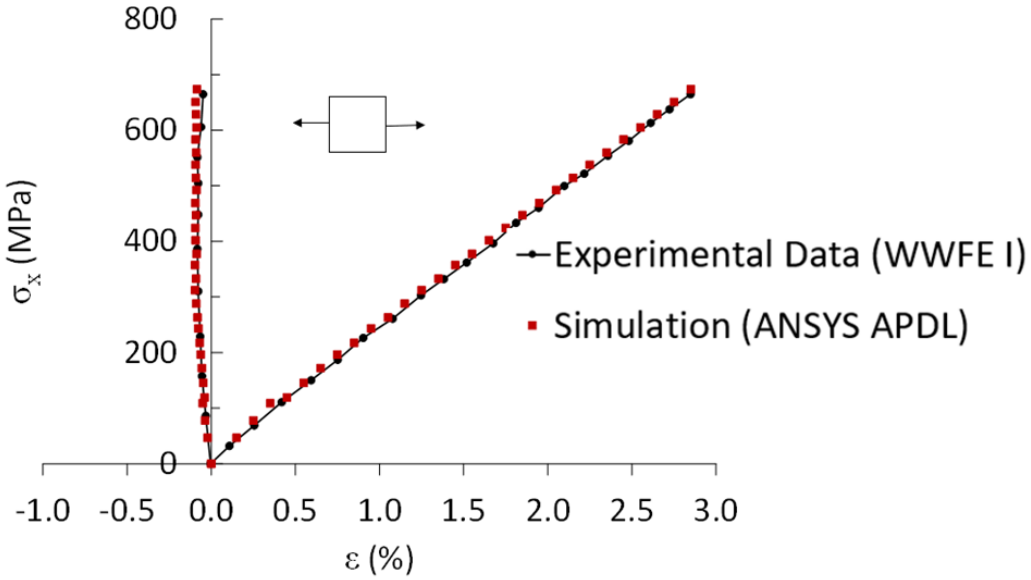

Figure 7.7. Validation of the ANSYS APDL Code for the progressive failure analysis of a $[0/90]_s$ GFRP MY750 laminate under σ_x uniaxial tension load based on Puck's damage model against experimental data [111].

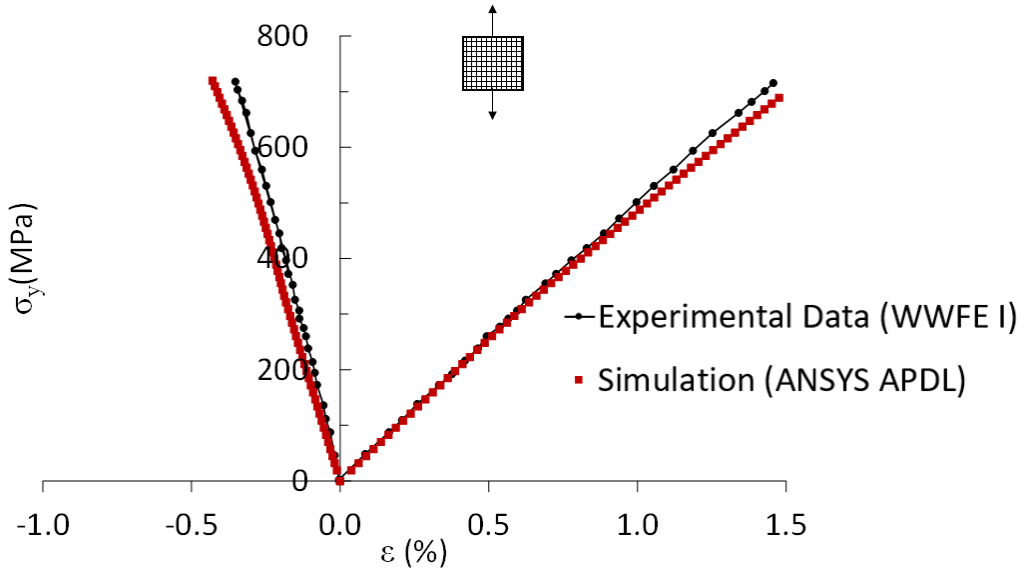

Figure 7.8. Validation of the ANSYS APDL Code for the progressive failure analysis of a $[0/\pm45/90]_s$ CFRP AS4 3501-6 laminate under σ_y uniaxial tension load based on Puck's damage model [111].

7.3 Results

7.3.1 Validation of the 5-m RUZGEM Wind Turbine Blade FE Model based on the Experimental Modal Analysis

In Table 7.3, the comparison of the first five eigenfrequencies of the RÜZGEM blade between experiments reported in Amer [140] and numerical simulations is summarized. According to the table, the deviation of the eigenfrequencies for the first four eigenfrequencies between experiments and FE simulations is less than 7%. For the fifth eigenmode which is torsion, the deviation between the experiment and the FE simulation is less than 11%. The reason for the higher deviation for the torsion eigenmode is attributed to the fact that shell elements used for building RÜZGEM blade FE Model cannot predict torsion mode accurately as reported in Pardo and Branner [144], Laird et al. [145] and Noever-Castelos et al. [65] In their recent study, Noever-Castelos et al [65] conducted an experimental modal analysis of a 20-m wind turbine blade and compared with FE simulations. For the 1st flap-wise, 1st edge-wise and 1st torsion eigenmodes, they were able to get an agreement of less than 6% and 12% for the free-free and fixed-free boundary conditions, respectively. Further, in the current validation study, the first five eigenmodes obtained from the fe simulations are compared with the tests and are found to be the same as in tests. In this report for demonstration reasons, only the 1st and 5th vibration eigenmodes from tests and FE simulations are displayed in Figure 7.9. Hence validation study of the 5-m RÜZGEM blade FE Model based on experimental modal analysis results is completed.

Table 7.3 Comparison of the 5-m RUZGEM blade modal analysis results between tests and FE simulations (adhesive mass included).

Mode Shape	Modal shaker tests	ANSYS FE Model	Deviation in % w.r.t. modal shaker tests
1	8.25	8.03	-3%
2	23.75	22.02	-7%
3	41.75	41.17	-1%
4	46.75	45.96	-2%
5	58.75	52.09	-11%

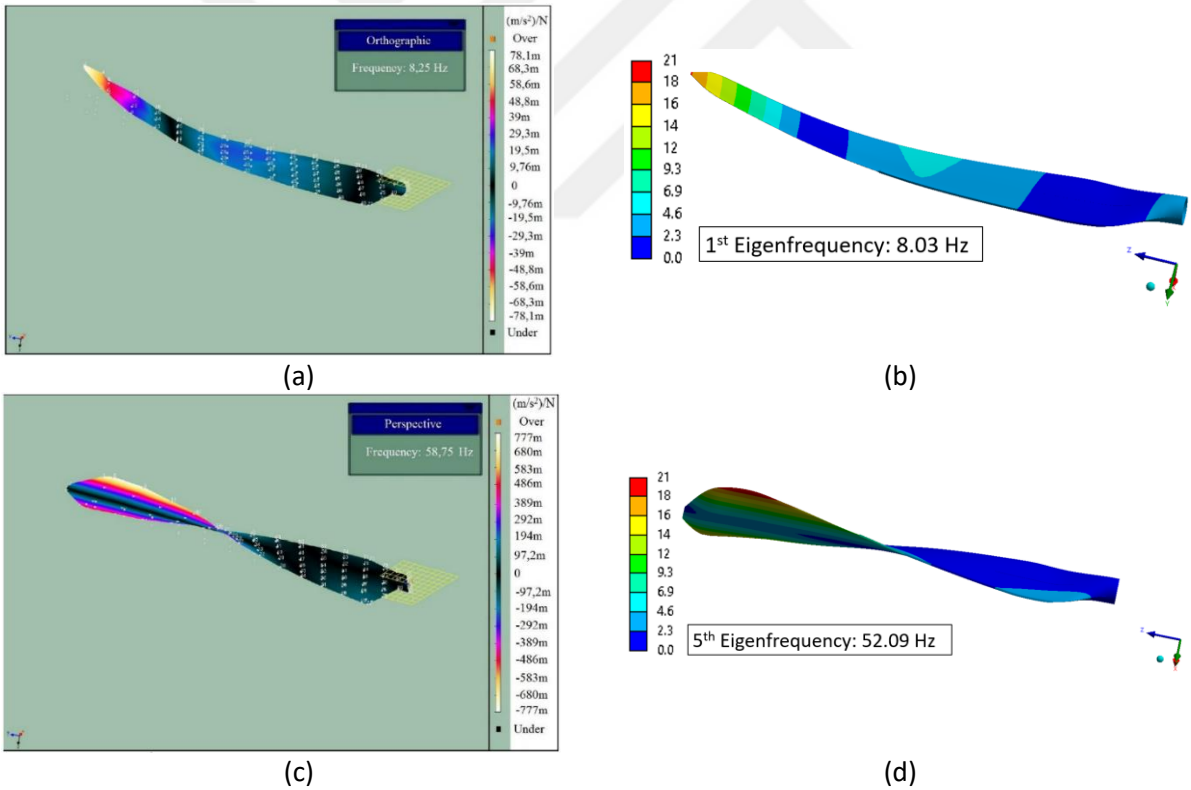

Figure 7.9. Comparison of the 5-m RÜZGEM blade 1st eigenmode between (a) experiment and (b) FE simulation, 5th eigenmode between (c) experiment and (d) fe simulation.

7.3.2 Progressive damage analysis of the 5-m RUZGEM Wind Turbine Blade using Puck's damage model

The load-displacement curve of the blade under extreme flapwise (max) loading for the linear elastic model and progressive damage model (Puck) is displayed in Figure 7.10. Load application and displacement measurement is done in flapwise (max) direction. According to the analysis results, after 99% loading, sudden drop is observed in the load-displacement curve. The total deformation of the nonlinear blade model under 99% flapwise (max) loading is displayed in Figure 7.11. As seen from the figure, the maximum deflection at the blade tip is 569 mm.

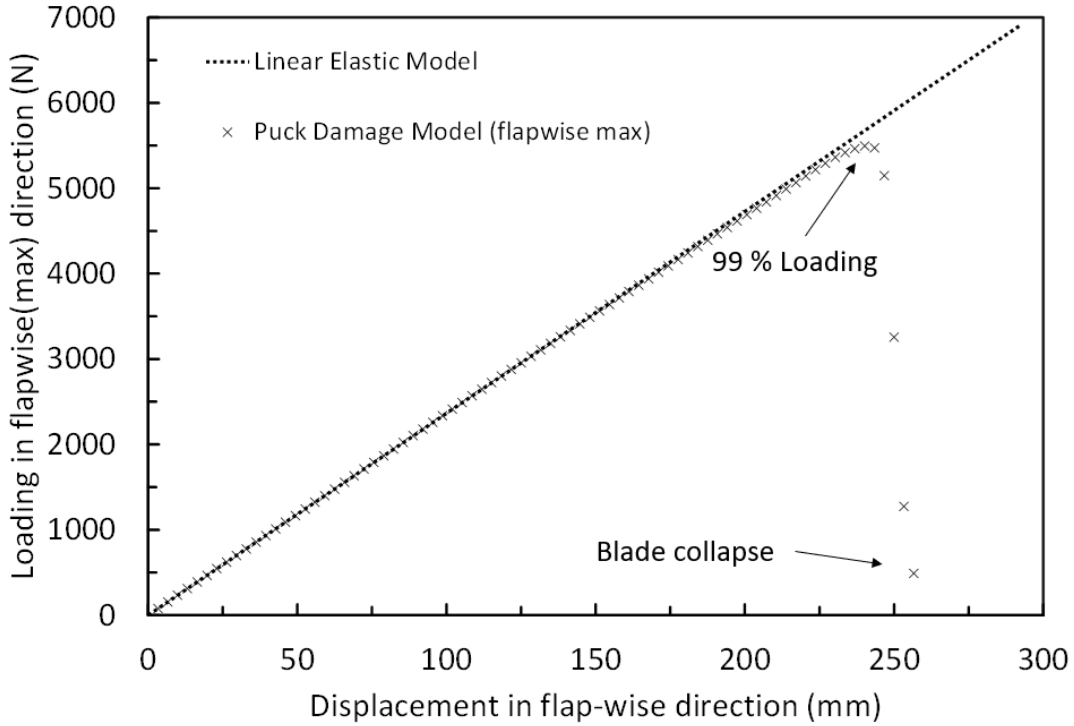

Figure 7.10. Load-displacement curves of the 5-m RÜZGEM blade using linear elastic model and progressive damage model (Puck) under flapwise (max) loading.

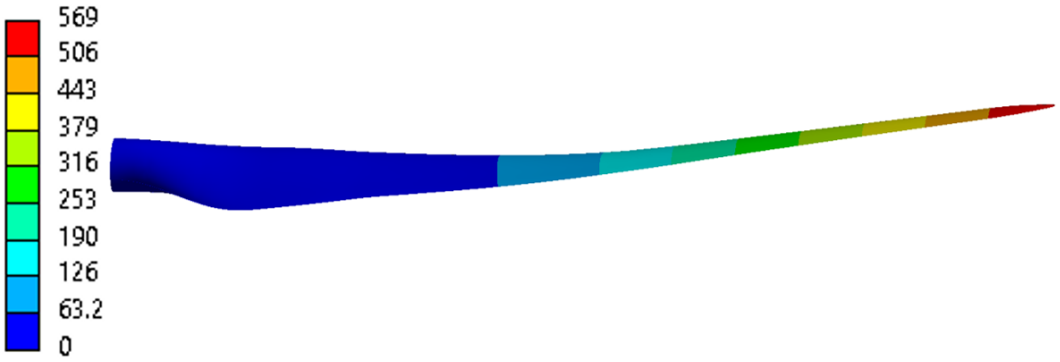

Figure 7.11. Total deformation of the 5-m RÜZGEM blade at 99% flapwise (max) loading (scale factor: × 2).

In Figure 7.12 interfiber failure mode A (IFF (A)) and interfiber failure mode B (IFF (B)) distribution in the suction side, internal flange, spar and pressure side of the blade at 93% flapwise (max) loading are shown. If both stress exposures are present in an element, the higher-stress-exposure IFF (A) or IFF (B) is shown. IFF (A) and IFF (B) do not lead to the element failure. When IFF (A) or IFF (B) occurs, only the transverse elasticity moduli, shear moduli, and Poisson's ratio are reduced according to the degradation rules [67]. Hence when IFF (A) or IFF (B) is detected sudden load drop in the load-displacement curve is not observed. From Figure 7.12, it is seen that in the root transition at the spar-pressure side and spar-suction intersection IFF (A) and IFF (B) failure exposures are higher in comparison to the other regions of the blade.

Damage evolution for fiber failure (FF) and interfiber failure mode (IFF (C)) in the pressure side, internal flange, spar and suction side at 93% flapwise (max) loading is depicted in Figure 7.13. From the figure it is observed that in the root transition at the spar-pressure side and spar-suction intersection FF and IFF (C) are higher in comparison to the other regions of the blade. According to the implemented methodology, element failure is done by setting its stiffness value to zero if FF or IFF (C) in at least one-third of the plies of a laminate is detected [67]. At 93% load level, the number of failed elements is not sufficient to cause a sudden drop in the load-displacement curve [67].

From Figure 7.12 and Figure 7.13, it is further noted that FF and IFF (C) initiate in the same location as IFF (A) and IFF (B), which can be considered as subcritical cracks. Similar to our findings, Montesano et al. [61] state that subcritical cracks can act as a precursor to more critical damage modes such as delamination or adhesive debonding. In the current study, IFF (C), which is a dangerous failure mode indicating risk of delamination, and FF are the critical failure modes which lead to element failure. Recently, Chen et al. [146]reported that matrix-dominant failure and delamination occurs before fiber-dominant failure at the trailing edge. Likewise, we observe IFF (A) or IFF (B) before FF or IFF(C) in the root transition region.

In Figure 7.14, element failure pattern in the pressure side, internal flange, spar and suction side of the RÜZGEM Blade (from top to bottom in a panel) under 99% of flapwise (max) loading is displayed. After 100% loading a sudden drop in the load-displacement curve is seen in Figure 7.10. As seen from Figure 7.15, failure initiation region is the spar-suction side intersection in the root transition region. This failure initiation region shows similarity with the findings in Chen et al. [53], where the collapse of a 52.3 wind turbine blade subjected to flapwise bending moment is investigated. In addition to this, Marin et al. estimated the fatigue life of a 300 kW wind turbine blade. Marin et al. [147] report that when there is an abrupt thickness, i.e. stiffness change in an aeroshell, bending stresses occur due to the thickness change in the airfoil. This situation causes an amplification of the stress level in this region. When this stress increase is combined with superficial cracks laminate failure occurs in this region. Similar to the findings in Marin et al. [147], RUZGEM blade fails at the spar-suction intersection, where we observe an abrupt change in the thickness, i.e. stiffness of the blade.

Element failure pattern in the pressure side, internal flange, spar and suction side of the RÜZGEM Blade (from top to bottom in a panel) before blade collapse under flapwise (max) loading is shown in Figure 7.15. Just before blade collapse, element failure region covers a larger area in the suction side and pressure side of the blade. Moreover, element failures are detected in the internal flange and spar at the root transition region.

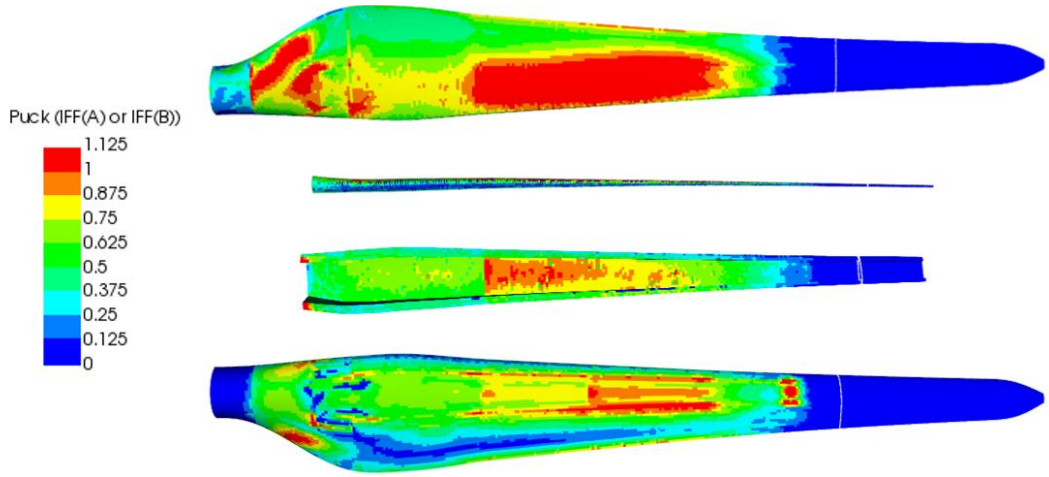

Figure 7.12. Damage evolution – IFF (A) or IFF (B) – in the pressure side, internal flange, spar and suction side of the blade (from top to bottom in a panel) at 93% of flapwise (max) loading.

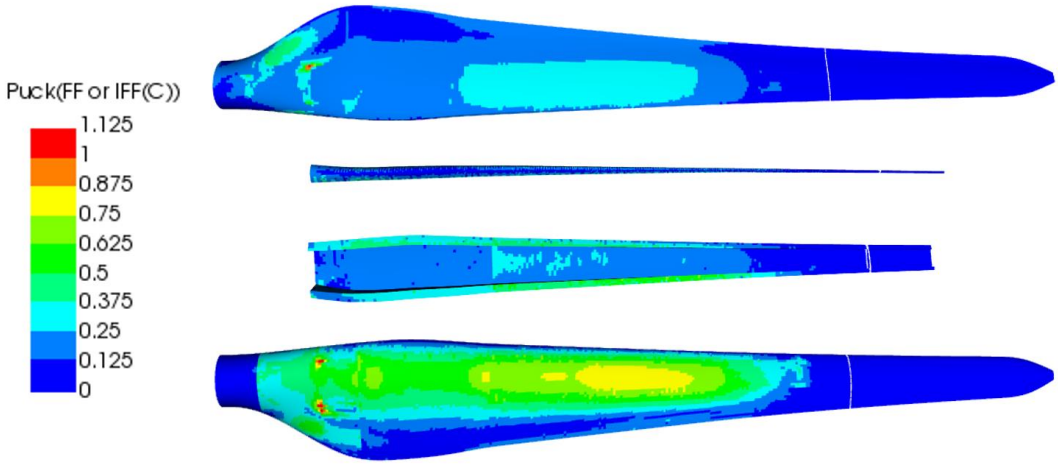

Figure 7.13. Damage evolution – FF or IFF (C) – in the pressure side, internal flange, spar and suction side of the blade (from top to bottom in a panel) at 93% of flapwise (max) loading.

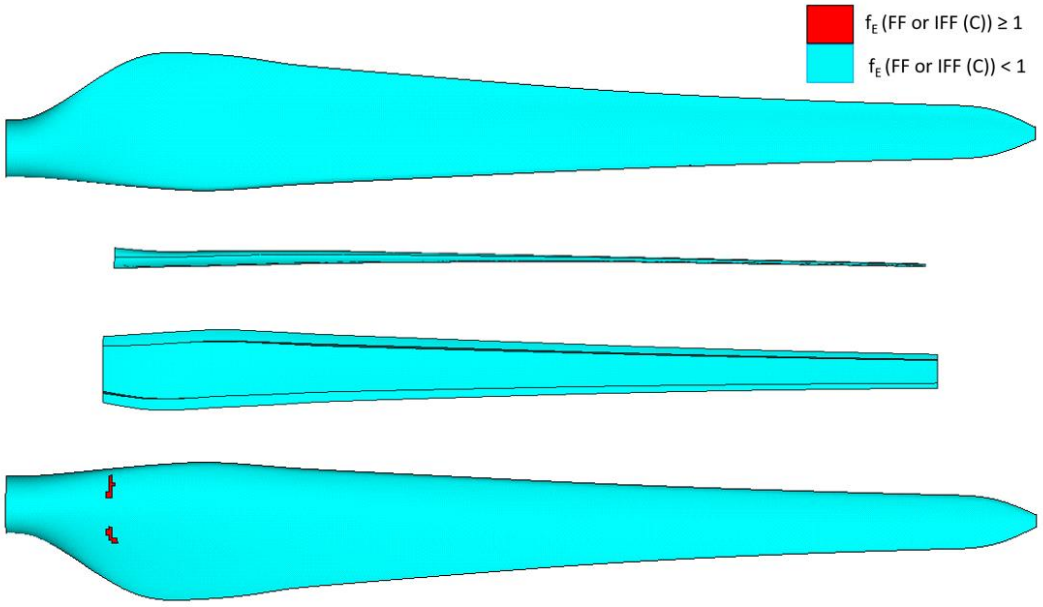

Figure 7.14. Element failure pattern in the pressure side, internal flange, spar and suction side of the blade (from top to bottom in a panel) at 99% of flapwise (max) loading.

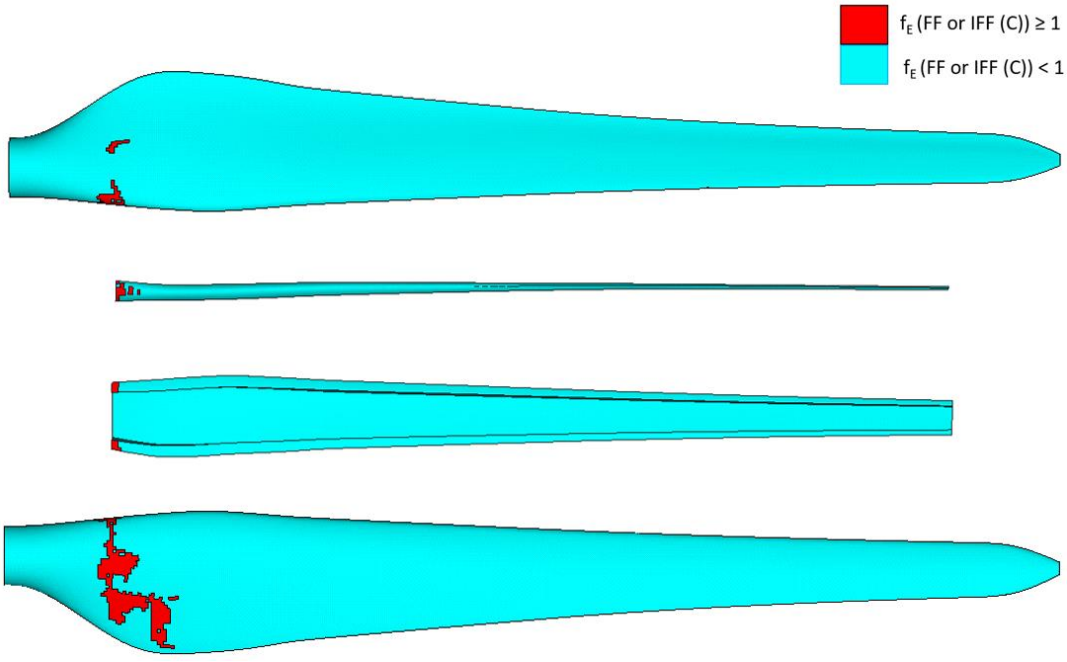

Figure 7.15. Element failure pattern in the pressure side, internal flange, spar and suction side of the blade (from top to bottom in a panel) before blade collapse under flapwise (max) loading.

7.4 Conclusions

In this work, the main failure mechanisms of the existing GFRP RÜZGEM wind turbine blade subjected to flapwise (max) loading are investigated by implementing Puck's physically based phenomenological model into the blade FE model. The implementation of Puck's damage model is done in ANSYS environment utilizing ANSYS APDL scripting language. The main conclusions are as follows:

- 5-m RUZGEM Blade is validated based on modal analysis results. The deviation of the eigenfrequencies for the first four eigenfrequencies between experiments and ANSYS simulations is less than 7%. For the fifth eigenmode which is torsion, the deviation between experiment and FE simulation is less than 11%. The reason for the higher deviation of the torsion eigenmode is attributed to the fact that shell elements used for building 5-m RÜZGEM blade FE Model cannot predict torsion mode accurately.
- Simulations are conducted for flapwise (max) loading using Puck's physically based phenomenological model as the intra-laminar damage model. Puck's model shows that laminate cracks initiate at the root transition region. Decrease in the load-displacement curve is observed after 99% loading under flapwise (max) loading due to the combined effect of delamination and fiber failure.
- According to the simulations using Puck's damage model, FF and IFF(C) initiate in the same location as IFF(A) and IFF(B). IFF(A) and IFF(B) denote subcritical ply cracks which precede more critical damage modes such as IFF(C) (which is an indicator of possible delamination), and FF.

CHAPTER 8

CONCLUSIONS AND FUTURE WORK

Within the scope of this thesis, three novel studies are presented:

(a) an analytical approach for the open hole strength prediction of composite laminates subjected uniaxial as well as bi-axial loading conditions,
(b) finite element model incorporating continuum damage and cohesive zone model for the prediction of size effects on sublaminate-scaled quasi-isotropic CFRP open hole tension laminates and
(c) finite element model using progressive damage analysis to predict failure and damage mechanisms of a 5-meter composite wind turbine blade.

These three independent studies all cover the same topic regarding the progressive failure models and their application to composite structures used in aircraft and wind energy industries. The specific conclusions regarding each study was given in their respective chapters. In this section, the overall conclusions and future work are presented.

8.1 Overall Conclusions

The overall conclusions drawn from this thesis can be summarized as following:

- Primary failure mechanism is the intralaminar failure in sublaminate-level scaled quasi-isotropic CFRP OHT laminates, however interface failure which is considered as a secondary failure mechanism is found to contribute significantly to the failure mechanism and must be included in the FE model for the experimentally observed damage pattern. Secondary failure mechanisms are crucial in modeling of composite structures, as they are

needed not only for the correct damage development and but also have a significant impact on the strength prediction of composite structures.

- Not only the nonlinear material damage model, but also the FE modeling technique using appropriate element types and boundary conditions is essential for simulating the realistic behavior of composite structures. Referring to the study on the numerical modeling of sublaminate-scaled quasi-isotropic CFRP open hole tension laminates, it was shown that layered shell elements and continuum shell elements with perfect bonding at interfaces lead to strength overpredictions of the OHT laminates. FE modeling technique with continuum shell elements per ply with interface failure is more successful in capturing the damage development and strength predictions observed in the experiments.

- Likewise, FE modeling wind turbine blades with shell elements underpredicted the torsion eigenmode when the simulations were compared with the modal shaker vibration test results. This result shows that the behavior of the blade modeled with shell elements may not be represented correctly under shear/torsion loading. To overcome this problem, wind turbine blades should be modeled using solid elements in combination with shell elements.

- In order to simulate the damage evolution in composite structure correctly, the first step is the analytical/numerical model building which represents the correct elastic material model. In this thesis, the significance of the validation study for the elastic as well as the damage model for a realistic analytical/numerical representation of the composite structure is highlighted. As an example, stress fields generated by the proposed analytical open hole strength calculation Extended Point Stress Method, is validated against the stress fields obtained using an FE model before implementing the material damage model. As another example of the validation study, the vibration analysis of 5-meter RÜZGEM wind turbine blade was conducted using the

blade FE model. The FE model was validated based on the test results obtained from the modal shaker. After the fe model validation, progressive damage analysis of the blade is carried out.

- For the preliminary design of composite structures fast and accurate analytical approaches are needed. However analytical approaches have limitations. Numerical models deliver more information regarding the failure characteristic of composite structures under complex loading scenarios. Yet, they are computationally expensive. Depending on the industrial application and research interest, the suitable analytical/numerical model must be selected.

8.2 Future Work

Future work proposals for the extension of the studies conducted within this thesis are as follows:

- In the proposed Extended Point Stress Method for the analytical strength prediction of composite laminates with open holes subjected to in-plane combined loading, instead of point stress criterion, average stress criterion can be implemented.

- As a further FE modeling strategy of open hole composite laminates, instead of continuum shell elements, solid elements can be used for modeling each ply individually. More advanced failure criteria, such as Puck, LarC04, Larc05 [148] can be used in the FE models built with solid elements. Regarding damage evolution, before and after the initiation of different failure modes, stress-strain responses proposed in [23] can be used.

- Severe convergence difficulties were encountered during the numerical solution of open hole laminates using an implicit solver and hence explicit solver was used for the simulations. In order to overcome convergence problems due to material softening, a zigzagging approach ([48],[49]) can be

implemented to approximate the linear material softening behavior in the stress-strain relationship.

- Size effect of the fiber strength can be considered in the open hole tension composite laminate FE simulations by a statistical strength distribution [117].
- The root cause of the damage initiation in the root transition region of the 5-meter RÜZGEM blade can further be investigated by a submodel of the blade root region using 3-D elements. Instead of the gradual degradation algorithm used in Puck's physically based phenomenological model, fracture energy-based degradation algorithm incorporating the crack band model [93], which alleviates mesh dependency can be implemented. Finally, when the 5-m RÜZGEM blade test rig is built, numerical results can be compared with the experimental results.

REFERENCES

[1] Davis Jr JG, Bohon HL. (1991) First NASA Advanced Composites Technology Conference, Part 2

[2] Lopes CS, González C, Falcó O, Naya F, LLorca J, Tijs B. (2016) Multiscale virtual testing: the roadmap to efficient design of composites for damage resistance and tolerance. CEAS Aeronautical Journal 7:607-19

[3] Nilsson S, Bredberg A, Asp L. (2009) Size effects on strength of notched CFRP laminates loaded in bending. InInternational Conference on Composite Materials: IOM Communications

[4] Falcó O, Ávila RL, Tijs B, Lopes CS. (2018) Modelling and simulation methodology for unidirectional composite laminates in a Virtual Test Lab framework. Composite Structures 190:137-59

[5] Sheng S. Report on wind turbine subsystem reliability-a survey of various databases (presentation) (2013). National Renewable Energy Lab.(NREL), Golden, CO (United States)

[6] Haselbach PU. (2015) Ultimate Strength of Wind Turbine Blades under Multiaxial Loading: DTU Wind Energy (Doctoral dissertation, PhD Thesis)

[7] Holmes JW, Sørensen BF, Brøndsted P. (2007) Reliability of wind turbine blades: An overview of materials testing. Proceedings of the Wind Power Shanghai. 35:36

[8] Chen X, Eder MA. (2020) A critical review of damage and failure of composite wind turbine blade structures. InIOP conference series: Materials science and engineering Vol. 942, No. 1, p. 012001 IOP Publishing.

[9] Camanho PP, Maimí P, Dávila CG (2007) Prediction of size effects in notched laminates using continuum damage mechanics. Composites Science and Technology 67:2715–2727

[10] Handbook MS. Composite Materials Handbook (2002) Volume 3, Polymer Matrix Composites, Guidelines for Characterization of Structural Materials, Department of Defense Handbook, USA. MILHDBK-17-1F

[11] Awerbuch J, Madhukar MS (1985) Notched Strength of Composite Laminates: Predictions and Experiments—A Review. Journal of Reinforced Plastics and Composites 4:3–159

[12] Chen BY, Tay TE, Baiz PM, Pinho ST (2013) Numerical analysis of size effects on open-hole tensile composite laminates. Composites Part A: Applied Science and Manufacturing 47:52–62

[13] Camanho PP, Erçin GH, Catalanotti G, Mahdi S, Linde P (2012) A finite fracture mechanics model for the prediction of the open-hole strength of composite laminates. Composites Part A: Applied Science and Manufacturing 43:1219–1225

[14] Waddoups ME, Eisenmann JR, Kaminski BE. (1971) Macroscopic fracture mechanics of advanced composite materials. Journal of composite materials 5(4):446-54

[15] Whitney JM, Nuismer RJ. Stress fracture criteria for laminated composites containing stress concentrations. Journal of composite materials. 1974 Jul;8(3):253-65.

[16] Karlak RF (1977) Hole effects in a related series of symmetrical laminates. In: Proceedings of the Fourth Joint ASM-Metallurgical Society of AIME Symposium on Failure Modes in Composites, 1977. pp 105–117

[17] Pipes RB, Wetherhold RC, Gillespie JW (1979) Notched Strength of Composite Materials. Journal of Composite Materials 13:148–160

[18] Tan SC. (1987) Notched strength prediction and design of laminated composites under in-plane loadings. Journal of Composite Materials 21(8):750-80

[19] Tan SC. (1988) Mixed-mode fracture of notched composite laminates under uniaxial and multiaxial loading. Engineering fracture mechanics 31(5):733-46.

[20] Taylor D (2009) On the application of the Theory of Critical Distances for prediction of fracture in fibre composites. Frattura ed Integrità Strutturale 4:3–9

[21] Günel M, Kayran A (2013) Non-linear progressive failure analysis of open-hole composite laminates under combined loading. Journal of Sandwich Structures and Materials 15:309–339

[22] Bao H, Liu G (2016) Progressive failure analysis on scaled open-hole tensile composite laminates. Composite Structures 150:173–180

[23] Furtado C, Catalanotti G, Arteiro A, Gray PJ, Wardle BL, Camanho PP (2019) Simulation of failure in laminated polymer composites: Building-block validation. Composite Structures 226:111168

[24] Soutis C, Fleck NA (1990) Static compression failure of carbon fibre T800/924C composite plate with a single hole. Journal of Composite Materials 24:536–558

[25] Ercin GH. (2013) Stress gradient effects in laminated composites (Doctoral dissertation, Universidade do Porto (Portugal))

[26] Erçin GH, Camanho PP, Xavier J, Catalanotti G, Mahdi S, Linde P (2013) Size effects on the tensile and compressive failure of notched composite laminates. Composite Structures 96:736–744

[27] Furtado C, Arteiro A, Bessa MA, Wardle BL, Camanho PP (2017) Prediction of size effects in open-hole laminates using only the Young's modulus, the strength, and the R-curve of the 0 ply. Composites Part A: Applied Science and Manufacturing 101:306–317

[28] Soutis C, Filiou C, Pateau V. (1998) Strength prediction of CFRP plates with a hole under biaxial compression-tension. In 39th AIAA/ASME/ASCE/AHS/ASC Structures, Structural Dynamics, and Materials Conference and Exhibit p. 1701

[29] Soutis C, Fleck NA, Smith PA (1991) Failure prediction technique for compression loaded carbon fibre-epoxy laminate with open holes. Journal of Composite Materials 25:1476–1498

[30] Daniel IM (1980) Behavior of graphite/epoxy plates with holes under biaxial loading. Experimental Mechanics 20:1–8

[31] Sutherland LS, Shenoi RA, Lewis SM. (1999) Size and scale effects in composites: I. Literature review. Composites Science and Technology 59(2):209-20

[32] Sutherland LS, Shenoi RA, Lewis SM. (1999) Size and scale effects in composites: II. Unidirectional laminates. Composites Science and Technology 59(2):221-33

[33] Sutherland LS, Shenoi RA, Lewis SM. (1999) Size and scale effects in composites: III. Woven-roving laminates. Composites Science and Technology 59(2):235-51

[34] Green BG, Wisnom MR, Hallett SR. (2007) An experimental investigation into the tensile strength scaling of notched composites. Composites Part A: Applied Science and Manufacturing 38(3):867-78

[35] Wisnom MR, Hallett SR, Soutis C. (2010) Scaling effects in notched composites. Journal of Composite Materials 44(2):195-210

[36] Chen BY, Tay TE. (2017) Progressive damage in fibre-reinforced composites: towards more accurate and efficient computational modelling and analysis. The Structural Integrity of Carbon Fiber Composites: Fifty Years of Progress and Achievement of the Science, Development, and Applications 391-423

[37] Wisnom MR, Hallett SR. (2009) The role of delamination in strength, failure mechanism and hole size effect in open hole tensile tests on quasi-isotropic laminates. Composites Part A: Applied Science and Manufacturing 40(4):335-42

[38] Hallett SR, Green BG, Jiang WG, Wisnom MR. (2009) An experimental and numerical investigation into the damage mechanisms in notched composites. Composites Part A: Applied Science and Manufacturing 40(5):613-24

[39] Nixon-Pearson OJ, Hallett SR, Harper PW, Kawashita LF. (2013) Damage development in open-hole composite specimens in fatigue. Part 2: Numerical modelling. Composite Structures 106:890-8

[40] Bao H, Liu G. (2016) Progressive failure analysis on scaled open-hole tensile composite laminates. Composite Structures 150:173-80

[41] Abisset E, Daghia F, Ladevèze P. (2011) On the validation of a damage mesomodel for laminated composites by means of open-hole tensile tests on quasi-isotropic laminates. Composites Part A: Applied Science and Manufacturing 42(10):1515-24

[42] Van der Meer FP, Sluys LJ, Hallett SR, Wisnom MR. (2012) Computational modeling of complex failure mechanisms in laminates. Journal of Composite Materials 46(5):603-23

[43] Ridha M, Wang CH, Chen BY, Tay TE. (2014) Modelling complex progressive failure in notched composite laminates with varying sizes and stacking sequences. Composites Part A: Applied Science and Manufacturing 58:16-23

[44] Aidi B, Case SW. (2015) Experimental and numerical analysis of notched composites under tension loading. Applied Composite Materials 22:837-55.

[45] Yoon D, Kim S, Kim J, Doh Y. (2019) Development and evaluation of crack band model implemented progressive failure analysis method for notched composite laminate. Applied Sciences 9(24):5572

[46] Lee J, Soutis C. (2008) Measuring the notched compressive strength of composite laminates: Specimen size effects. Composites Science and Technology 68(12):2359-66

[47] Su ZC, Tay TE, Ridha M, Chen BY. (2015) Progressive damage modeling of open-hole composite laminates under compression. Composite Structures 122:507-17

[48] Graça-e-Costa R, Alfaiate J, Dias-da-Costa D, Sluys LJ. (2012) A non-iterative approach for the modelling of quasi-brittle materials. International Journal of Fracture 178:281-98

[49] Rots JG, Invernizzi S, Belletti B. (2006) Saw-tooth softening/stiffening-a stable computational procedure for RC structures. Computers and Concrete 3(4):213-33

[50] Zhou S, Zhang J, Sun Y, Tian K. (2019) Experimental and numerical investigation of open hole carbon fiber composite laminates under

compression with three different stacking sequences. Journal of Materials Research and Technology 8(3):2957-68

[51] Hoffman O. (1967) The brittle strength of orthotropic materials. Journal of Composite materials 1(2):200-6

[52] Hu YL, Madenci E. (2017) Peridynamics for fatigue life and residual strength prediction of composite laminates. Composite Structures 160:169-84.

[53] Chen X, Zhao X, Xu J (2017) Revisiting the structural collapse of a 52.3 m composite wind turbine blade in a full-scale bending test. Wind Energy 20:1111–1127

[54] Jensen FM, Falzon BG, Ankersen J, Stang H (2006) Structural testing and numerical simulation of a 34 m composite wind turbine blade. Compos Struct 76:52–61

[55] Overgaard LCT, Lund E, Thomsen OT (2010) Structural collapse of a wind turbine blade. Part A: Static test and equivalent single layered models. Composites Part A: Applied Science and Manufacturing 41:257–270

[56] Overgaard LC, Lund E. (2010) Structural collapse of a wind turbine blade. Part B: Progressive interlaminar failure models. Composites Part A: Applied Science and Manufacturing 41(2):271-83

[57] Yang J, Peng C, Xiao J, Zeng J, Xing S, Jin J, Deng H (2013) Structural investigation of composite wind turbine blade considering structural collapse in full-scale static tests. Composite Structures 97:15–29

[58] Kim S-H, Bang H-J, Shin H-K, Jang M-S (2014) Composite structural analysis of flat-back shaped blade for multi-MW class wind turbine. Applied Composite Materials 21:525–539

[59] Chen X, Zhao W, Zhao XL, Xu JZ (2014) Failure test and finite element simulation of a large wind turbine composite blade under static loading. Energies (Basel) 7:2274–2297

[60] Haselbach PU, Branner K (2016) Initiation of trailing edge failure in full-scale wind turbine blade test. Engineering Fracture Mechanics 162:136–154

[61] Montesano J, Chu H, Singh CV (2016) Development of a physics-based multi-scale progressive damage model for assessing the durability of wind turbine blades. Composite Structures 141:50–62

[62] Zuo Y, Montesano J, Singh CV (2018) Assessing progressive failure in long wind turbine blades under quasi-static and cyclic loads. Renewable Energy 119:754–766

[63] Paquette JA, Veers PS (2007) Increased Strength in Wind Turbine Blades through Innovative Structural Design. Sandia National Lab.(SNL-NM), Albuquerque, NM (United States)

[64] Chen X, Qin Z, Yang K, Zhao X, Xu J (2015) Numerical analysis and experimental investigation of wind turbine blades with innovative features: Structural response and characteristics. Science China Technological Sciences 58:1–8

[65] Noever-Castelos P, Haller B, Balzani C (2022) Validation of a modeling methodology for wind turbine rotor blades based on a full-scale blade test. Wind Energy Science 7:105–127

[66] Ozyildiz M, Muyan C, Coker D (2018) Strength analysis of a composite turbine blade using puck failure criteria. In: Journal of Physics: Conference Series. IOP Publishing, p 042027

[67] Muyan C, Coker D (2020) Finite element simulations for investigating the strength characteristics of a 5 m composite wind turbine blade. Wind Energy Science 5:1339–1358

[68] Muyan C, Coker D (2020) Strength analysis of a 5-m composite wind turbine blade under static and fatigue loading conditions. In: IOP Conference Series: Materials Science and Engineering. IOP Publishing, p 012045

[69] Daniel IM, Ishai O, Daniel IM, Daniel I (2006) Engineering mechanics of composite materials. Oxford university press New York

[70] Kelly A, Macmillan NH (1966) Strong Solids' Clarendon Press

[71] Hill R (1948) A theory of the yielding and plastic flow of anisotropic metals. Proceedings of the Royal Society of London Series A Mathematical and Physical Sciences 193:281–297

[72] Tsai SW (1968) Strength theories of filamentary structure. Fundamental aspects of fiber reinforced plastic composites

[73] Jones RM (1999) Mechanics of Composite Materials, Taylor & Francis. Inc., USA

[74] Tsai SW, Wu EM (1971) A general theory of strength for anisotropic materials. J Compos Mater 5:58–80

[75] Liu K-S, Tsai SW (2004) A progressive quadratic failure criterion for a laminate. In: Failure Criteria in Fibre-Reinforced-Polymer Composites. Elsevier, pp 334–352

[76] Yamada SE, Sun CT (1978) Analysis of laminate strength and its distribution. J Compos Mater 12:275–284

[77] Hashin Z, Rotem A (1973) A fatigue failure criterion for fiber reinforced materials. J Compos Mater 7:448–464

[78] Hashin Z (1980) Failure criteria for unidirectional fiber composites.

[79] Lutz G, Getriebebau V (2006) The Puck theory of failure in laminates in the context of the new guideline VDI 2014 Part 3. Conference on damage in composite materials

[80] Puck A (1969) Festigkeitsberechnung an Glasfaser/Kunststoff-Laminaten bei zusammengesetzter Beanspruchung. Kunststoffe 59:780–787

[81] Puck A, Schneider W (1969) On failure mechanisms and failure criteria of filament-wound glass-fibre/resin composites. Plastics and Polymers 37:33–43

[82] Knops M (2008) Analysis of failure in fiber polymer laminates: the theory of Alfred Puck. Springer Science & Business Media

[83] Puck A, Schürmann H (2002) Failure analysis of FRP laminates by means of physically based phenomenological models. Compos Sci Technol 62:1633–1662

[84] Puck A, Schürmann H (1998) FAILURE ANALYSIS OF FRP LAMINATES BY MEANS OF PHYSICALLY BASED PHENOMENOLOGICAL MODELS. Composites Science and Technology 58:1045–1067

[85] Puck A, Mannigel M (2007) Physically based non-linear stress–strain relations for the inter-fibre fracture analysis of FRP laminates. composites science and technology 67:1955–1964

[86] Tan SC (1994) Stress concentrations in laminated composites. Routledge

[87] Sutcliffe MPF, Xin A, Fleck NA, Curtis PT (1999) Composite compressive strength modeller. Engineering Department, Cambridge University, Cambridge, UK

[88] Cornetti P, Pugno N, Carpinteri A, Taylor D (2006) Finite fracture mechanics: a coupled stress and energy failure criterion. Engineering Fracture Mechanics 73:2021–2033

[89] Bowie OL (1956) Analysis of an infinite plate containing radial cracks originating at the boundary of an internal circular hole. Journal of Mathematics and Physics 35:60–71

[90] Lekhnitskii SG (1968) Anisotropic Plates (translated from second Russian edition by Tsai, SW and Cheron, T.) Gordon and Breach Science Publishers. New York

[91] Ugural AC, Fenster SK (2011) Advanced mechanics of materials and applied elasticity. Pearson Education

[92] Kundu T (2008) Fundamentals of fracture mechanics. CRC press

[93] Lapczyk I, Hurtado JA (2007) Progressive damage modeling in fiber-reinforced materials. Compos Part A Appl Sci Manuf 38:2333–2341

[94] Matzenmiller A, Lubliner J, Taylor RL (1995) A constitutive model for anisotropic damage in fiber-composites. Mechanics of materials 20:125–152

[95] Highsmith AL, Reifsnider KL. (1982) Stiffness-reduction mechanisms in composite laminates. ASTM International

[96] Talreja R. (1985) Transverse cracking and stiffness reduction in composite laminates. Journal of composite materials 19(4):355-75

[97] Maimí P, Camanho PP, Mayugo JA, Dávila CG. (2006) A thermodynamically consistent damage model for advanced composites

[98] Maimí P, Camanho PP, Mayugo JA, Dávila CG. (2007) A continuum damage model for composite laminates: Part I–Constitutive model. Mechanics of materials 39(10):897-908

[99] Davila CG, Camanho PP, Rose CA. (2005) Failure criteria for FRP laminates. Journal of Composite materials 39(4):323-45

[100] Dávila CG, Camanho PP. (2003) Failure criteria for FRP laminates in plane stress. Report NASA. TM-2003-212663

[101] Pinho ST, Dávila CG, Camanho PP, Iannucci L, Robinson P. (2005) Failure models and criteria for FRP under in-plane or three-dimensional stress states including shear non-linearity

[102] Camanho PP, Dávila CG. (2002) Mixed-mode decohesion finite elements for the simulation of delamination in composite materials

[103] Bažant ZP, Oh BH (1983) Crack band theory for fracture of concrete. Matériaux et construction 16:155–177

[104] Berbinau P, Filiou C, Soutis C (2001) Stress and failure analysis of composite laminates with an inclusion under multiaxial compression-tension loading. Applied composite materials 8:307–326

[105] Konish HJ, Whitney JM. (1975) Approximate stresses in an orthotropic plate containing a circular hole. Journal of composite materials 9(2):157-66.

[106] Barbero EJ. (2013) Finite element analysis of composite materials using AbaqusTM. Boca Raton: CRC press

[107] Benzeggagh ML, Kenane MJ. (1996) Measurement of mixed-mode delamination fracture toughness of unidirectional glass/epoxy composites with mixed-mode bending apparatus. Composites science and technology 56(4):439-49

[108] May M, Hallett SR. (2010) A combined model for initiation and propagation of damage under fatigue loading for cohesive interface elements. Composites Part A: Applied Science and Manufacturing 41(12):1787-96

[109] The Mathworks Inc. (2021) MATLAB Release R2021a

[110] Aircraft Engineering TU Dresden (2022) elamX Open Source Composite Calculator

[111] Hinton MJ, Kaddour AS, Soden PD (2002) Evaluation of failure prediction in composite laminates: background to 'part B'of the exercise. Composites Science and Technology 62:1481–1488

[112] Yamada SE, Sun CT (1978) Analysis of laminate strength and its distribution. J Compos Mater 12:275–284

[113] Materials AS for T and (2018) Standard test method for open-hole tensile strength of polymer matrix composite laminates.

[114] Camanho PP, Lambert M (2006) A design methodology for mechanically fastened joints in laminated composite materials. Composites Science and Technology 66:3004–3020

[115] Moure MM, Herrero-Cuenca J, Garcia-Castillo SK, Barbero E (2020) Design tool to predict the open-hole failure strength of composite laminates subjected to in-plane loads. Composite Structures 238:111970

[116] Green BG, Wisnom MR, Hallett SR (2007) An experimental investigation into the tensile strength scaling of notched composites. Composites Part A: Applied Science and Manufacturing 38:867–878

[117] Wisnom MR, Khan B, Hallett SR (2008) Size effects in unnotched tensile strength of unidirectional and quasi-isotropic carbon/epoxy composites. Composite Structures 84:21–28

[118] OBrien TK, Krueger R. (2001) Analysis of ninety-degree flexure tests for characterization of composite transverse tensile strength. No. NAS 1.15: 211227

[119] Hexcel Product Data Sheet (2020) Prepreg properties – HexPly 8552 UD Carbon Prepregs.https://www.hexcel.com/user_area/content_media/raw/HexPly_8552_eu_DataSheet.pdf

[120] Colavita M, Bowler A, Zhang X, Irving PE (2006) Adhesively bonded CFRP straps as fatigue crack growth retarders on AA2024-T3. Proceedings of SAMPE Conference 2006

[121] Huang Y, Ha SK, Koyanagi J, Melo JDD, Kumazawa H, Susuki I (2010) Effects of an open hole on the biaxial strengths of composite laminates. J Compos Mater 44:2429–2445

[122] Khan B, Potter K, Hallett SR, Wisnom MR (2004) Size effects in unidirectional and quasi-isotropic composites loaded in tension. 2nd International Conference on Composites Testing and Model Identification

[123] Peterson RE (1974) Stress concentration factors: Charts and relations useful in making strength calculations for machine parts and structural elements (Book). New York, Wiley-Interscience, 1974. 329 p

[124] SIMULIA Inc., Dassault Systems (2019) ABAQUS User's Manual

[125] Bessa M. (2010) Meso-mechanical model of the structural integrity of advanced composite laminates (Master of Science dissertation, Universidade do Porto (Portugal))

[126] Camanho PP, Davila CG, De Moura MF. (2003) Numerical simulation of mixed-mode progressive delamination in composite materials. Journal of composite materials 37(16):1415-38

[127] Lopes CS, Camanho PP, Gürdal Z, Maimí P, González EV. (2009) Low-velocity impact damage on dispersed stacking sequence laminates. Part II: Numerical simulations. Composites Science and Technology 69(7-8):937-47

[128] Tavares CM, Camanho PP, de Melo FQ. (2006) Fracture of advanced composite materials: experimental basis for a constitutive model. Tech rep, University of Porto report SMAP, Porto, Portugal

[129] Yang Q, Cox B. (2005) Cohesive models for damage evolution in laminated composites. International Journal of Fracture 133(2):107-37

[130] Turon A, Davila CG, Camanho PP, Costa J. (2007) An engineering solution for mesh size effects in the simulation of delamination using cohesive zone models. Engineering fracture mechanics 74(10):1665-82

[131] Harper PW, Hallett SR. (2008) Cohesive zone length in numerical simulations of composite delamination. Engineering Fracture Mechanics 75(16):4774-92

[132] Camanho PP, Dávila CG, Pinho ST, Remmers JJ, Turon A, Costa J, Camanho PP, Maimí P. (2008) Analytical and numerical investigation of the length of the cohesive zone in delaminated composite materials. In Mechanical response of composites (pp. 77-97).Springer Netherlands

[133] González E v, Maimí P, Camanho PP, Turon A, Mayugo JA (2012) Simulation of drop-weight impact and compression after impact tests on composite laminates. Compos Struct 94:3364–3378

[134] Su, Z. C., Tay, T. E., Ridha, M., & Chen, B. Y. (2015). Progressive damage modeling of open-hole composite laminates under compression. Composite Structures, 122, 507–517

[135] Pinho ST, Iannucci L, Robinson P. (2006) Physically-based failure models and criteria for laminated fibre-reinforced composites with emphasis on fibre kinking: Part I: Development. Compos Part A Appl Sci Manuf. 37:63–73.

[136] ANSYS Inc. (2021) ANSYS Mechanical APDL Release R2021a

[137] Philippidis, T. and Roukis, G. (2013) Structure design report of METUWIND small rotor Blade, Confidential Interim Report, CORE team of the University of Patras, Greece

[138] Lloyd G (2010) Rules and Regulations, IV-Industrial Services. Part l—Guideline for Certification of Wind Turbines

[139] International Electrotechnical Comission IEC 61400-23: Wind Turbine Part 23 (2015) Full-Scale Structural Testing of Rotor Blades

[140] Amer C (2015) Development of a high-fidelity finite element model of a wind turbine blade via modal testing. Master's thesis, Middle East Tecnical University

[141] Dean A, Kumar PKAV, Reinoso J, Gerendt C, Paggi M, Mahdi E, Rolfes R (2020) A multi phase-field fracture model for long fiber reinforced composites based on the puck theory of failure. Composite Structures 51:11244665

[142] Passipoularidis VA, Philippidis TP, Brondsted P. (2011) Fatigue life prediction in composites using progressive damage modelling under block and spectrum loading. International Journal of Fatigue 33(2):132-44

[143] Knops M, Bögle C. (2006) Gradual failure in fibre/polymer laminates. Composites Science and Technology 66(5):616-25

[144] Pardo DR, Branner K (2005) Finite element analysis of the cross-section of wind turbine blades; a comparison between shell and 2D-solid models. Wind Engineering 29:25–31

[145] Laird D, Montoya F, Malcolm D (2005) Finite element modeling of wind turbine blades. In: 43rd AIAA Aerospace Sciences Meeting and Exhibit. p 195

[146] Chen X, Berring P, Madsen SH, Branner K, Semenov S (2019) Understanding progressive failure mechanisms of a wind turbine blade trailing edge section through subcomponent tests and nonlinear FE analysis. Composite Structures 214:422–438

[147] Marin JC, Barroso A, Paris F, Canas J. (2009) Study of fatigue damage in wind turbine blades. Engineering failure analysis 16(2):656-68

[148] Pinho ST, Darvizeh R, Robinson P, Schuecker C, Camanho PP. (2012) Material and structural response of polymer-matrix fibre-reinforced composites. Journal of Composite Materials 46(19-20):2313-41

APPENDICES

A. Material Database

Table A.1 Mechanical Properties for IMA/M21E Lamina

Material Data for IMA/M21E Lamina			
Longitudinal Modulus,	E_1	=	154000 (MPa)
Transverse Modulus,	E_2	=	8500 (MPa)
In-plane Shear Modulus,	G_{12}	=	4200 (MPa)
Major Poisson's Ratio,	υ_{12}	=	0.35 (MPa)
Longitudinal Tensile Strength,	Xt	=	2610 (MPa)
LongitudinalCompressive Strength,	Xc	=	1450 (MPa)
Transverse Tensile Strength,	Yt	=	55 (MPa)
Transverse Compressive Strength,	Yc	=	285 (MPa)
In-plane Shear Strength,	S	=	105 (MPa)

Table A.2 Mechanical Properties for Carbon / Epoxy (AS4/3501-6) Lamina [69]

Material Data for Carbon/Epoxy (AS4/3501-6) Lamina			
Longitudinal Modulus,	E_1	=	147000 (MPa)
Transverse Modulus,	E_2	=	10300 (MPa)
In-plane Shear Modulus,	G_{12}	=	7000 (MPa)
Major Poisson's Ratio,	υ_{12}	=	0.27 (MPa)
Longitudinal Tensile Strength,	Xt	=	2280 (MPa)
LongitudinalCompressive Strength,	Xc	=	1725 (MPa)
Transverse Tensile Strength,	Yt	=	57 (MPa)
Transverse Compressive Strength,	Yc	=	228 (MPa)
In-plane Shear Strength,	S	=	76 (MPa)

B. Validation Study for the Stress Field Generated by the Extended Point Stress Method MATLAB Code

In this appendix, results from the sample runs are presented to show the validation study of the developed Extended Point Stress Method (EPSM) MATLAB Code with the Finite Element Method (FEM) results. For this purpose, stress field distributions obtained from the EPSM MATLAB Code for a quasi-isotropic IMA/M21E laminate with an open hole subjected to uniaxial and combined loading conditions are compared with Finite Element Analysis results.

B.1 FE Model of the Laminate with an Open Hole (width-to-hole diameter: 40) under Uniaxial Loading

Finite Element Model of a $[45°/90°/-45°/0°]_s$ CFRP (IMA/M21E) 200 mm x 200 mm square laminate with a 5 mm diameter circular hole under uniaxial loading is modeled in ANSYS environment. The dimensions of the CFRP OHT laminate are chosen so that the finite width effect is neglected and the stress field of an infinite plate with a hole is simulated. Since the model is symmetric with respect to its midplane in the thickness direction, only half of the layers are modeled. For this reason, rotational degrees of freedom in x and y directions as well as displacement degree of freedom in z direction are fixed on the symmetry plane. FEM model uses orthotropic material properties and classical lamination theory. Mechanical properties for carbon/epoxy (IMA/M21E) are summarized in Table A.1. The necessary boundary conditions for this modeling technique are shown in Figure B.1, where a uniform flux of 100 N/mm is applied to the right and left edges. Plane stress elements (SHELL 181) are used for generating the mesh of the open hole composite laminate.

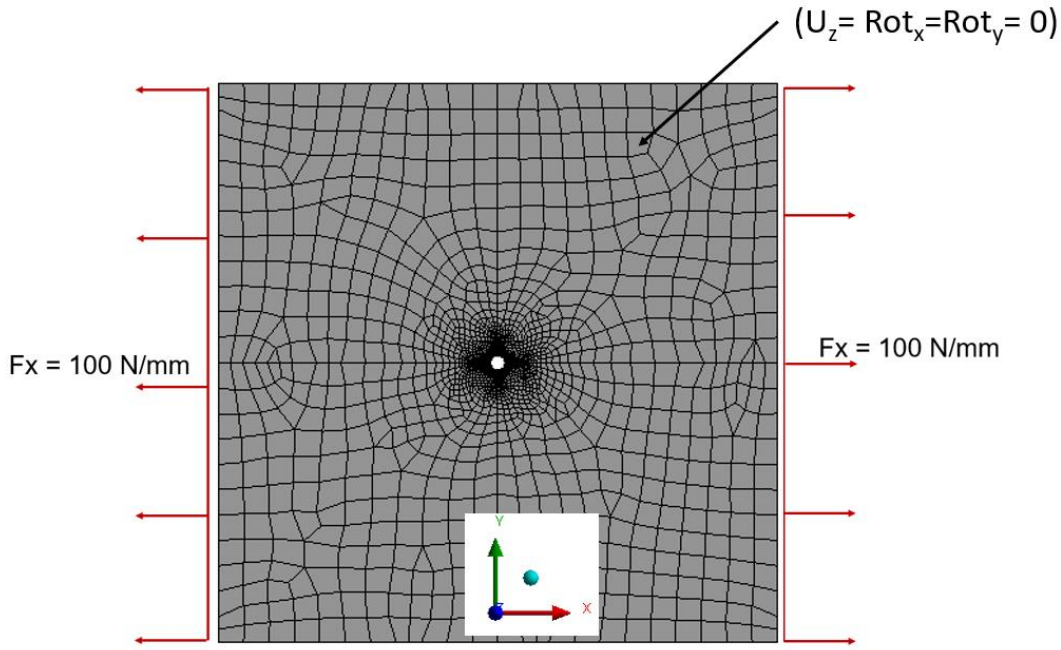

Figure B.1. Loads and boundary conditions of the $[45º/90º/-45º/0º]_s$ CFRP laminate (IMA/M21E) with an open hole (width-to-hole diameter=40) under uniaxial loading.

B.2 Comparison of Stress Fields Generated by the Semi-Analytical EPSM Method and FEM for the Laminate with an Open Hole under Uniaxial Loading

In this part of the PhD thesis, FEM of the open hole laminated composite developed in the previous section is utilized to validate the stress fields for the $[45°/90°/-45°/0°]_s$ IMA/M21E CFRP laminate generated using the analytical method are summarized in section 3.1.2 and chapter 5. Figure B.2 shows the total deformation of the laminate versus undeformed model plotted with multiplication factor of 35. Location of the detail region for stress plots on the quasi-isotropic laminate is depicted in Figure B.3. On the detail region normal stress distributions σ_x for each ply under uniaxial tension loading are displayed in Figure B.4. Figures show that depending on the fiber orientation, stress distribution in the vicinity of the hole changes. As we move away from the hole, homogenous stress distribution is observed. Figure B.5-Figure B.15 show contour plots of stress distributions for components σ_x, σ_y and τ_{xy}. We note that EPSM uses Lekhnitskii's[90] analytical

equations for determining the stress field in the CFRP OHT laminate. As seen from the figures, there is a good agreement between the analytical model and FEM.

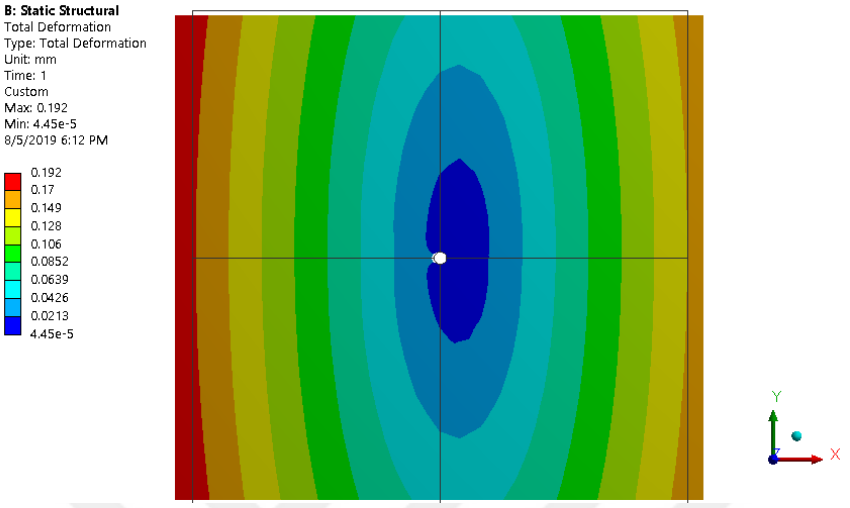

Figure B.2. Total deformation for the $[45°/90°/-45°/0°]_s$ IMA/M21E CFRP laminate vs. undeformed model.

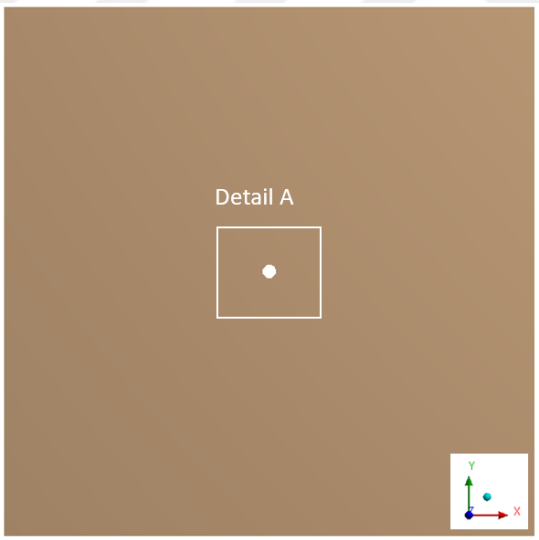

Figure B.3. Location of the detail region for stress plots on ply level of the IMA/M21E CFRP laminate under uniaxial tension loading.

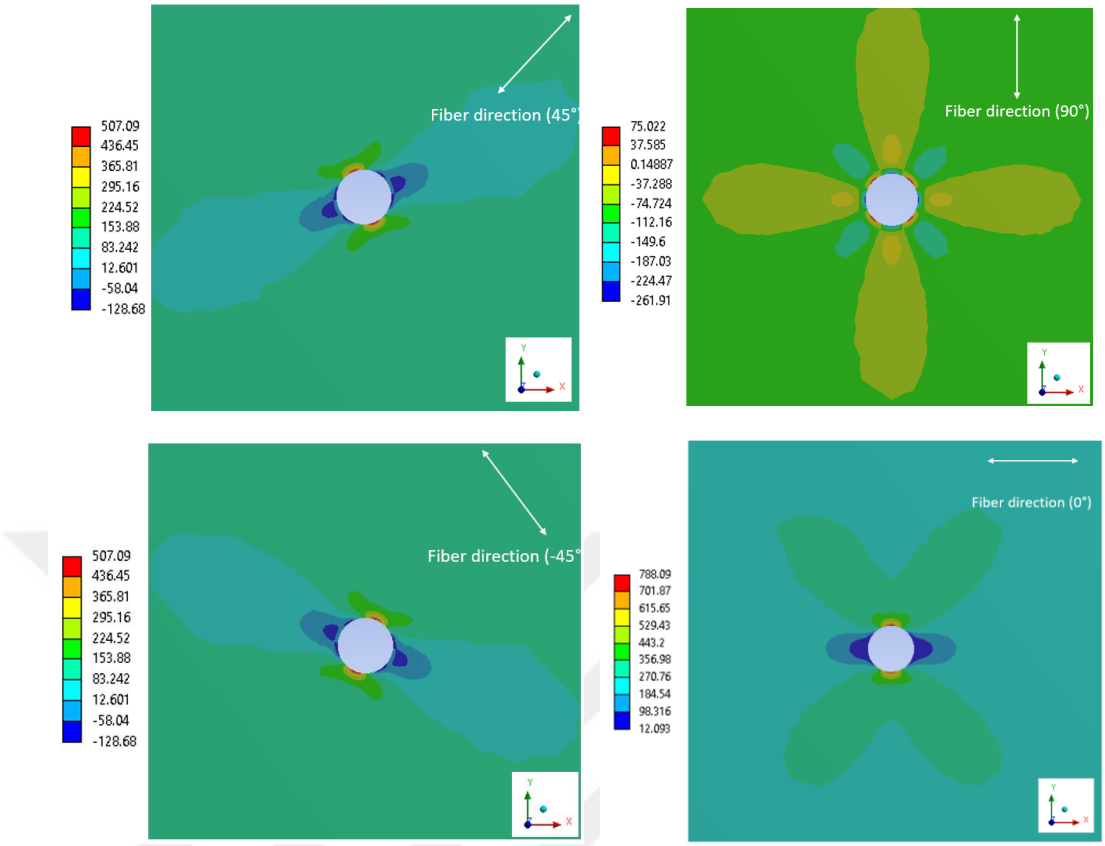

Figure B.4. σ_x distribution for 45°, 90°, -45°, 0° plies in the IMA/M21E CFRP laminate under uniaxial tension loading (Detail A).

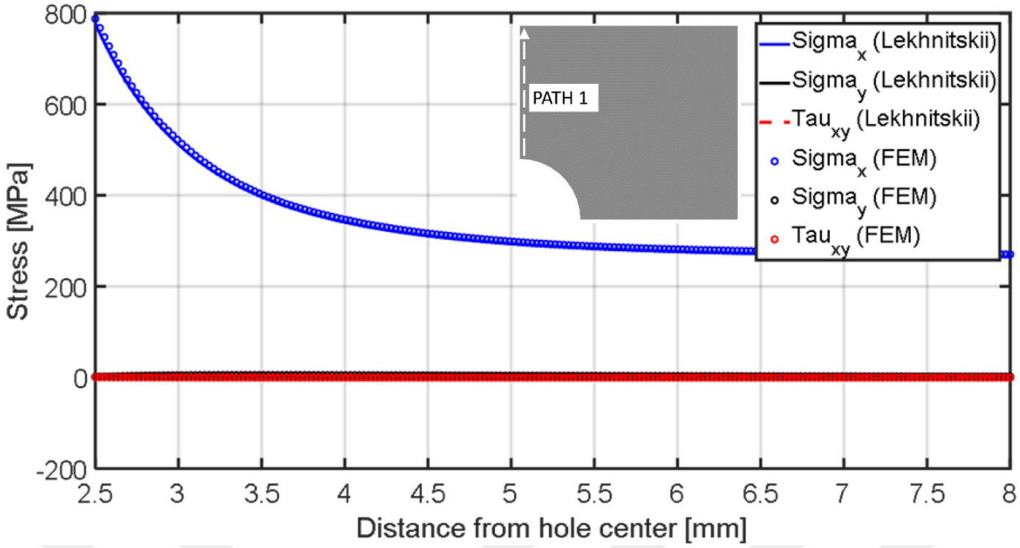

Figure B.5. Comparison of stress distributions along Path 1 in between analytical solution (Lekhnitskii) and FEM (orthotropic) for the 0° ply of the IMA/M21E laminate.

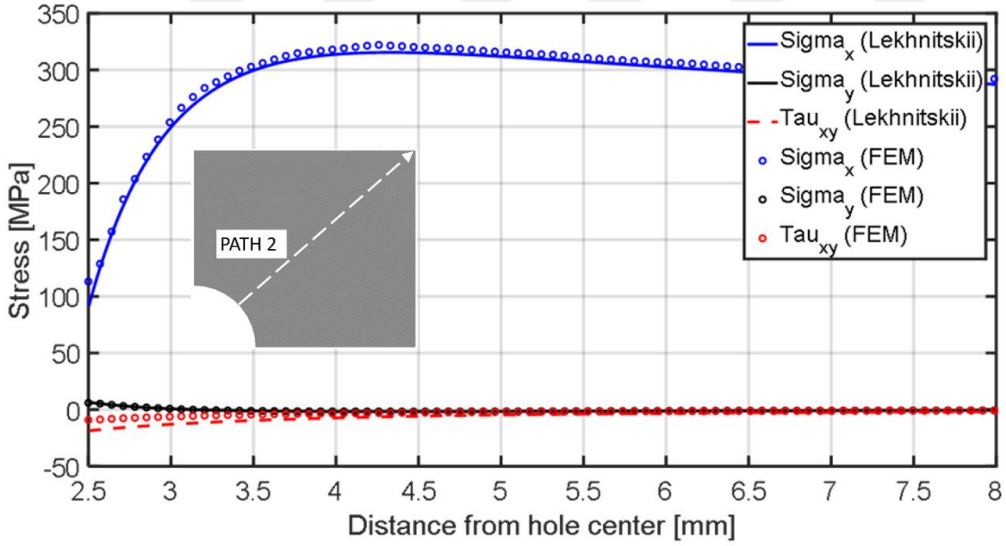

Figure B.6. Comparison of stress distributions along Path 2 in between analytical solution (Lekhnitskii) and FEM (orthotropic) for the 0° ply of the IMA/M21E laminate.

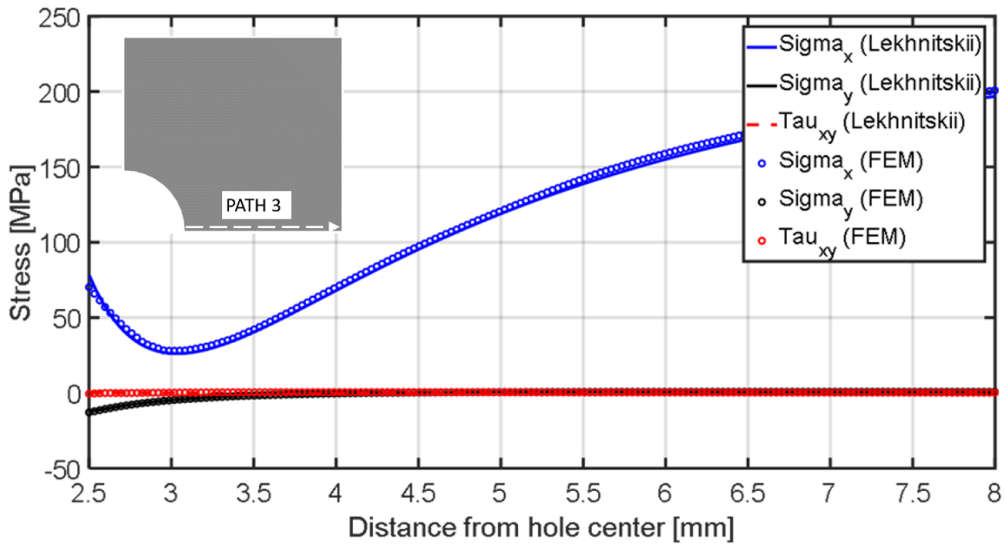

Figure B.7. Comparison of stress distributions along Path 3 in between analytical solution (Lekhnitskii) and FEM (orthotropic) for the 0° ply of the IMA/M21E laminate.

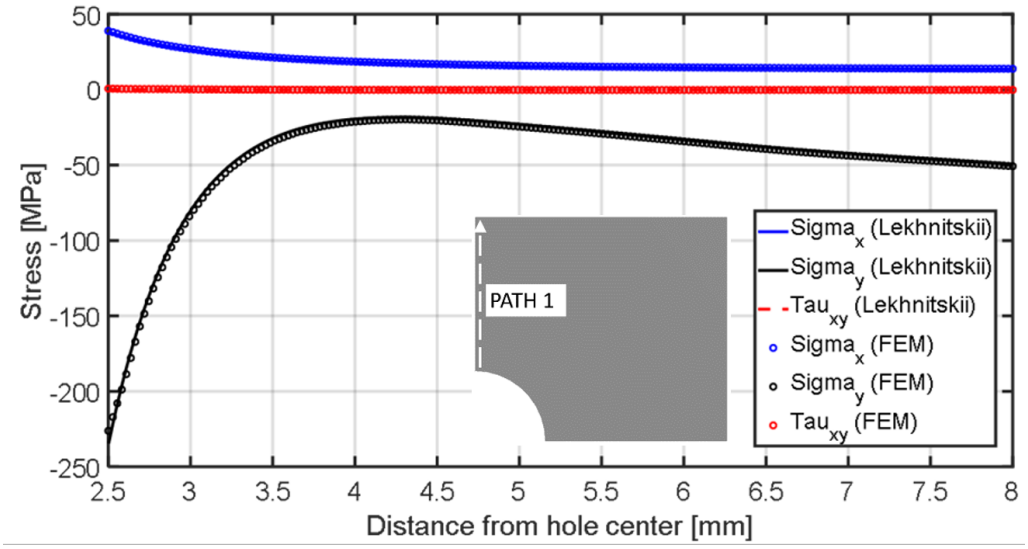

Figure B.8. Comparison of stress distributions along Path 1 in between analytical solution (Lekhnitskii) and FEM (orthotropic) for the 90° ply of the IMA/M21E laminate.

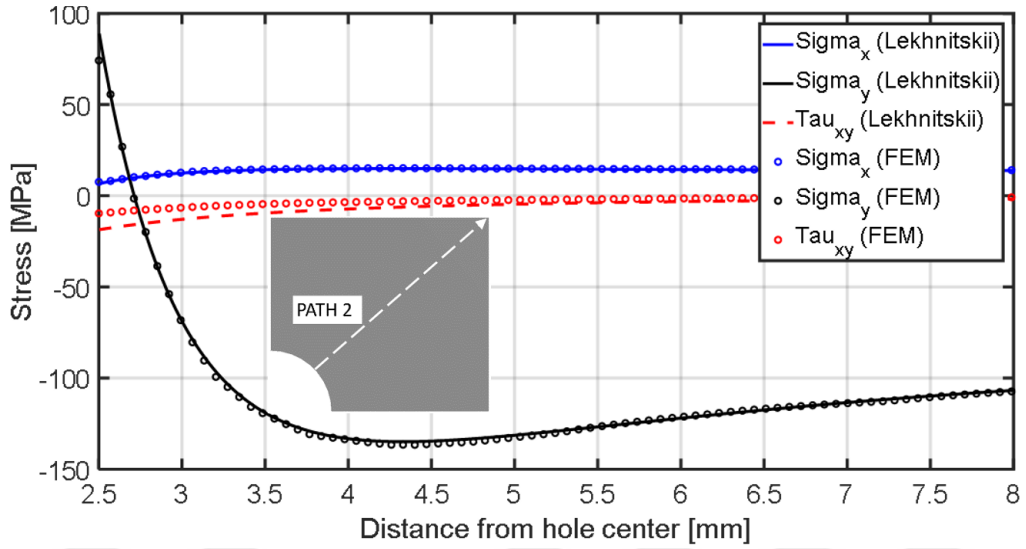

Figure B.9. Comparison of stress distributions along Path 2 in between analytical solution (Lekhnitskii) and FEM (orthotropic) for the 90° ply of the IMA/M21E laminate.

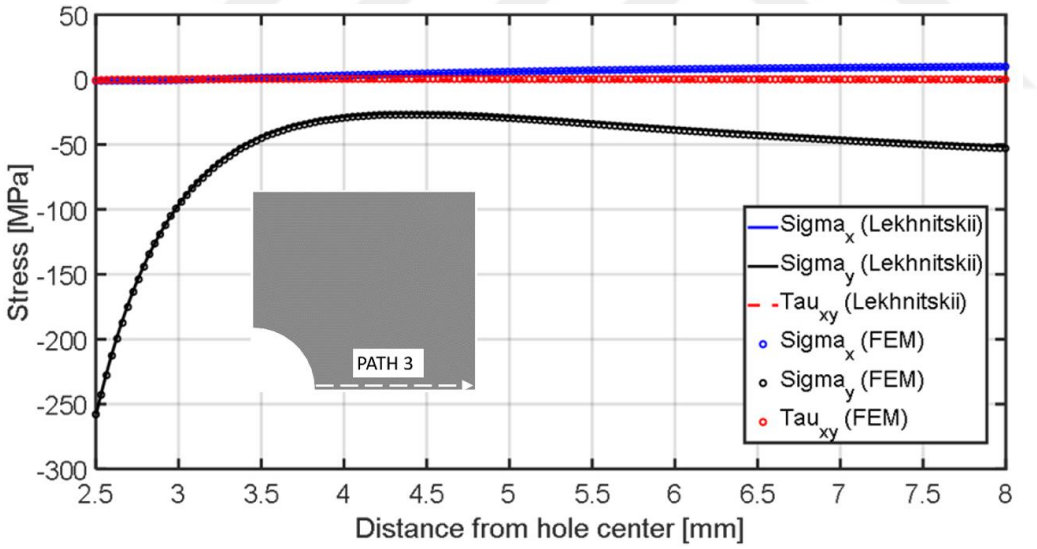

Figure B.10. Comparison of stress distributions along Path 3 in between analytical solution (Lekhnitskii) and FEM (orthotropic) for the 90° ply of the IMA/M21E laminate.

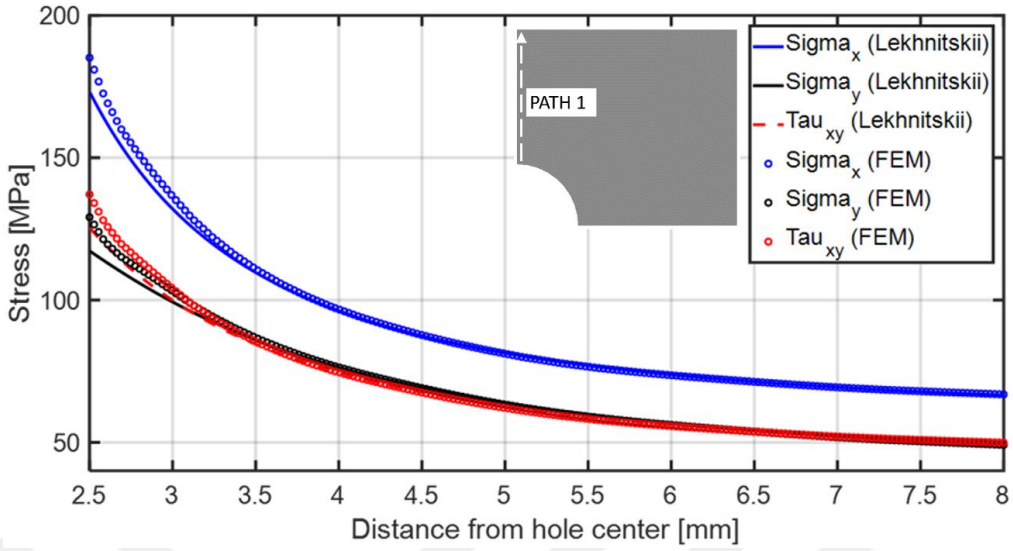

Figure B.11. Comparison of stress distributions along Path 1 in between analytical solution (Lekhnitskii) and FEM (orthotropic) for the 45° ply of the IMA/M21E laminate.

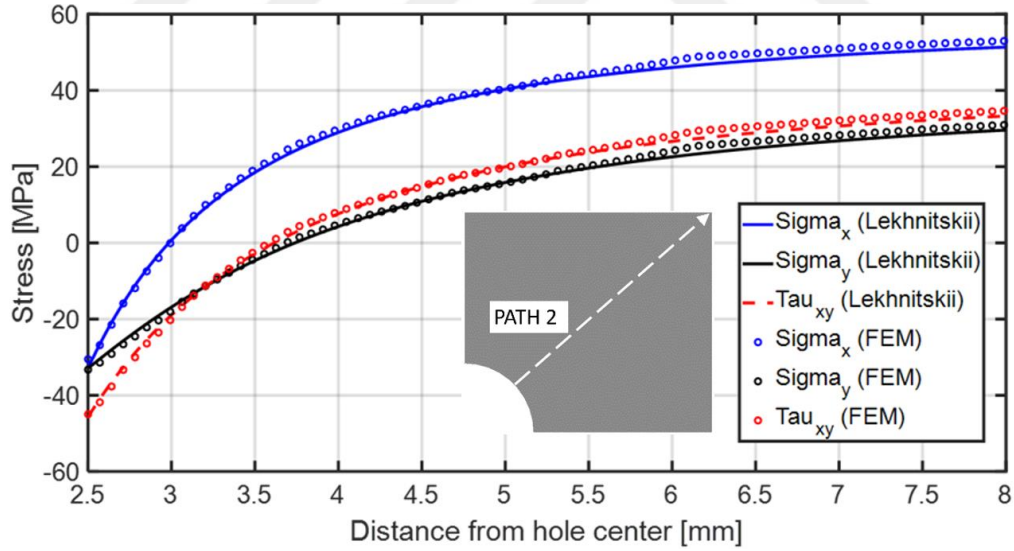

Figure B.12. Comparison of stress distributions along Path 2 in between analytical solution (Lekhnitskii) and FEM (orthotropic) for the 45° ply of the IMA/M21E laminate.

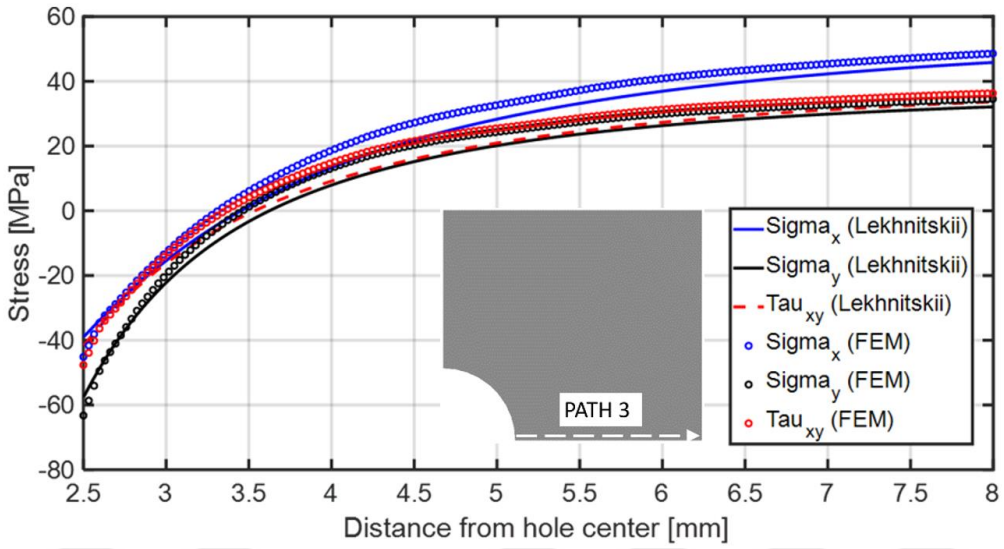

Figure B.13. Comparison of stress distributions along Path 3 in between analytical solution (Lekhnitskii) and FEM (orthotropic) for the 45° ply of the IMA/M21E laminate.

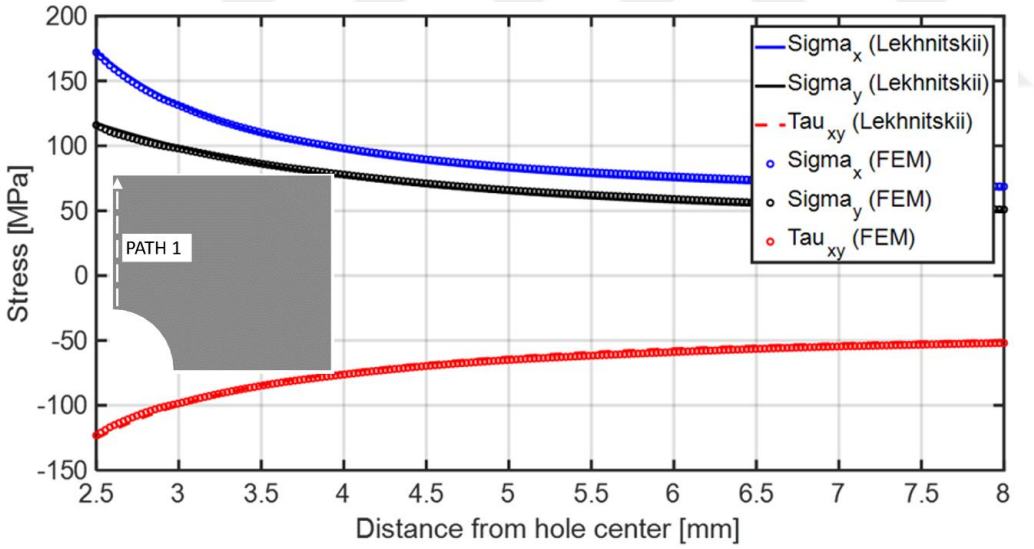

Figure B.14. Comparison of stress distributions along Path 1 in between analytical solution (Lekhnitskii) and FEM (orthotropic) for the -45° ply of the IMA/M21E laminate.

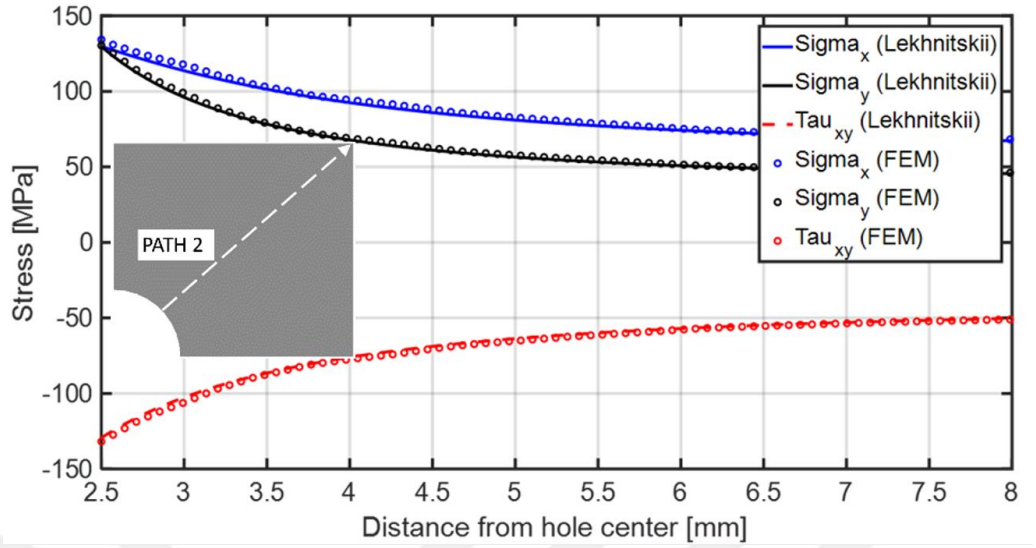

Figure B.15. Comparison of stress distributions along Path 2 in between analytical solution (Lekhnitskii) and FEM (orthotropic) for the -45° ply of the IMA/M21E laminate.

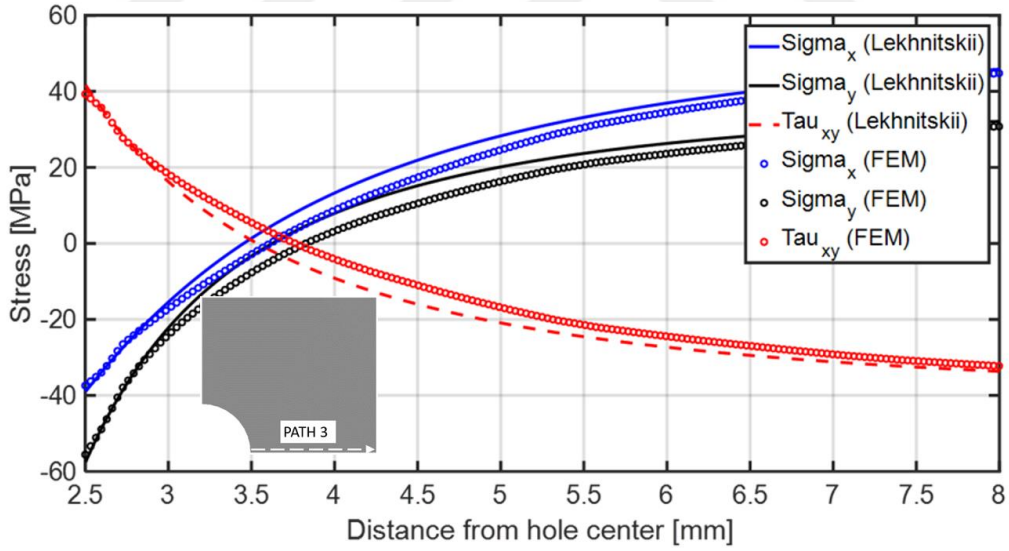

Figure B.16. Comparison of stress distributions along Path 3 in between analytical solution (Lekhnitskii) and FEM (orthotropic) for the -45° ply of the IMA/M21E laminate.

B.3 FE Model of the Laminate with an Open Hole (width-to-hole diameter: 40) under Biaxial Loading (shear plus uniaxial tension)

In this subsection FE Model of the laminate with an open hole under combined loading is explained. The same material properties, element types and boundary conditions applied to the FE Model in subsection B.1 is applied. In addition to the axial loading of N_x of 100 N/mm, shear loading of 100 N/mm is applied to the FE Model depicted in Figure B.17.

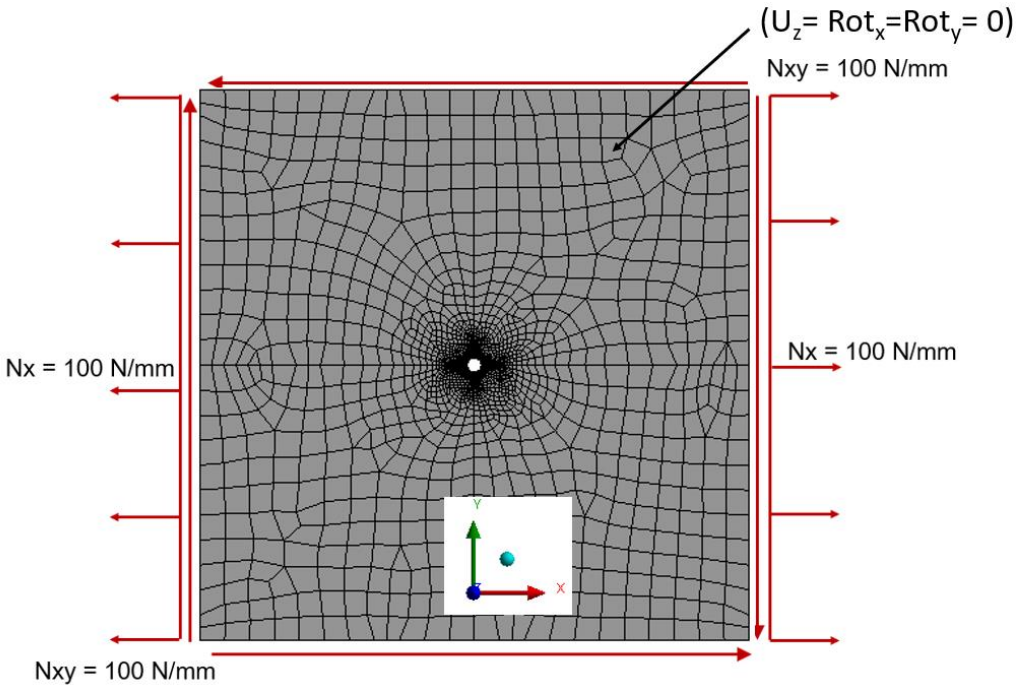

Figure B.17. Loads and boundary conditions of the $[45^o/90^o/-45^o/0^o]_s$ CFRP laminate (IMA/M21E) with an open hole (width-to-hole diameter=40) under biaxial loading.

B.4 Comparison of Stress Fields Generated by the Semi-Analytical EPSM Method and FEM for the Laminate with an Open Hole under Biaxial Loading (shear plus uniaxial tension)

In this subsection, FEM of the open hole laminated composite developed in the previous section is utilized to validate the stress fields for the $[45^o/90^o/-45^o/0^o]_s$ IMA/M21E CFRP laminate, which are generated using the semi-analytical method

summarized in section 3.1.2 and chapter 5. Under biaxial loading total deformation of the open hole laminate with a magnification factor 19 is displayed in Figure B.18. Figure B.19-Figure B.21 show contour plots of the stress distributions for the stress components σ_x, σ_y and τ_{xy}. As seen from the figures, the correlation of the results from the semi-analytical model and FEM is good.

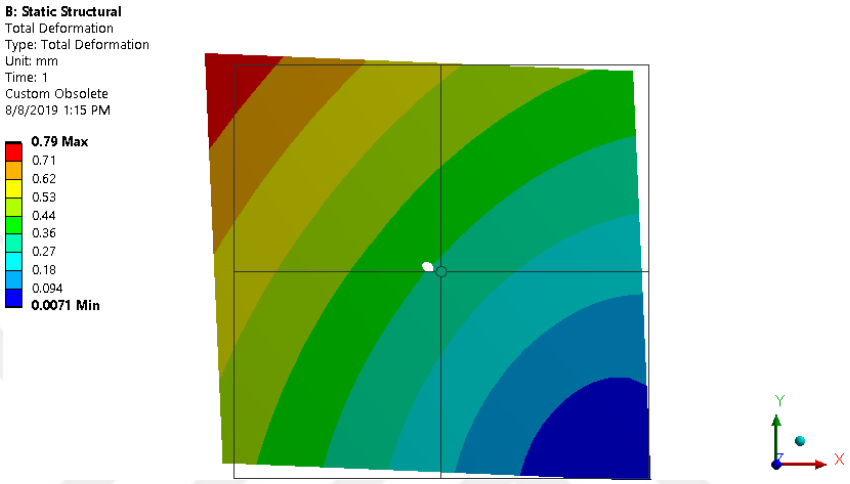

Figure B.18. Total deformation for the $[45°/90°/-45°/0°]_s$ IMA/M21E CFRP laminate vs. undeformed model.

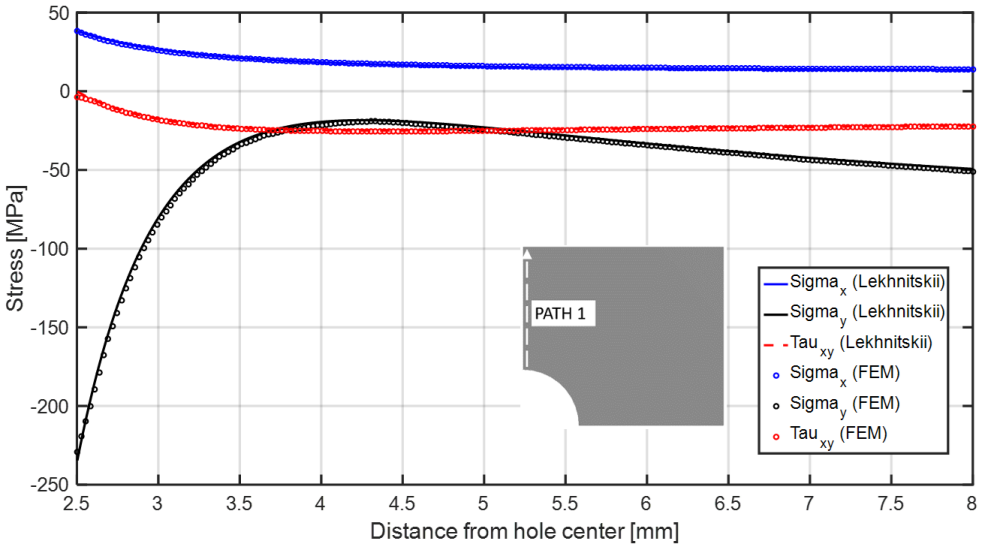

Figure B.19. Comparison of stress distributions along Path 1 between analytical solution (Lekhnitskii) and FEM (orthotropic) for the 90° ply of the IMA/M21E laminate.

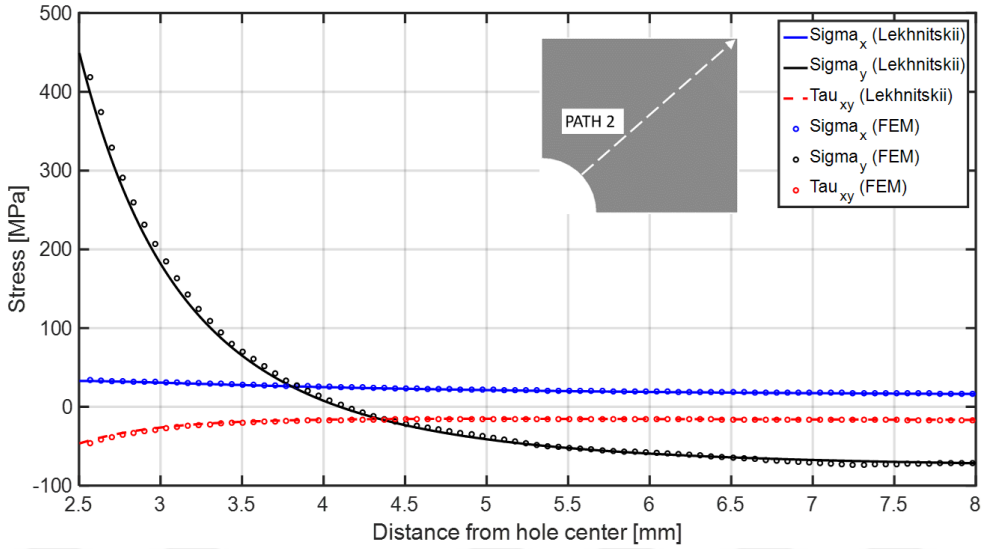

Figure B.20. Comparison of stress distributions along Path 2 between analytical solution (Lekhnitskii) and FEM (orthotropic) for the 90° ply of the IMA/M21E laminate.

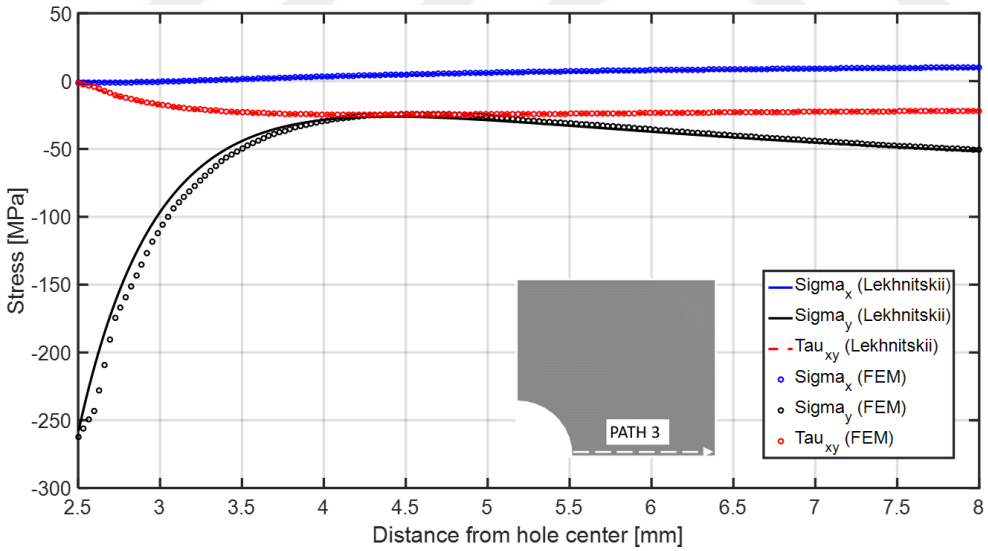

Figure B.21. Comparison of stress distributions along Path 3 between analytical solution (Lekhnitskii) and FEM (orthotropic) for the 90° ply of the IMA/M21E laminate.

B.5 FEM of the Laminate with an Open Hole (width-to-hole diameter=4) under Biaxial Loading (tension-tension)

FE Model of a 20 mm x 20 mm square $[45/90/-45/0]_s$ CFRP laminate (IMA/M21E) with an open hole under biaxial loading is depicted in Figure B.22. The same material properties and element types as in subsection B.1 are used in the FE Model. Since the model is symmetric with respect to its midplane in the thickness direction, only half of the layers are modeled. For this reason, rotational degrees of freedom in x and y directions as well as displacement degree of freedom in z direction are fixed on the symmetry plane. The necessary boundary conditions for this modeling technique are shown in Figure B.22. Regarding the loading condition, uniform displacements of 0.027 mm are applied to the right and upper edges of the laminate and the displacement degrees of freedom in the x-direction and y-directions are fixed on the left and lower laminate edges, respectively. This displacement loading produce reaction forces, which are membrane fluxes of N_x=100 N/mm on the left edge and N_y=100 N/mm on the lower side of the laminate. Since width to hole ratio is much lower compared to the model in B.1, displacement loading is implemented in the FEM in order to assure the desired uniform load distribution throughout the laminate.

B.6 Comparison of Stress Fields Generated by the Semi-Analytical EPSM Method and FEM for the Laminate with an Open Hole under Biaxial Loading (tension-tension)

In this subsection, FEM of the open hole laminated composite developed in the previous section is utilized to validate the stress fields for the $[45°/90°/-45°/0°]_s$ IMA/M21E CFRP laminate generated using the EPSM semi-analytical method summarized in section 3.1.2 and chapter 5. Since width to hole ratio is low in this case, finite width correction factor is included in the analytical method. Under biaxial loading, total deformation of the open hole laminate with a magnification factor of 52 is displayed in Figure B.23. Figure B.24-Figure B.26 show contour plots of stress

distributions for components σ_x, σ_y and τ_{xy}. As seen from the figures, the correlation of the results from the analytical model and FEM is good.

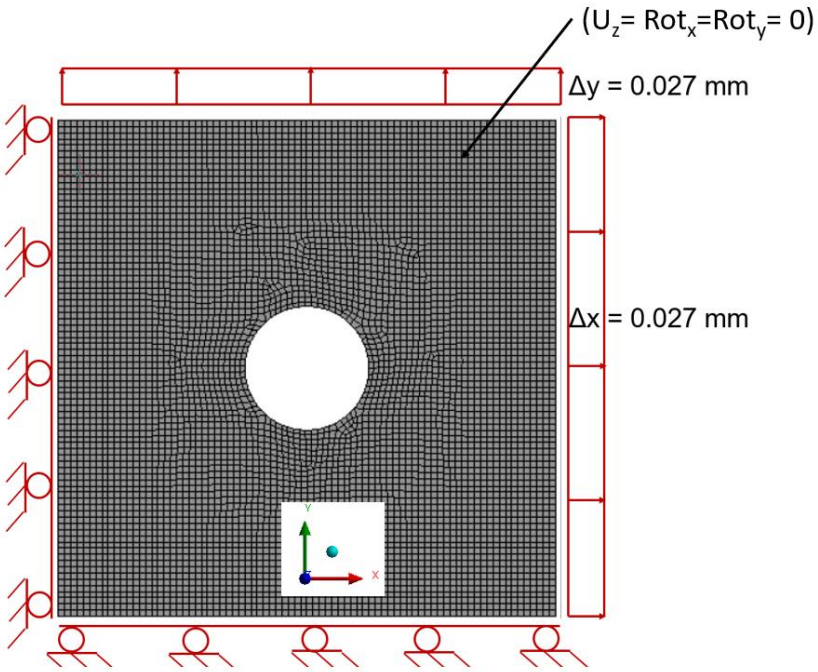

Figure B.22. Loads and boundary conditions of the $[45^o/90^o/-45^o/0^o]_s$ CFRP laminate (IMA/M21E) with an open hole (width/hole diameter=4).

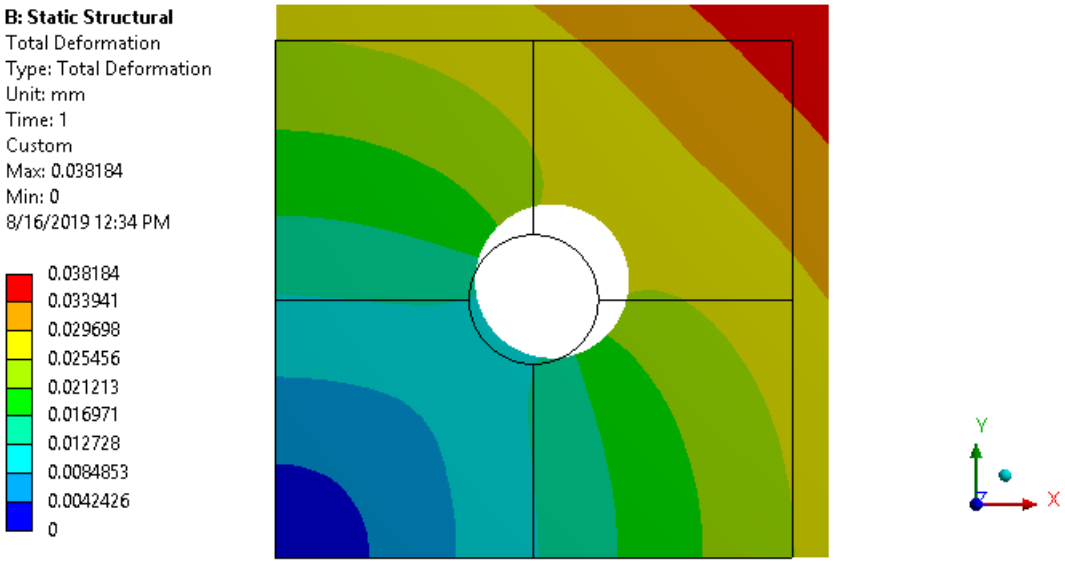

Figure B.23. Total deformation for the $[45°/90°/-45°/0°]_s$ IMA/M21E CFRP laminate vs. undeformed model.

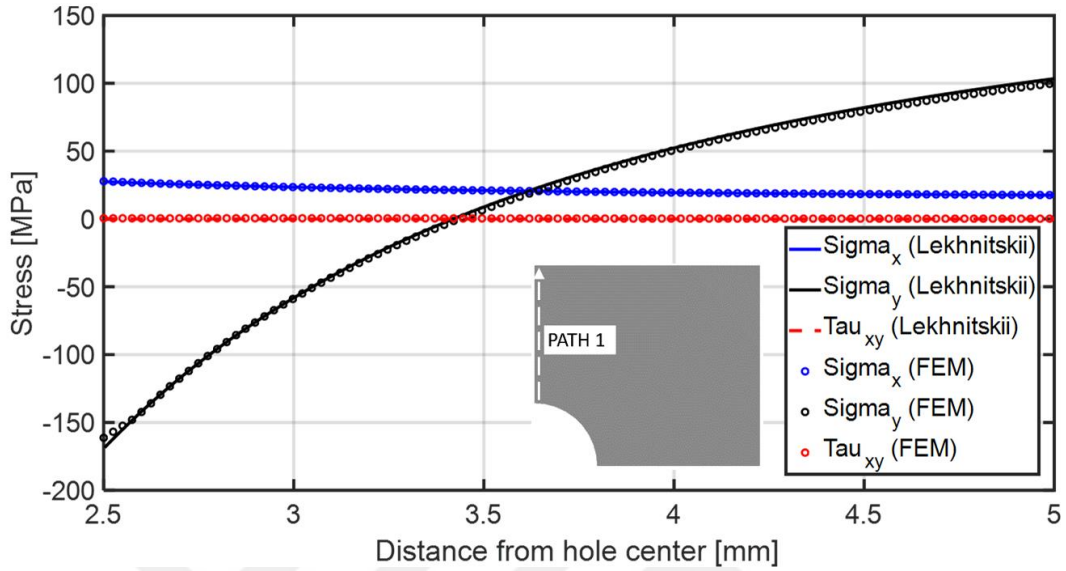

Figure B.24. Comparison of stress distributions along Path 1 between analytical solution (Lekhnitskii) and FEM (orthotropic) for the 90° ply of the IMA/M21E laminate.

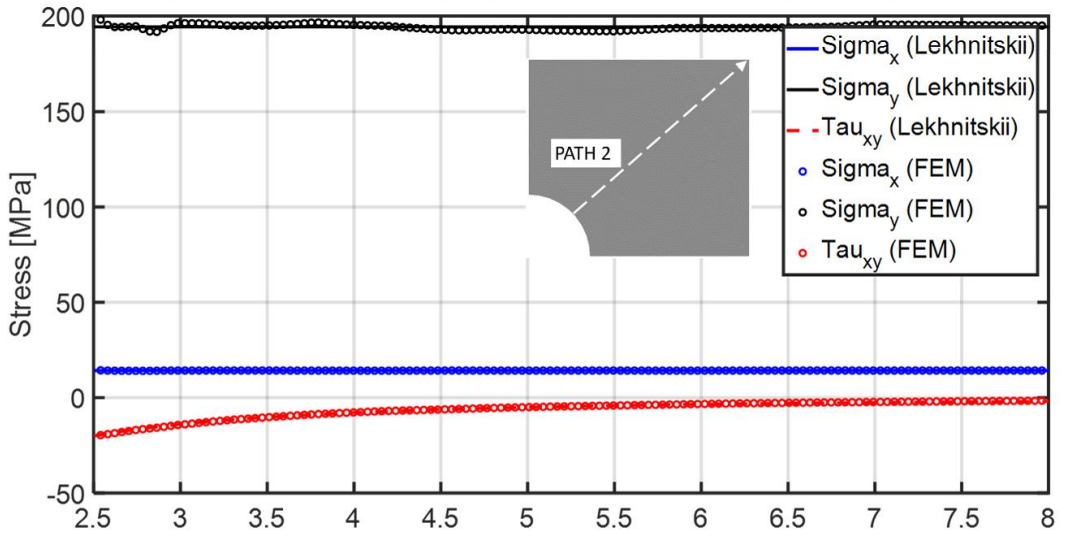

Figure B.25. Comparison of stress distributions along Path 2 between analytical solution (Lekhnitskii) and FEM (orthotropic) for the 90° ply of the IMA/M21E laminate.

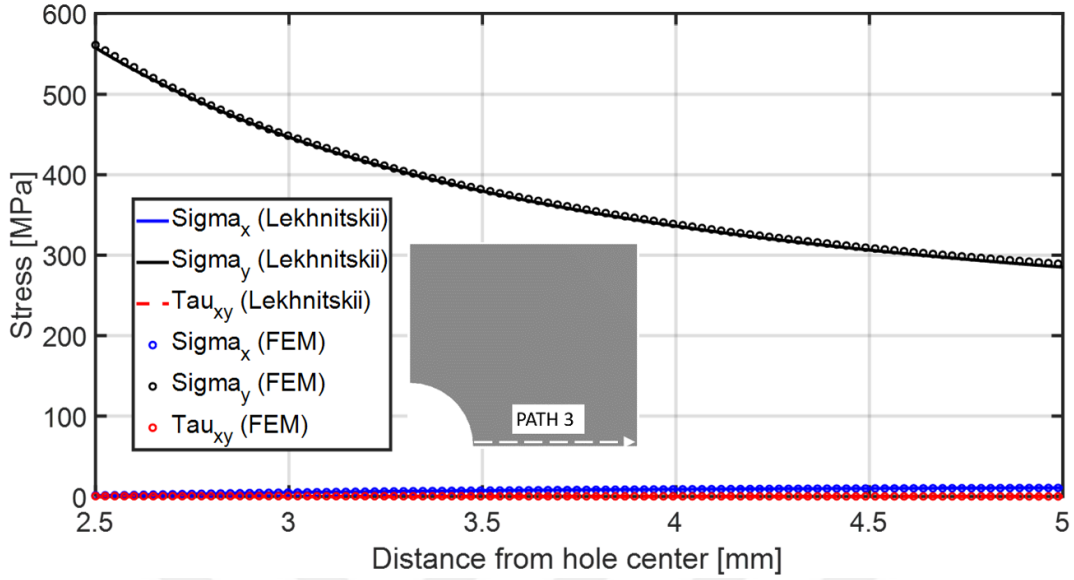

Figure B.26. Comparison of stress distributions along Path 3 between analytical solution (Lekhnitskii) and FEM (orthotropic) for the 90° ply of the IMA/M21E laminate.

C. Test Matrix of UD Tape Materials for Determining the Characteristic Distance

In this section test matrix for determining the characteristic distance and strength of the unidirectional composite material with different hole sizes and lay-up configurations is introduced. As a representative example for UD tape materials IMA/M21E (134 gr/m^2) is given. The variation of characteristic distance with lay-up influence and hole size is given by Karlak [16] by the following relation:

$$b_o = f(\frac{E_x}{G_{xy}})\sqrt{R} \tag{C.1}$$

where,

b_o : $characteristic\ distance$
E_x : $effective\ elasticity\ modulus$
G_{xy} : $effective\ shear\ modulus$
R : $hole\ radius$

Rearranging (C.1), the following relation is obtained:

$$\frac{b_o}{\sqrt{R}} = f(\frac{E_x}{G_{xy}}) \tag{C.2}$$

In equation (C.2) $f(\frac{E_x}{G_{xy}})$ is obtained by plotting $\frac{E_x}{G_{xy}}$ versus $\frac{b_o}{\sqrt{R}}$ as seen in Figure C.1 and has the form in (C.3). After curve fitting (C.3) the coefficients a_0, a_1, and a_2 are determined.

$$f(\frac{E_x}{G_{xy}}) = a_0 + a_1\left(\frac{E_x}{G_{xy}}\right) + a_2\left(\frac{E_x}{G_{xy}}\right)^2 \tag{C.3}$$

Open hole tensile/compressive strength of the open laminate is needed for calculating the characteristic distance. Tensile and compressive strengths are determined according to ASTM D5766 and ASTM D6484, respectively. Schematic representation of open hole test specimen is depicted in Figure C.2.

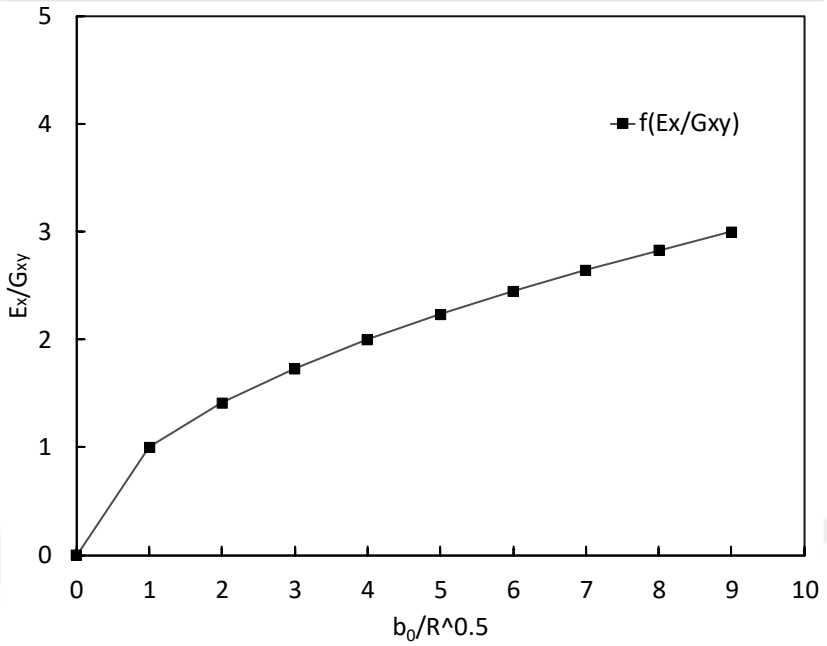

Figure C.1. Schematic representation of the variation of $\frac{b_0}{\sqrt{R}}$ with $\frac{E_x}{G_{xy}}$.

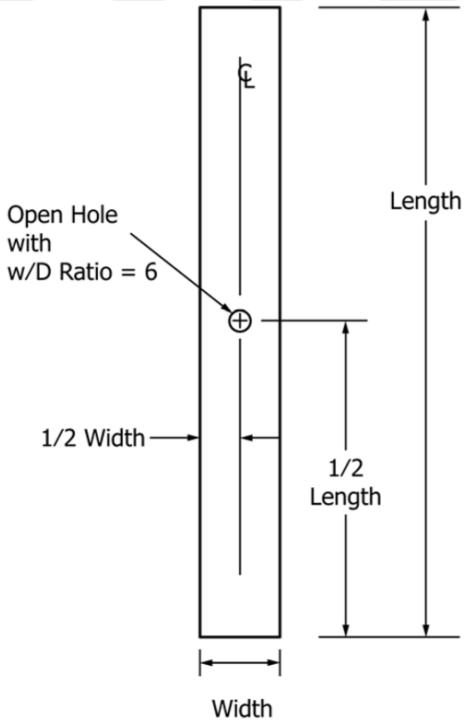

Figure C.2. Schematic representation of open hole test specimen according to ASTM D5766 and ASTM D6484.

Dimensions of the test specimen are chosen as:

Length=300, ply thickness ≅ 0.127

Note that, results are affected by the ratio of specimen width to hole diameter (w/D). According to the above-mentioned ASTM standards, this ratio should be maintained at 6, unless the experiment is investigating the influence of this ratio.

The following test matrix with 30 points (stacking sequence with 5 different variations versus 5 different hole diameters) is proposed to be used for plotting the curve in Figure C.2.

Table C.3. Test matrix for open hole IMA/M21E laminate for determining characteristic distance and strength.

		Hole Radius (mm)				
		2	4	6	8	10
Stacking Sequence	**Ex/Gxy**					
$[45/-45]_{8s}$	**0.39**	x	x	x	x	x
$[45/90/-45/90]_{4s}$	**1.07**	x	x	x	x	x
$[45/0/-45/90]_{4s}$	**2.64**	x	x	x	x	x
$[45/90/-45/0]_{4s}$	**3.92**	x	x	x	x	x
$[45/0/90/0]_{4s}$	**7.74**	x	x	x	x	x
$[90/0]_{8s}$	**19.45**	x	x	x	x	x

Test matrix above will be used for determining characteristic distance under tensile and compressive loading conditions.

CURRICULUM VITAE

PERSONAL INFORMATION

Surname, Name: Muyan, Mevlüt Can

EDUCATION

Degree	Institution	Year of Graduation	C.GPa
MS	DEU Mechanical Engineering	2006	3.44
BS	DEU Mechanical Engineering	2002	2.72

RESEARCH EXPERIENCE

Year	Place	Enrollment	Project, Responsibility
2020-2023	METUWIND	Scientific Project Expert	Static and dynamic analysis of the fan blades for the METUWIND large scale multi-purpose wind tunnel Research activities on the existing 5-m composite RÜZGEM wind turbine blade including progressive damage analysis, fatigue and vibration analysis
2020-2022	TUBITAK	TUBITAK PhD Candidate Scholar	Design, analysis, fabrication and test of a novel small horizontal axis wind turbine blade for use in urban areas

PROFESSIONAL EXPERIENCE

Year	Place	Enrollment	Project, Responsibility
2017-2019	METU PARGE	Research and Development Engineer	Development and validation of semi-analytical design methods for the static strength calculation of composite laminates with and without holes

2010-2014	AREVA Wind GmbH	Research and Development Engineer	Strength calculation of 5MW Offshore Wind Energy Converter components and constructions
2010-2010	Liebherr-Aerospace Lindenberg GmbH	CAE Engineer	Post-processing and evaluation of the stress analysis of the landing gear of AIRBUS A350 XWB aircraft and definition of optimization directions
2008-2010	MAN Turbo AG	Research and Development Engineer	Structural analysis of steam turbine rotor-blade systems
2005-2008	PMG Füssen GmbH	Mechanical Design Engineer	Stress calculation and optimization of P/M (Powder Metallurgy) gear/motor parts, high class precision tools (press- and calibration tools) and assemblies using FEM-Simulations
2004-2004	ISMB Dautermann GmbH	CAE Engineer	Structural vibration analysis of gearbox and electromechanical parts and assemblies using Finite Element Analysis
2002-2003	FAZ Elektrik A.Ş.	Research and Development Engineer	Research, development and optimization of the manufacturing process of an electromotor

FOREIGN LANGUAGES

Advanced English, Upper-Intermediate German

AWARDS & SCHOLARSHIPS

Awarded scholarship for the scientific stay as an Exchange Student at Rosenheim University of Applied Science during Spring 2003.

PUBLICATIONS

Published in peer-reviewed journals

C. Muyan, and D. Coker, "Finite element simulations for investigating the strength characteristics of a 5 m composite wind turbine blade", *Wind Energy Science,* vol. 5, 1339–1358, (2020). https://doi.org/10.5194/wes-5-1339-2020 (ESCI)

Journal manuscripts under review

Can Muyan, Onur Ali Batmaz, Abolfazl Pourrajabian, Demirkan Çöker, Altan Kayran, David Wood,"Efficient Inclusion of Structural Analysis in the Multi-dimensional Optimization of Small Wind Turbine Blades" submitted on 30.10.2022 to Energy for Sustainable Development (SCIE).

Journal manuscripts in preparation

C. Muyan, A. Gezer, and D. Coker, "A Comparative Study of Analytical Approaches for the Open Hole Strength Prediction of Composite Laminates Subjected to Uniaxial and Biaxial Loading Conditions" to be submitted to Composite Structures (SCIE).

International Proceedings / Conference Papers

C. Muyan and D. Coker, "Strength Analysis of a 5-m Composite Wind Turbine Blade under Static and Fatigue Loading Conditions", IOP Conference Series: Materials Science and Engineering, vol. 942, No.1, (2020). https://doi.org/10.1088/1757-899X/942/1/012045 (SCI).

M. Ozyildiz, C. Muyan and D. Coker, "Strength Analysis of a Composite Turbine Blade Using Puck Failure Criteria", Journal of Physics: Conference Series, vol. 1037, 042027, (2018). https://doi.org/10.1088/1742-6596/1037/4/042027 (SCI).

National Proceedings / Conference Papers

C. Muyan, O.A. Batmaz ve D. Coker, "5-m Kompozit Rüzgar Türbini Kanadı Sonlu Elemanlar Modelinin Doğrulanması ve İlerlemeli Intralaminar Hasar Analizi", 6. İzmir Rüzgar Sempozyumu, 23-24 Eylül 2021, Çevrimiçi Etkinlik.

O.A. Batmaz, C. Muyan ve D. Coker, "Rüzgar Türbin Kanatlarında Yapıştırıcı Ayrılma Hasarının Kanat Yapısal Bütünlüğüne Etkisi", 6. İzmir Rüzgar Sempozyumu, 23-24 Eylül 2021, Çevrimiçi Etkinlik.

C. Muyan, D. Coker, “Kompozit Rüzgar Türbin Kanadının Mukavemet Özelliklerinin İlerlemeli Hasar Analizi Yöntemiyle İyileştirilmesi”, 5. İzmir Rüzgar Sempozyumu, 3-5 Ekim 2019, İzmir, Türkiye.

Technical Periodicals

A. Piepenbrink, F. X. Brunner, F. Aschl, S. Kurz, C. Muyan and M. Schaule, “FEM-Modellvalidierung komplexer Konvektions-Temperierung elecktronischer Bauteile im Leadframe mit I-DEAS ESC/TMG”, Interface Magazine, SIEMENS PLM Software, Ausgabe 2-2004. (Article, which is about my M. Sc. Thesis, is published in the technical periodical of SIEMENS PLM Software in German Language) https://www.plm.automation.siemens.com/de_de/Images/if2-2004_tcm73-62614.pdf (pages 18-19).

Oral Presentations

C. Muyan, O.A. Batmaz and D. Coker, “FE Model Validation and Progressive Damage Analysis of a 5-m Composite Wind Turbine Blade under Monotonic Loading”, EAWE PhD Seminar 2022, November 2-4, 2022, Bruges, Belgium.

C. Muyan, O.A. Batmaz ve D. Coker, “5-m Kompozit Rüzgar Türbini Kanadı Sonlu Elemanlar Modelinin Doğrulanması ve İlerlemeli Intralaminar Hasar Analizi”, 6. İzmir Rüzgar Sempozyumu, 23-24 Eylül 2021, Çevrimiçi Etkinlik.

O.A. Batmaz, C. Muyan ve D. Coker, “Rüzgar Türbin Kanatlarında Yapıştırıcı Ayrılma Hasarının Kanat Yapısal Bütünlüğüne Etkisi”, 6. İzmir Rüzgar Sempozyumu, 23-24 Eylül 2021, Çevrimiçi Etkinlik.

C. Muyan and D. Coker, “Strength Analysis of a 5-m Composite Wind Turbine Blade Subjected to Monotonic and Cyclic Loading”, EAWE PhD Seminar 2020, December 14-16, 2020, Online Event.

C. Muyan and D. Coker, “Strength Analysis of a 5-m Composite Wind Turbine Blade under Static and Fatigue Loading Conditions”, 41st International Risoe Symposium on Materials Science, 7-10 September 2020, Roskilde, Denmark.

C. Muyan and D. Coker,” Progressive Damage Modeling for Improving Strength Characteristics a Composite Wind Turbine Blade”, Wind Energy Science Conference (WESC 2019), 17-20 June, 2019, Cork, Ireland.

C. Muyan and D. Coker, “A Study on the Progressive Damage Development of a Wind Turbine Aeroshell during Virtual Full-Scale Structural Test”, EAWE PhD Seminar 2019, October 29-31, 2019, Nantes, France.

C. Muyan ve D. Coker, “Kompozit Rüzgar Türbin Kanadının Mukavemet Özelliklerinin İlerlemeli Hasar Analizi Yöntemiyle İyileştirilmesi”, 5. İzmir Rüzgar Sempozyumu, 3-5 Ekim 2019, İzmir, Türkiye.

Poster Presentations

A. Gezer, C. Muyan and D. Coker,”A Comparative Study of Analytical and Numerical Approaches for the Open Hole Strength Prediction of Composite Laminates”, Aerospace Europe Conference (AEC 2020), 20-25 February, 2020, Bordeaux, France.

M. Ozyildiz, C. Muyan and D. Coker,”Strength Analysis of a Composite Wind Turbine Blade Using Puck and Tsai-Wu Failure Criteria”, 7th Conference on Science of Making Torque from Wind (TORQUE 2018), 20-22 June, 2018, Milan, Italy.